PhD Dissertation

COMPLEX SYSTEMS BASED ON COORDINATION CAGES

Submitted by

Christoph Drechsler

Prepared at the

Department of Chemistry and Chemical Biology

TU Dortmund University

Dortmund 2024

This work has been prepared from November 2019 to July 2023 at the Department of Chemistry and Chemical Biology at TU Dortmund University under supervision of Prof. Dr. Guido H. Clever.

May all beings be happy.

Examiner: **Prof. Dr. Guido H. Clever**

Faculty of Chemistry and Chemical Biology,
TU Dortmund University,
Otto-Hahn-Straße 6, 44227 Dortmund

Coexaminer: **Prof. Dr. Stefan M. Kast**

Faculty of Chemistry and Chemical Biology,
TU Dortmund University,
Otto-Hahn-Straße 4a, 44227 Dortmund

Submission Date: 15.07.2024

Eidesstattliche Versicherung

(Affidavit)

Drechsler, Christoph

Name, Vorname
(surname, first name)

167526

Matrikelnummer
(student ID number)

☒ Doktorarbeit
(dissertation)

Titel
(Title)

Complex Systems based on Coordination Cages

Ich versichere hiermit an Eides statt, dass ich die vorliegende Abschlussarbeit mit dem oben genannten Titel selbstständig und ohne unzulässige fremde Hilfe erbracht habe. Ich habe keine anderen als die angegebenen Quellen und Hilfsmittel benutzt sowie wörtliche und sinngemäße Zitate kenntlich gemacht. Die Arbeit hat in gleicher oder ähnlicher Form noch keiner Prüfungsbehörde vorgelegen.

I declare in lieu of oath that I have completed the present thesis with the above-mentioned title independently and without any unauthorized assistance. I have not used any other sources or aids than the ones listed and have documented quotations and paraphrases as such. The thesis in its current or similar version has not been submitted to an auditing institution before.

Ort, Datum
(place, date)

Unterschrift
(signature)

Belehrung:
Wer vorsätzlich gegen eine die Täuschung über Prüfungsleistungen betreffende Regelung einer Hochschulprüfungsordnung verstößt, handelt ordnungswidrig. Die Ordnungswidrigkeit kann mit einer Geldbuße von bis zu 50.000,00 € geahndet werden. Zuständige Verwaltungsbehörde für die Verfolgung und Ahndung von Ordnungswidrigkeiten ist der Kanzler/die Kanzlerin der Technischen Universität Dortmund. Im Falle eines mehrfachen oder sonstigen schwerwiegenden Täuschungsversuches kann der Prüfling zudem exmatrikuliert werden. (§ 63 Abs. 5 Hochschulgesetz - HG -).

Die Abgabe einer falschen Versicherung an Eides statt wird mit Freiheitsstrafe bis zu 3 Jahren oder mit Geldstrafe bestraft.

Die Technische Universität Dortmund wird ggf. elektronische Vergleichswerkzeuge (wie z.B. die Software „turnitin“) zur Überprüfung von Ordnungswidrigkeiten in Prüfungsverfahren nutzen.

Die oben stehende Belehrung habe ich zur Kenntnis genommen:

Official notification:
Any person who intentionally breaches any regulation of university examination regulations relating to deception in examination performance is acting improperly. This offense can be punished with a fine of up to EUR 50,000.00. The competent administrative authority for the pursuit and prosecution of offenses of this type is the Chancellor of TU Dortmund University. In the case of multiple or other serious attempts at deception, the examinee can also be unenrolled, Section 63 (5) North Rhine-Westphalia Higher Education Act (*Hochschulgesetz, HG*).

The submission of a false affidavit will be punished with a prison sentence of up to three years or a fine.

As may be necessary, TU Dortmund University will make use of electronic plagiarism-prevention tools (e.g. the "turnitin" service) in order to monitor violations during the examination procedures.

I have taken note of the above official notification:*

Ort, Datum
(place, date)

Unterschrift
(signature)

Abstract

Systems chemistry draws profound inspiration from the intricate and dynamic systems observed in nature. It examines the collective behaviors and interactions of molecular networks striving to uncover the principles that govern their self-organization, adaptation, and evolution, unlike traditional chemistry, which often focuses on individual molecules and their isolated reactions. By mimicking nature's strategies, where complex systems such as cellular processes and other biological networks demonstrate remarkable resilience, efficiency, and adaptability, researchers aim to design artificial systems that exhibit similar properties. This approach not only enhances our understanding of fundamental chemical processes but also holds potential for revolutionary applications in materials science, medicine, and nanotechnology, offering solutions that are both innovative and sustainable.

Coordination cage chemistry, a sub-field of supramolecular chemistry, deals about large and hollow and thus enzyme-like molecular structures formed by metal ions and organic linkers or ligands. Coordination cages are ideal to contribute to systems chemistry because the reversible coordination bonds and dynamic guest binding make them flexible and adaptive. They make excellent models for understanding and imitating the complex systems found in nature. In our group we focus on lantern-shaped $Pd^{II}_2\mathbf{L}_4$ species, where **L** is a bent, bis-monodentate ligand so that the cavity has four apertures and small guests, often anions, can bind inside.

The increasing complexity of artificial chemical systems causes challenges in analytics. Mass spectrometry, especially in combination with ion mobility spectrometry, is a valuable tool for the detailed breakdown of complex mixtures. In the first part of this work, Trapped Ion Mobility Spectrometry is used in combination with computational collisional cross section calculation to investigate the structure of palladium(II) based coordination cages. The experimentally obtained ion mobility *K* is transformed into the collisional cross section. For the theoretical counterpart, an *in silico* model of the coordination cage is either geometry optimized or used for a short molecular dynamics simulation to obtain an ensemble of conformations. The theoretical collisional cross section of the obtained structure(s) is calculated and compared with the experimental value to see if the model matches the real situation. Especially the in the gas phase more relevant London dispersion has a large influence not only on the side chain behavior but also on the whole structure of the cages. Possible dispersion driven compactions of cages in the gas phase are investigated using the described workflow as well as *ab initio* quantum mechanical calculations.

Returning to systems chemistry, in the second part of this work, complex mixtures of coordination cages containing photoswitches are investigated. Here, new heteroleptic cages (cages containing more than one type of ligand) containing photoswitchable dithienylethene (DTE) units were formed and characterized. Combinations of these heteroleptic cages and subcomponents thereof led to interesting, interconnected complex mixtures. Irradiation experiments causing the DTE units to photoswitch induced changes in the whole complex mixture due to the strong interconnectivity of the systems' subcomponents. It was possible to switch between different mixtures of coordination cages with varying complexity.

Of special interest are systems that exist outside the chemical equilibrium due to their similarity to biological, living systems. In the third part, the slow formation of interpenetrated double cages with three small pockets from monomeric cages with large pockets is used to temporarily encapsulate a large guest inside the monomeric cage that would be too large for the small pockets of the double cage. The transient state, being the monomeric cage that is able to encapsulate the guest, is kept up as long as enough fuel is available. In this system, fuel would be the palladium(II) metal ions and the free banana-shaped ligand and the double cage is the waste. This new concept for transient guest binding is investigated regarding its properties and boundaries.

Zusammenfassung

Die Systemchemie lässt sich von den komplizierten und dynamischen Systemen in der Natur inspirieren. Im Gegensatz zur traditionellen Chemie, die sich oft auf einzelne Moleküle und ihre isolierten Reaktionen konzentriert, untersucht die Systemchemie das kollektive Verhalten und die Interaktionen molekularer Netzwerke und versucht, die Prinzipien aufzudecken, die ihre Selbstorganisation, Anpassung und Evolution bestimmen. Indem sie die Strategien der Natur nachahmen, in der komplexe Systeme wie zelluläre Prozesse und andere biologische Netzwerke eine bemerkenswerte Widerstandsfähigkeit, Effizienz und Anpassungsfähigkeit aufweisen, wird versucht, künstliche Systeme zu entwerfen, die ähnliche Eigenschaften aufweisen. Dieser Ansatz verbessert nicht nur unser Verständnis grundlegender chemischer Prozesse, sondern birgt auch das Potenzial für revolutionäre Anwendungen in den Materialwissenschaften, der Medizin und der Nanotechnologie. Die Koordinationskäfigchemie, ein Teilgebiet der supramolekularen Chemie, befasst sich mit großen und hohlen und damit enzymähnlichen Molekülstrukturen, die durch Metallionen und koordinierende organische Linker gebildet werden. Koordinationskäfige sind ideal, um zur Systemchemie beizutragen, da die reversiblen Koordinations- und dynamische Gastbindungen sie flexibel und anpassungsfähig machen. Sie sind hervorragende Modelle für Verständnis und Nachahmung natürlicher komplexer Systeme.

Die zunehmende Komplexität der Systeme führt zu Herausforderungen in der Analytik. Die Massenspektrometrie, insbesondere in Kombination mit der Ionenmobilitätsspektrometrie (IMS), ist ein wertvolles Instrument für die Aufschlüsselung komplexer Gemische. Im ersten Teil dieser Arbeit wird die IMS in Kombination mit der theoretischen Berechnung des Kollisionsquerschnitts (CCS) eingesetzt, um die Struktur von Pd^{II}-Koordinationskäfigen zu untersuchen. Für das theoretische Gegenstück wird entweder ein geometrisch optimiertes *in silico* Modell des Koordinationskäfigs oder ein durch kurze Molekulardynamiksimulation generiertes Konformationsensemble verwendet. Der theoretische CCS der erhaltenen Struktur(en) wird berechnet und mit dem experimentellen Wert verglichen, um festzustellen, ob das Modell mit der realen Situation übereinstimmt. Insbesondere die in der Gasphase relevantere London-Dispersion hat einen großen Einfluss nicht nur auf das Verhalten der Seitenketten, sondern auch auf die gesamte Struktur der Käfige. Mögliche dispersionsbedingte Faltungen von Käfigen in der Gasphase werden mit dem beschriebenen Arbeitsablauf sowie mit *ab initio* quantenmechanischen Berechnungen untersucht.

Im zweiten Teil dieser Arbeit werden komplexe Mischungen von Koordinationskäfigen, die Photoschalter enthalten, untersucht, um zur Systemchemie zurückzukehren. Hier wurden neue heteroleptische Käfige mit photoschaltbaren Dithienylethen-Einheiten (DTE) gebildet und charakterisiert. Kombinationen dieser heteroleptischen Käfige und ihrer Teilkomponenten führten zu interessanten, miteinander verbundenen komplexen Gemischen. Bestrahlungsexperimente zur Schaltung der DTE-Einheiten führten zu Veränderungen im gesamten komplexen Gemisch, da die Teilkomponenten des Systems miteinander verbunden waren. Es war möglich, zwischen verschiedenen Mischungen von Koordinationskäfigen mit unterschiedlicher Komplexität zu wechseln.

Besonders interessant sind Systeme, die aufgrund ihrer Ähnlichkeit mit biologischen, lebenden Systemen außerhalb des chemischen Gleichgewichts existieren. Im dritten Teil wird die langsame Bildung von interpenetrierenden Doppelkäfigen mit drei kleinen Bindungstaschen aus monomeren Käfigen mit je einer großen Bindungstasche genutzt, um einen großen Gast vorübergehend im Inneren des monomeren Käfigs zu binden, der für die kleinen Taschen des Doppelkäfigs zu groß wäre. Der Übergangszustand, indem der Gast gebunden ist, wird so lange aufrechterhalten, wie genügend *fuel* vorhanden ist. In diesem System wären die Pd^{II}-Metallionen und der freie bananenförmige Ligand das *fuel* und der Doppelkäfig das *waste*. Dieses neue Konzept für temporäre Gastbindung wird auf seine Eigenschaften und Grenzen hin untersucht.

Table of Content

1 Introduction

This work deals with complex systems made from coordination cages. For a classification of the here investigated subjects into the scientific world and for the motivation behind the research, first a brief overview of three very broad areas of chemistry, namely Supramolecular Chemistry and its subfield Coordination Cage Chemistry and Systems Chemistry, are given.

1.1 Supramolecular Chemistry

Supramolecular chemists design and study usually discrete molecular systems with emphasis on intermolecular interactions.[1,2] The importance of this gigantic field of research is ever growing as the consideration of non-covalent interactions allows the creation of more complex nanoscale architectures and allows out-of-the-box thinking when trying to find solutions to chemical problems and thus represents the base for the bottom-up approach of nanotechnology.[3,4] In addition, supramolecular interactions between molecules are reversible and dynamic, which allows contribution to the field of transient and out-of-equilibrium chemistry.[5]

Supramolecules can be defined as systems containing usually two or more molecules that are bound to each other either non-covalently or via hydrogen bonds, mechanical bonds or dynamic covalent or coordinative bonds (metallosupramolecular). They can be catalogized into different classes, for example host-guest complexes, macrocycles, knots, foldamers,[6] rotaxanes, catenanes,[7,8] helicates,[9] cages and capsules[10] to name a few. The field of molecular machines, based on as switches[11] and motors[12] is usually considered as a part of supramolecular chemistry as well as it usually deals with discrete molecules and requires the extended possibilities enabled by considering not only covalent bonds but also non-covalent interactions.[2]

It is important to state that for supramolecular chemistry, nature on a molecular level has been the paragon of efficiency regarding selectivity, functionality and longevity. Biochemical mechanisms have been perfected through evolutionary processes for billions of years while artificial systems that incorporate intermolecular binding interactions have been thoroughly developed and investigated since only a few decades.[13] Chemists try to understand and mimic nature and use its methods to converge to its efficiency, resilience and adaptability.

In the following, different types of interactions between molecules or between groups within the same molecular entity will be elucidated in detail.

The most obvious non-covalent interaction would be the attractive force between a cation and an anion, often labeled as ion bonding, ion pairing or salt bridges. Because the net charge of the cation is positive and the net charge of the anion is negative, they attract each other following Coulomb's law.

Furthermore, uncharged molecules can attract each other electrostatically depending on their dipole moments which result from a distribution of negatively charged electrons spatially not matching the distribution of the positively charged nuclei. This dipole – dipole interaction is also called Keesom interaction (named after Willem H. Keesom), which also includes ion – dipole interactions in a wider sense. A molecule with a strong dipole can induce a dipole on a rather nonpolar molecule causing the electron density to shift, leading to partial charges that would not be there otherwise. This dipole – induced dipole interaction is called Debye interaction (named after Peter Debye), which also includes ion – induced dipole interactions in a wider sense.

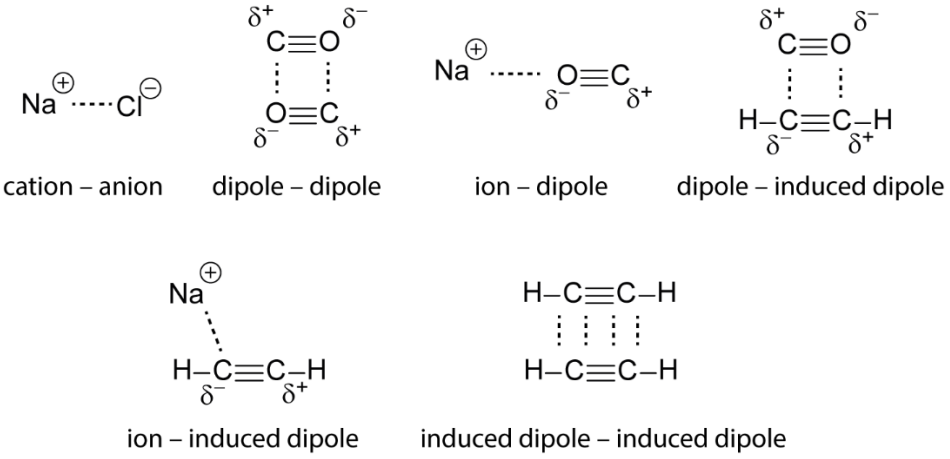

Figure 1.1. Overview of the very basic types of non-covalent interactions.

Another form of non-covalent interactions is the induced dipole – induced dipole interaction, which is also called London interaction (named after Fritz London). This attractive force is caused by electron correlation between two adjacent molecules. The fluctuations of the electron distribution of the molecules influence each other, which leads to momentary dipole moments. This long-range electron correlation is especially significant when the molecules are very close to each other and the distance dependency is given by r^{-6}, with r being the intermolecular distance. Another relevant factor is the polarizability of the electron cloud. The larger and the softer (according to the HSAB principle) the atom is, the better it can be polarized and thus the stronger the attractive force. As the variation of a quantity (here the partial charges) with frequency is termed dispersion in physics, this phenomenon is usually called London dispersion. The term van-der-Waals interaction means this as well, strictly speaking, but in a broader sense it is a general phrase for all three types of interactions, namely Keesom, Debye and London interaction. An overview is given in Figure 1.1.

Regarding repulsive non-covalent interactions, next to the obvious electrostatic repulsion between two cations for example, another type of repulsion is relevant: As the molecules approach each other, their wavefunctions begin to overlap more significantly, compelling the electrons to occupy higher energy states due to the Pauli exclusion principle, which forbids identical quantum numbers. This energy

increase is unfavorable, consequently preventing the molecules from approaching too closely. This is called Pauli repulsion, named after Wolfgang Pauli.

Many types of intermolecular interactions, that are based on the mentioned types are known, such as hydrogen bonding: When a hydrogen atom is covalently bound to a rather electronegative atom E, such as an oxygen or nitrogen atom, electron density is pulled away from the hydrogen atom, making it more electropositive. When a molecule with a free electron pair comes close, it is likely to orient the free electron pair towards the hydrogen atom and it further increases the dipole moment of the E–H bond. Because this group has a certain Brønsted acid character and the molecule with the free electron pair has a certain Brønsted base character, it is often not clear, to which molecule the proton is allocated and it likely alternates between both.

Another important non-covalent interaction in supramolecular chemistry is the π-π interaction between two aromatic groups for example two benzene molecules. They can stack on top of each other with the π surfaces parallel, which is driven by London dispersion because the benzene rings have many delocalized electrons and can therefore be polarized well. Interestingly, the stacking of two benzene molecules directly on top of each other is not energetically favored; rather a 'slip-stacked' structure, in which the π-surfaces are slightly shifted, is favored. The reason for this is rather complicated and is connected to Pauli repulsion, rather than electrostatic potentials, which was assumed before.[14]

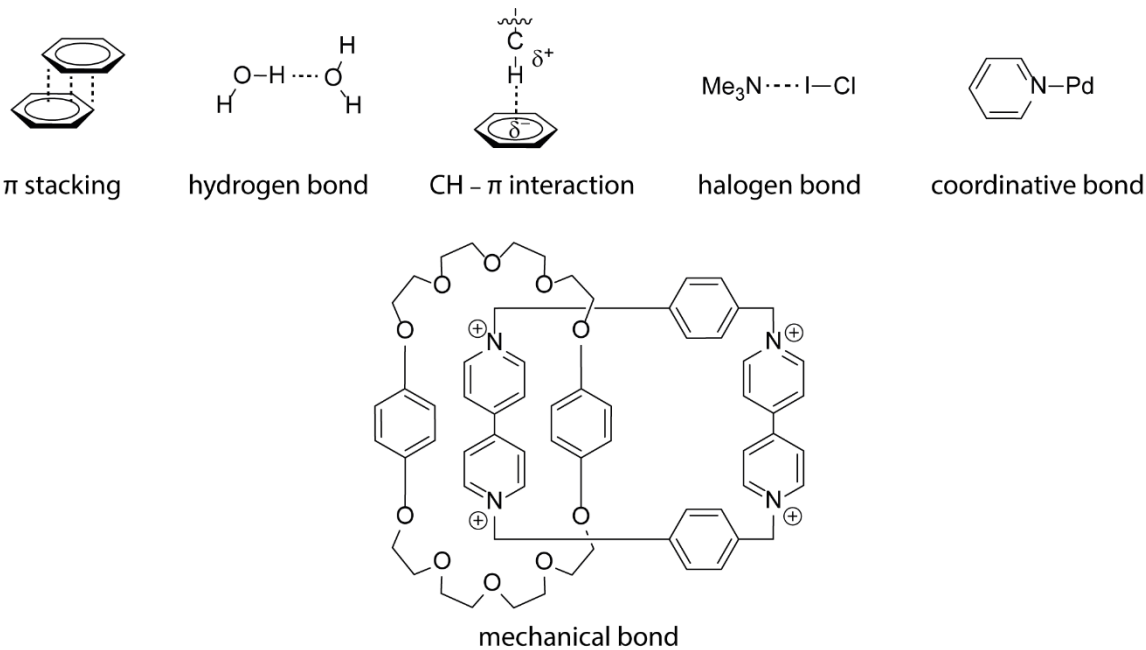

Figure 1.2. Overview of further classes of supramolecular interactions and bonds. For the mechanical bond a catenane is shown representatively.[15]

Further notable types of interactions and bonds in supramolecular chemistry are C–H-π or cation-π interactions, halogen bonds, dative or coordinative bonds or mechanical bonds. These are shown in Figure 1.2. In the latter case the molecules do not necessarily have to significantly attract each other with any of the mentioned van-der-Waals interactions but are topologically locked together so that dissociation usually requires covalent bond breaking. It opens the field of molecular knots, catenanes and rotaxanes.[2,16]

An in supramolecular chemistry important pseudo force derives from the solvophobic effect, which is called hydrophobic effect in case of water being the solvent. The formation of a solvation shell around a solute decreases the entropy of the solvent and reduces enthalpically favored solvent–solvent contacts which counteracts the entropy gain from breaking up the crystal structure and dispersing the solute molecules in solution and the enthalpy gain from solute–solvent interaction. If the solute is rather nonpolar and the electrostatic interaction with the solvent is weak the solvophobic effect causes either low solubility or aggregation in solution, for example in form of dimerization or host-guest complex formation.[16]

Having elucidated some physical basics of supramolecular chemistry it is now important to bring up the core principle of self-assembly in which preprogrammed molecular building blocks aggregate from a disordered state to an ordered structure. Preprogramming here means that the molecules are designed to bind and attract each other and assemble in the desired way. This makes it possible to easily create large, complex and multifunctional structures that can be stimuli responsive, especially if the interactions of the building blocks are dynamic. The often weak interactions between the building blocks allow for reversible reactions which enables the system to reach the thermodynamic minimum and to not get stuck in kinetic traps as shown in Figure 1.3.

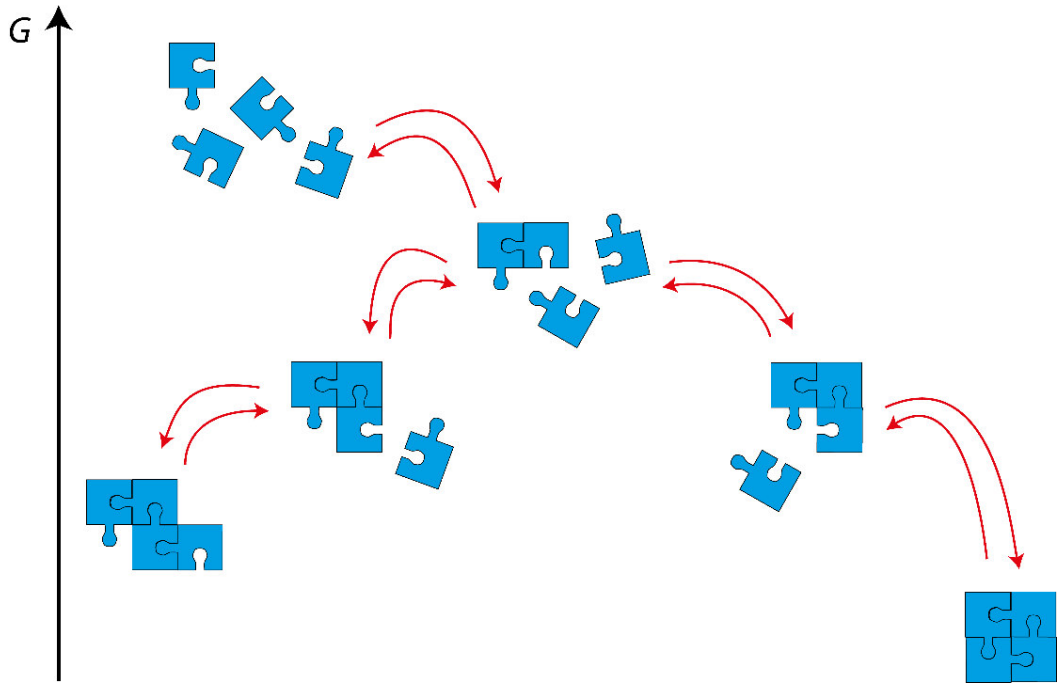

Figure 1.3. Schematic stepwise self-assembly. Every binding reduces the free energy *G* and while there are kinetic traps there is only one assembly that has the lowest energy and is the thermodynamically favored product.

1.2 Systems Chemistry

Interconnected multicomponent chemical systems require in-depth research to uncover the fundamental principles of self-organization and adaptability in natural and artificial systems. The field of systems chemistry embraces the investigation not of isolated reactions or individual molecules but of interlinked chemical processes within interconnected networks and dynamic environments. The goals are to understand key concepts of the origin of life, self-assembly and self-replication of complex structures and behavior of dynamic systems outside the thermodynamic equilibrium.[17]

While systems biology tries to understand and model computationally all pathways and their connections with each other in a living system like a cell in its entity,[18] systems chemists rather pursue a bottom-up approach starting from only a handful of different model compounds to keep the system analyzable, to grasp the core concepts and to develop new ideas.

Complex systems in dissipative, transient, or out-of-equilibrium states are of particular interest due to their resemblance to natural systems and their significance as a precursor to the even more intricate and rare class of oscillating reactions.[19] Many model systems that show interesting out-of-equilibrium behavior have been developed and investigated, ranging from polymers and materials to small molecules.[20–23]

As tools for creating complex systems, dynamic bonds and interactions (dynamic constitutional chemistry)[24] are helpful as they keep the system flexible and thus stimuli responsive and allow

temporal formation of transient species and give control over orthogonality.[25] Systems chemistry, especially when dealing with discrete species, is thus strongly connected to supramolecular chemistry.[26,27] Lehn and coworkers showed in a recent study a beautiful example of an artificial complex system with multiple, interconnected compounds, see Figure 1.4.[28] A library of three primary amines (**1**, **3**, **5**), three aldehydes (**2**, **4**, **6**) and three transition metal cations (Fe^{2+}, Cu^{+}, Zn^{2+}) combined yield three complexes selectively, namely $[Fe(\mathbf{1},\mathbf{2})_2]^{2+}$, $[Cu(\mathbf{3},\mathbf{4})_2]^{+}$ and $[Zn(\mathbf{5},\mathbf{6})]^{2+}$. Less precise product formation is observed when only parts of the library are combined, for example **1**, **2**, **5**, **6**, Fe^{2+} and Zn^{2+} together result in a $[Zn(\mathbf{1},\mathbf{2})_2]^{2+}$ complex as side product next to the other two, expected complexes. This is an example of "simplexity" as the outcome of the initially more complex mixture is less complex than the outcomes of small fractions of the library.

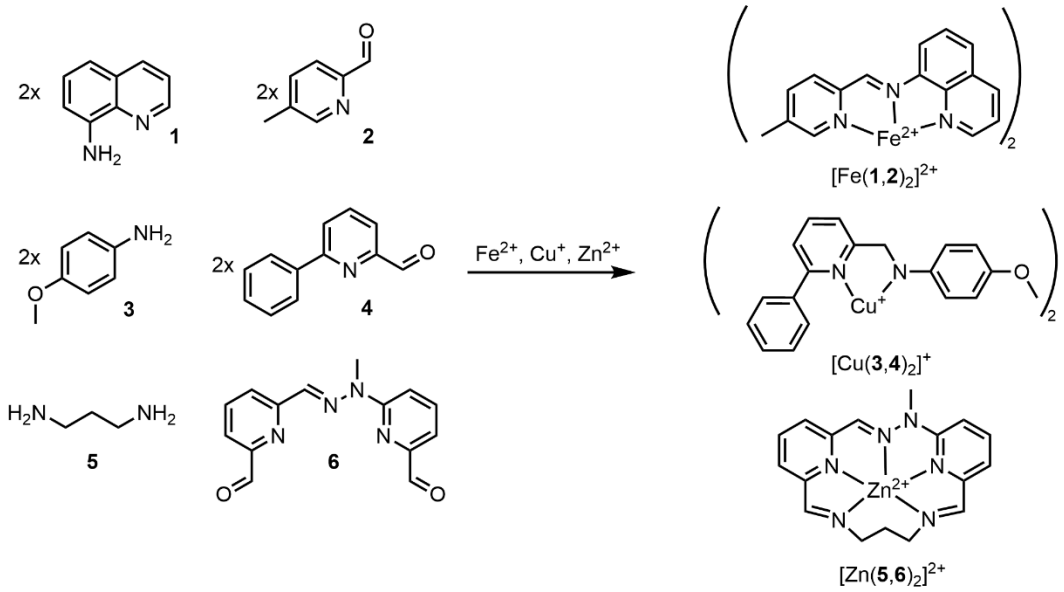

Figure 1.4. Selective formation of three different complexes from a mixture of nine building blocks.[28]

A non-discrete, but fuel-driven dissipative system is presented by Guan and coworkers, see Figure 1.5. E-fueled and waste-free dissipative system by Guan and coworkers.[29] The general principle in this work is the oxidation of a cysteine derivative (by a catalytic oxidant that is activated by an anode) so that it dimerizes via a disulfide bridge to its according cystine derivative. Three properties make this system very interesting. 1) A negative fuel is used to reduce the cystine derivative again to two monomers (by a catalytic reductant that is activated by a cathode). Here, the transient species, which is the cystine derivative, does not slowly decay by itself but is depleted by the negative fuel. 2) The transient species is active and can do something that the monomer in the lowest energy state cannot do, which is the self-assembly to fibers through polymeric π stacking. This dynamic, dissipative process is reduced and stopped again by the reduction. This activity of a transient state, that is kept up by constant supply of some sort of fuel, is especially interesting as it draws parallels to life itself. 3) This system is purely fueled by electricity and no chemical waste piles up. Other examples of complex systems in the literature are mentioned in Chapter 4.

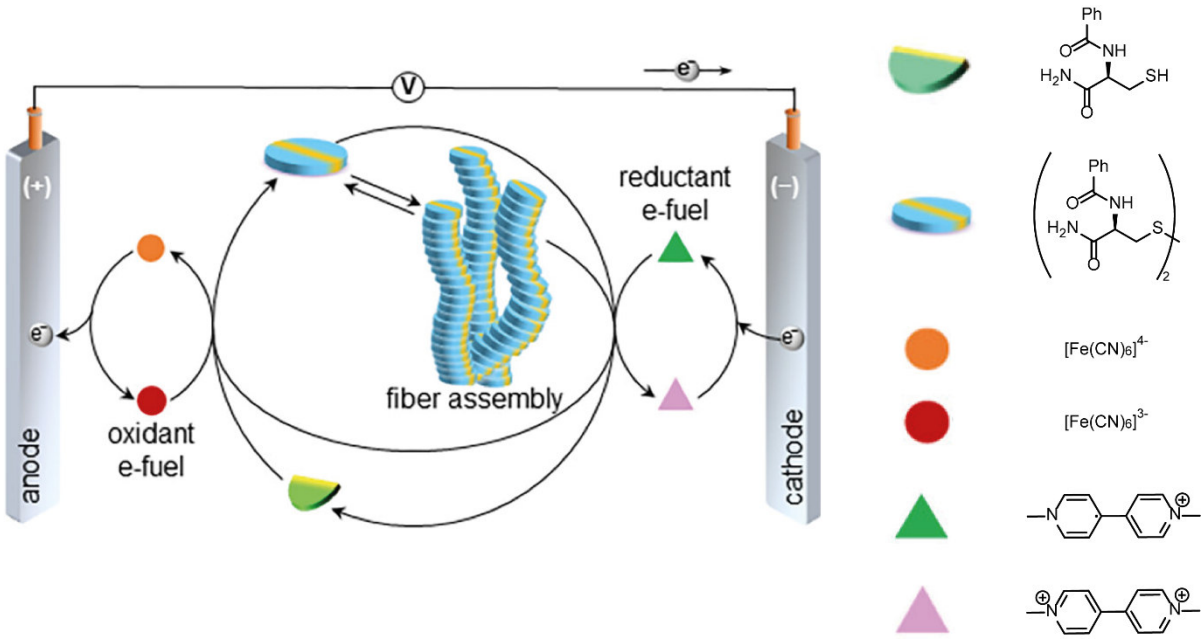

Figure 1.5. E-fueled and waste-free dissipative system by Guan and coworkers.[29] The graphic was taken from the article and slightly modified. Permission was obtained and is appended in Chapter 5.

1.3 Coordination Cages

Encapsulating a small molecule inside a larger one is one of the key concepts of supramolecular chemistry and it is a big step towards increasing system complexity. As it is so often the case in supramolecular chemistry, nature is taken as archetype, namely here enzymes, which bind and process metabolites. This host–guest chemistry allows influence on the small molecule from all directions, which opens up new ideas for the fields of catalysis and separation[30] with the aims of making industrial chemistry greener[31] and more efficient[32,33] and for the fields of sensing, bioimaging and therapeutics.[34]

In general, supramolecular host molecules can be classified as one of three types: rings, cages and capsules, see Figure ***1.6***. Rings have large openings but the contact area between ring and guest is rather small. This causes a fast guest uptake but weak guest binding. Capsules on the other hand are rather sealed so that guest binding is kinetically hindered but once the guest is inside the binding strength can be assumed comparably high. Cages can be seen as an intermediate as they have larger openings than capsules but the cavity is more defined than those of rings. Of course, this classification only gives a brief overview; guest binding kinetics and thermodynamics may strongly vary within each class of host molecules.[2]

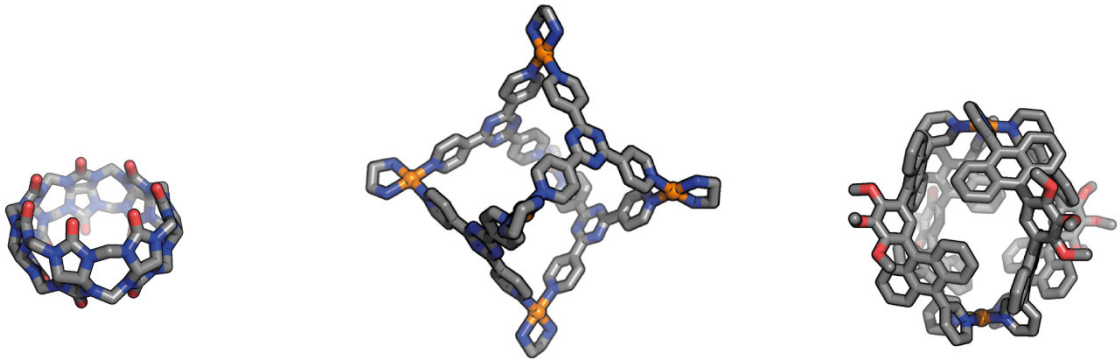

Figure 1.6. Example of a molecular ring,[35] cage[36] and capsule[37] as host molecules. Hydrogen atoms and side chains omitted for clarity.

Many purely organic cages have been reported.[38–43] Alternatively, one can create cages via self-assembly of organic multi-monodentate linkers or ligands with (transition) metal ions.[44–48] This way the cage synthesis is fast and uncomplicated and the choice of organic ligand and metal ion (pre-programming) makes the outcome predictable. Over the past decades the infinite world of possible topologies has been greatly explored leading to hundreds of structures with different sizes, metal-to-ligand ratios, number of cavities and interlocking modes by methods like varying metals, ligand shapes and ligand denticities.[44–48]

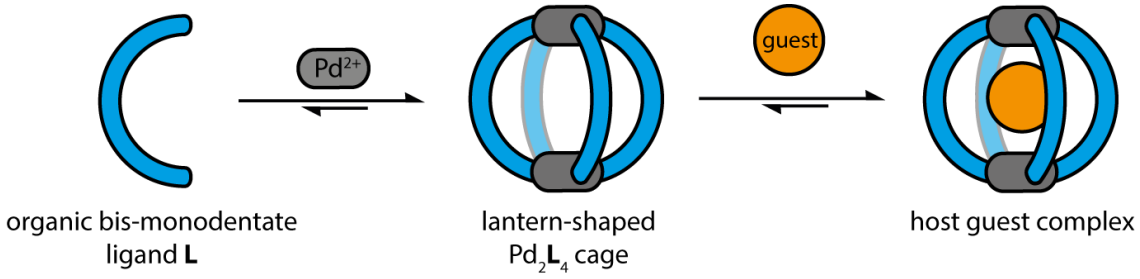

Figure 1.7. Schematic representation of a Palladium based self-assembled metallosupramolecular coordination cage that can take up a small guest molecule.

One of the most basic types of coordination cages is of the topology $M_2\mathbf{L}_4$, which self-assembles from four bis-monodentate bent (banana-shaped) ligands **L** and two metal cations M that prefer a square-planar coordination geometry like palladium(II), see Figure 1.7. This sort of cage has four openings and reminds a bit of a lantern. In our group we focus on palladium(II) based lantern-shaped coordination cages and develop and investigate new concepts for increasing both structural and functional complexity, see Figure 1.8.[45]

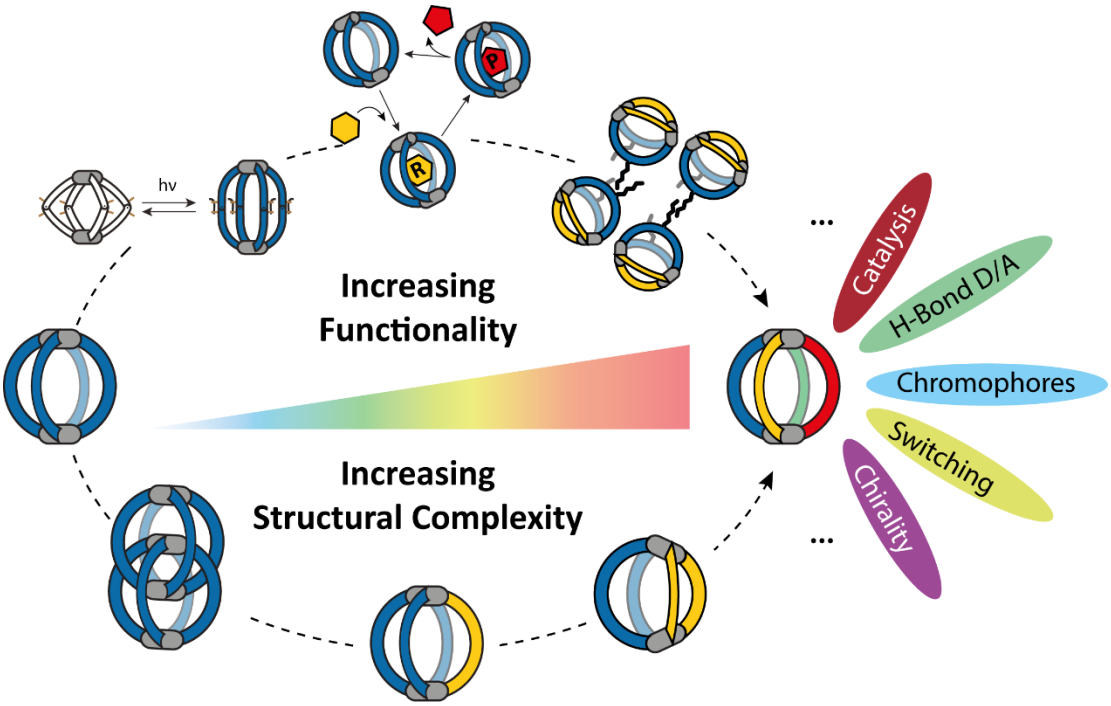

Figure 1.8. Schematic representation of metallosupramolecular coordination cages. Clever Lab in TU Dortmund focusses on developing new concepts for increasing both functional and structural complexity in these model systems.[45] The graphic was taken from the article, which is open access.

As Figure 1.8 makes clear, increasing functionality and structural complexity in coordination cages at some point requires them to be built up by more than one type of ligand, meaning they are heteroleptic instead of homoleptic cages. Here, the big challenge is the selective formation of the desired cage with the different ligands in the correct ratio and arrangement. One big milestone was achieved by our group by reporting a *cis*-$Pd_2\mathbf{L}^{\mathbf{A}}{}_2\mathbf{L}^{\mathbf{B}}{}_2$ cage in which the two ligands $\mathbf{L}^{\mathbf{A}}$ are oversized and have a negative binding angle and the two ligands $\mathbf{L}^{\mathbf{B}}$ are undersized and have a positive binding angle.[49] This way, the *cis*-$Pd_2\mathbf{L}^{\mathbf{A}}{}_2\mathbf{L}^{\mathbf{B}}{}_2$ cage forms selectively. It is schematically shown in Figure 1.8 in the lower right corner. There are several other methods to force selective heteroleptic cage formation, such as templation effect, donor-site engineering, ligand – ligand interaction or steric hindrance.[50,51]

Assemblies based on ligand-metal combinations have several disadvantages. They are labile due to their coordination bond (which can also be advantageous), especially towards acids, bases, oxidizing or reducing agents and even dilution. It is often difficult to achieve water solubility even though most coordination cages are charged.[52] The metal is often expensive and toxic and the ligand is usually organic but not based on biological building blocks and thus the physiological and environmental danger has to be tested. While there are solutions to these problems, for example the use of cheap, non-toxic metals like Iron and more stable chelating ligands,[53] these systems are currently usually used

for fundamental, academic research to develop and investigate new supramolecular concepts that are applicable for other supramolecular systems as well as for nanotechnology and materials sciences.

1.4 Motivation

Coordination cages provide two types of dynamic interactions already by their nature. The coordinative bond that keeps the assembly together is often weak and reversible. Therefore, the formation can be easily controlled via external stimuli. The other dynamic interaction is with a guest molecule, which binds non-covalently and is in an equilibrium between the inside and outside state. Cage chemistry therefore provides interesting tools and features for systems chemistry. Because of this dynamic and complex behavior many studies on cage systems can already be seen as a part of systems chemistry. Much work has been done on switchable and stimuli-responsive cages and the interconnectivity of cages or subcomponents thereof have been exploited for new ideas.[54,55] However, especially complex systems containing more than one type of cage need further investigation. To contribute to this area, one part of this work deals with photoswitchable complex systems of interconnected building blocks that can assemble to homo- or heteroleptic cages for possible guest uptake and release.

Only very few examples exist in which the very interesting out-of-equilibrium aspect of systems chemistry is exploited in cage chemistry.[56–60] Here, many more concepts and techniques are needed as a base for more complex, hopefully even cyclic and thus more life-like systems. Therefore, in another part a new example for dissipative guest uptake is investigated.

Complex mixtures tend to require more sophisticated analytical tools like mass spectrometry.[61] Ion mobility spectrometry as add-on to the latter can yield valuable additional structural information, especially when combined with theoretical chemistry, which is why the first part of this thesis is dedicated to this combination to yield valuable structural insights.

1.5 Literature

[1] J.-M. Lehn, *Science* **1993**, *260*, 1762–1763.

[2] J. W. Steed, J. L. Atwood, *Supramolecular Chemistry*, John Wiley & Sons, Ltd., **2009**.

[3] I. V. Kolesnichenko, E. V. Anslyn, *Chem. Soc. Rev.* **2017**, *46*, 2385–2390.

[4] J.-M. Lehn, *Chem. Soc. Rev.* **2017**, *46*, 2378–2379.

[5] K. Das, L. Gabrielli, L. J. Prins, *Angew. Chem. Int. Ed.* **2021**, *60*, 20120–20143.

[6] E. A. John, C. J. Massena, O. B. Berryman, *Chem. Rev.* **2020**, *120*, 2759–2782.

[7] G. Gil-Ramírez, D. A. Leigh, A. J. Stephens, *Angew. Chem. Int. Ed.* **2015**, *54*, 6110–6150.

[8] J. F. Stoddart, *Chem. Soc. Rev.* **2009**, *38*, 1802–1820.

[9] A. P. Paneerselvam, S. S. Mishra, D. K. Chand, *J. Chem. Sci.* **2018**, *130*, 96.

[10] S. J. Dalgarno, N. P. Power, J. L. Atwood, *Coord. Chem. Rev.* **2008**, *252*, 825–841.

[11] S. Erbas-Cakmak, D. A. Leigh, C. T. McTernan, A. L. Nussbaumer, *Chem. Rev.* **2015**, *115*, 10081–10206.

[12] S. Kassem, T. van Leeuwen, A. S. Lubbe, M. R. Wilson, B. L. Feringa, D. A. Leigh, *Chem. Soc. Rev.* **2017**, *46*, 2592–2621.

[13] C. J. Pedersen, *Angew. Chem. Int. Ed. Engl.* **1988**, *27*, 1021–1027.

[14] K. Carter-Fenk, J. M. Herbert, *Chem. Sci.* **2020**, *11*, 6758–6765.

[15] P. R. Ashton, T. T. Goodnow, A. E. Kaifer, M. V. Reddington, A. M. Z. Slawin, N. Spencer, J. F. Stoddart, C. Vicent, D. J. Williams, *Angew. Chem. Int. Ed. Engl.* **1989**, *28*, 1396–1399.

[16] P. W. Atkins, J. de Paula, J. J. Keeler, *Physikalische Chemie*, Wiley-VCH, **2022**.

[17] G. Ashkenasy, T. M. Hermans, S. Otto, A. F. Taylor, *Chem. Soc. Rev.* **2017**, *46*, 2543–2554.

[18] I. Tavassoly, J. Goldfarb, R. Iyengar, *Essays Biochem.* **2018**, *62*, 487–500.

[19] A. Cassani, A. Monteverde, M. Piumetti, *J. Math. Chem.* **2021**, *59*, 792–826.

[20] S. De, R. Klajn, *Adv. Mater.* **2018**, *30*, 1706750.

[21] G. Ragazzon, L. J. Prins, *Nat Nanotechnol* **2018**, *13*, 882–889.

[22] J. L. -Y. Chen, S. Maiti, I. Fortunati, C. Ferrante, L. J. Prins, *Chem European J* **2017**, *23*, 11549–11559.

[23] F. della Sala, S. Neri, S. Maiti, J. L.-Y. Chen, L. J. Prins, *Curr Opin Biotech* **2017**, *46*, 27–33.

[24] F. Schaufelberger, B. J. J. Timmer, O. Ramström, **2017**, 1–30.

[25] A. Wilson, G. Gasparini, S. Matile, *Chem. Soc. Rev.* **2013**, *43*, 1948–1962.

[26] J.-M. Lehn, *Chem. Soc. Rev.* **2006**, *36*, 151–160.

[27] J. R. Nitschke, *Nature* **2009**, *462*, 736–738.

[28] J. Ayme, S. Dhers, J. Lehn, *Angew. Chem. Int. Ed.* **2020**, *59*, 12484–12492.

[29] D. Barpuzary, P. J. Hurst, J. P. Patterson, Z. Guan, *J. Am. Chem. Soc.* **2023**, *145*, 3727–3735.

[30] D. Zhang, T. K. Ronson, Y.-Q. Zou, J. R. Nitschke, *Nat. Rev. Chem.* **2021**, *5*, 168–182.

[31] N. Noto, Y. Hyodo, M. Yoshizawa, T. Koike, M. Akita, *ACS Catal.* **2020**, *10*, 14283–14289.

[32] A. C. H. Jans, X. Caumes, J. N. H. Reek, *ChemCatChem* **2019**, *11*, 287–297.

[33] W. Cullen, M. C. Misuraca, C. A. Hunter, N. H. Williams, M. D. Ward, *Nat. Chem.* **2016**, *8*, 231–236.

[34] W.-T. Dou, C.-Y. Yang, L.-R. Hu, B. Song, T. Jin, P.-P. Jia, X. Ji, F. Zheng, H.-B. Yang, L. Xu, *ACS Mater. Lett.* **2023**, *5*, 1061–1082.

[35] J. Kim, I.-S. Jung, S.-Y. Kim, E. Lee, J.-K. Kang, S. Sakamoto, K. Yamaguchi, K. Kim, *J. Am. Chem. Soc.* **2000**, *122*, 540–541.

[36] M. Fujita, D. Oguro, M. Miyazawa, H. Oka, K. Yamaguchi, K. Ogura, *Nature* **1995**, *378*, 469–471.

[37] M. Yamashina, Y. Sei, M. Akita, M. Yoshizawa, *Nat. Commun.* **2014**, *5*, 4662.

[38] B. Moosa, L. O. Alimi, A. Shkurenko, A. Fakim, P. M. Bhatt, G. Zhang, M. Eddaoudi, N. M. Khashab, *Angew. Chem. Int. Ed.* **2020**, *59*, 21367–21371.

[39] C. Liu, K. Liu, C. Wang, H. Liu, H. Wang, H. Su, X. Li, B. Chen, J. Jiang, *Nat. Commun.* **2020**, *11*, 1047.

[40] T. Mitra, K. E. Jelfs, M. Schmidtmann, A. Ahmed, S. Y. Chong, D. J. Adams, A. I. Cooper, *Nat. Chem.* **2013**, *5*, 276–281.

[41] X. Zhao, Y. Liu, Z. Zhang, Y. Wang, X. Jia, C. Li, *Angew. Chem. Int. Ed.* **2021**, *60*, 17904–17909.

[42] Y. Shi, K. Cai, H. Xiao, Z. Liu, J. Zhou, D. Shen, Y. Qiu, Q.-H. Guo, C. Stern, M. R. Wasielewski, F. Diederich, W. A. Goddard, J. F. Stoddart, *J. Am. Chem. Soc.* **2018**, *140*, 13835–13842.

[43] P. Bhandari, P. S. Mukherjee, *ACS Catal.* **2023**, *13*, 6126–6143.

[44] M. M. J. Smulders, I. A. Riddell, C. Browne, J. R. Nitschke, *Chem. Soc. Rev.* **2012**, *42*, 1728–1754.

[45] S. Pullen, J. Tessarolo, G. H. Clever, *Chem. Sci.* **2021**, *12*, 7269–7293.

[46] A. J. McConnell, *Chem. Soc. Rev.* **2022**, *51*, 2957–2971.

[47] J. E. M. Lewis, *Chem. Commun.* **2022**, *58*, 13873–13886.

[48] T. R. Cook, P. J. Stang, *Chem. Rev.* **2015**, *115*, 7001–7045.

[49] W. M. Bloch, Y. Abe, J. J. Holstein, C. M. Wandtke, B. Dittrich, G. H. Clever, *J Am Chem Soc* **2016**, DOI 10.1021/jacs.6b08694.

[50] W. M. Bloch, G. H. Clever, *Chem Commun* **2017**, *53*, 8506–8516.

[51] J. Tessarolo, H. Lee, E. Sakuda, K. Umakoshi, G. H. Clever, *J Am Chem Soc* **2021**, *143*, 6339–6344.

[52] E. G. Percástegui, T. K. Ronson, J. R. Nitschke, *Chem. Rev.* **2020**, *120*, 13480–13544.

[53] P. Mal, B. Breiner, K. Rissanen, J. R. Nitschke, *Science* **2009**, *324*, 1697–1699.

[54] T. Y. Kim, R. A. S. Vasdev, D. Preston, J. D. Crowley, *Chem. A Eur. J.* **2018**, *24*, 14878–14890.

[55] H.-Y. Lin, Y.-T. Wang, X. Shi, H.-B. Yang, L. Xu, *Chem. Soc. Rev.* **2023**, *52*, 1129–1154.

[56] V. W. L. Gunawardana, T. J. Finnegan, C. E. Ward, C. E. Moore, J. D. Badjić, *Angew. Chem. Int. Ed.* **2022**, *61*, e202207418.

[57] D. Mondal, A. Ghosh, I. Paul, M. Schmittel, *Org Lett* **2022**, *24*, 69–73.

[58] C. S. Wood, C. Browne, D. M. Wood, J. R. Nitschke, *Acs Central Sci* **2015**, *1*, 504–509.

[59] H. Lee, J. Tessarolo, D. Langbehn, A. Baksi, R. Herges, G. H. Clever, *J Am Chem Soc* **2022**, *7*, 3099–3105.

[60] T. Tateishi, S. Takahashi, A. Okazawa, V. Martí-Centelles, J. Wang, T. Kojima, P. J. Lusby, H. Sato, S. Hiraoka, *J. Am. Chem. Soc.* **2019**, *141*, 19669–19676.

[61] K. E. Ebbert, L. Schneider, A. Platzek, C. Drechsler, B. Chen, R. Rudolf, G. H. Clever, *Dalton T* **2019**, DOI 10.1039/c9dt01814j.

2 Structural Investigation of Coordination Cages via Ion Mobility Spectrometry and Collision Cross Section Calculation

2.1 Introduction and Theory

Investigation of mixtures of coordination cages becomes increasingly challenging by increasing system size. NMR spectroscopy, usually the method of choice, has its limitations regarding resolution, which can be crucial for distinguishing different species. Mass spectrometry is a valuable addition as it is much more sensitive. Recently, we showed that mass spectrometry in tandem with trapped ion mobility spectrometry is a highly suitable and very promising technique for the analysis of complex mixtures of coordination cages.[1]

2.1.1 Trapped Ion Mobility Spectrometry

Ion mobility spectrometry (IMS) is one of several analytical methods that are frequently combined with mass spectrometry to increase the information output. In IMS ionized species are accelerated by a weak electric field through a drift tube filled with an inert buffer gas such as He or N_2 and the time needed is measured. Subsequently, the ions are analyzed by the mass spectrometer. From the measured time the velocity *v* is obtained. Division by the applied electronic field strength *E* yields the ion mobility *K*. Usually the reduced ion mobility K_0, defined as

$$K_0 = K\frac{T_0}{T}\frac{p}{p_0} \quad (1)$$

(K_0: reduced ion mobility, K: ion mobility, T_0: standard temperature, T: temperature, p: pressure, p_0: standard pressure)

is considered as it is less dependent on measurement settings but already quite substrate specific. A smaller and thus more mobile ion moves faster through the buffer gas than a larger one, which is why the ion mobility strongly correlates to the size but also the charge as this influences the impact by the electric field.

A resolution increase could be achieved by lengthening the drift tube. This way, the ions collide more often with the buffer gas which increases the separation between smaller and larger ions. At some point, the technical realization becomes difficult, which is why Trapped Ion Mobility Spectrometry (TIMS) as opposed to Drift Tube Ion Mobility Spectrometry (DTIMS) was developed.[2–7] Here, the inert gas is not stationary but mobile and the electric field is reversed. The now called carrier gas

mechanically pushes the just ionized analytes against the electric field. The ions are trapped between the carrier gas and the electric field, see Figure 2.1.

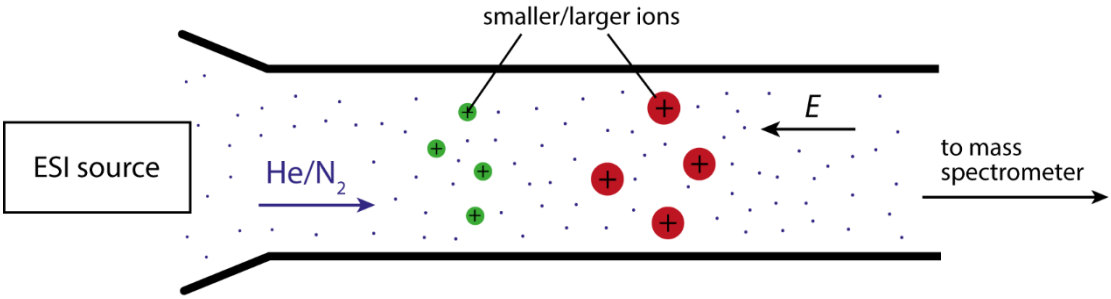

Figure 2.1. Scheme of a trapped ion mobility spectrometer (TIMS) in combination with an electrospray ionization source (ESI) and a mass spectrometer.

More detailed, the analytical process is divided into three stages. First, in the accumulation stage, the ions are accumulated in the TIMS tunnel. This is required to obtain a large number of ions so that they are detectable by the mass spectrometer. In the trapping stage, the accumulated ions are trapped in space between the carrier gas and the electric field. The electric field strength increases linearly towards the exit so that ions of a broad range of *K* are trapped. Ions with higher mobilities collide less often with the carrier gas and thus require a weaker electric field to be trapped. During the trapping stage, the ions with high mobilities are populated at the beginning of the ramp in electric field strength, while the ions with low mobilities are populated more towards the end of the ramp, because they collide more often with the carrier gas and therefore need a higher electric field strength to be trapped in space. The length of this stage (milliseconds to seconds) and the carrier gas flow have a direct influence on the resolution on this measurement technique and correspond to the length of the tube in DTIMS. In the final, eluting phase the electric field is slowly reduced leading to elution of the trapped ions, which are then detected by the mass spectrometer. The speed in which the E-field is reduced and the length of the electronic field gradient (EFG) plateau are further important factors for the overall resolution. The resolving power of a TIMS measurement is given by:[5]

$$R = v_g \cdot \sqrt[4]{\frac{2L_p}{\beta}} \cdot \frac{1}{\sqrt[4]{K^3}} \cdot \sqrt{\frac{ze}{16\ln(2)\,k_B T}} \qquad (2)$$

(*R*: resolving power, v_g: carrier gas velocity, L_p: EFG plateau length, β: electric field scan rate, *K*: ion mobility, *z*: charge, e: elementary charge, k_B: Boltzmann constant, *T*: temperature)

Several more alternatives to DTIMS and TIMS exist, such as traveling wave ion mobility spectrometry (TWIMS),[8] high-field asymmetric waveform ion mobility spectrometry (FAIMS)[9] and cyclic ion mobility spectrometry (cIM).[10]

To provide an even more chemically relevant physical quantity, the reduced ion mobility K_0 is further transformed into the collision cross section (CCS) via the low field ion mobility equation:[11–14]

$$\mathrm{CCS} = \frac{3}{16}\sqrt{\frac{2\pi}{\mu \mathrm{k_B} T}}\frac{ze}{K_0} \quad (3)$$

(CCS: collision cross section, μ: reduced mass of ion and inert gas molecule, k_B: Boltzmann constant, T: temperature, z: ion charge, e: elementary charge, K_0: reduced ion mobility)

The CCS is not directly depending on the temperature, pressure, reduced mass and charge, although the mass of the analyte often scales with its CCS and a higher ion charge causes stronger ion-induced dipole interactions with the uncharged carrier gas.[15–17] Interestingly, when N_2 is chosen as carrier gas, even charge dependent ion-quadrupole interactions play a role.[15,18] Even though the CCS is very specific for every ion, the measurement technique is usually specified as superscript and the used buffer/carrier gas as subscript, for example $^{\mathrm{TIMS}}\mathrm{CCS}_{\mathrm{N2}}$ means the CCS obtained *via* TIMS and with N_2 as carrier gas. The CCS can be considered as a momentum transfer collision integral, so the momentum transfer between ion and carrier gas averaged over all ion-gas relative velocities,[13] which becomes important for theoretical CCS calculation methods, see Section 2.1.2. In a simplified way it can be considered as the averaged projected two-dimensional area of an ion and is usually reported in Å^2. It can give very valuable insights into size and shape of the investigated analyte.

In recent years, studies on metallosupramolecular cages and other complexes that include structural investigation with IMS measurements, have been reported,[19–22] however, insights from IMS that significantly contribute to the understanding of the system's structure and not just confirm observations from ^{1}H DOSY NMR and single-crystal X-ray analysis are still rare. Li et al. used IMS to determine that only one isomer of the investigated system is present, as different isomers would have the same *m*/*z* value but different ion mobilities or CCS.[23] Bowers et al. could show that two quickly interconverting conformers of a family of macrocycles exist by decreasing the temperature in the drift tube to 80 K. Rissanen et al. managed to monitor the transformation from a highly chiral and flexible Pd_3L_6 macrocycle to a $Pd_3L_3Cl_3$ species with IM-MS and could observe that several different conformers or even constitution isomers coexist. Our group compared the CCS of empty hosts with host-guest complexes in several studies.[1,24–26] In one case, with a rather flexible cationic cage as host, we noticed a decrease in CCS upon anionic guest binding indicating a contraction of the cage.[24] In another case, with a rather rigid cage, an increase in CCS occurs when an anionic guest is bound, because empty space in the structure is filled.[25] The group of Peris reported similar results, in which the influence of different guests on the structural distortion of the host could be detected with IMS.[27]

2.1.2 Theoretical collision cross section calculation

Because IMS alone often only indicates that there is a difference in size or shape between different species and that one is "bigger" than the other, it is often combined with computational modeling, geometry optimization, molecular dynamics (MD) simulation and even approximation of the CCS by

the *in silico* models. If the calculated ^{theo}CCS matches the experimental CCS, then the model fits the structure of the analyte well. Many different calculation techniques have been developed and used in the last decades.[18,28] A simple approach would be taking distance measurements from a model or crystal structure, assuming a spherical shape and calculating the two-dimensional projected area. This can be especially successful if the ion is indeed rather spherical.[29] For systems that stronger deviate from the spherical shape the so called projected area method may be more beneficial.[30,31] This method is already implemented in multiple different CCS calculation programs. Here, hard spheres with radii equal to Van-der-Waals radii of the according elements are assigned to the atoms of the model of the ion. The two-dimensional area of the three-dimensional model is projected and orientationally averaged. Several effects are neglected such as the ion-induced dipole interaction and therefore the influence of the ion's charge, location-dependent scattering as well as the momentum transfer, which is why correcting parameters are often used.[32] The projected area method is also not suitable for concave structures like cages with cavities or proteins with binding pockets because these cannot be mapped this way. Bleiholder, Bowers et al. further developed the projected area method by applying a shape factor to account for any concaveness and a local collision probability approximation which makes the edges of the projected area "softer".[33–35]

Several CCS prediction tools based on molecular descriptors and machine learning have been developed,[36–42] and can produce accurate results very fast, however, these algorithms are only suitable for the class of chemicals they were trained for, which are currently only metabolites and lipids. Coordination cages and other supramolecular assemblies structurally differ not only from metabolites and lipids, but also heavily from each other in their size, shape, cavity size, composition and counter anions which is why it is unlikely that the currently existing machine learning tools for CCS calculation may be suitable for this kind of chemistry.

High accuracy for a broad range of types of analytes is achieved by simulating the collisions of the ion with the inert gas. Here, the ion is usually fixed inside a simulation box and single gas molecules enter, either collide or do not collide, and exit again. From the scattering angle χ the CCS can be approximated.[43] First attempts were based on assigning hard spheres to the atoms in the molecule, just like in the projected area method, and collisions are considered specular and elastic.[17] Here, the trajectories of the gas molecules are rectilinear and can be easily calculated without the use of MD simulation, making the CCS calculation very fast, similar to the projected area approaches. This technique allows for multiple collisions, which is necessary for concave areas in the ion's surface, and allows differentiation between collisions in which the gas molecule only slightly brushes the ion and in which it hits the ion more frontally. In the latter case both the momentum transfer and the scattering angle is large causing a higher weight for this particular differential cross section area, see Figure 2.2.

Integration over the three angles φ, θ and γ, which define the collision geometry, and the impact parameter b yields the CCS:

$$^{\text{theo}}\text{CCS} = \frac{1}{4\pi^2}\int_0^{2\pi} d\theta \int_0^{\pi} d\varphi \sin\varphi \int_0^{2\pi} d\gamma \int_0^{\infty} db\ 2b(1-\cos\chi) \qquad (4)$$

($^{\text{theo}}$CCS: theoretical collision cross section; for definition of φ, θ, γ and b see Figure 2.2)

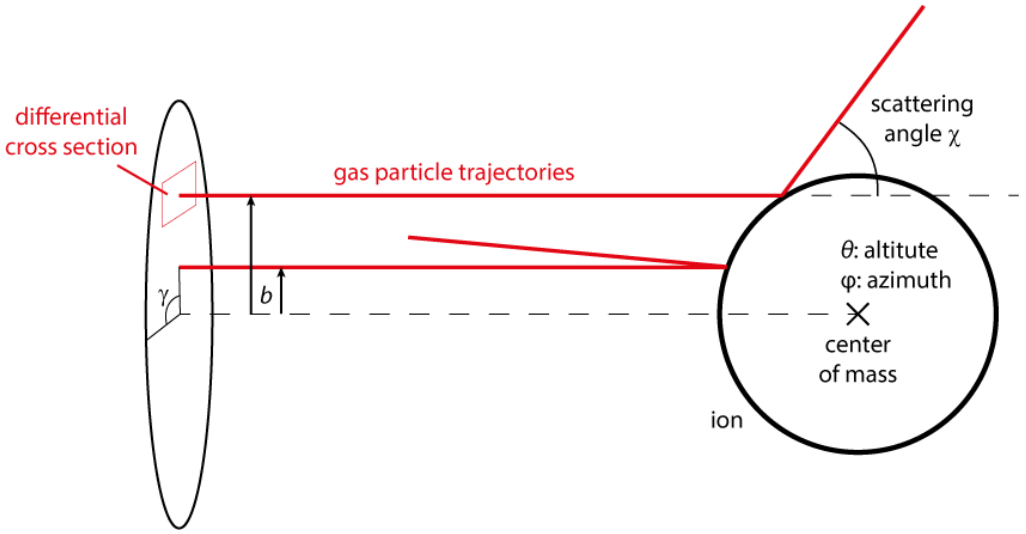

Figure 2.2. Schematic presentation of two collisions between ion and gas molecule with different scattering angles.

This method neglects the relative velocity of ion and gas molecule, charge dependent ion – induced dipole interactions and diffusive and inelastic scattering. To counter these shortcomings, Larriba et al. developed the diffusive hard sphere scattering method, that considers the collisions partially diffusive or inelastic.[32]

The current gold standard in CCS calculation is called the Trajectory Method.[17] Here, the ion is also fixed but the gas molecules experience a potential and the trajectories are calculated in timesteps. The potential consists of a Lennard-Jones (LJ) part and a part for the ion – induced dipole interactions:

$$V = 4\varepsilon\sum_i\left[\left(\frac{\sigma}{r_i}\right)^{12} - \left(\frac{\sigma}{r_i}\right)^{6}\right] - \frac{\alpha}{2}\left(\frac{e}{n}\right)^2\left[\left(\sum_i z_i\frac{r_{x,i}}{r_i^3}\right)^2 + \left(\sum_i z_i\frac{r_{y,i}}{r_i^3}\right)^2 + \left(\sum_i z_i\frac{r_{z,i}}{r_i^3}\right)^2\right] \qquad (5)$$

(V: potential energy experienced by the gas molecule, ε and σ: element-specific LJ parameters, r_i: distance between gas molecule and atom i, α: polarizability of the gas molecule, e: elementary charge, n: overall charge, z_i: atomic point charge of atom i, $r_{x,i}$, $r_{y,i}$, $r_{z,i}$: vector between gas particle and atom i)

The LJ parameters ε and σ are specific for each element and type of gas particle and require parameterization to experimental data. The atomic point charges can be obtained from an electronic structure calculation, charge placement algorithms or an equal distribution of charges can be assumed.

With this potential, no hard spheres based on Van-der-Waals radii are necessary and the scattering is more realistic. Because of the additional term for the ion – induced dipole interactions even higher charged species can be calculated accurately. The relative velocity *g* is considered as well, which is why the CCS in the trajectory method is calculated as

$$^{\text{theo}}\Omega\text{CCS} = \frac{1}{8\pi^2}\int_0^{2\pi} \mathrm{d}\theta \int_0^{\pi} \mathrm{d}\varphi \sin\varphi \int_0^{2\pi} \mathrm{d}\gamma \, \frac{\pi}{8}\left(\frac{\mu}{k_B T}\right)^3 \int_0^{\infty} \mathrm{d}g \, e^{-\mu g^2/(2k_B T)} g^5 \int_0^{\infty} \mathrm{d}b \, 2b \, (1 - \cos\chi) \quad (6)$$

The trajectory method is widely used and has been implemented in various software, for example MOBCAL,[17] IMoS,[32] MobCal-MPI,[44] HPCCS[45] and Collidoscope.[46] Several approaches for even more accuracy are made, for example the addition of a term for the ion – quadrupole interaction to the potential, replacing the LJ term with the more accurate MM3 force field[44,47] or incorporating the two-temperature model.[48,49] In all mentioned CCS calculation methods, the ion is considered fixed in space and thus molecular vibration and rotation is neglected. The momentum transfer upon collision is partially incorporated in ε and σ during parametrization but also depends on the ion's size and shape which may differ significantly from the ions in the training set. Several groups already calculated CCS values with MD simulations, in which the analyte is allowed to move freely.[18,50] This approach is very promising but requires large effort and computation time. An alternative that at least considers different conformers is the CCS calculation of not only of a single structure but of an ensemble of different possible conformers and reporting the (weighted) average.[51] This procedure is already widely used, and software that performs the whole workflow is available.[52,53] Conformation sampling requires MD simulation, which requires a theoretical model, usually a force field, that can describe the geometry and motion of the analyte of interest accurately. For coordination cages MD simulations have been done[25,54–58] but usually require tedious parametrization for the transition metal atoms. The solution may be higher level, electronic structure calculation methods, which are more applicable for a broader range of compounds.

2.1.3 Density Functional Theory

To fully grasp the electronic structure of a molecular system, its wavefunction needs to be obtained by solving Schrödinger's equation:[59]

$$i\hbar\frac{\partial\Psi}{\partial t} = \hat{H}\Psi \quad (7)$$

(ħ: reduced Planck constant, Ψ: wavefunction, t: time, $\hat{H}$: Hamiltonian)

This is impossible if the wavefunction describes more than one particle, which is why several approximations are being made, such as considering only the time-independent variant of the equation, the Born-Oppenheimer approximation, which allows separate treatment of nuclei and

electrons, and describing the wavefunction as a linear combination of atomic, hydrogenic orbitals, of which the wavefunction can be calculated using the first two approximations. The calculation of the electrons' correlation with each other is another challenge, for which different procedures, that vary in their accuracy and computational demand, especially regarding the scaling with the molecular system's size, exist and are summarized as *ab initio* methods or wave function theory (WFT) methods.[60,61]

In applied computational chemistry, another approach for obtaining the electronic structure is more frequently used, which is called density functional theory (DFT). DFT is based on the two Hohenberg-Kohn theorems. The first states that all molecular properties of a system in a ground state, such as the energy *E*, can be completely obtained if the system's electron density ρ is known. The electron density is calculated from the Kohn-Sham molecular orbitals f_i, which are calculated from a linear combination of atomic, hydrogenic orbitals.

$$E[\rho] = E\left[\sum_i |\phi_i(\boldsymbol{r})|^2\right] \tag{8}$$

(*E*: electronic energy, ρ: electron density, f_i: Kohn-Sham molecular orbital *i*, $\boldsymbol{r}$: electron position vector)
The second Hohenberg-Kohn theorem states that variation of the electron density starting from the ground state only leads to states of higher energy. Thus, for optimizing the electron density, the linear combination of atomic hydrogenic orbitals needs to be varied to minimize the energy.[62]

The relation between *E* and ρ is given by

$$E[\rho] = T_e[\rho] + V_{ee}[\rho] + V_{eN}[\rho] + V_{NN} + T_N \tag{9}$$

(*T*: kinetic energy, *V*: potential energy, *e*: electrons, *N*: nuclei)
The kinetic energy of the nuclei is zero, because the calculation is usually done on a model with fixed coordinates. The potential energy between the nuclei is trivial and not dependent on ρ. $V_{eN}[\rho]$ is calculated as

$$V_{eN}[\rho] = \sum_i \int \frac{Z_i \rho(\boldsymbol{r})}{|\boldsymbol{R}_i - \boldsymbol{r}|} d\boldsymbol{r} \tag{10}$$

(Z_i: charge of nucleus *i*, R_i: nucleus position vector)
$V_{ee}[\rho]$ is divided into a classical part $J[\rho]$ and a non-classical part $K[\rho]$. $J[\rho]$ is calculated by the following expression:

$$J[\rho] = \frac{1}{2} \iint \frac{\rho(\boldsymbol{r})\rho(\boldsymbol{r}')}{|\boldsymbol{r} - \boldsymbol{r}'|} \mathrm{d}\boldsymbol{r}\mathrm{d}\boldsymbol{r}' \tag{11}$$

Kohn and Sham proposed that the kinetic energy $T_e[\rho]$ can be divided into the kinetic energy under the assumption of non-interacting electrons $T_{e,KS}[\rho]$ and a small correction term.[63]

$$T_{e,\mathrm{KS}}[\rho] = \sum_i \left\langle \phi_i \middle| -\frac{1}{2}\nabla^2 \middle| \phi_i \right\rangle \tag{12}$$

The correction for the kinetic energy is combined with $K[\rho]$ to the exchange-correlation functional $E_{\mathrm{XC}}[\rho]$, so that Equation 9 is transformed to

$$E[\rho] = T_{e,\mathrm{KS}}[\rho] + J[\rho] + V_{eN}[\rho] + E_{\mathrm{XC}}[\rho] + V_{NN} \tag{13}$$

Finding a suitable approximation for E_{XC} is the big challenge in DFT research.[60,61] Many different solutions have been developed for which E_{XC} usually contains empirical parameters that were fit to energies calculated with higher level *ab initio* methods.[64] A big jump in accuracy is made when the exchange energy is partially calculated with WFT.[65] A further improvement to these so called hybrid DFT models are double-hybrid DFT models, in which also the correlation energy is partially calculated with WFT, namely with Møller-Plesset perturbation theory.[66]

Still, especially regular and hybrid DFT models lack long range electron correlation, meaning induced dipole-induced dipole or dispersion interaction. The most obvious solution is the addition of a corrective force field that causes this weak attraction between atoms and molecules but many more approaches exist.

However, with increasing accuracy usually comes increasing computational demands, which is why methods that are less accurate than regular DFT or WFT but therefore faster are being developed. So called semiempirical methods close the gap between DFT or WFT and molecular mechanics force fields.[67–69] These methods are often based on a parental higher level method but neglect several less important terms in the underlying equations for computational speedup. These terms are substituted with other, simpler terms containing parameters that are fit to either experimental or higher level theoretical data.

The semiempirical method GFN2-xTB (Geometries, Frequencies, Non-covalent interactions, version 2, extended Tight Binding) developed by Grimme and co-workers is such a semiempirical method based on DFT.[70] It is parameterized for all elements in the periodic table up to Radon and fast enough that not only energy calculations and geometry optimizations but also frequency calculations and MD simulations of large structures are possible. It is therefore very suitable for coordination cages, which are usually large in size and contain heavy transition metals.

2.2 Motivation

Investigation of compounds via ion mobility spectrometry and theoretical CCS calculation is a promising technique to yield valuable structural insights. For coordination cages it could help distinguishing isomers, determining conformations and give information about host-guest binding. But because these

kinds of systems differ quite substantially from compound classes, namely proteins or metabolites, for which ion mobility-theoretical CCS workflows already exist, a new workflow has to be established. The workflow presented in Figure 2.3 is thoroughly tested in this work.

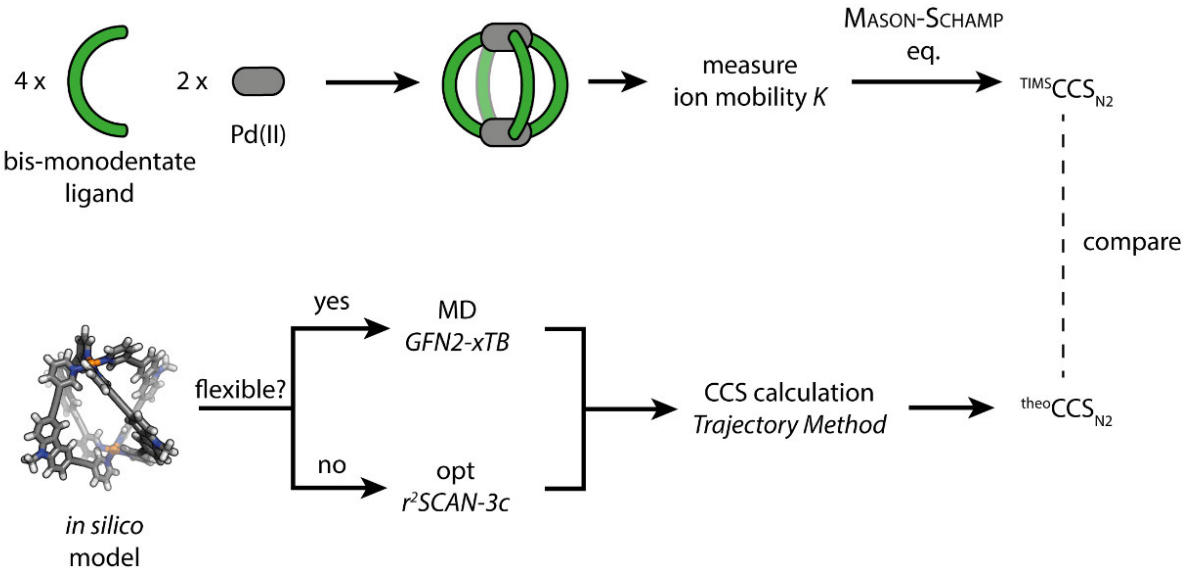

Figure 2.3. General workflow for structural investigation of coordination cages via ion mobility spectrometry and theoretical CCS calculation.

On the experimental side after cage formation via self-assembly the ion mobility is measured using easily available N_2 as inert gas and a trapped ion mobility spectrometer for sufficient resolving power. The ion mobility *K* is transformed into the $^{TIMS}CCS_{N2}$ which is more independent of measurement parameters. Parallel to that, on the theoretical side, a proposed model of the cage has to be drawn *in silico*. If the system is rather rigid, geometry optimization using dispersion corrected DFT should be sufficient. The freshly developed DFT functional r^{2}SCAN-3c[71] from Grimme and co-workers promises both accuracy and computational speed, which is important to enable high-throughput screening even of larger systems. For more flexible systems a conformation sampling technique is more useful, for example using meta-dynamics simulations or simulated annealing and subsequent multilevel geometry optimizations. Alternatively, to safe computation time, only a single MD simulation on GFN2-xTB level of theory is done here and snapshots are taken from the trajectory without further geometry optimization to achieve Boltzmann weighting implicitly. Subsequently, the theoretical CCS of the optimized structure or the conformation ensemble is calculated using the trajectory method, which is accurate for a broad range of compound classes. Comparison of the theoretical and experimental CCS values gives insights on how well the model or ensemble matches the experimental situation.

In the gas phase, in which the IMS experiment takes place, non-covalent intramolecular interactions play a larger role, because of the absence of the solvent the analyte can only interact with itself. In early trials we found that dispersion corrected DFT, including GFN2-xTB and r^{2}SCAN-3c, suggests that

the systems of our interest may conformationally differ in the gas phase as compared to the solved state. This could be a drawback because coordination cages are usually made for chemistry in solution. It is therefore worth investigating how coordination cages behave in the gas phase and to what degree they differ structurally from the solved state.

As a model system we investigated a series of palladium coordination cages based on a bis-monodentate organic ligand **L** consisting of a carbazole backbone, two pyridine donor groups and alkyne spacers.[72] Upon addition of 0.5 eq. $[Pd(CH_3CN)_4](BF_4)_2$ a simple, homoleptic, lantern-shaped $Pd_2\mathbf{L}_4$ cage is formed. To get an idea of the system's size, the Pd–Pd distance in the obtained crystal structure was measured as 14.3 Å. In the original publication **L** was derivatized with a hexyl chain at the nitrogen atom in the carbazole backbone for increased solubility, which is very common for coordination cages. Testing chains of different length could give insights on at what length dispersion driven backfolding occurs. Suhm and coworkers reported that linear alkanes prefer a folded conformation for chains longer than about 17 carbon atoms.[73] Here, backfolding is expected to happen already with shorter chains because the chains do not only interact with themselves but with the cage they are attached to. As the chains are at the very outside of the system, they have a high impact on the CCS, which is why studying their behavior in the gas phase is very important in this field. Because the side chains bring in flexibility conformation sampling is required and it is important to test whether the planned workflow leads to a good representation of the real gas phase behavior.

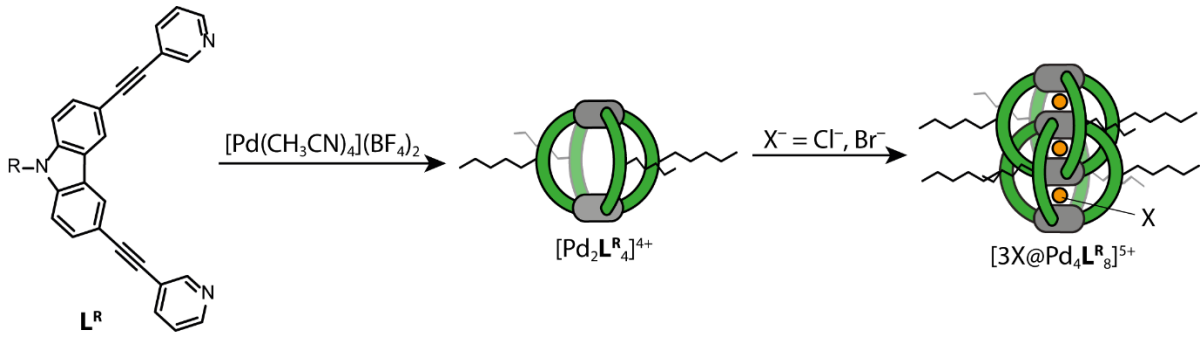

Figure 2.4. Simplified scheme of the findings in Ref. 72. R =hexyl in the original publication.

Small anions such as chloride and bromide induce dimerization of the lantern-shaped $Pd_2\mathbf{L}_4$ cages to quadruply catenated double cages via template effect, see Figure 2.4. Here it is not only interesting to see whether the behavior of the side chains differ from the monomeric cage, but also whether the minor size differences on the extension or compaction by different anions in the pockets is detectable both with high-resolution TIMS and with theoretical CCS calculation.

The plane spanned by the carbazole and the two pyridine groups in **L** is perpendicular to the cavity of $Pd_2\mathbf{L}_4$, as it is the case for many other coordination cages, both from others and from our group. This suggests that a neighboring pair of ligands could stack together due to π-π interactions. Especially in

the gas phase this phenomenon could be realistic because as mentioned earlier non-covalent intramolecular interactions become more relevant in the absence of solvent. However, this folding would require distortions in the ligand or at the Pd center, which is why it is interesting, how large the π surface of **L** has to be to cause this folding.

2.3 Results and Discussion

2.3.1 Analysis of alkyl side chains

Ligand $\mathbf{L^R}$ was resynthesized but with different alkyl chains, ranging from ethyl to dodecyl in steps of two methylene groups, see experimental section for the procedure. For each ligand $\mathbf{L^R}$ (R = ethyl, butyl, hexyl, octyl, decyl, dodecyl) the addition of 0.5 eq. $[Pd(CH_3CN)_4](BF_4)_2$ led to the quantitative formation of $Pd_2\mathbf{L^R}_4$ as can be observed by the typical downfield shift of ^{1}H NMR signals of protons close to the nitrogen donor atom. Further, the shifts of the aromatic ^{1}H NMR signals of the formed species match the previously reported shifts of $Pd_2\mathbf{L^{hexyl}}_4$ showing also that the effect of the alkyl side chain length has negligible effects on the electronic structure of the ligand. To induce double cage formation, 1.0 cage eq. of tetrabutylammonium bromide (TBA-Br) was added. After heating, precipitation was observed and the ^{1}H NMR spectrum shows signals of the free ligand, the monomeric $Pd_2\mathbf{L^R}_4$ and signals assigned to the dimeric cage $3Br@Pd_4\mathbf{L^R}_8$, see Figure 2.5. Appearance of the free ligand and the precipitate indicates the formation of insoluble {*trans*-$[(PdBr_2)_2\mathbf{L^R}_2]$}$_n$ ($n \in \{1,2,3\}$) rings and catenanes.

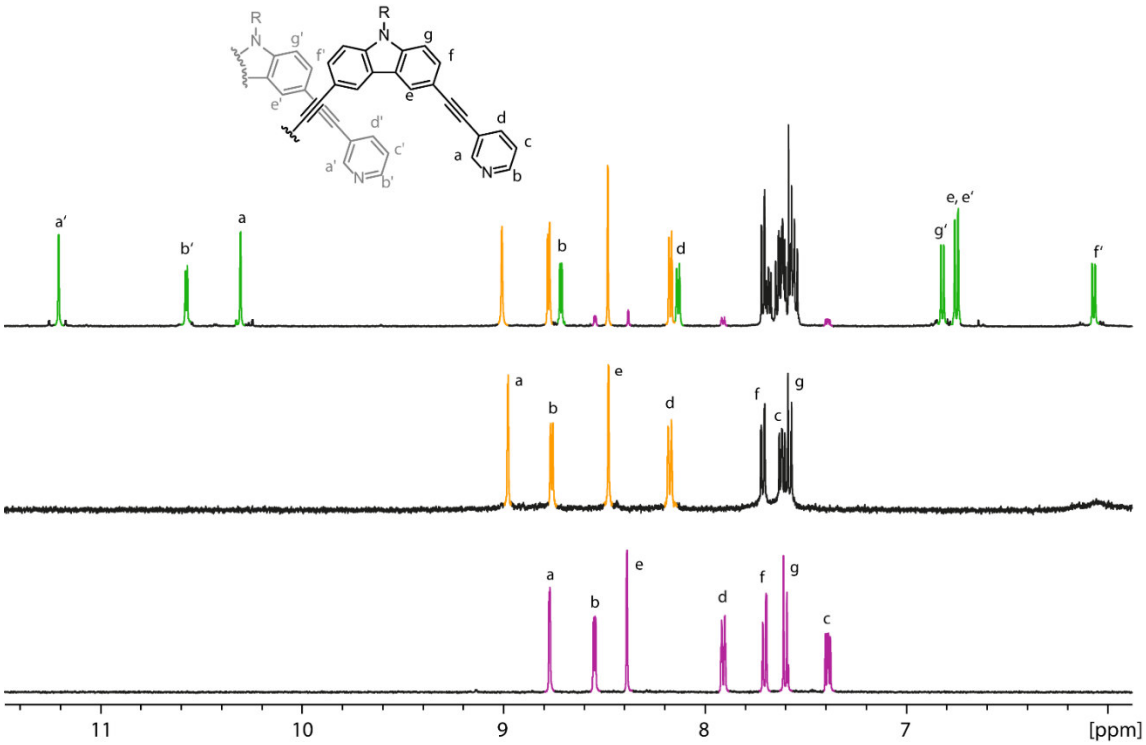

Figure 2.5. ^{1}H NMR spectra (600 MHz top, 500 MHz center and bottom) of free ligand $\mathbf{L^R}$ (bottom), $Pd_2\mathbf{L^R}_4$ (middle) and mixture of free ligand, monomeric cage and double cage $3Br@Pd_4\mathbf{L^R}_8$ (top). Exemplary shown for $\mathbf{L^{hexyl}}$.

The samples were filtered and injected into a Bruker timsTOF ion mobility mass spectrometer. For all samples the species of interest, $[Pd_2\mathbf{L}^{\mathbf{R}}{}_4]^{4+}$ and $[3Br@Pd_4\mathbf{L}^{\mathbf{R}}{}_8]^{5+}$, could be detected among others. To minimize the error, only species without freely moving counter anions were investigated. See Section 2.3.4 for a detailed discussion regarding problems related to counter anions. The species of interest were analyzed with TIMS separately (using N_2 as carrier gas), using a 450 ms ramp time for optimal resolution. The measured ion mobilities were transformed to the $^{TIMS}CCS_{N2}$, which are shown in Figure ***2.6***.

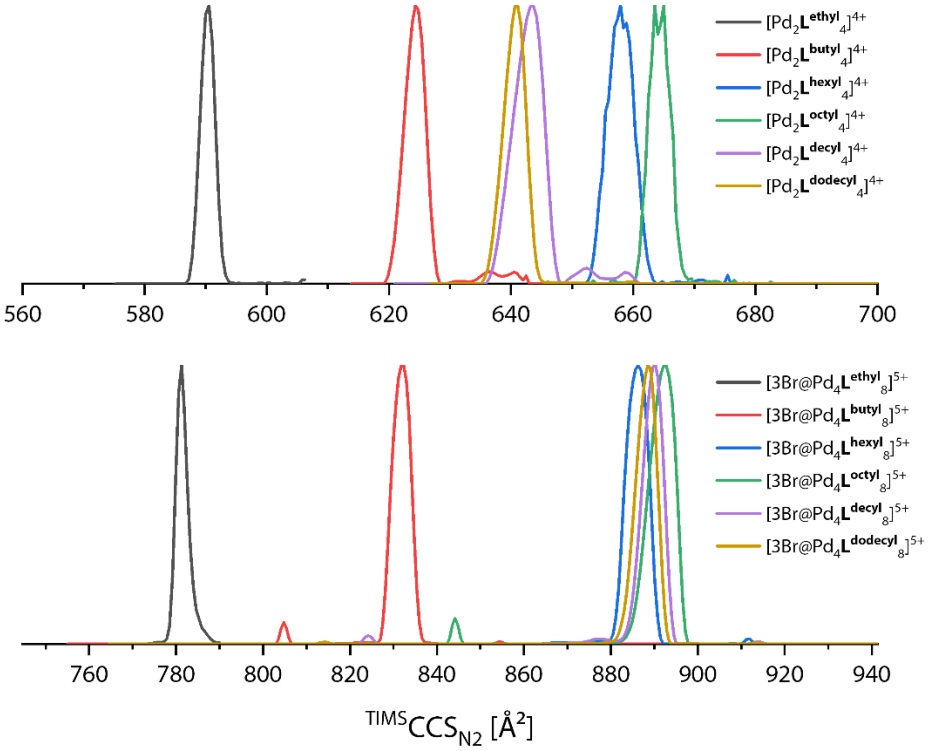

Figure 2.6. Ion mobility spectra, converted to $^{TIMS}CCS_{N2}$, of the monomeric cage $[Pd_2\mathbf{L}^{\mathbf{R}}{}_4]^{4+}$ (top) and double cage $[3Br@Pd_4\mathbf{L}^{\mathbf{R}}{}_8]^{5+}$ (bottom) with different alkyl side chains.

As can be seen, all signals are Gauss-shaped and narrow. Smaller signals were also detected, which are likely noise or fragments. The $^{TIMS}CCS_{N2}$ for the monomeric cages are between 580 Å^2 and 680 Å^2 and for the double cages between 760 Å^2 and 900 Å^2, which is only around 1.3 times larger than the former, due to the cages being interlocked. While the system with $\mathbf{L}^{\mathbf{ethyl}}$ is for both species the smallest, followed by the system with $\mathbf{L}^{\mathbf{butyl}}$, the trend differs quite significantly between monomeric and double cage, which is more demonstratively shown in Figure 2.7. As can be seen, for the monomeric cage the $^{TIMS}CCS_{N2}$ increases linearly from $[Pd_2\mathbf{L}^{\mathbf{ethyl}}{}_4]^{4+}$ to $[Pd_2\mathbf{L}^{\mathbf{butyl}}{}_4]^{4+}$ and $[Pd_2\mathbf{L}^{\mathbf{hexyl}}{}_4]^{4+}$. Apparently, no significant backfolding occurs until at least this chain length. It is assumed that for these chains the energetically lowest conformation is the perfectly straight all-*trans* form. When moving from $[Pd_2\mathbf{L}^{\mathbf{hexyl}}{}_4]^{4+}$ to $[Pd_2\mathbf{L}^{\mathbf{octyl}}{}_4]^{4+}$, the $^{TIMS}CCS_{N2}$ increases only marginally. The octyl chains seem to fold back to the cage more likely than the hexyl chain do. The octyl chains are longer and thus both more flexible and have more remaining surface after backfolding to interact with the ligand via dispersion. That the $^{TIMS}CCS_{N2}$

still increases shows that the octyl chains are not completely backfolded during the whole experiment but are in an equilibrium between backfolded and rather extended conformations. For $[Pd_2\mathbf{L}^{\mathbf{decyl}}_4]^{4+}$ the $^{TIMS}CCS_{N2}$ is between those of $[Pd_2\mathbf{L}^{\mathbf{butyl}}_4]^{4+}$ and $[Pd_2\mathbf{L}^{\mathbf{hexyl}}_4]^{4+}$. This is a clear sign that the decyl chains are much more likely backfolded into the gaps of the monomeric cage. For $[Pd_2\mathbf{L}^{\mathbf{dodcyl}}_4]^{4+}$ the $^{TIMS}CCS_{N2}$ is even slightly smaller, even though the chains are by two methylene groups longer. This is an indication that the decyl chains are still in a balance between extended and backfolded conformations, although the equilibrium is here clearly on the backfolded side. For $[Pd_2\mathbf{L}^{\mathbf{dodcyl}}_4]^{4+}$ it seems that a plateau is reached leading to the assumption that here the chains are completely backfolded during the experiment.

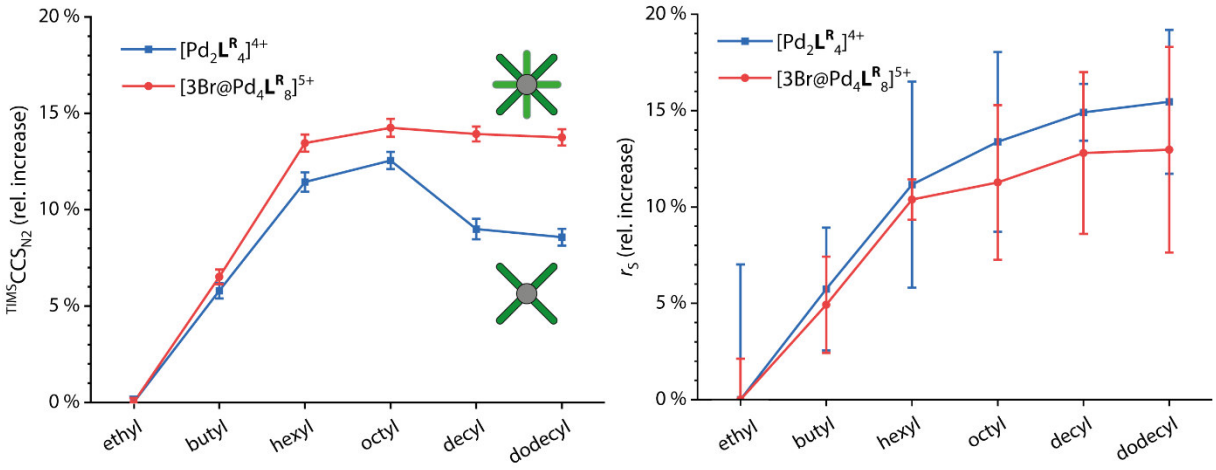

Figure 2.7. Relative increase of $^{TIMS}CCS_{N2}$ (left) and solvodynamic radius r_S (right) with increasing chain length for $[Pd_2\mathbf{L}^{\mathbf{R}}_4]^{4+}$ and $[3Br@Pd_4\mathbf{L}^{\mathbf{R}}_8]^{5+}$. Error bars stem from the FWHM of the TIMS signals and from the standard deviations of the ^{1}H DOSY NMR signals. Inserts: top view of schematic representation of monomeric and double cage showing larger gaps for the former.

For the double cage the trend starts similarly. the $^{TIMS}CCS_{N2}$ increases linearly until $[3Br@Pd_4\mathbf{L}^{\mathbf{hexyl}}_8]^{5+}$. This similarity to the monomeric cage shows that the interaction of ethyl, butyl and hexyl chains with the rest of the complex is negligible. Interestingly, for all follow-up species the $^{TIMS}CCS_{N2}$ is nearly identical to that of $[3Br@Pd_4\mathbf{L}^{\mathbf{hexyl}}_8]^{5+}$, which can also nicely be seen in Figure 2.6. The hypothesis here is that for every step the size increase by the addition of two methylene groups is exactly compensated by the stronger backfolding of the longer chain. No significant decrease in $^{TIMS}CCS_{N2}$ by increasing chain length is observed, which is explained by the double cage having smaller gaps than the monomeric cage and therefore the alkyl chains are more exposed to the collisions with the N_2 gas molecules.

Of the same samples ^{1}H DOSY NMR was measured. The solvodynamic radii were calculated from the measured diffusion coefficients and the relative increase with increasing chain length is plotted in Figure 2.7. Here, the trend is nearly identical for monomeric and double cage. The curve shows steady

increase of r_S with flattening towards longer chains. We assume here that the chains do not fold back as strongly as they do in the gas phase because they can interact with the solvent. Longer chains are more curling, which explains the flattening, but rather because of entropic reasons and not mainly because of intramolecular dispersive interactions. MD simulations of $[3Br@Pd_4\mathbf{L}^{\mathbf{dodecyl}}_8]^{5+}$ with GFN2-xTB with and without implicit solvent (COSMO,[74] acetonitrile) were performed. In the starting structure for both runs the dodecyl side chains were in a perfectly straight, all *trans* conformation. In the gas phase MD the chains folded back immediately while their movement in the solved state MD is rather random. Figure 2.8 shows snapshots from these simulations.

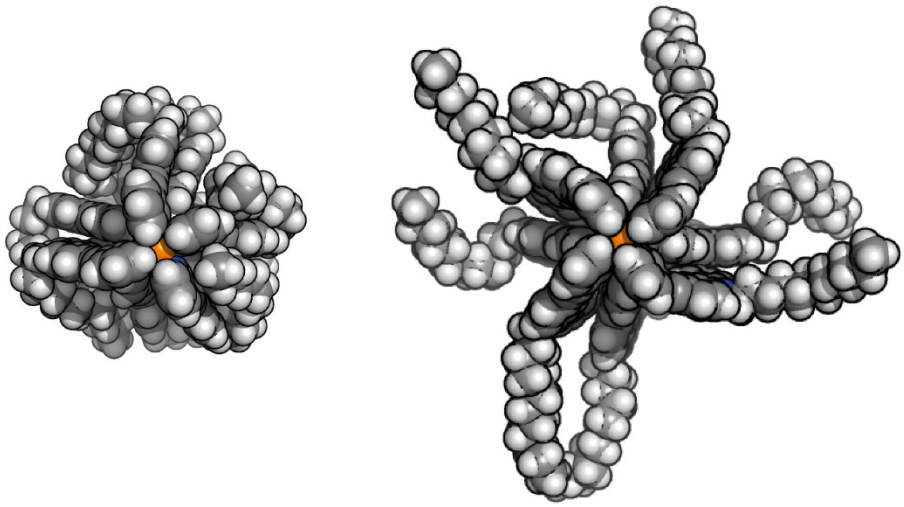

Figure 2.8. Snapshots from MD simulations of $[3Br@Pd_4\mathbf{L}^{\mathbf{dodecyl}}_8]^{5+}$ on GFN2-xTB level without (left) and with (right) implicit solvent (COSMO, MeCN).

For the theoretical reproduction of the experimental TIMS results first gas phase MD simulations with GFN2-xTB on all investigated systems were performed. From the resulting trajectories snapshots for every picosecond were taken. Without further geometry optimization the $^{theo}CCS_{N2}$ of each snapshot was calculated using the trajectory method as implemented in the Collidoscope software. The plots showing the $^{theo}CCS_{N2}$ values and their relative deviations to the $^{TIMS}CCS_{N2}$ values over the simulation time are given in Figure 2.62, Figure 2.63 and Figure 2.64. For $[Pd_2\mathbf{L}^{\mathbf{decyl}}_4]^{4+}$ and $[Pd_2\mathbf{L}^{\mathbf{dodecyl}}_4]^{4+}$ these plots are exemplary shown in Figure 2.9. Figure 2.10 shows the averaged values compared to the experimental ones in plots. In general, the theoretical values are in good agreement with the experimental ones. for most rigid systems $[Pd_2\mathbf{L}^{\mathbf{ethyl}}_4]^{4+}$ and $[3Br@Pd_4\mathbf{L}^{\mathbf{ethyl}}_8]^{5+}$ the relative deviations are very low (+2.9 % and +3.8 %), which shows that the in principle trajectory method is suitable for these kinds of systems. The experimental trend could be reproduced nicely for the monomeric cages. The relative increase is almost identical; the highest deviation is observed for $[Pd_2\mathbf{L}^{\mathbf{octyl}}_4]^{4+}$. It is assumed that the octyl chains are in a rather balanced equilibrium between extended and backfolded conformations

and perfectly reproducing this balance computationally is rather challenging. Regarding $[Pd_2\mathbf{L}^{\mathbf{decyl}}{}_4]^{4+}$ and $[Pd_2\mathbf{L}^{\mathbf{dodecyl}}{}_4]^{4+}$, the hypothesis that the decyl chains are still in an equilibrium between extended and backfolded conformations, although heavily shifted to the latter state, and that opposed to that the dodecyl chains tightly cling to the core, could be reproduced very nicely with the GFN2-xTB MD simulations as Figure 2.9 shows.

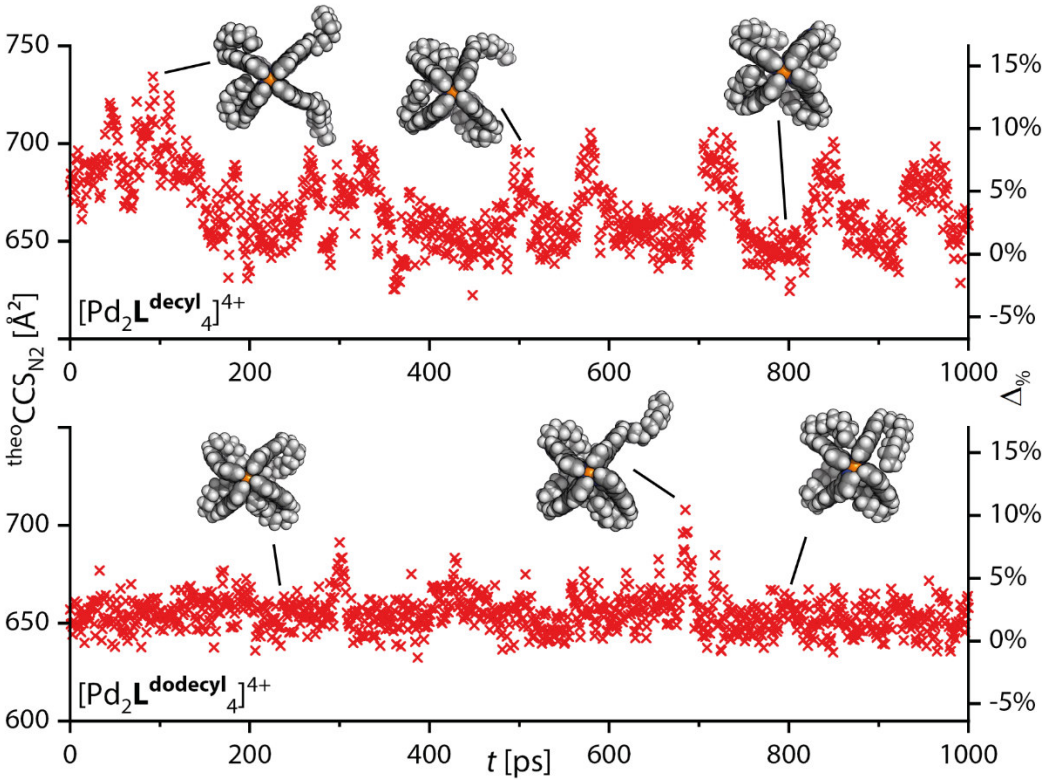

Figure 2.9. $^{theo}CCS_{N2}$ values of snapshots from the MD simulations of $[Pd_2\mathbf{L}^{\mathbf{decyl}}{}_4]^{4+}$ and $[Pd_2\mathbf{L}^{\mathbf{dodecyl}}{}_4]^{4+}$ and the relative deviations to the experiments. Three snapshots each are inserted exemplarily.

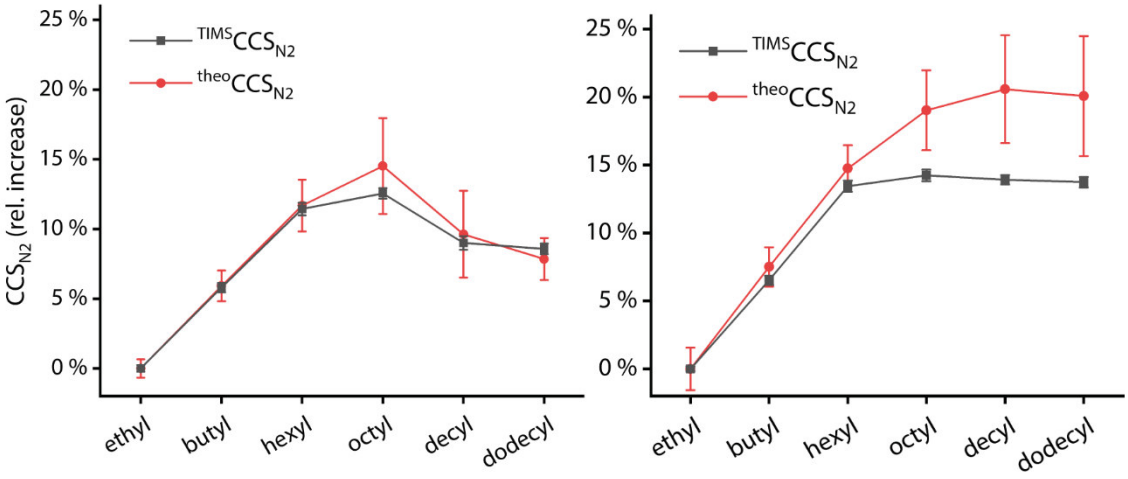

Figure 2.10. Relative increase of $^{theo}CCS_{N2}$ values calculated from the snapshots taken every picosecond from the MD simulations averaged over time (red) and compared with experimental $^{TIMS}CCS_{N2}$ (black) for monomeric cages $[Pd_2\mathbf{L}^{\mathbf{R}}{}_4]^{4+}$ (left) and double cages $[3Br@Pd_4\mathbf{L}^{\mathbf{R}}{}_8]^{5+}$ (right). MD time for $[3Br@Pd_4\mathbf{L}^{\mathbf{octyl}}{}_8]^{5+}$, $[3Br@Pd_4\mathbf{L}^{\mathbf{decyl}}{}_8]^{5+}$ and $[3Br@Pd_4\mathbf{L}^{\mathbf{dodecyl}}{}_8]^{5+}$: 5 ns, all other species 1 ns.

For the double cages the linear trend until [3Br@Pd_4**L**$^{hexyl}_8$]$^{5+}$ could be reproduced nicely. For the last three systems high deviations are observed. Here it seems as if the balance between extended and backfolded conformations are not represented well enough in the MD simulations. One possible explanation could be that the dispersive forces between the chains and the aromatic parts of the ligands are underestimated in GFN2-xTB. An alternative reason could be that the MD time was not long enough which is why they were repeated, this time for 5 nanoseconds. Slight improvements are observed (see Table 2.6) but the values are still too high. Longer simulation times or more thorough conformation sampling techniques like CREST[75] are computationally not feasible.

2.3.2 Guest controlled extension of double cages

When measuring the ion mobilities of the [3Br@Pd_4**L**$^{R}_8$]$^{5+}$ species we could also detect [1Cl,2Br@Pd_4**L**$^{R}_8$]$^{5+}$ and [2Cl,1Br@Pd_4**L**$^{R}_8$]$^{5+}$ (Figure 2.26). In order to complete the series, the double cage 3Cl@Pd_4**L**$^{ethyl}_8$ was formed by titrating TBA-Cl to the monomeric Pd_2**L**$^{ethyl}_4$. The ion mobility spectra of the species [3Cl@Pd_4**L**$^{ethyl}_8$]$^{5+}$, [2Cl,1Br@Pd_4**L**$^{ethyl}_8$]$^{5+}$, [1Cl,2Br@Pd_4**L**$^{ethyl}_8$]$^{5+}$ and [3Br@Pd_4**L**$^{ethyl}_8$]$^{5+}$ are shown in Figure 2.11. Interestingly, the species with more than one type of halide show a larger and a smaller signal, while the species with three chlorides and with three bromides only show single, Gauss-shaped signals. For [2Cl,1Br@Pd_4**L**$^{ethyl}_8$]$^{5+}$ the bromide could either occupy one of the outer pockets or the central one, which is likely the explanation for the observation of two signals. Because Br^- is larger (more accurately: the valence electrons experience a lower effective nuclear charge) the cavity it occupies is expanded. Therefore, if one Br^- is in the central cavity and one Cl^- is in each outer pocket the cage should be maximally compacted, according to previous reports.[76] We thus assign the signal with the lower $^{TIMS}CCS_{N2}$ to this species and the signal with the higher $^{TIMS}CCS_{N2}$ to the other possible species, in which the Br^- is in one of the outer cavities. For [1Cl,2Br@Pd_4**L**$^{ethyl}_8$]$^{5+}$ it is the other way around; here the cage should be maximally expanded if the Cl^- occupies the central pocket and the two Br^- the outer ones, which is why we assume that the signal with the higher $^{TIMS}CCS_{N2}$ belongs to this species and the other belongs to the species in which the Cl^- occupies one of the outer cavities. Interestingly, for both [2Cl,1Br@Pd_4**L**$^{ethyl}_8$]$^{5+}$ and [1Cl,2Br@Pd_4**L**$^{ethyl}_8$]$^{5+}$ not the statistically most likely or the most symmetric variant but the more contracted variant and shows the larger signal in the ion mobility spectrum, although no precise quantitative assertions can be made here.

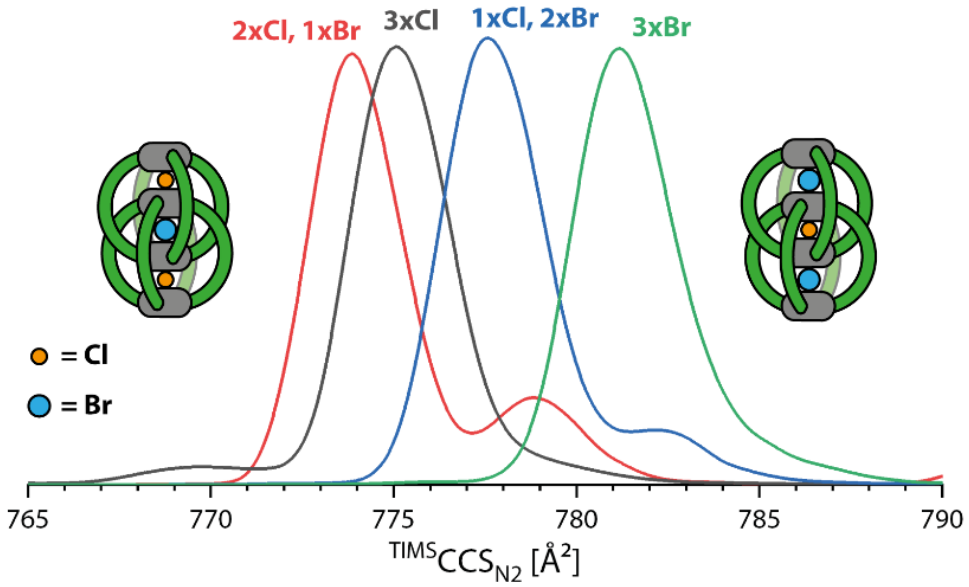

Figure 2.11. Ion mobility spectra converted to $^{TIMS}CCS_{N2}$ of the double cage with ethyl side chains and different halides in the small pockets ($[3X@Pd_4\mathbf{L}^{ethyl}_8]^{5+}$, X = Cl, Br).

For the computational reproduction of this trend we also relied on MD simulations, even though the ethyl side chains are not very flexible. The MDs and subsequent $^{theo}CCS_{N2}$ calculations for all six different species were conducted following the same procedure as for the analysis of the side chains. $^{TIMS}CCS_{N2}$, $^{theo}CCS_{N2}$ and relative deviations are listed in Table 2.6. $^{TIMS}CCS_{N2}$, $^{theo}CCS_{N2}$ and average Pd–Pd distances in the central cavities are plotted in Figure 2.12. As can be seen, except for one outlier, namely $[Br,Cl,Cl@Pd_4\mathbf{L}^{ethyl}_8]^{5+}$ (meaning Br^- in one of the outer pockets), the experimental trend can be reproduced. Especially for the cases in which two signals are observed experimentally the on assumptions based assignments could be confirmed.

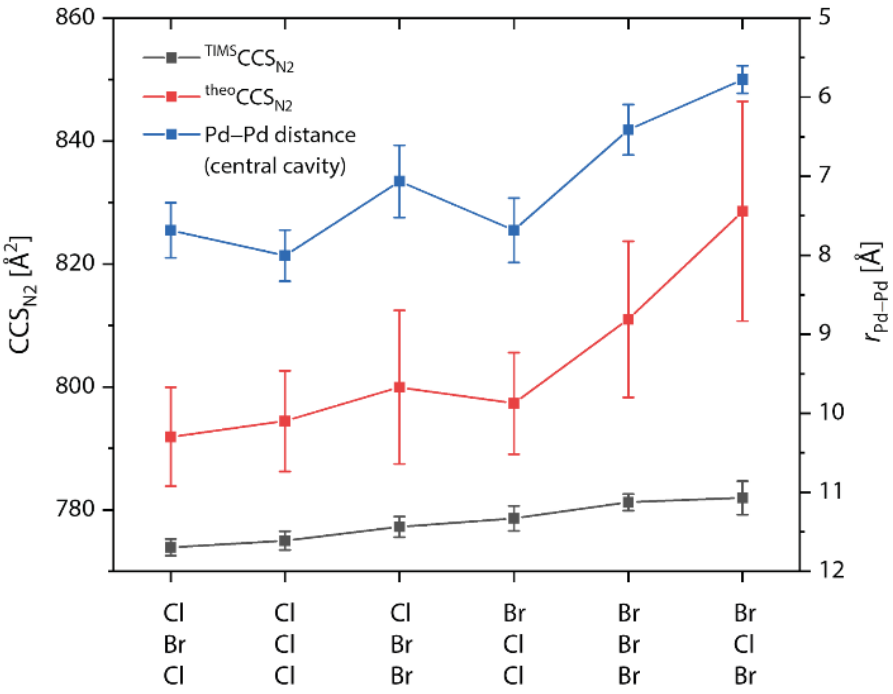

Figure 2.12. $^{TIMS}CCS_{N2}$ values of the six possible species of $[3X@Pd_4\mathbf{L}^{ethyl}_8]^{5+}$ (X = Cl, Br) (black), averaged $^{theo}CCS_{N2}$ values (red) and the average Pd–Pd distances in the central cavity (blue) from the snapshots of the MDs.

For all species except $[Br,Cl,Br@Pd_4\mathbf{L}^{ethyl}_8]^{5+}$ the relative deviation to the experiment is between +2.2 % and +3.8 %, which is completely acceptable and can be traced back to inaccuracies in the trajectory method but for $[Br,Cl,Br@Pd_4\mathbf{L}^{ethyl}_8]^{5+}$ the error is with +6.6 % quite large. We observe in the MD simulations for the smaller species that they alternate between a helically twisted conformer (D_4 symmetry) and a more straightened conformer (D_{4d} symmetry). For $[Br,Cl,Br@Pd_4\mathbf{L}^{ethyl}_8]^{5+}$ both conformations are shown in Figure 2.13. In the helically twisted conformer, the ligands are in close contact and attract each other via London dispersion. In the more symmetric conformer, the ligands are further apart and the cage is more expanded. Driving force for the expansion is the repulsion between the anions and the Pd complexes. So, similar to the side chains the GFN2-xTB based MD simulations have to represent the equilibrium between both conformers accurately to obtain matching $^{theo}CCS_{N2}$ values, which does not seem to be the case for $[Br,Cl,Br@Pd_4\mathbf{L}^{ethyl}_8]^{5+}$.

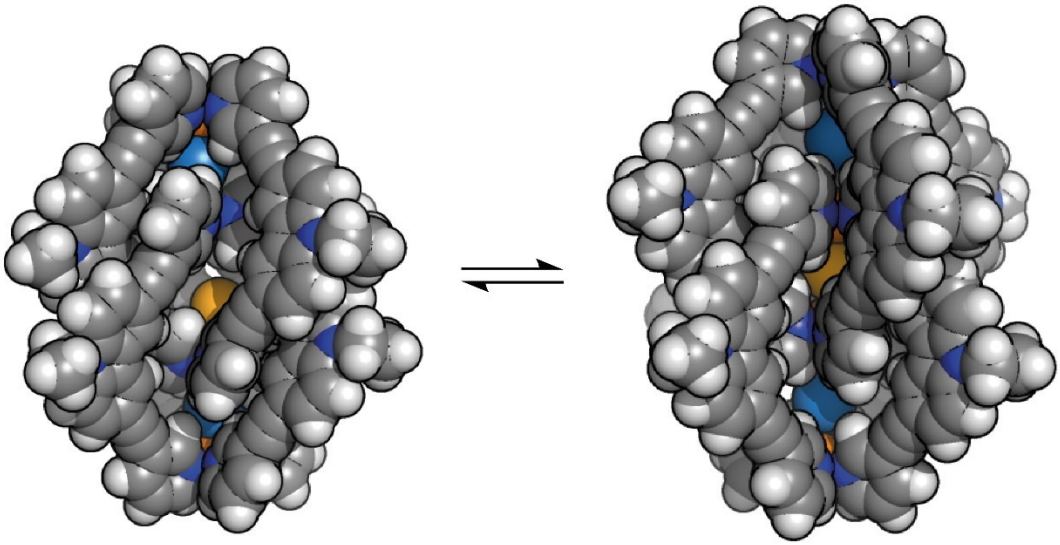

Figure 2.13. Two possible conformations of [Br,Cl,Br@$Pd_4\mathbf{L}^{\mathbf{ethyl}}_8$]$^{5+}$. The left conformer was optimized with GFN2-xTB, which has a dispersion correction. The right conformer was optimized with TPSS/def2-SVP, not using any dispersion correction.

2.3.3 Compaction through ligand-ligand π stacking in the gas phase

The theoretically possible folding of monomeric $Pd_2\mathbf{L}_4$ cages by dispersion driven π stacking of the ligands, especially likely in absence of solvent, was investigated using three more carbazole based ligands $\mathbf{L}^{\mathbf{methyl}}$, $\mathbf{L}^{\mathbf{phenyl}}$ and $\mathbf{L}^{\mathbf{pyrenyl}}$. The synthesis of $\mathbf{L}^{\mathbf{methyl}}$ was possible following the same procedure as for the other $\mathbf{L}^{\mathbf{alkyl}}$ ligands. For $\mathbf{L}^{\mathbf{phenyl}}$ fortunately 3,6-dibromo-*N*-phenylcarbazole was commercially available making the ligand synthesis possible with just a single Sonogashira coupling reaction. For $\mathbf{L}^{\mathbf{pyrenyl}}$ especially the Buchwald Hartwig coupling reaction for the bond formation between the carbazole nitrogen atom and the pyrene was challenging. The coupling was only possible with electron donating (trimethylsilyl)alkynyl groups at positions 3 and 6 at the carbazole unit. Figure 2.14 shows the three ligands used in this study. The available π surface varies from ligand to ligand, however, there is notable steric hindrance between the protons in ortho position in the phenyl and pyrenyl groups with the carbazole backbone. This causes the backbone not to be perfectly flat which could hinder π stacking to a certain degree.

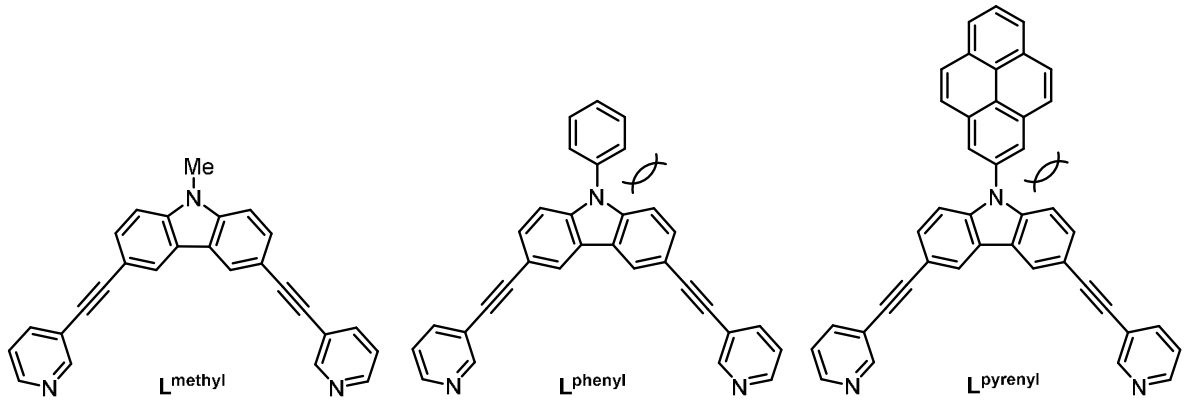

Figure 2.14. Banana shaped bis-monodentate ligands $\mathbf{L}^{\mathbf{methyl}}$, $\mathbf{L}^{\mathbf{phenyl}}$ and $\mathbf{L}^{\mathbf{pyrenyl}}$. Intra-ligand steric hindrance for the latter two is marked.

Monomeric cage formation was conducted by adding 0.5 eq. $[Pd(CH_3CN)_4](BF_4)_2$ to each ligand in acetonitrile and cage formation was indicated with downfield shift of ^{1}H NMR signals of protons close to the nitrogen donor atom. The samples were injected into the timsTOF device, the expected *m/z* values of the according monomeric cages were detected and the high resolution ion mobilities were measured. The spectra of the 4+ species are shown in Figure 2.15. The spectra of the 3+ and, if available, the 2+ species are shown in Figure 2.38, Figure 2.43 and Figure 2.48.

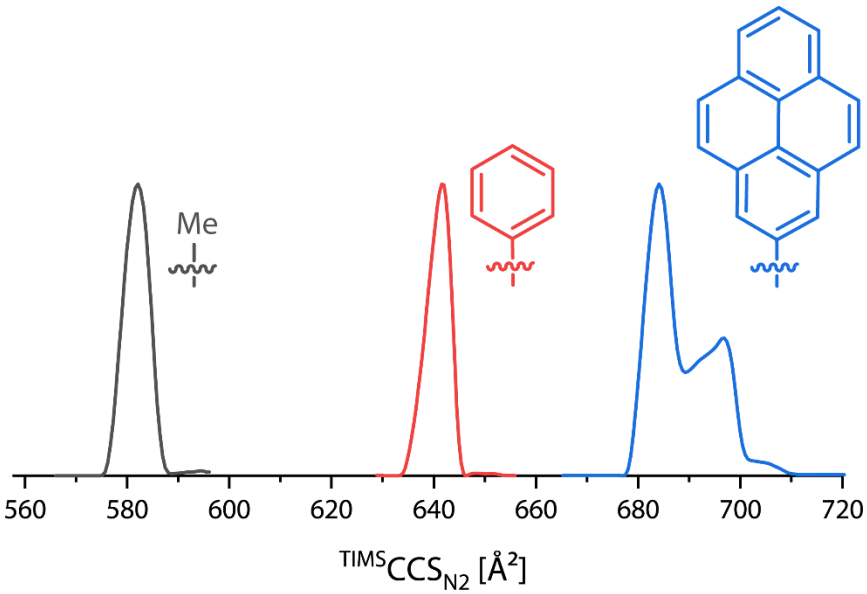

Figure 2.15. Ion mobility spectra converted to $^{TIMS}CCS_{N2}$ of $[Pd_2\mathbf{L}^{\mathbf{methyl}}{}_4]^{4+}$ (grey), $[Pd_2\mathbf{L}^{\mathbf{phenyl}}{}_4]^{4+}$ (red) and $[Pd_2L^{\mathbf{pyrenyl}}{}_4]^{4+}$ (blue). Inserts show the different substituents at the carbazole nitrogen atom.

$[Pd_2\mathbf{L}^{\mathbf{methyl}}{}_4]^{4+}$ has a $^{TIMS}CCS_{N2}$ of 582 ± 3 Å, $[Pd_2\mathbf{L}^{\mathbf{phenyl}}{}_4]^{4+}$ has one of 642 ± 3 Å and the two signals of $[Pd_2\mathbf{L}^{\mathbf{phenyl}}{}_4]^{4+}$ are at 684 ± 3 Å and 697 ± 3 Å. The $^{TIMS}CCS_{N2}$ increases from $[Pd_2\mathbf{L}^{\mathbf{methyl}}{}_4]^{4+}$ to $[Pd_2\mathbf{L}^{\mathbf{phenyl}}{}_4]^{4+}$ by 10.2 % and from the latter to $[Pd_2\mathbf{L}^{\mathbf{pyrenyl}}{}_4]^{4+}$ only by 6.6 % or 8.6 % even though the increase of

bulkiness in these outwards pointing groups is larger from phenyl to pyrenyl than from methyl to phenyl, which is the first indication that $[Pd_2\mathbf{L}^{\mathbf{pyrenyl}}{}_4]^{4+}$ folds in the gas phase while the other two do not.

While the spectra of $[Pd_2\mathbf{L}^{\mathbf{methyl}}{}_4]^{4+}$ and $[Pd_2\mathbf{L}^{\mathbf{phenyl}}{}_4]^{4+}$ are Gauss-shaped, the spectrum of $[Pd_2\mathbf{L}^{\mathbf{pyrenyl}}{}_4]^{4+}$ shows two overlapping signals. A folding of this cage could explain the observation of two signals as explained in the following. A model of a folded conformation of $[Pd_2L^{\mathbf{pyrenyl}}{}_4]^{4+}$ was optimized using r^{2}SCAN-3c. In the model for each stacked pair of ligands both the carbazole units are parallel to each other and the pyrenyl units are parallel to each other but are tilted by an angle of about 50° to the carbazole units due to the earlier mentioned steric hindrance. Therefore, the two pairs of pyrenyl groups in the folded cage could either point in the opposite direction leading to a D_2 symmetry or in the same direction causing a C_2 symmetry. Both possible conformations are shown in Figure 2.16. Notable here is the short distance between the proton in ortho position of the pyrenyl group of one ligand to one of the protons in the carbazole group in the other ligand. This steric hindrance may counteract the folding.

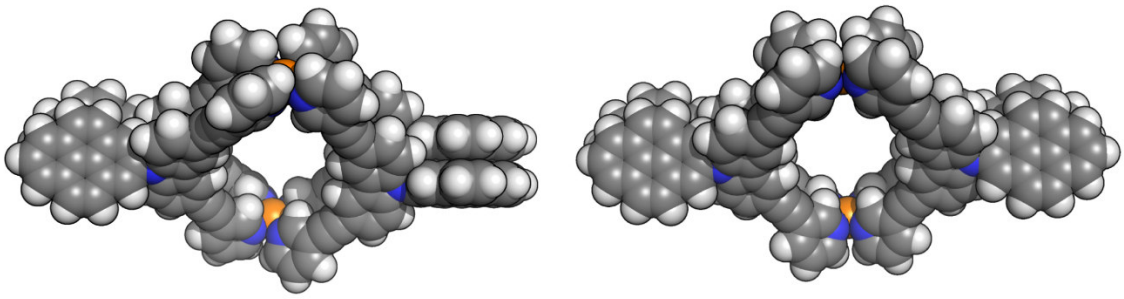

Figure 2.16. Models of two possible conformations of $[Pd_2\mathbf{L}^{\mathbf{pyrenyl}}{}_4]^{4+}$ in the folded state. Left: D_2 symmetry, right: C_S symmetry.

The three cages in this experiment are rather rigid and no significant dynamics are expected which is why only geometry optimized models are used for $^{\text{theo}}CCS_{N2}$ calculation. Of each cage open single folded and double folded conformers (for $[Pd_2\mathbf{L}^{\mathbf{phenyl}}{}_4]^{4+}$ and $[Pd_2L^{\mathbf{pyrenyl}}{}_4]^{4+}$ both the D_2 symmetric and the C_2 symmetric conformers were considered) were modeled and optimized using the r^{2}SCAN-3c functional. The models are depicted in Section 2.6.10. The open conformers did not fold during optimization meaning that they represent a local minimum in the energy landscape. The experimental $^{\text{TIMS}}CCS_{N2}$ and theoretical $^{\text{theo}}CCS_{N2}$ values as well as the relative deviations are listed in Table 2.7.

The open conformer of $[Pd_2\mathbf{L}^{\mathbf{methyl}}{}_4]^{4+}$ has a $^{\text{theo}}CCS_{N2}$ of 596.8 Å^2 (+2.5 %), which is perfectly matching the experimental value and the folded conformer has one of 532.6 Å^2 (–8.5 %), which is clearly too low. For $[Pd_2\mathbf{L}^{\mathbf{phenyl}}{}_4]^{4+}$ the results from the trajectory method are similar; here the open form has with 667.0 Å^2 an error of +4.0 %, which is quite high but still acceptable, and the two folded conformations

are at 592.7 Å^2 and 592.4 Å^2 (–7.6 % and –7.7 %), which are both too low. So, according to the results from the trajectory method, both $[Pd_2\mathbf{L}^{\mathbf{methyl}}{}_4]^{4+}$ and $[Pd_2\mathbf{L}^{\mathbf{phenyl}}{}_4]^{4+}$ stay open in the gas phase. For $[Pd_2\mathbf{L}^{\mathbf{pyrenyl}}{}_4]^{4+}$ it is the other way around. Here, the open conformer has a too high $^{theo}CCS_{N2}$ value of 807.3 Å^2 (+16.9 %) and the two folded conformers match the two experimentally observed signals nicely with 679.6 Å^2 and 686.0 Å^2 (–0.7 % and –1.6 %). Because the C_S conformer has a slightly higher $^{theo}CCS_{N2}$, it is assigned to the signal with the larger $^{TIMS}CCS_{N2}$.

Table 2.1. Experimental and theoretical CCS_{N2} values as well as relative deviations ($\Delta_{\%}$). Energy differences ΔE (= $E_{folded} - E_{open}$) regarding uncorrected DFT single point energies on ωB97M/def2-TZVP level (ΔE_{DFT}), dispersion corrections D4 (ΔE_{D4}) and VV10 (ΔE_{VV10}), G_{RRHO} corrections (ΔG_{RRHO}) and free energies (ΔG_{D4} and ΔG_{VV10}). Inter-fragment dispersion between the ligands in the folded conformation (HFLD/cc-pVTZ/TightPNO). CCS_{N2} values in Å², energies in kJ/mol.

system	$[Pd_2\mathbf{L}^{\mathbf{methyl}}{}_4]^{4+}$		$[Pd_2\mathbf{L}^{\mathbf{phenyl}}{}_4]^{4+}$			$[Pd_2\mathbf{L}^{\mathbf{pyrenyl}}{}_4]^{4+}$		
conformation	open	folded	open	folded, D_2	folded, C_S	open	folded, D_2	folded, C_S
$^{TIMS}CCS_{N2}$ [Å²]	582 ± 3			642 ± 3		684 ± 3, 697 ± 3		
$^{theo}CCS_{N2}$ [Å²]	596.8	532.6	667.0	592.7	592.4	807.3	679.6	686.0
$\Delta_{\%}$	+2.5 %	–8.5 %	+4.0 %	–7.6 %	–7.7 %	+16.9 %	–0.7 %	–1.6 %
ΔE_{DFT}	-	+135.1	-	+144.1	+147.9	-	+167.1	+172.8
ΔE_{D4}	-	–127.0	-	–151.3	–151.7	-	–255.5	–257.7
ΔE_{VV10}	-	–135.8	-	–163.8	–163.4	-	–276.7	–277.8
ΔG_{RRHO}	-	+13.3	-	+16.3	+15.6	-	+26.7	+28.5
ΔG_{D4}	-	+21.4	-	+8.9	+13.7	-	–61.7	–56.3
ΔG_{VV10}	-	+12.6	-	–3.5	+2.0	-	–82.9	–76.4
inter-frag. disp.	-	–149.7	-	–168.2	-	-	–258.2	-

Additionally, the systems were also investigated by electronic structure calculation. Gas phase Gibbs free energy differences ($\Delta G = G_{folded} - G_{open}$) were calculated on DFT level following the equation:[77]

$$\Delta G = \Delta E_{\mathrm{DFT}} + \Delta E_{\mathrm{disp.corr.}} + \Delta G_{\mathrm{RRHO}} \quad (14)$$

(G: Gibbs free energy, E_{DFT}: DFT electronic energy, $E_{disp.corr.}$: dispersion correction, G_{RRHO}: rigid rotator-harmonic oscillator correction)

Two different popular dispersion corrections, D4[78] and VV10,[79] were used and compared. In general, for all three systems the electronic energy ΔE_{DFT} has a highly positive value ranging from +135.1 kJ/mol for $[Pd_2\mathbf{L}^{\mathbf{methyl}}{}_4]^{4+}$ to +172.8 kJ/mol for the C_2 conformer of $[Pd_2\mathbf{L}^{\mathbf{pyrenyl}}{}_4]^{4+}$. The folding causes on the one hand distortions mainly of the N–Pd–N angles, the Pd–N–C_{para} angles and the angles at the alkynes. The exact distribution of distortion over the angles is unknown, however, in section 2.6.12 models optimized with different functionals are compared. On the other hand, π stacking for non-dispersion corrected DFT is wrongly unfavored. The larger the π surface the larger the electrostatic repulsion. Both dispersion corrections lead to highly negative values for $\Delta E_{disp.corr}$. Interestingly, VV10 shows by 6.9 % to 8.3 % stronger dispersive forces than D4. The benchmarking of both corrections with DLPNO-CCSD(T)[80]

in section 2.6.13 shows in short that VV10 slightly over- and D4 slightly underestimates the dispersion for these systems. ΔE_{DFT} and $\Delta E_{disp.corr}$ are in general in absolute terms in the same order of magnitude. For $[Pd_2\mathbf{L}^{methyl}_4]^{4+}$ ΔE_{DFT} is slightly larger, for $[Pd_2\mathbf{L}^{phenyl}_4]^{4+}$ $\Delta E_{disp.corr}$ is slightly larger and for $[Pd_2\mathbf{L}^{pyrenyl}_4]^{4+}$ $\Delta E_{disp.corr}$ is significantly larger than ΔE_{DFT}. ΔG_{RRHO} is positive for all systems with values ranging from +13.3 kJ/mol for $[Pd_2\mathbf{L}^{methyl}_4]^{4+}$ to +28.5 kJ/mol for the C_S conformer of $[Pd_2\mathbf{L}^{pyrenyl}_4]^{4+}$. It is assumed that this penalty stems mostly from the out-of-plane vibration of the atoms in the π surface. For all terms, differences between the D_2 and the C_2 conformer of $[Pd_2\mathbf{L}^{phenyl}_4]^{4+}$ and $[Pd_2\mathbf{L}^{pyrenyl}_4]^{4+}$ are rather small, as expected. The free energy difference for $[Pd_2\mathbf{L}^{methyl}_4]^{4+}$ strongly indicates with either +12.6 kJ/mol or +21.4 kJ/mol that this cage stays open in the gas phase. For $[Pd_2\mathbf{L}^{phenyl}_4]^{4+}$ the results are less obvious. Here, ΔG was calculated as either –3.5 kJ/mol or +8.9 kJ/mol for the D_2 conformer and as either +2.0 kJ/mol or +13.7 kJ/mol for the C_2 conformer. These energies suggest that the cage likely stays open in the gas phase or that there is a certain balance between open and folded conformers. Alternatively, the possibility of a single-folded conformation, in which only one pair of ligands folds, for any of the systems is discussed in Sections 2.6.8 and 2.6.11 including $^{theo}CCS_{N2}$ and DFT energies. For $[Pd_2\mathbf{L}^{pyrenyl}_4]^{4+}$ ΔG was calculated as either –82.9 kJ/mol or –61.7 kJ/mol for the D_2 conformer and as either –76.4 kJ/mol or –56.3 kJ/mol for the C_2 conformer, which strongly suggests that the cage is folded. The inter-fragment dispersion between the ligands was calculated using HFLD[81], which is done by a local energy decomposition on DLPNO-CCSD level. For this, one pair of ligands and both palladium atoms were cut out from the folded models so that only one pair of ligands are investigated. The computed inter-fragment dispersion for $[Pd_2\mathbf{L}^{methyl}_4]^{4+}$ is –149.7 kJ/mol, for $[Pd_2\mathbf{L}^{phenyl}_4]^{4+}$ it is –168.2 kJ/mol and for $[Pd_2\mathbf{L}^{pyrenyl}_4]^{4+}$ it is –258.2 kJ/mol. This way discrete values for the required dispersive forces to cause such a folding in the gas phase could be provided.

2.3.4 Counter anions in the trajectory method

As mentioned earlier, counter anions turn out to be rather problematic for $^{theo}CCS_{N2}$ calculation. We observed increasing positive deviation from the experiment with increasing amounts of counter anions, which is usually tetrafluoroborate, BF_4^-. One possible explanation could be missing Lennard Jones (LJ) parameters ε and σ for fluorine. Parameters are also missing for palladium and boron, but these atoms are usually buried deep, which is why simply the parameters from carbon were chosen for these two elements. Strong variation of the parameters led to no significant changes in the $^{theo}CCS_{N2}$. For fluorine we first chose the parameters from oxygen but then noticed that slight changes in the parameters indeed had an effect. Thus, the LJ parameters for fluorine had to be optimized following the procedure reported by Larriba et al.[82] The new parameters were obtained as ε_F = 500 Å, σ_F = 2.67 J/mol and were tested both for systems with counter anions and for cages with several fluorine atoms in the ligand backbones. An improvement could be noticed clearly, although the error still increases with increasing amount of counter anions. This phenomenon was also observed when other $^{theo}CCS_{N2}$ calculation

programs or different point charge schemes were used. See Section 2.6.5 and Section 2.6.6 for more details.

In the trajectory method the molecule's coordinates are fixed and therefore the structure is not influenced by collisions with the N_2 gas particles. This error is partially compensated by the LJ parameters, because they were fit to experimental data, however, counter anions are usually very lightweight which is why collisions with N_2 should considerably bump the counter anions away. This could have a significant effect on the scattering angle, from which the $^{theo}CCS_{N2}$ is approximated from. If the anion is inside the cavity, which is likely the case if only one anion is present, the cavity is less permeable if the anion is fixed and does not respond to collision, which also artificially increases the $^{theo}CCS_{N2}$.

2.3.5 Folding in the solid state and in solution

The folding of lantern-shaped $Pd_2\mathbf{L}_4$ cages by π stacking of the ligands leads to a less defined cavity, similar to that of a ring. Thus, a change in guest binding behavior might occur. It is therefore important to test whether the folding could also occur in other states, for example in the solid, crystalline state and especially in solution. First, a single-crystal X-ray structure of $Pd_2\mathbf{L}^{pyrenyl}_4$ was obtained by slow diffusion of isopropyl ether into a solution of $[Pd_2\mathbf{L}^{pyrenyl}_4](BF_4)_4$ in deuterated nitromethane (Section 2.5.10 for details). The asymmetric unit contains two cages, both in the open conformation. The cages are slightly twisted helicates (one left-handed, one right-handed) as are the DFT-optimized models. In this regard they differ from the rather orthogonal positioned ligands in the crystal structure of $[Pd_2\mathbf{L}^{hexyl}_4]^{4+}$, as reported in Ref. 72. Looking at the packing, we see that the cages show π-stacking with each other, probably making intramolecular folding in the solid state redundant. The crystal packing is shown in Figure 2.50 and Figure 2.51, the asymmetric unit is shown in Figure 2.52. Figure ***2.17*** shows two intertwined cages from the crystal packing that interact via π stacking with each other.

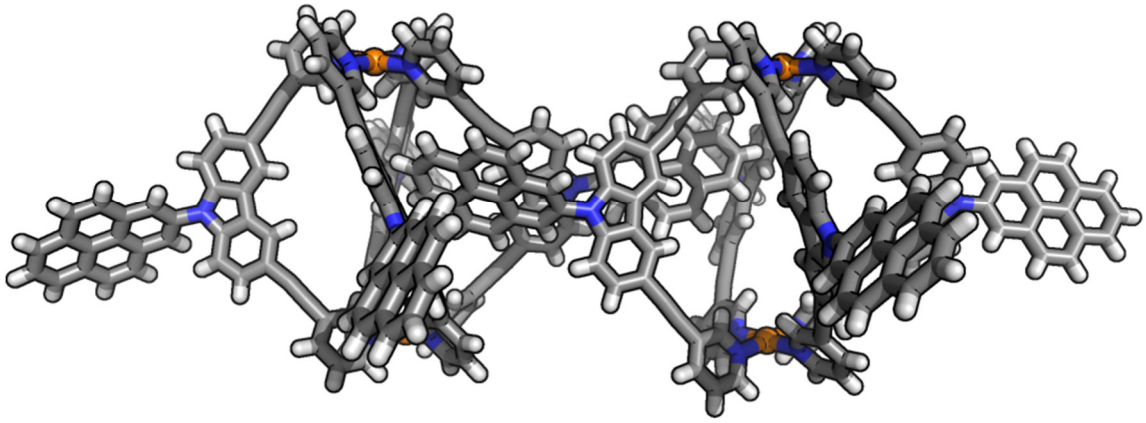

Figure 2.17. Two $Pd_2\mathbf{L}^{pyrenyl}_4$ cages from the crystal packing that interact via π stacking with each other. Counter anions omitted for clarity.

Interestingly, we observed the folding phenomenon in a crystal structure of another homoleptic cage, $Pd_2\mathbf{L}^{\mathbf{FL}}{}_4$, with $\mathbf{L}^{\mathbf{FL}}$ being a bent, bis-monodentate ligand with pyridine donor groups, phenyl linkers and a fluorenone backbone.[83] Figure 2.18 shows both $\mathbf{L}^{\mathbf{FL}}$ and the asymmetric unit containing two cages of which one is in an open and the other is in a single-folded conformation. More images of this crystal structure are shown in Figure 2.53 and Figure 2.54.

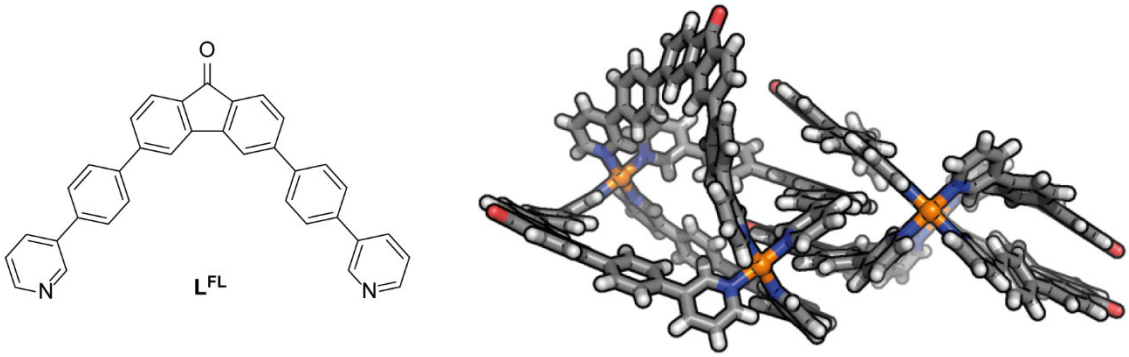

Figure 2.18. $\mathbf{L}^{\mathbf{FL}}$ and the asymmetric unit of the crystal structure of $Pd_2\mathbf{L}^{\mathbf{FL}}{}_4$. Counter anions omitted for clarity.

This unambiguously shows that folding is indeed possible with ligands of regular size. The DFT free energy difference between the open and the double-folded conformer was calculated for $[Pd_2\mathbf{L}^{\mathbf{FL}}{}_4]^{4+}$ as $\Delta G_{D4} = -53.1$ kJ/mol, a similar value as calculated for $[Pd_2\mathbf{L}^{\mathbf{pyrenyl}}{}_4]^{4+}$. $\mathbf{L}^{\mathbf{FL}}$ has a smaller aromatic π surface than $\mathbf{L}^{\mathbf{pyrenyl}}$, which mirrors in the dispersion correction energy difference of only $\Delta E_{D4} = -176.2$ kJ/mol; about 100 kJ/mol weaker than for $[Pd_2\mathbf{L}^{\mathbf{pyrenyl}}{}_4]^{4+}$. But the repulsive parts of the interaction are weaker as well, probably because the phenyl rings in $\mathbf{L}^{\mathbf{FL}}$ can rotate and optimize their positions to minimize repulsion and maximize attraction, while $[Pd_2\mathbf{L}^{\mathbf{pyrenyl}}{}_4]^{4+}$ suffers from the earlier mentioned steric hindrance between the hydrogen atoms of the carbazole and of the pyrene moieties. All obtained energy terms regarding $[Pd_2\mathbf{L}^{\mathbf{FL}}{}_4]^{4+}$ are listed in Table 2.8. That the asymmetric unit of $Pd_2\mathbf{L}^{\mathbf{pyrenyl}}{}_4$ contains two open cages and the one of $Pd_2\mathbf{L}^{\mathbf{FL}}{}_4$ contains an open and a single-folded cage seems to be also due to crystal packing effects, which are difficult to retrace.

The obtained crystal structure for $Pd_2\mathbf{L}^{\mathbf{pyrenyl}}{}_4$ already gives indications for the situation in solution. In the crystal the cage does not fold because it has other cages to interact with. In solution the situation is similar because it can interact with the solvent and thus does not have to interact with itself. For the solvated state, ^{1}H DOSY NMR in acetonitrile of $Pd_2\mathbf{L}^{\mathbf{methyl}}{}_4$, $Pd_2\mathbf{L}^{\mathbf{phenyl}}{}_4$ and $Pd_2\mathbf{L}^{\mathbf{pyrenyl}}{}_4$ was measured. The solvodynamic radius increases with increasing bulkiness of the substituent from 10.8 Å to 11.6 Å (+7.3 %) and 13.1 Å (+21 %). The larger jump from $Pd_2\mathbf{L}^{\mathbf{phenyl}}{}_4$ to $Pd_2\mathbf{L}^{\mathbf{pyrenyl}}{}_4$ indicates that the latter cage stays open in acetonitrile as well. To be noted is that if $Pd_2\mathbf{L}^{\mathbf{pyrenyl}}{}_4$ stays folded in solution, it deviates strongly from a spherical shape, making the used equations to transfer the diffusion coefficient to the

solvodynamic radius unsuitable. Additionally, a balance between open and (single-)folded conformers cannot be ruled out.

Interestingly, pyrene is known to show excimer behavior, meaning that the excited state of a pyrene dimer is lower in energy than the according monomer, leading to a bathochromic shift in fluorescence.[84] It would be highly interesting to see whether this phenomenon could be observed for $Pd_2\mathbf{L}^{\mathbf{pyrenyl}}{}_4$ as well, as a bathochromic shift in fluorescence could indicate folding. If the cage stays open in acetonitrile, perhaps an increase of water content could induce folding by hydrophobic effect.

To improve solubility of this cage, the ligand was resynthesized but with EG4 chains at the pyridine donor groups. The resulting $\mathbf{L}^{\mathbf{pyEG4}}$ is shown in Figure 2.19, synthesis and characterization in Section 2.5.11.

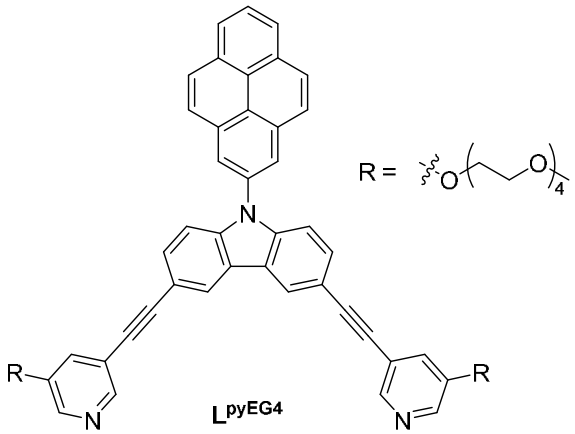

Figure 2.19. Structure of $\mathbf{L}^{\mathbf{pyEG4}}$.

The fluorescence (excitation wavelength λ_{ex} = 340 nm) of the ligand $\mathbf{L}^{\mathbf{pyEG4}}$ and the cage $Pd_2\mathbf{L}^{\mathbf{pyEG4}}{}_4$ was measured in pure acetonitrile and in samples with up to 50 % water content. The fluorescence spectra are shown in Figure 2.20. The highest fluorescence is observed at about 425 nm for every measurement, both for ligand and cage. When the water content reaches 50 %, the spectrum of the sample with the free ligand shows an additional shoulder from around 500 nm to 600 nm. This indicates that the free ligands start aggregating and show excimer fluorescence.

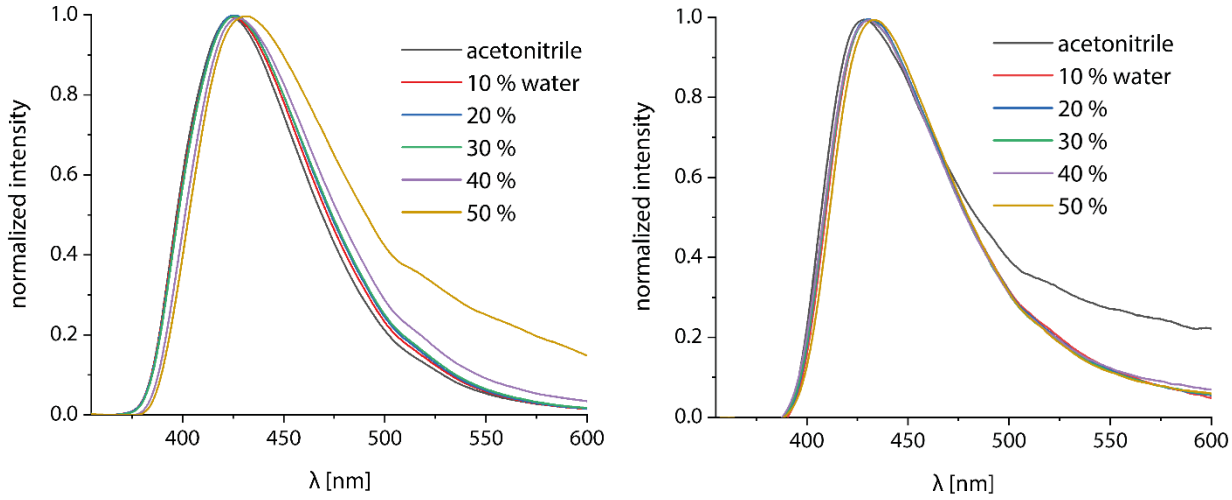

Figure 2.20. Fluorescence of free $\mathbf{L}^{\mathbf{PyEG4}}$ (left) and $Pd_2\mathbf{L}^{\mathbf{PyEG4}}{}_4$ (right) in acetonitrile/water with varying ratios. ligand concentration: 0.28 mM. λ_{ex} = 340 nm.

For the cage a shoulder is only visible in the spectrum of the sample with pure acetonitrile and not in those of the samples with water content. A possible explanation for this is that $Pd_2\mathbf{L}^{\mathbf{PyEG4}}{}_4$ does alternate between an open and a folded conformation in pure acetonitrile but with higher water content the cages aggregate and show aggregation induced emission. These findings are merely indications for possible folding in solution and much more research needs to be done in this direction. More details are found in Section 2.5.12.

2.4 Conclusion

To conclude, Trapped Ion Mobility Spectrometry in combination with Trajectory Method based collision cross section calculation is a powerful method for gaining structural insights into complex large structures such as Pd based monomeric and double coordination cages. A major difficulty stems from solubility groups like alkyl chains which were thoroughly investigated via MD simulations on semiempirical level. As a rule of thumb, alkyl side chains start showing significant backfolding behavior from a length of C_8. Although it was possible to reproduce experimental trends quite well more accurate results could be obtained with more precise London dispersion calculation methods.

Thanks to the high resolution of TIMS, we were able to detect very minor differences in double cage expansion caused by chloride and bromide guests, which nicely complements previous data on this subject. The trend could be mostly reproduced and significant dispersion driven twisting of double cages in the gas phase could be shown.

Folding or compacting of monomeric cages in the gas phase, driven by π-π interactions and causing distortions at the Pd centers, are rather unlikely, yet it was possible to synthesize a new cage with very large π surfaces that does indeed follow this behavior and provide values in the form of inter-fragment

dispersion for quantification. An example of this folding phenomenon in the solid state and indications that this might also happen in solution were found.

2.5 Experimental Details

2.5.1 Synthesis of $\mathbf{L^R}$

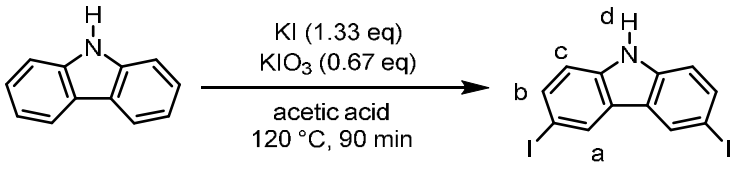

Scheme 2.1. Synthesis of 3,6-Diiodocarbazole.

To a suspension of carbazole (1 eq, 5 mmol, 836 mg) and KI (1.33 eq, 6.65 mmol, 1104 mg) in 50 mL acetic acid was given KIO_3 (0.67 eq, 3.35 mmol, 717 mg) and the mixture was stirred at 120 °C for 90 min. The reaction mixture was then first allowed to cool down and subsequently taken up in a water/ethyl acetate mixture. The organic phase was washed with water three times and then the solvent was removed *in vacuo*. The remaining solid was then purified using automated flash chromatography (*n*-pentane/EtOAc, 0 % to 25 %). 3,6-Diiodocarbazole was obtained as white solid (61 %, 3.03 mmol 1268 mg).

^{1}H NMR (600 MHz, $CDCl_3$) of 3,6-diiodocarbazole: δ [ppm] = 8.33 (s, 2H, a), 8.08 (br, 1H, d), 7.68 (d, J = 8.4 Hz, 2H, b), 7.21 (d, J = 8.5 Hz, 2H, c).

^{13}C{^{1}H} NMR (151 MHz, $CDCl_3$) of 3,6-diiodocarbazole: δ [ppm] = 138.68, 134.97, 129.59, 124.74, 112.88, 82.60.

ESI-MS of 3,6-diiodocarbazole (neg. mode): measured: 417.8568, calculated for $[C_{12}H_7NI_2–H]^-$: 417.8595.

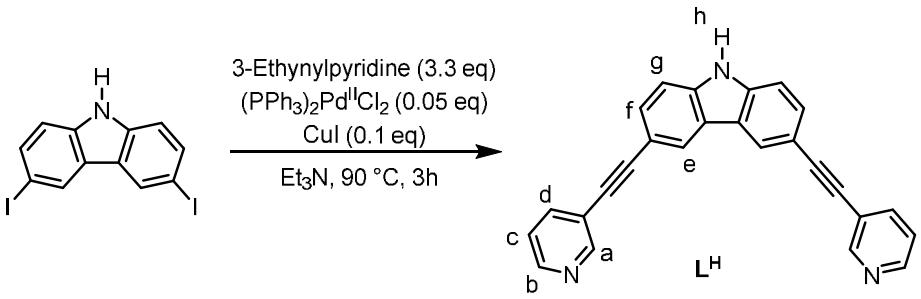

Scheme 2.2. Synthesis of $\mathbf{L^H}$.

For the synthesis of **L^{H}**, 3,6-diiodocarbazole (1.0 eq, 1.19 mmol, 500 mg) and 3-ethynylpyridine (3.3 eq, 3.93 mmol, 405 mg) were dissolved in 12 mL NEt_3 and degassed with three *freeze-pump-thaw*-cycles. After the addition of $(PPh_3)_2Pd(II)Cl_2$ (0.05 eq, 0.119 mmol, 83.5 mg) and CuI (0.1 eq., 0.238 mmol, 45.3 mg) three more *freeze-pump-thaw*-cycles were conducted. The reaction mixture was then heated and stirred at 90 °C for 3 h. As **L^{H}** is insoluble in MeCN, the mixture was filtered and the remaining solid was washed with MeCN yielding **L^{H}** as yellow powder (85 %, 1.01 mmol, 374 mg).

^{1}H NMR (DMSO-d$_6$) of L^{H}: δ [ppm] = 11.90 (s, 1H, h), 8.90 (br, a), 8.71 (br, b), 8.55 (s, 2H, e), 8.04 (d, J = 7.9 Hz, 2H, d), 7.69 (d, J = 8.5, 2H, f), 7.61 (d, J = 8.4, 2H, g), 7.54 (br, c).

^{13}C{^{1}H} NMR (DMSO-d$_6$) of L^{H}: δ [ppm] = 140.21, 138.25, 129,67, 124.43, 122.13, 112.05, 111.82, 94.09. Of 11 expected signals only 8 were detected, likely due to poor solubility of this ligand.

ESI-MS of L^{H}: measured: 370.1348, calculated for $[C_{26}H_{15}N_3+H]^+$: 370.1339.

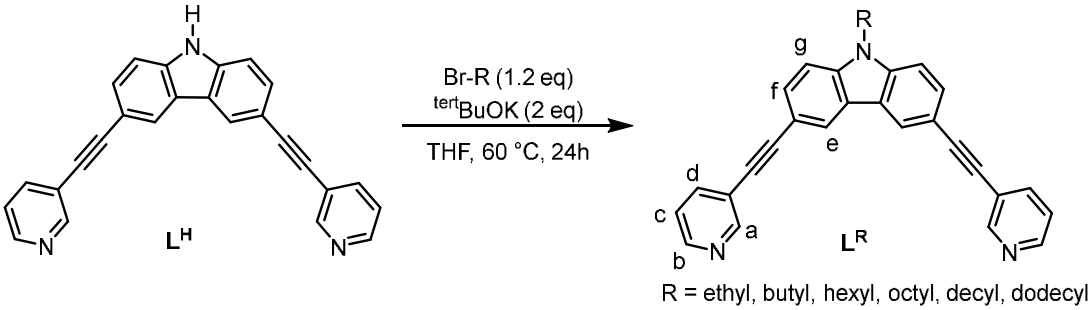

Scheme 2.3. Synthesis of **L^{R}**.

For each of the final ligands **L^{R}** (1.0 eq, 81.2 µmol, 30 mg), ^{tert}BuOK (2.0 eq, 162 µmol, 18.2 mg) and 1-bromoalkane (1.2 eq, 97.44 µmol) was dissolved in 3 mL THF and heated and stirred at 60 °C for 24 h. Afterwards, the reaction mixture was transferred into a round bottom flask, silica was added and the solvent was removed *in vacuo*. The resulting ligands were obtained after automated flash chromatography (*n*-pentane/ethyl acetate in varying ratios) as yellow-white solids (41-99 %).

^{1}H NMR (400 MHz) of L^{ethyl}: δ [ppm] = 8.78 (s, 2H, a), 8.55 (d, J = 4.9 Hz, 2H, b), 8.39 (s, 2H, e), 7.91 (d, J = 7.9 Hz, 2H, d), 7.72 (d, J = 8.5, 2H, f), 7.61 (d, J = 8.5, 2H, g), 7.39 (dd, J_1 = 7.9 Hz, J_2 = 4.8 Hz, 2H, c), 4.46 (q, J = 7.2, 2H, N-CH_2-), 1.41 (t, J = 7.2, 3H, -CH_3).

^{13}C{^{1}H} NMR (DMSO-d$_6$) of L^{ethyl}: δ [ppm] = 151.62, 148.66, 140.12, 138.38, 129.85, 124.62, 123.75, 122.01, 120.09, 112.43, 110.16, 93.88, 84.65, 17.28, 14.10.

ESI-MS of L^{ethyl}: measured: 398.1658, calculated for $[C_{28}H_{19}N_3+H]^+$: 397.1573.

^{1}H NMR (400 MHz) of L^{butyl}: *δ* [ppm] = 8.77 (s, 2H, a), 8.55 (d, J = 4.9 Hz, 2H, b), 8.39 (s, 2H, e), 7.91 (d, J = 7.9 Hz, 2H, d), 7.70 (d, J = 8.5, 2H, f), 7.60 (d, J = 8.5, 2H, g), 7.39 (dd, J_1 = 7.9 Hz, J_2 = 4.8 Hz, 2H, c), 4.41 (q, J = 7.2, 2H, N-CH_2-), 1.85 (m, 2H, N-CH_2-C*H*$_2$-), 1.38 (m, 2H, -CH_2-), 0.94 (t, J = 7.2, 3H, -CH_3).

^{13}C{^{1}H} NMR (DMSO-d_6) of L^{butyl}: *δ* [ppm] = 151.5, 148.7, 140.6, 138.4, 129.9, 124.6, 123.8, 121.9, 120.0, 112.4, 110.4, 94.1, 84.7, 42.5, 30.7, 19.7, 13.8.

ESI-MS of L^{butyl}: measured: 425.1925, calculated for $[C_{30}H_{22}N_3+H]^+$: 425.1886.

^{1}H NMR of L^{hexyl}: *δ* [ppm] = 8.77 (s, 2H, a), 8.55 (d, J = 4.9 Hz, 2H, b), 8.39 (s, 2H, e), 7.91 (d, J = 7.9 Hz, 2H, d), 7.70 (d, J = 8.5, 2H, f), 7.60 (d, J = 8.5, 2H, g), 7.39 (dd, J_1 = 7.9 Hz, J_2 = 4.8 Hz, 2H, c), 4.40 (q, J = 7.2, 2H, N-CH_2-), 1.87 (m, 2H, N-CH_2-C*H*$_2$-), 1.21-1.40 (m, 6H, -CH_2-), 0.85 (t, J = 7.2, 3H, -CH_3).

^{13}C{^{1}H} NMR (DMSO-d_6) of L^{hexyl}: *δ* [ppm] = 151.4, 148.7, 140.6, 138.3, 129.8, 124.5, 123.7, 121.8, 120.0, 112.3, 110.3, 93.9, 84.7, 42.9, 30.9, 28.5, 26.1, 22.0, 13.8.

ESI-MS of L^{hexyl}: measured: 454.2348, calculated for $[C_{32}H_{27}N_3+H]^+$: 454.2278.

^{1}H NMR (600 MHz) of L^{octyl}: *δ* [ppm] = 8.77 (s, 2H, a), 8.55 (d, J = 4.9 Hz, 2H, b), 8.39 (s, 2H, e), 7.91 (d, J = 7.9 Hz, 2H, d), 7.70 (d, J = 8.5, 2H, f), 7.60 (d, J = 8.5, 2H, g), 7.39 (dd, J_1 = 7.9 Hz, J_2 = 4.8 Hz, 2H, c), 4.40 (q, J = 7.2, 2H, N-CH_2-), 1.86 (m, 2H, N-CH_2-C*H*$_2$-), 1.16-1.40 (m, 10H, -CH_2-), 0.85 (t, J = 7.2, 3H, -CH_3).

^{13}C{^{1}H} NMR (DMSO-d_6) of L^{octyl}: *δ* [ppm] = 151.4, 148.7, 140.5, 138.3, 129.8, 124.5, 123.7, 121.8, 120.0, 112.3, 110.3, 93.9, 84.7, 42.6, 31.1, 28.7, 28.6, 28.5, 26.4, 22.0, 13.9.

ESI-MS of L^{octyl}: measured: 482.2650, calculated for $[C_{34}H_{31}N_3+H]^+$: 482.2591.

^{1}H NMR (400 MHz) of L^{decyl}: *δ* [ppm] = 8.77 (s, 2H, a), 8.55 (d, J = 4.9 Hz, 2H, b), 8.39 (s, 2H, e), 7.91 (d, J = 7.9 Hz, 2H, d), 7.70 (d, J = 8.5, 2H, f), 7.60 (d, J = 8.5, 2H, g), 7.39 (dd, J_1 = 7.9 Hz, J_2 = 4.8 Hz, 2H, c), 4.40 (q, J = 7.2, 2H, N-CH_2-), 1.86 (m, 2H, N-CH_2-C*H*$_2$-), 1.16-1.40 (m, 14H, -CH_2-), 0.87 (t, J = 7.2, 3H, -CH_3).

^{13}C{^{1}H} NMR (DMSO-d_6) of L^{decyl}: *δ* [ppm] = 151.43, 148.64, 140.47, 138.31, 129.77, 124.51, 123.73, 121.82, 112.28, 110.31, 93.90, 84.62, 31.24, 28.90, 28.81, 28.67, 28.62, 28.46, 26.34, 22.06, 13.94. 23 signals are expected, 21 are observed, likely due to signal overlap.

ESI-MS of L^{decyl}: measured: 510.2966, calculated for $[C_{36}H_{35}N_3+H]^+$: 510.2904.

^{1}H NMR of $L^{dodecyl}$: *δ* [ppm] = 8.77 (s, 2H, a), 8.55 (d, J = 4.9 Hz, 2H, b), 8.39 (s, 2H, e), 7.91 (d, J = 7.9 Hz, 2H, d), 7.70 (d, J = 8.5, 2H, f), 7.60 (d, J = 8.5, 2H, g), 7.39 (dd, J_1 = 7.9 Hz, J_2 = 4.8 Hz, 2H, c), 4.40 (q, J = 7.2, 2H, h), 1.86 (m, 2H, i), 1.16-1.38 (m, 18H, j), 0.87 (t, J = 7.2, 3H, k).

$^{13}C\{^{1}H\}$ NMR (DMSO-d_6) of $L^{dodecyl}$: δ [ppm] = 152.30, 148.26, 140.87, 138.41, 129.98, 124.51, 123.20, 122.60, 113.35, 109.30, 94.14, 84.74, 43.56, 32.07, 29.73, 29.66, 29.61, 29.48, 29.46, 29.09, 22.94, 14.26. 25 signals are expected, 22 are observed, likely due to signal overlap.

ESI-MS of $L^{dodecyl}$: measured: 538.3271, calculated for $[C_{38}H_{39}N_3+H]^+$: 538.3217.

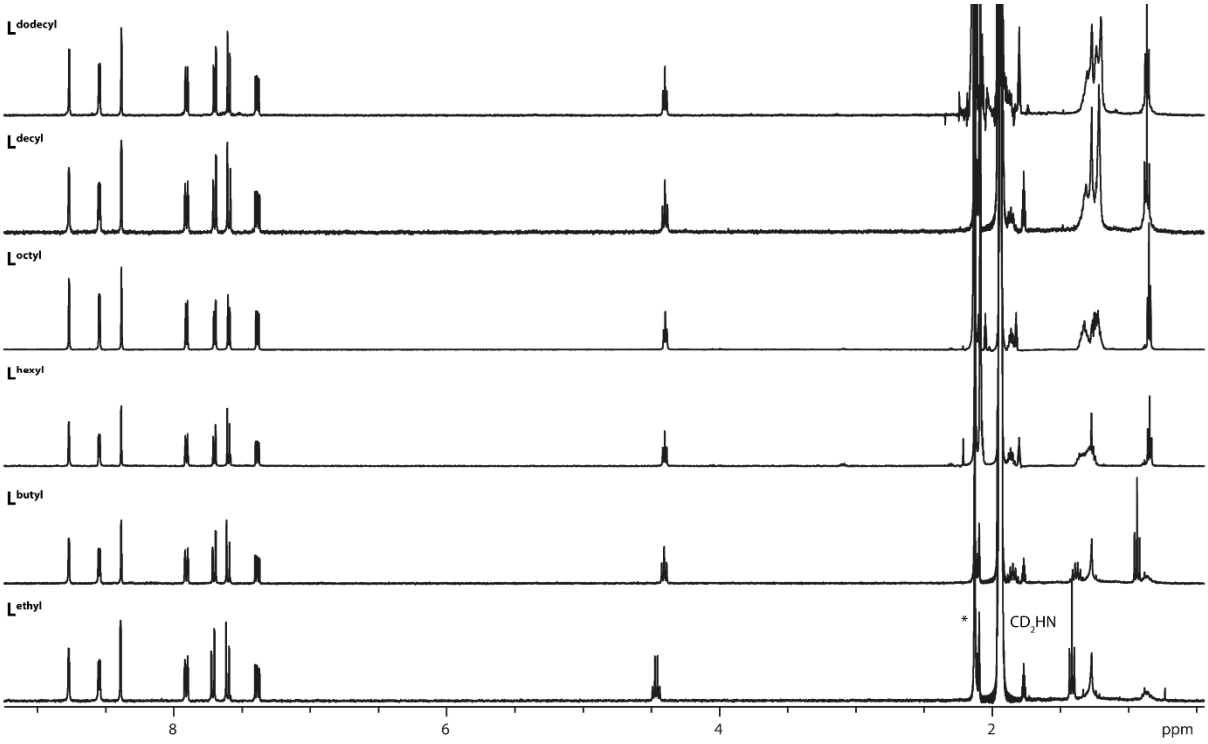

Figure 2.21. ^{1}H NMR spectra of $\mathbf{L^R}$.

2.5.2 Formation and characterization of cages $Pd_2\mathbf{L^R}_4$

294 µL of a 3 mM suspension of $\mathbf{L^R}$ in CD_3CN (1.0 eq) were combined with 29.4 µL of a 15 mM stock solution of $[Pd(CH_3CN)_4](BF_4)_2$ in CD_3CN (0.5 eq) and 227 µL CD_3CN yielding 550 µL of a 0.4 mM solution of $[Pd_2\mathbf{L^R}_4](BF_4)_4$.

^{1}H NMR (400 MHz) of $Pd_2\mathbf{L^{ethyl}}_4$**:** δ [ppm] = 9.00 (s, 8H, a), 8.77 (d, J = 5.9 Hz, 8H, b), 8.49 (s, 8H, e), 8.17 (d, J = 8.2, 8H, d), 7.73 (d, J = 8.5, 8H, f), 7.62 (dd, J_1 = 8.2 Hz, J_2 = 5.9 Hz, 8H, c), 7.59 (d, J = 8.6 Hz, 8H, g), 4.40 (q, J = 7.1, 8H, h), 1.34 (t, J = 7.2, 12H, k).

^{1}H NMR (400 MHz) of $Pd_2\mathbf{L^{butyl}}_4$**:** δ [ppm] = 9.00 (s, 8H, a), 8.77 (d, J = 5.9 Hz, 8H, b), 8.48 (s, 8H, e), 8.17 (d, J = 8.2, 8H, d), 7.71 (d, J = 8.5, 8H, f), 7.62 (dd, J_1 = 8.2 Hz, J_2 = 5.9 Hz, 8H, c), 7.58 (d, J = 8.6 Hz, 8H, g), 4.34 (t, J = 7.1, 8H, h), 1.77 (m, 8H, i), 1.30 (m, 8H, j), 0.86 (t, J = 7.5, 12H, k).

^{1}H NMR of $Pd_2\mathbf{L}^{hexyl}_4$**:** δ [ppm] = 8.99 (s, 8H, a), 8.77 (d, J = 5.8 Hz, 8H, b), 8.45 (s, 8H, e), 8.17 (d, J = 8.1, 8H, d), 7.71 (d, J = 8.7, 8H, f), 7.62 (dd, J_1 = 8.2 Hz, J_2 = 5.9 Hz, 8H, c), 7.58 (d, J = 8.3 Hz, 8H, g), 4.34 (t, J = 7.1, 8H, h), 1.78 (m, 8H, i), 1.13-1.33 (m, 24H, j), 0.76 (t, J = 7.5, 12H, k).

^{1}H NMR (400 MHz) of $Pd_2\mathbf{L}^{octyl}_4$**:** δ [ppm] = 9.00 (s, 8H, a), 8.77 (d, J = 5.8 Hz, 8H, b), 8.45 (s, 8H, e), 8.17 (d, J = 8.1, 8H, d), 7.71 (d, J = 8.7, 8H, f), 7.62 (dd, J_1 = 8.2 Hz, J_2 = 5.9 Hz, 8H, c), 7.57 (d, J = 8.3 Hz, 8H, g), 4.34 (t, J = 7.1, 8H, h), 1.78 (m, 8H, i), 1.06-1.34 (m, 40H, j), 0.77 (t, J = 7.5, 12H, k).

^{1}H NMR (400 MHz) of $Pd_2\mathbf{L}^{decyl}_4$**:** δ [ppm] = 8.99 (s, 8H, a), 8.77 (d, J = 5.8 Hz, 8H, b), 8.47 (s, 8H, e), 8.17 (d, J = 8.1, 8H, d), 7.71 (d, J = 8.7, 8H, f), 7.62 (dd, J_1 = 8.2 Hz, J_2 = 5.9 Hz, 8H, c), 7.57 (d, J = 8.3 Hz, 8H, g), 4.34 (t, J = 7.1, 8H, h), 1.78 (m, 8H, i), 1.06-1.34 (m, 56H, j), 0.79 (t, J = 7.5, 12H, k).

^{1}H NMR (400 MHz) of $Pd_2\mathbf{L}^{dodecyl}_4$**:** δ [ppm] = 9.00 (s, 8H, a), 8.78 (d, J = 5.8 Hz, 8H, b), 8.48 (s, 8H, e), 8.17 (d, J = 8.1, 8H, d), 7.71 (d, J = 8.7, 8H, f), 7.62 (dd, J_1 = 8.2 Hz, J_2 = 5.9 Hz, 8H, c), 7.57 (d, J = 8.3 Hz, 8H, g), 4.34 (t, J = 7.1, 8H, h), 1.78 (m, 8H, i), 1.00-1.34 (m, 72H, j), 0.80 (t, J = 7.5, 12H, k).

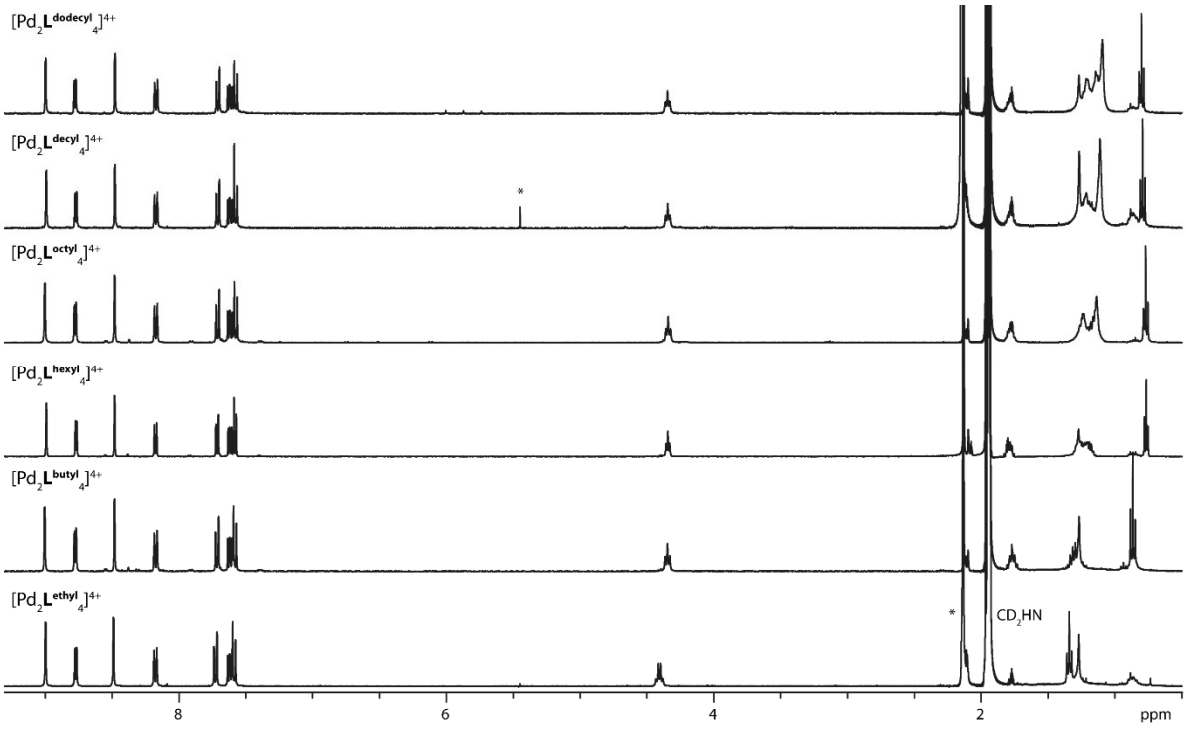

Figure 2.22. ^{1}H NMR spectra of $Pd_2\mathbf{L}^{R}_4$.

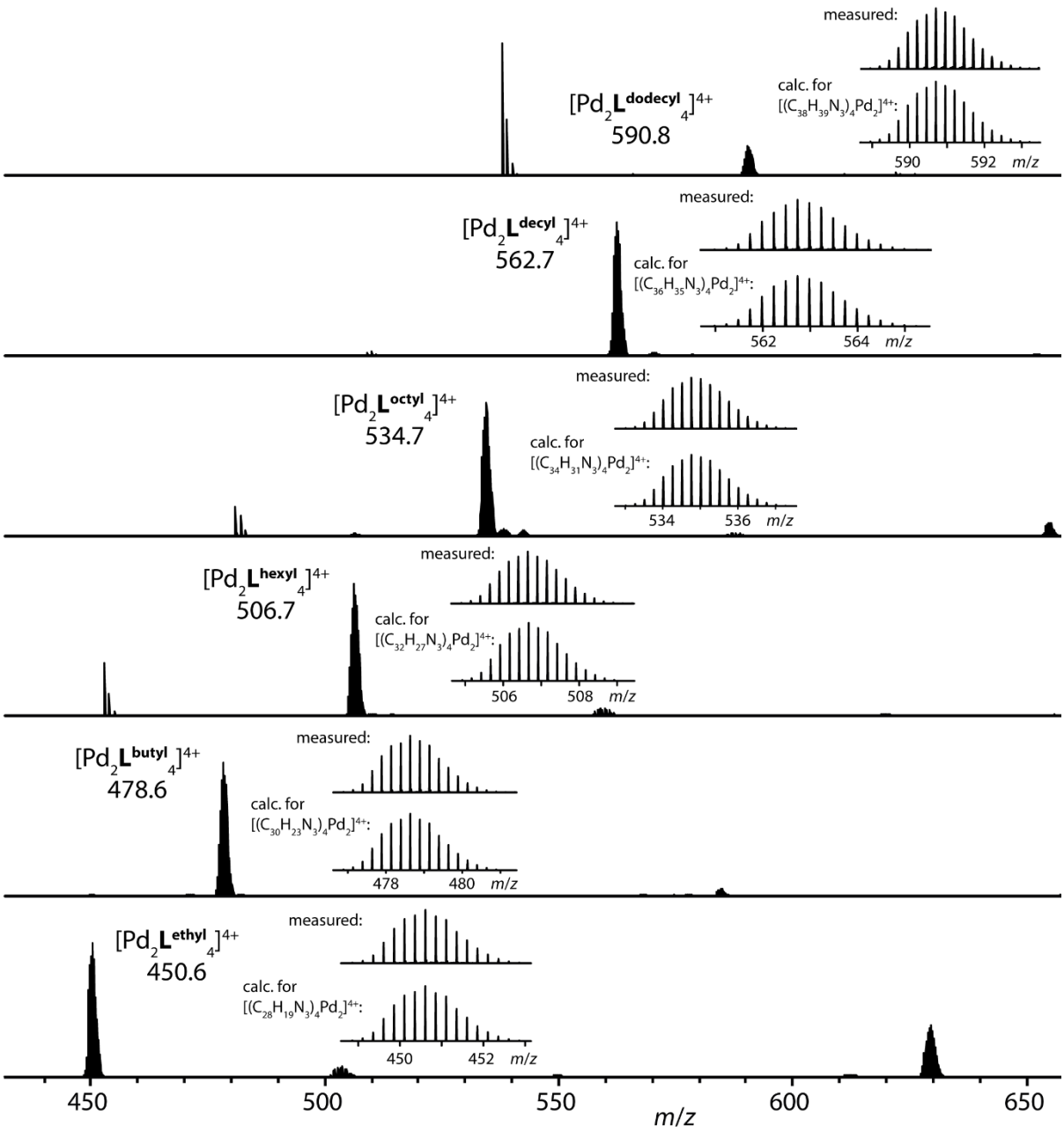

Figure 2.23. ESI MS spectra of $Pd_2L^R{}_4$.

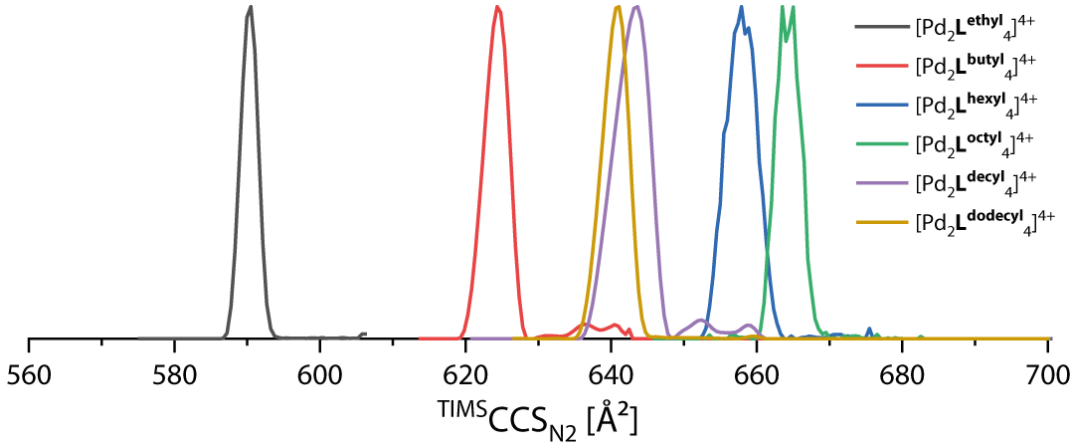

Figure S4: Overlaid TIMS mobilograms of $[Pd_2\mathbf{L}^{\mathbf{R}}_4]^{4+}$. Inverse mobilities were normalized and converted into CCS values.

2.5.3 Formation and characterization of $3X@Pd_4\mathbf{L}^{\mathbf{R}}_8$

To the 0.4 mM monomeric cage solution, 22 µL of a 10 mM solution of $(Bu_4N)Br$ in CD_3CN (1.0 cage eq) was added. The resulting solution contained both monomeric cage $Pd_2\mathbf{L}^{\mathbf{R}}_4$ and interpenetrated double cage $3Br@Pd_4\mathbf{L}^{\mathbf{R}}_8$ in the equilibrated mixture.[72] For $\mathbf{L}^{\mathbf{ethyl}}$, alternatively, also a mixture with $(Bu_4N)Cl$ was prepared to form $3Cl@Pd_4\mathbf{L}^{\mathbf{ethyl}}_8$.

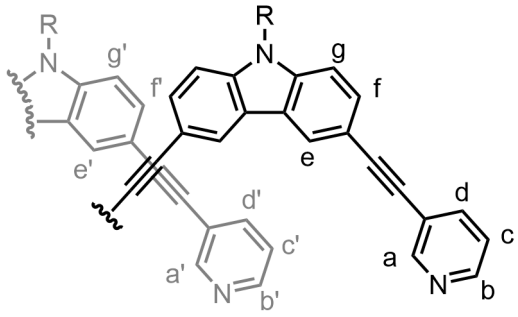

Figure 2.24. Proton labeling for $3Br@Pd_4\mathbf{L}^{\mathbf{R}}_8$. a^L: Proton a of free ligand, a^M: Proton a of monomeric cage, a^D, $a^{D\prime}$: Protons a and a' of double cage.

^{1}H NMR of $3Br@Pd_4\mathbf{L}^{\mathbf{ethyl}}_8$**:** δ [ppm] = 11.20 (s, 8H, $a^{D\prime}$), 10.57 (d, J = 5.5 Hz, 8H, $b^{D\prime}$), 10.31 (s, 8H, a^D), 9.02 (s, a^M), 8.78 (m, b^M, a^L), 8.72 (d, J = 5.6 Hz, 8H, b^D), 8.57 (s, b^L), 8.49 (s, e^M), 8.41 (s, e^L), 8.17 (d, d^M), 8.13 (d, J = 8.0, 8H, d^D), 8.04 (d, d^L), 7.53-7.76 (m, f^L, c^M, f^M, c^D, $c^{D\prime}$, g^D, f^D, $d^{D\prime}$), 7.51 (dd, c^L), 6.88 (d, J = 8.7, 8H, $g^{D\prime}$), 6.77 (s, 8H, $e^{D\prime}$), 6.73 (s, 8H, e^D), 6.06 (d, J = 8.5, 8H, $f^{D\prime}$), 4.47 (m, h^L), 4.40 (q, h^M), 4.34 (q, J = 7.1 Hz, 8H, h^D).

^{1}H NMR of $3Br@Pd_4\mathbf{L}^{\mathbf{butyl}}_8$**:** δ [ppm] = 11.20 (s, 8H, $a^{D\prime}$), 10.57 (d, J = 5.5 Hz, 8H, $b^{D\prime}$), 10.31 (s, 8H, a^D), 9.02 (s, a^M), 8.78 (m, b^M, a^L), 8.72 (d, J = 5.6 Hz, 8H, b^D), 8.55 (s, b^L), 8.48 (s, e^M), 8.39 (s, e^L), 8.18 (d, d^M), 8.14 (d, J = 8.0, 8H, d^D), 7.95 (d, d^L), 7.51-7.76 (m, f^L, c^M, f^M, c^D, $c^{D\prime}$, g^D, f^D, $d^{D\prime}$), 7.42 (dd, c^L), 6.84

(d, J = 8.7, 8H, $g^{D'}$), 6.76 (s, 8H, $e^{D'}$), 6.75 (s, 8H, e^{D}), 6.09 (d, J = 8.5, 8H, $f^{D'}$), 4.40 (m, h^{L}), 4.34 (q, h^{M}), 4.27 (q, J = 7.1 Hz, 8H, h^{D}).

^{1}H NMR of 3Br@Pd_4**L**$^{hexyl}_8$**:** δ [ppm] = 11.20 (s, 8H, $a^{D'}$), 10.57 (d, J = 5.5 Hz, 8H, $b^{D'}$), 10.30 (s, 8H, a^{D}), 9.02 (s, a^{M}), 8.78 (m, b^{M}, a^{L}), 8.71 (d, J = 5.6 Hz, 8H, b^{D}), 8.55 (s, b^{L}), 8.48 (s, e^{M}), 8.39 (s, e^{L}), 8.17 (d, d^{M}), 8.13 (d, J = 8.0, 8H, d^{D}), 7.91 (d, d^{L}), 7.49-7.74 (m, f^{L}, c^{M}, f^{M}, c^{D}, $c^{D'}$, g^{D}, f^{D}, $d^{D'}$), 7.39 (dd, c^{L}), 6.82 (d, J = 8.7, 8H, $g^{D'}$), 6.75 (s, 8H, $e^{D'}$), 6.74 (s, 8H, e^{D}), 6.06 (d, J = 8.5, 8H, $f^{D'}$), 4.40 (m, h^{L}), 4.34 (q, h^{M}), 4.26 (q, J = 7.1 Hz, 8H, h^{D}).

^{1}H NMR (400 MHz) of 3Br@Pd_4**L**$^{octyl}_8$**:** δ [ppm] = 11.21 (s, 8H, $a^{D'}$), 10.57 (d, J = 5.5 Hz, 8H, $b^{D'}$), 10.31 (s, 8H, a^{D}), 9.01 (s, a^{M}), 8.78 (m, b^{M}, a^{L}), 8.72 (d, J = 5.6 Hz, 8H, b^{D}), 8.55 (s, b^{L}), 8.48 (s, e^{M}), 8.38 (s, e^{L}), 8.17 (d, d^{M}), 8.13 (d, J = 8.0, 8H, d^{D}), 7.90 (d, d^{L}), 7.49-7.74 (m, f^{L}, c^{M}, f^{M}, c^{D}, $c^{D'}$, g^{D}, f^{D}, $d^{D'}$), 7.39 (dd, c^{L}), 6.82 (d, J = 8.7, 8H, $g^{D'}$), 6.76 (s, 8H, $e^{D'}$), 6.74 (s, 8H, e^{D}), 6.07 (d, J = 8.5, 8H, $f^{D'}$), 4.38 (m, h^{L}), 4.34 (q, h^{M}), 4.26 (q, J = 7.1 Hz, 8H, h^{D}).

^{1}H NMR of 3Br@Pd_4**L**$^{decyl}_8$**:** δ [ppm] = 11.21 (s, 8H, $a^{D'}$), 10.58 (d, J = 5.5 Hz, 8H, $b^{D'}$), 10.31 (s, 8H, a^{D}), 9.00 (s, a^{M}), 8.78 (m, b^{M}, a^{L}), 8.71 (d, J = 5.6 Hz, 8H, b^{D}), 8.57 (s, b^{L}), 8.48 (s, e^{M}), 8.41 (s, e^{L}), 8.17 (d, d^{M}), 8.13 (d, J = 8.0, 8H, d^{D}), 7.49-7.76 (m, f^{L}, c^{M}, f^{M}, c^{D}, $c^{D'}$, g^{D}, f^{D}, $d^{D'}$), 6.81 (d, J = 8.7, 8H, $g^{D'}$), 6.76 (s, 8H, $e^{D'}$), 6.74 (s, 8H, e^{D}), 6.06 (d, J = 8.5, 8H, $f^{D'}$), 4.40 (m, h^{L}), 4.34 (q, h^{M}), 4.26 (q, J = 7.1 Hz, 8H, h^{D}).

^{1}H NMR of 3Br@Pd_4**L**$^{dodecyl}_8$**:** δ [ppm] = 11.21 (s, 8H, $a^{D'}$), 10.59 (d, J = 5.5 Hz, 8H, $b^{D'}$), 10.32 (s, 8H, a^{D}), 9.01 (s, a^{M}), 8.78 (m, b^{M}, a^{L}), 8.72 (d, J = 5.6 Hz, 8H, b^{D}), 8.55 (s, b^{L}), 8.48 (s, e^{M}), 8.39 (s, e^{L}), 8.17 (d, d^{M}), 8.13 (d, J = 8.0, 8H, d^{D}), 7.90 (d, d^{L}), 7.48-7.74 (m, f^{L}, c^{M}, f^{M}, c^{D}, $c^{D'}$, g^{D}, f^{D}, $d^{D'}$), 7.39 (dd, c^{L}), 6.81 (d, J = 8.7, 8H, $g^{D'}$), 6.76 (s, 8H, $e^{D'}$), 6.74 (s, 8H, e^{D}), 6.06 (d, J = 8.5, 8H, $f^{D'}$), 4.34 (q, h^{M}), 4.26 (q, J = 7.1 Hz, 8H, h^{D}).

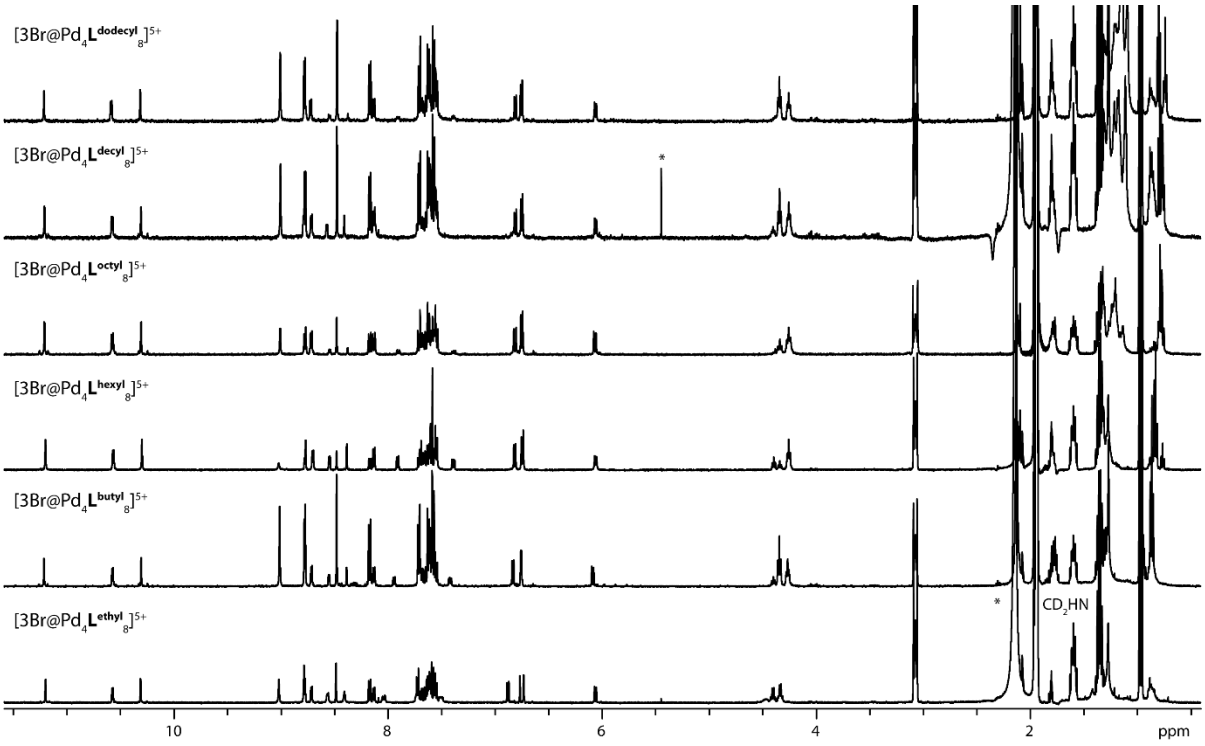

Figure 2.25. ^{1}H NMR of 3Br@$Pd_4\mathbf{L}^{\mathbf{R}}_8$.

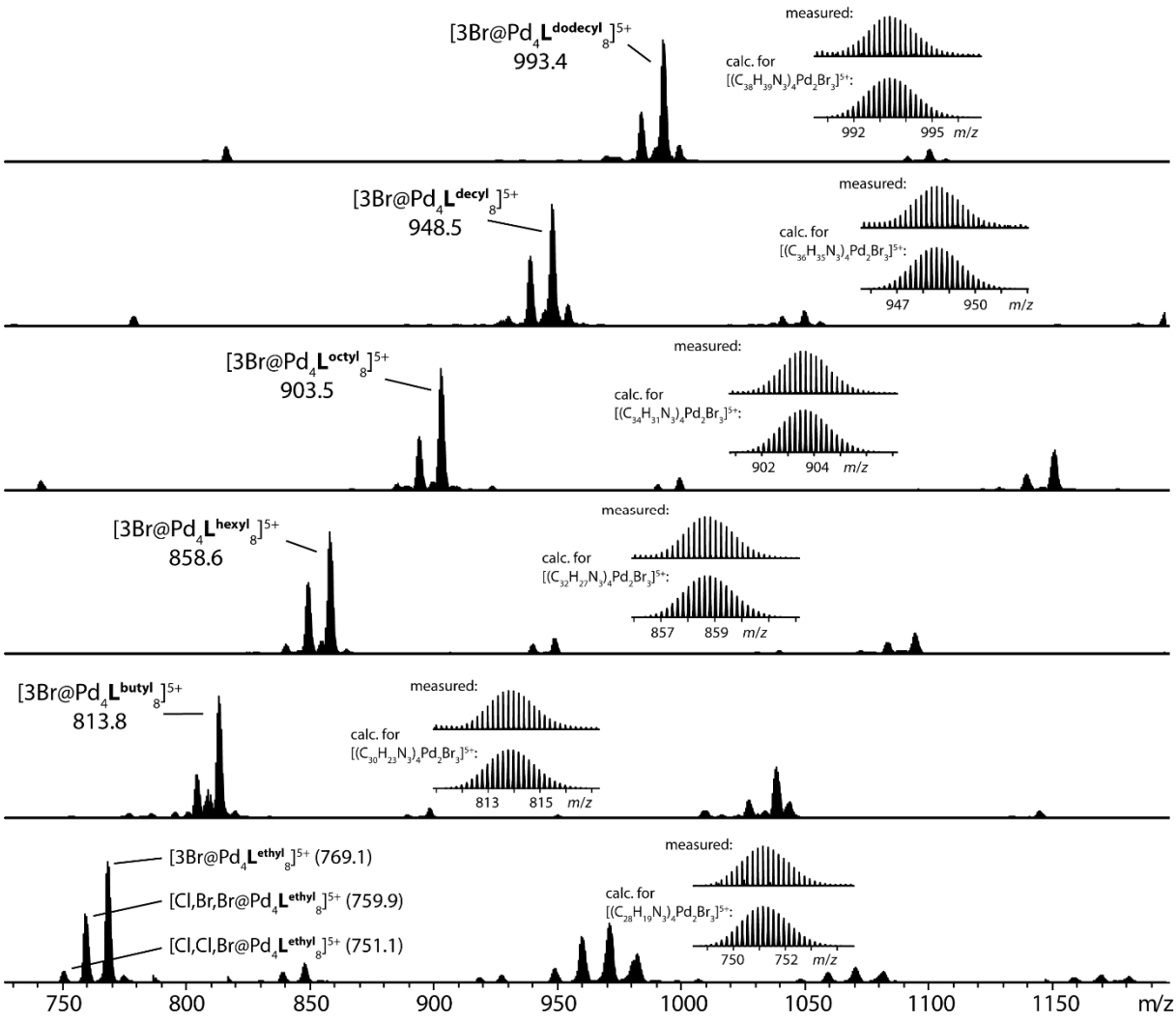

Figure 2.26. ESI-MS spectra of $3Br@Pd_4L^R_8$.

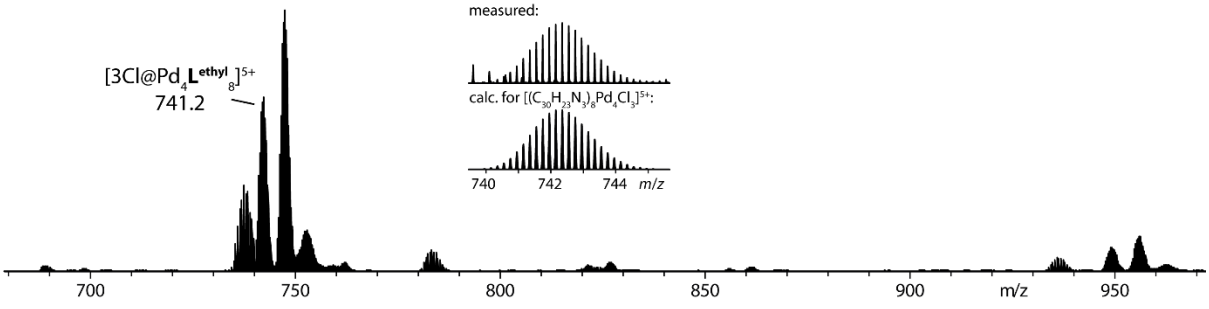

Figure 2.27. ESI MS spectrum of $3Cl@Pd_4L^{ethyl}_8$.

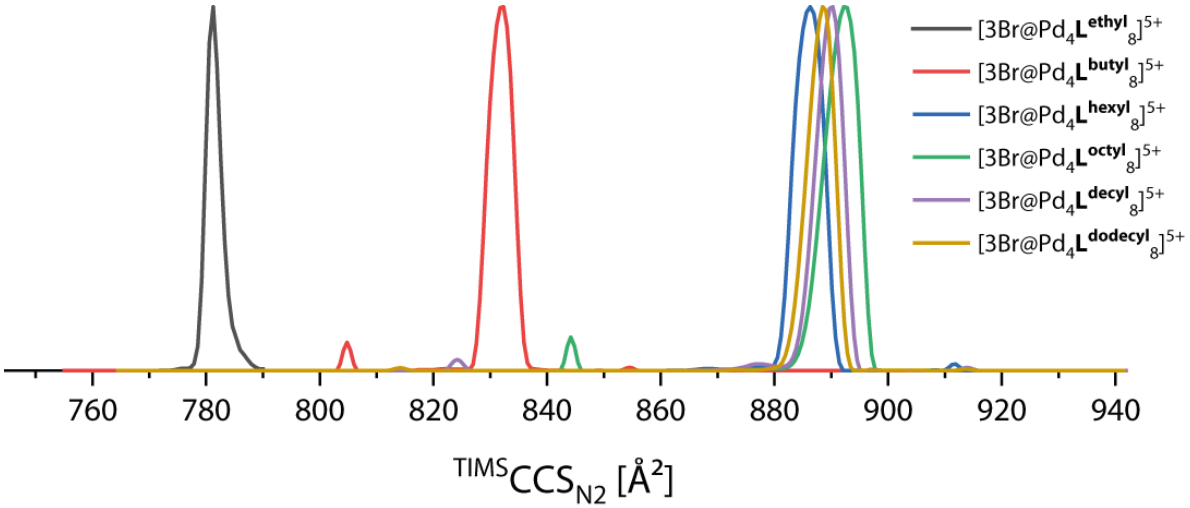

Figure 2.28. Overlaid TIMS mobilograms of $[3Br@Pd_4\mathbf{L}^{R}_8]^{5+}$. Inverse mobilities were normalized and converted into CCS values.

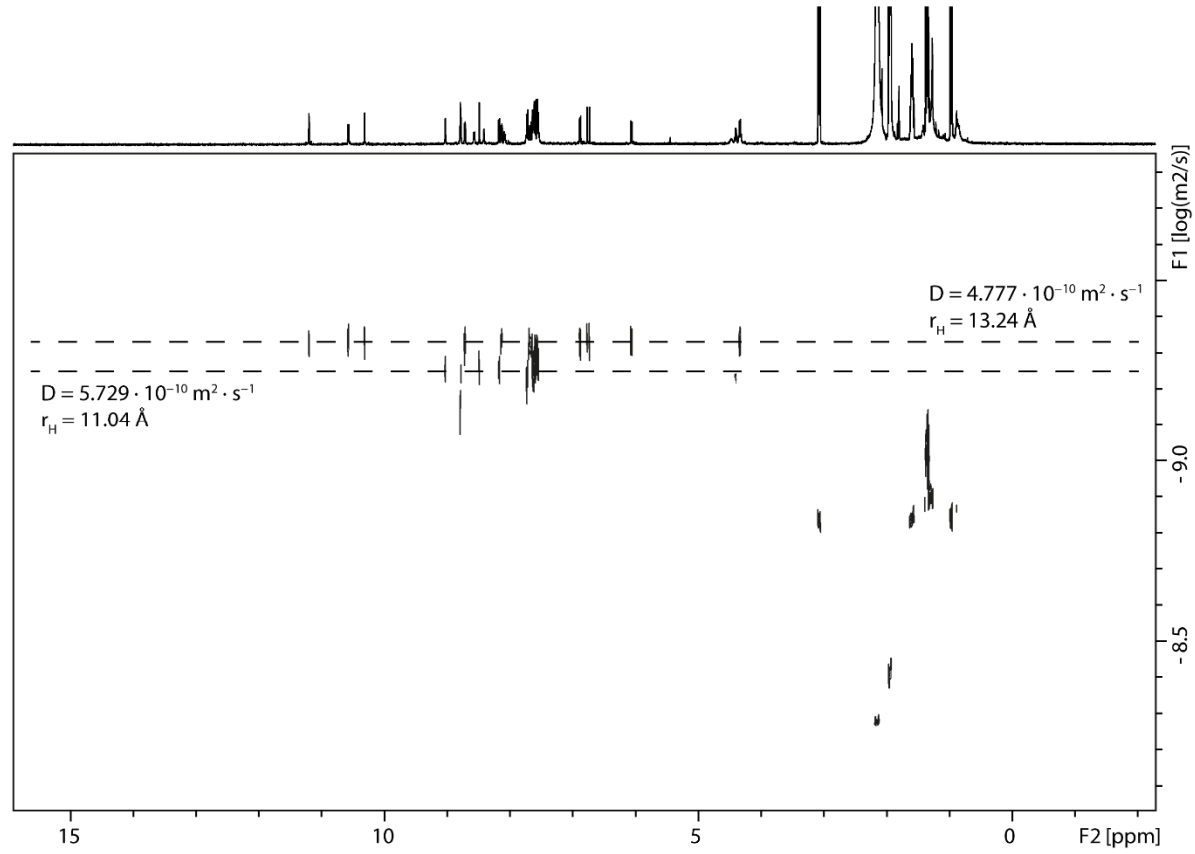

Figure 2.29. ^{1}H DOSY NMR of a mixture of $Pd_2\mathbf{L}^{ethyl}_4$ and $3Br@Pd_4\mathbf{L}^{ethyl}_8$.

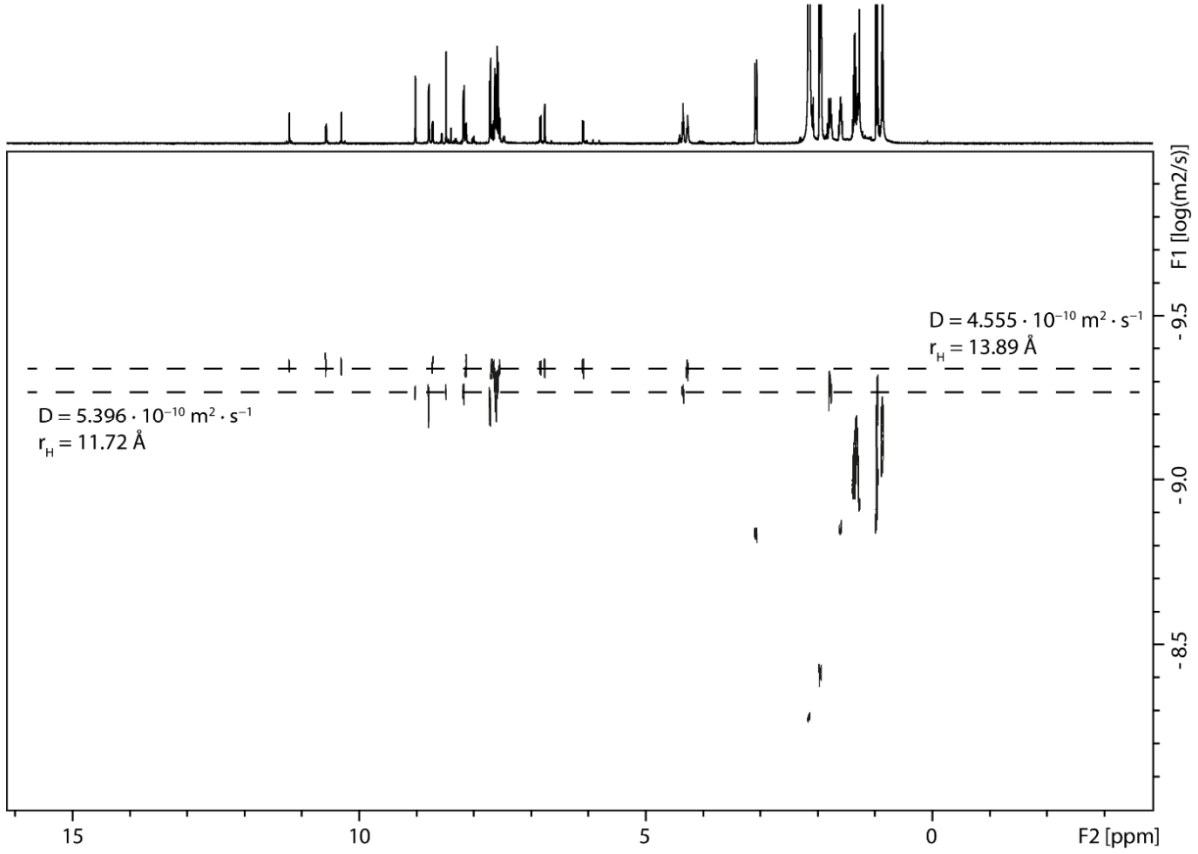

Figure 2.30. ^{1}H DOSY NMR of a mixture of $Pd_2\mathbf{L}^{\mathbf{butyl}}_4$ and $3Br@Pd_4\mathbf{L}^{\mathbf{butyl}}_8$.

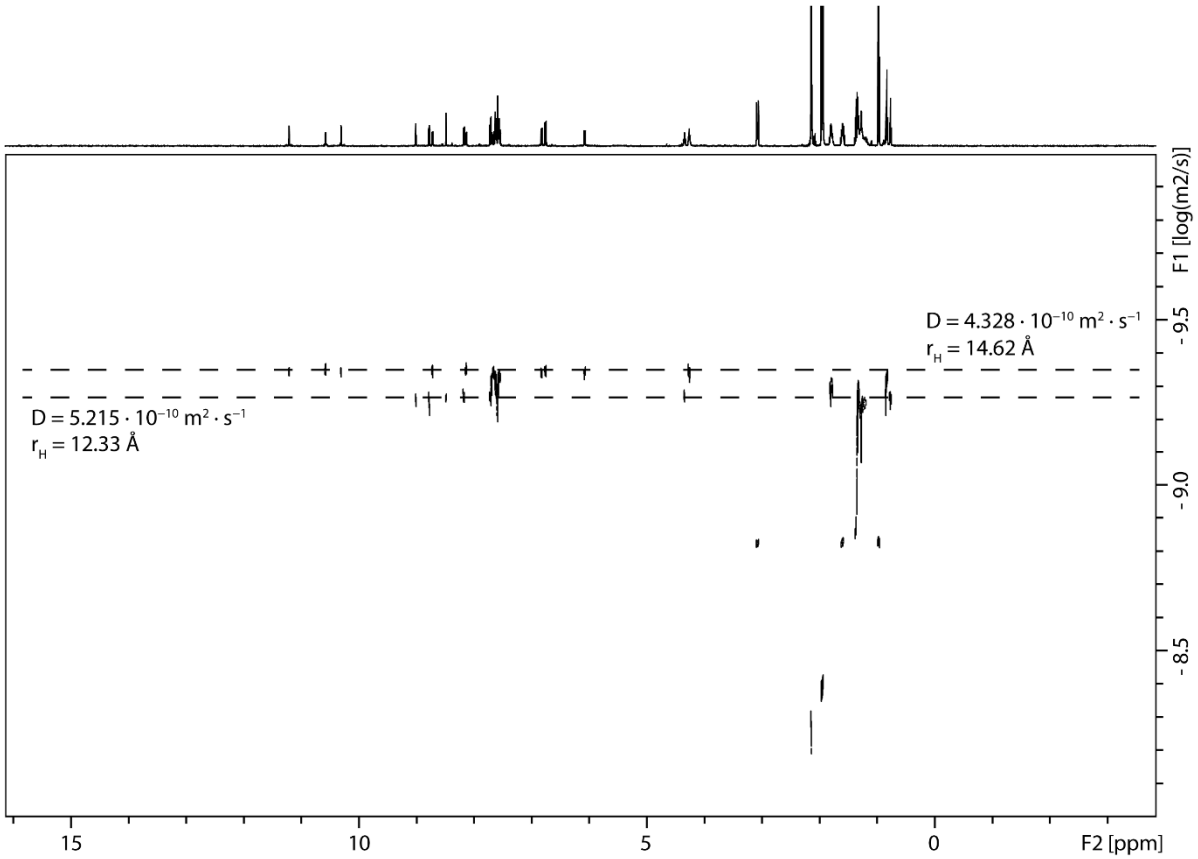

Figure 2.31. ^{1}H DOSY NMR of a mixture of $Pd_2\mathbf{L}^{\mathbf{hexyl}}_4$ and $3Br@Pd_4\mathbf{L}^{\mathbf{hexyl}}_8$.

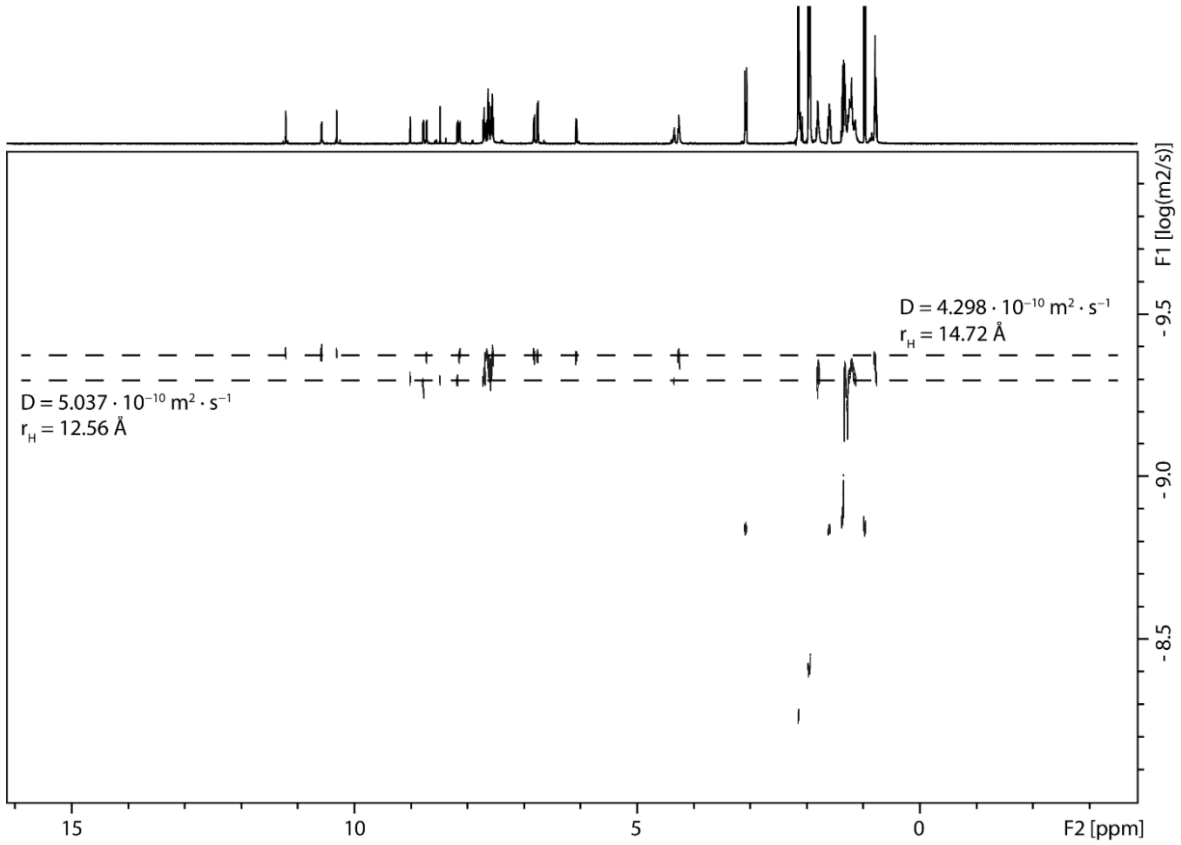

Figure 2.32. ^{1}H DOSY NMR of a mixture of $Pd_2\mathbf{L}^{octyl}{}_4$ and $3Br@Pd_4\mathbf{L}^{octyl}{}_8$.

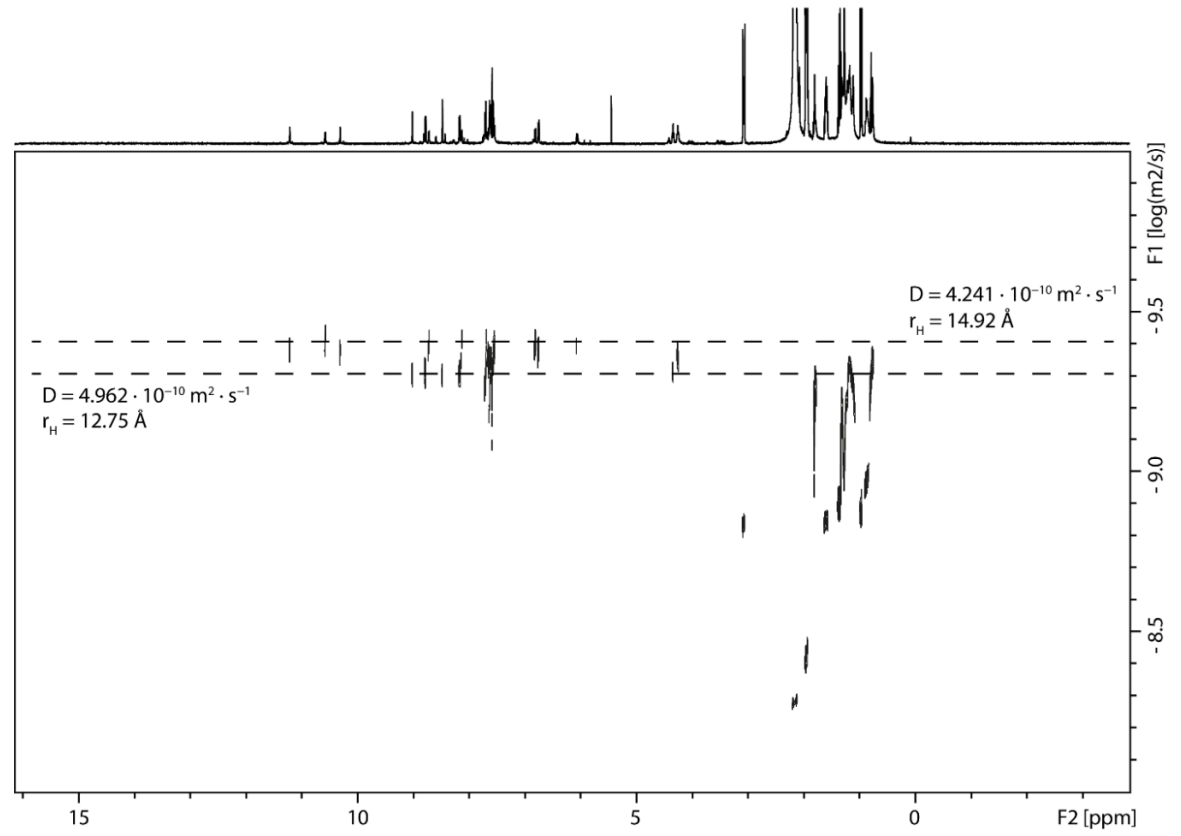

Figure 2.33. ^{1}H DOSY NMR of a mixture of $Pd_2\mathbf{L}^{decyl}{}_4$ and $3Br@Pd_4\mathbf{L}^{decyl}{}_8$.

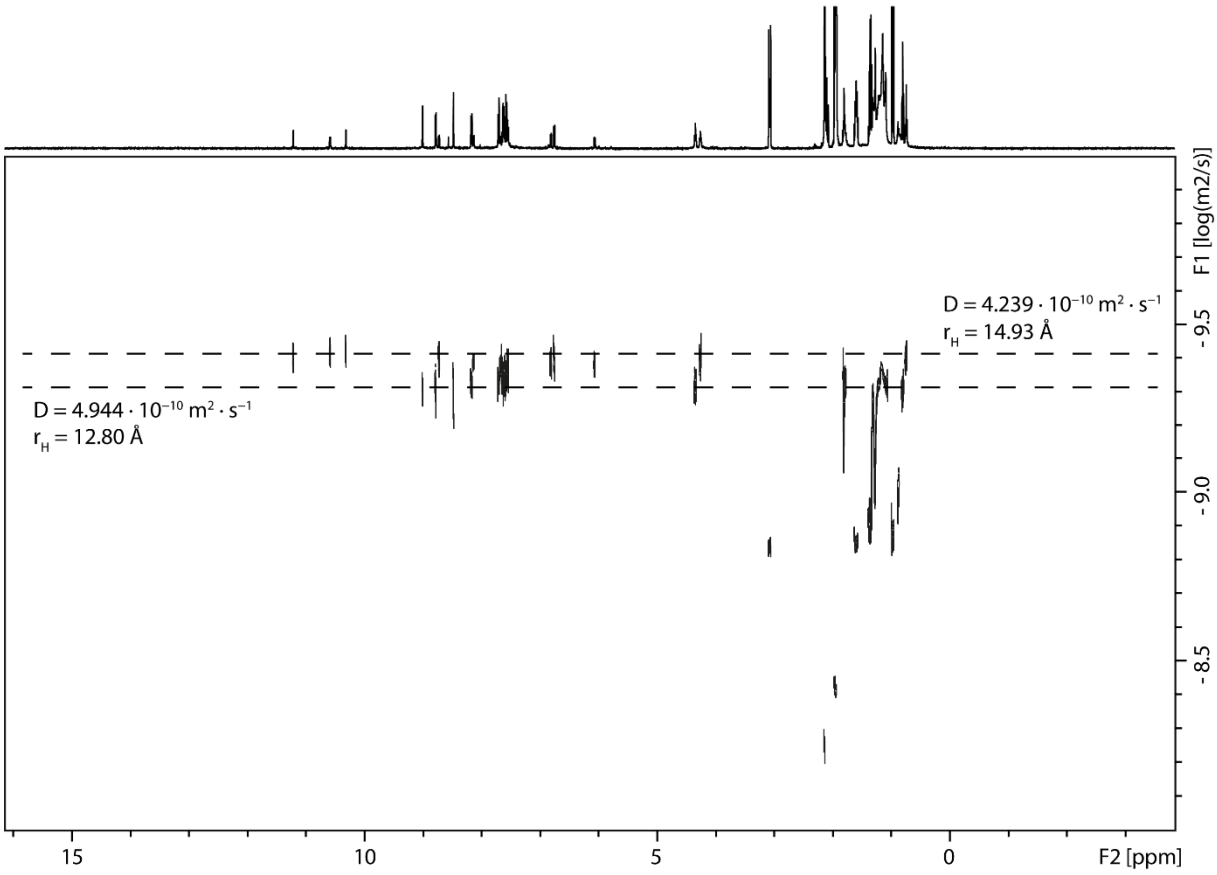

Figure 2.34. ^{1}H DOSY NMR of a mixture of $Pd_2\mathbf{L}^{\mathbf{dodecyl}}{}_4$ and $3Br@Pd_4\mathbf{L}^{\mathbf{dodecyl}}{}_8$.

2.5.4 Synthesis of $\mathbf{L}^{\mathbf{methyl}}$

$\mathbf{L}^{\mathbf{methyl}}$ was prepared following the procedure described in Section 2.5.1 but using iodomethane instead of bromoalkanes.

^{1}H NMR of $\mathbf{L}^{\mathbf{methyl}}$: δ [ppm] = 8.77 (s, 2H, a), 8.55 (d, J = 4.9 Hz, 2H, b), 8.39 (s, 2H, e), 7.91 (d, J = 7.9 Hz, 2H, d), 7.73 (d, J = 8.5, 2H, f), 7.59 (d, J = 8.5, 2H, g), 7.39 (dd, J_1 = 7.9 Hz, J_2 = 4.8 Hz, 2H, c), 3.91 (s, 3H, h).

^{13}C{^{1}H} NMR (DMSO-d_6) of $\mathbf{L}^{\mathbf{methyl}}$: δ [ppm] = 151.43, 148.56, 141.04, 138.33, 129.82, 124.43, 123.69, 121.71, 119.98, 118.06, 112.32, 110.20, 93.88, 84.64, 29.40.

ESI-MS of $\mathbf{L}^{\mathbf{methyl}}$: measured: 384.1477, calculated for $[C_{27}H_{17}N_3+H]^+$: 384.1495.

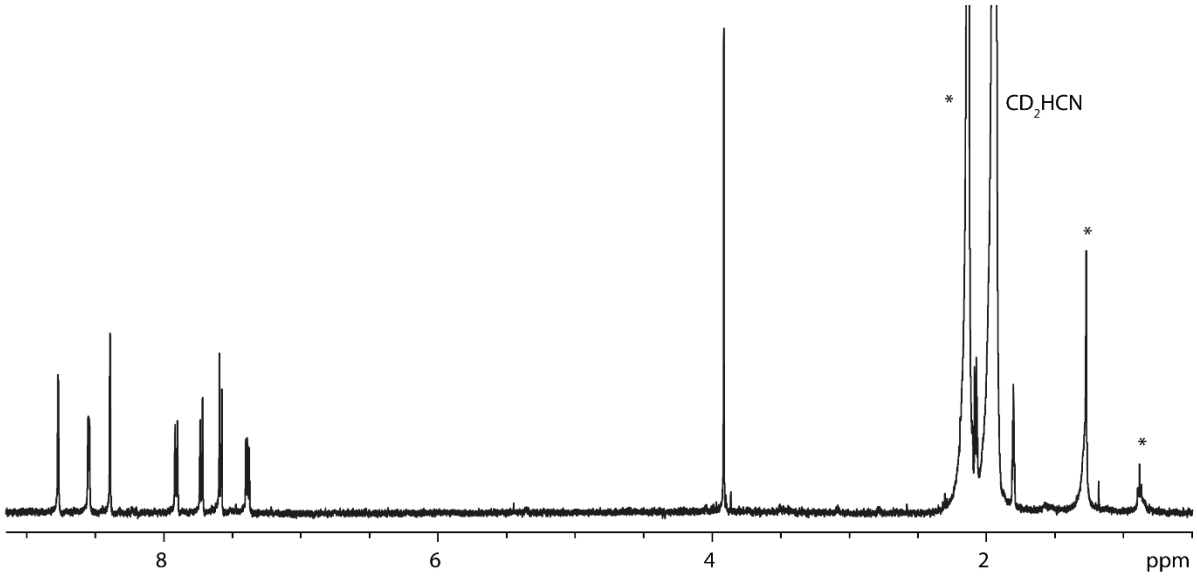

Figure 2.35. ^{1}H NMR of **L^{methyl}**.

2.5.5 Formation and characterization of Pd_2**L^{methyl}**$_4$

To form Pd_2**L^{methyl}**$_4$, the procedure described in 2.5.2 was followed.

^{1}H NMR of Pd_2**L^{methyl}**$_4$**:** δ [ppm] = 8.98 (s, 8H, a), 8.76 (d, J = 5.9 Hz, 8H, b), 8.48 (s, 8H, e), 8.17 (d, J = 8.2, 8H, d), 7.74 (d, J = 8.5, 8H, f), 7.62 (dd, J_1 = 8.2 Hz, J_2 = 5.9 Hz, 8H, c), 7.56 (d, J = 8.6 Hz, 8H, g), 3.85 (s, , 12H, h).

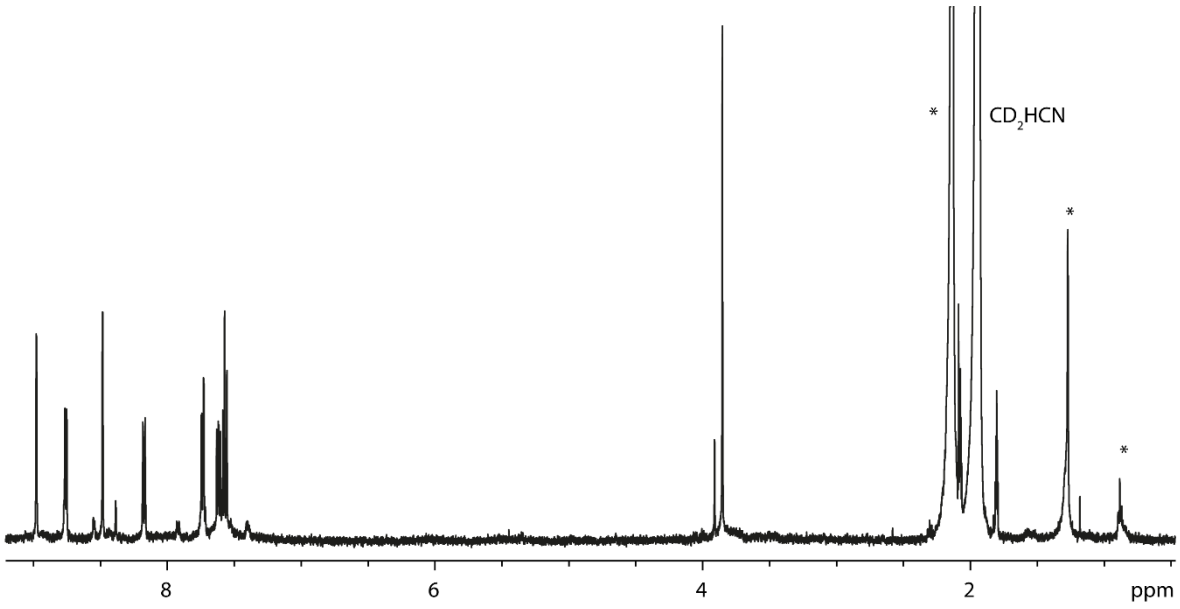

Figure 2.36. ^{1}H NMR of Pd_2**L^{methyl}**$_4$.

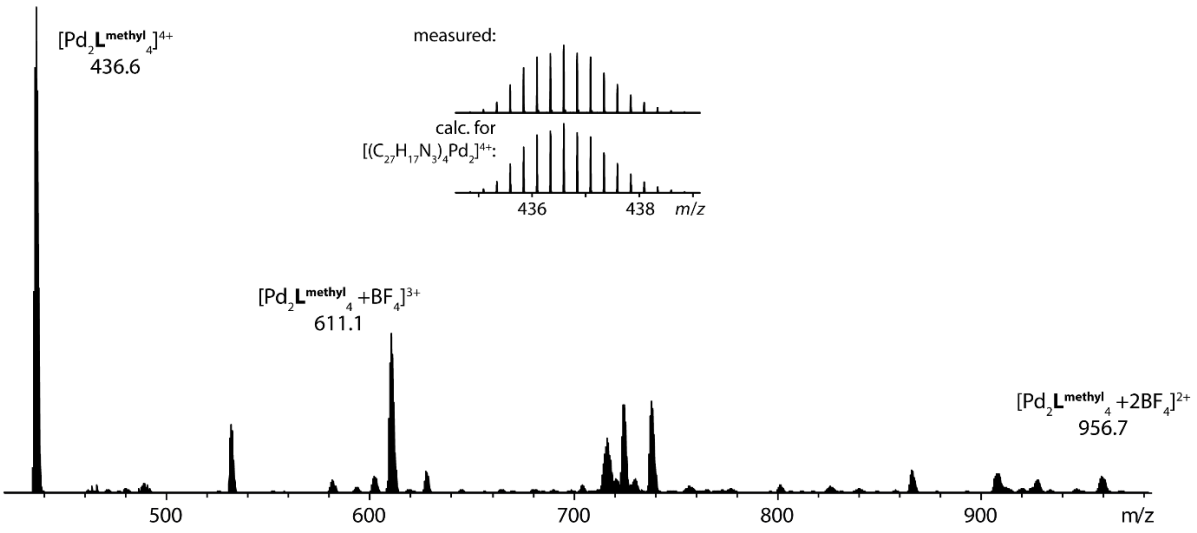

Figure 2.37. ESI MS spectrum of $Pd_2\mathbf{L}^{methyl}_4$.

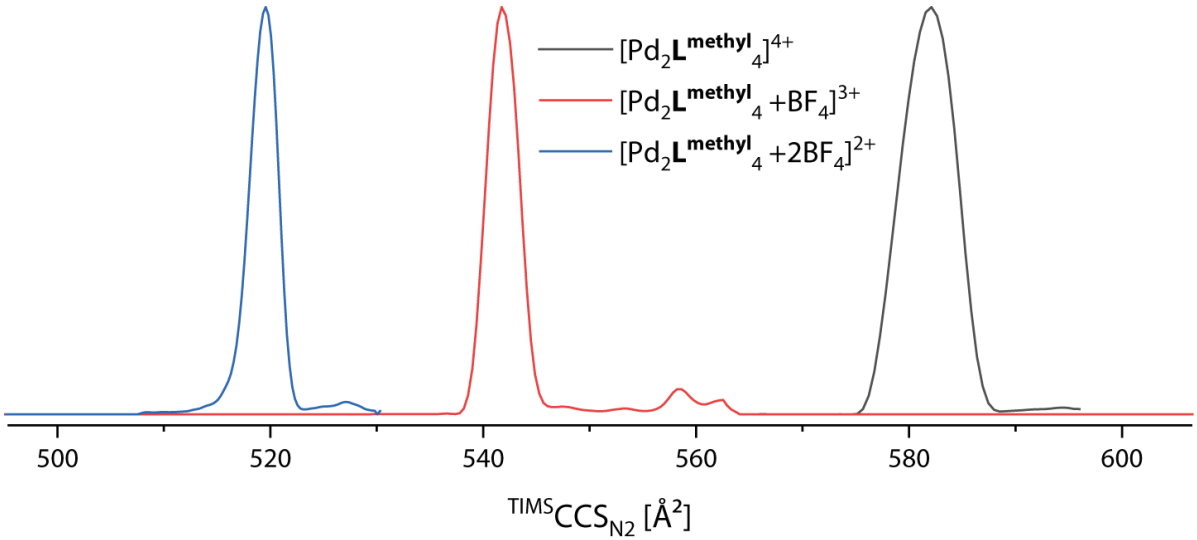

Figure 2.38. Overlaid TIMS mobilograms of $[Pd_2\mathbf{L}^{methyl}_4](BF_4)_4$. Inverse mobilities were normalized and converted into CCS values.

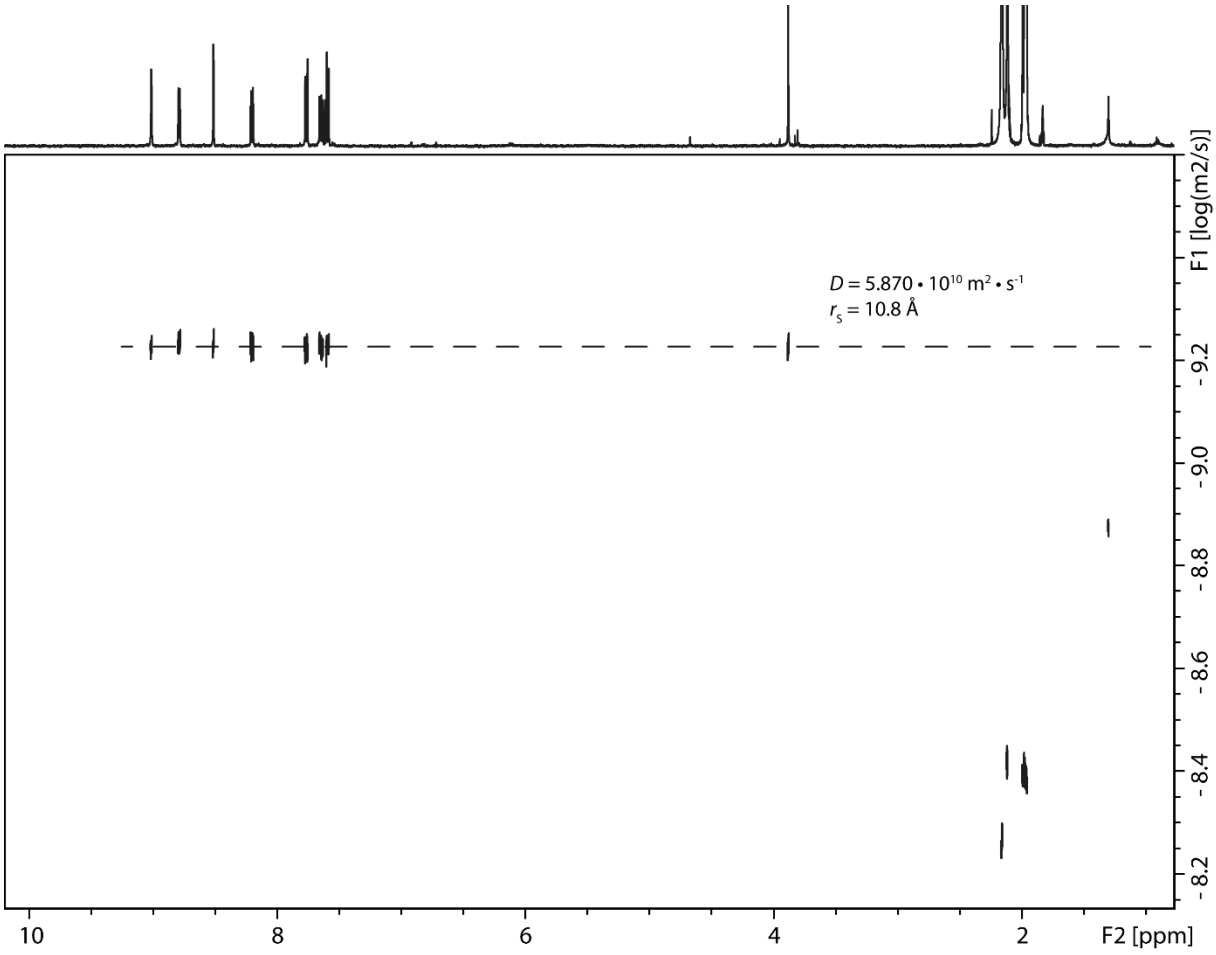

Figure 2.39. ^{1}H DOSY NMR of $Pd_2\mathbf{L}^{\mathbf{methyl}}{}_4$.

2.5.6 Synthesis of $\mathbf{L}^{\mathbf{phenyl}}$

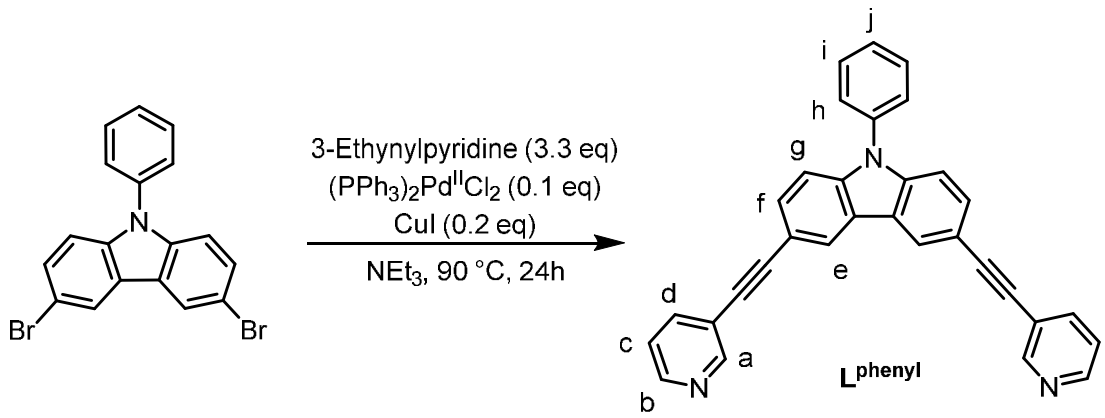

Scheme 2.4. Synthesis of $\mathbf{L}^{\mathbf{phenyl}}$.

For the synthesis of $\mathbf{L}^{\mathbf{phenyl}}$, 3,6-dibromo-9-phenylcarbazole (1.0 eq., 0.29 mmol, 100 mg) and 3-ethynylpyridine (3.3 eq., 0.82 mmol, 84.7 mg) were dissolved in a mixture of 5 mL THF and 2 mL NEt_3 and degassed with three *freeze-pump-thaw*-cycles. After the addition of $(PPh_3)_2Pd(II)Cl_2$ (0.1 eq., 0.025 mmol, 17.5 mg) and CuI (0.2 eq., 0.050 mmol, 9.48 mg) two more *freeze-pump-thaw*-cycles were done. The reaction mixture was then heated and stirred at 90 °C for 24 h. After the reaction the solvent was removed *in vacuo* and the solids were adsorbed to silica. The product could be obtained after

purification with automated flash chromatography (100 % EtOAc) and gel permeation chromatography as a white-yellow solid (81 %).

^{1}H NMR (500 MHz, 298 K, CD_3CN) of L^{phenyl}: δ [ppm] = 8.78 (s, 2H, a), 8.56 (d, J = 4.9 Hz, 2H, b), 8.46 (s, 2H, e), 7.92 (d, J = 7.9 Hz, 2H, d), 7.57-7.74 (m, 7H, f, h, i, j), 7.42 (d, J = 8.5, 2H, g) 7.39 (dd, J_1 = 7.9 Hz, J_2 = 4.8 Hz, 2H, c).

$^{13}C\{^{1}H\}$ NMR (126 MHz, 298 K, DMSO-d_6) of L^{phenyl}: δ [ppm] = 151.54, 148.78, 140.64, 138.40, 135.85, 130.43, 128.50, 126.99, 124.75, 123.75, 122.66, 122.45, 119.90, 113.59, 110.57, 93.47, 85.00.

ESI-MS of L^{phenyl}: measured: 445.1566, calculated for $[C_{32}H_{19}N_3+H]^+$: 445.1573.

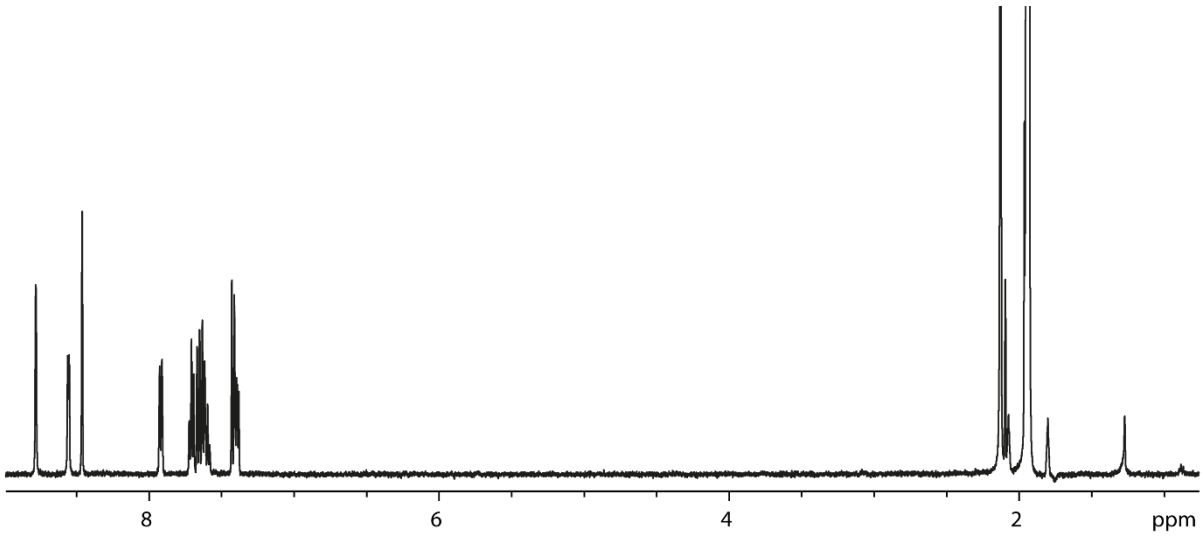

Figure 2.40. ^{1}H NMR of L^{phenyl}.

2.5.7 Formation and characterization of $Pd_2L^{phenyl}_4$

To form $Pd_2L^{phenyl}_4$, the procedure described in 2.5.2 was followed.

^{1}H NMR of $Pd_2L^{phenyl}_4$: δ [ppm] = 9.02 (s, 8H, a), 8.77 (d, J = 5.9 Hz, 8H, b), 8.59 (s, 8H, e), 8.19 (d, J = 8.2, 8H, d), 7.51-1.71 (m, 35H, c, f, h, i, j), 7.40 (d, J = 8.6 Hz, 8H, g), 3.85 (s, 12H, h).

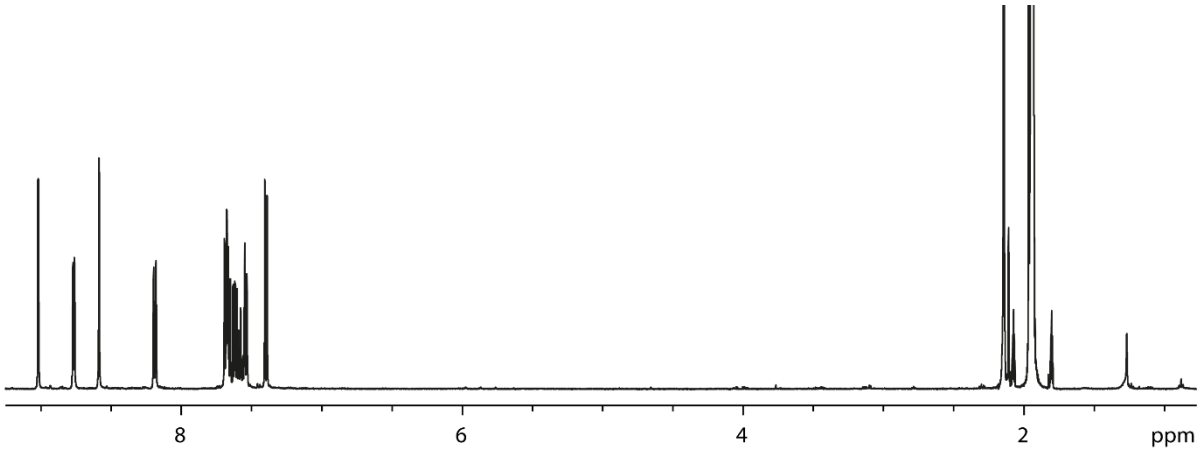

Figure 2.41. ^{1}H NMR of $Pd_2\mathbf{L}^{\mathbf{phenyl}}{}_4$.

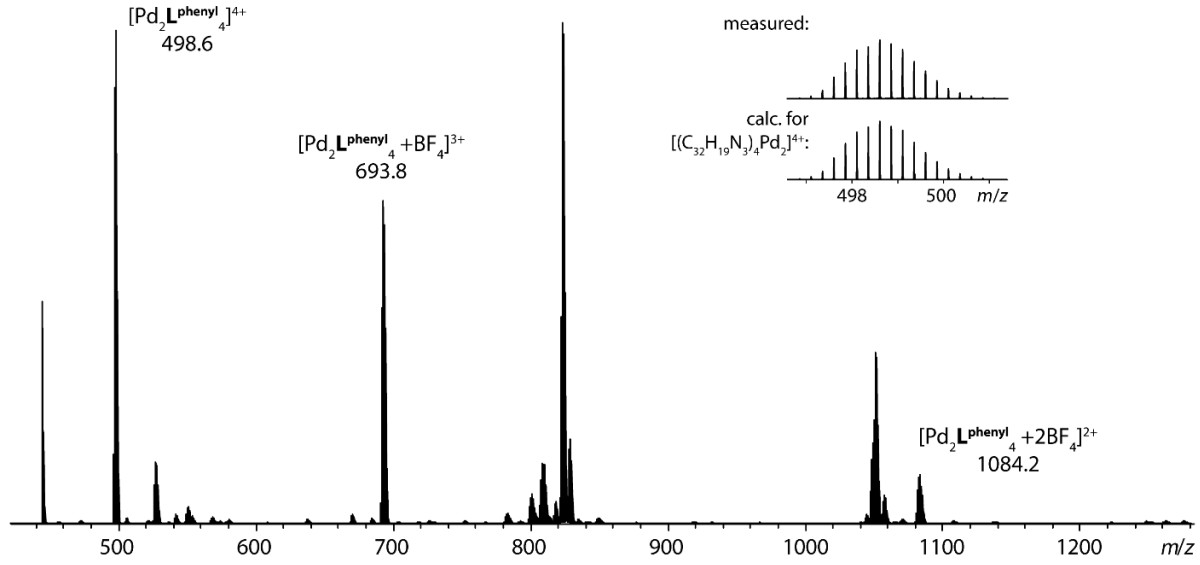

Figure 2.42. ESI MS spectrum of $[Pd_2\mathbf{L}^{\mathbf{phenyl}}{}_4](BF_4)_4$.

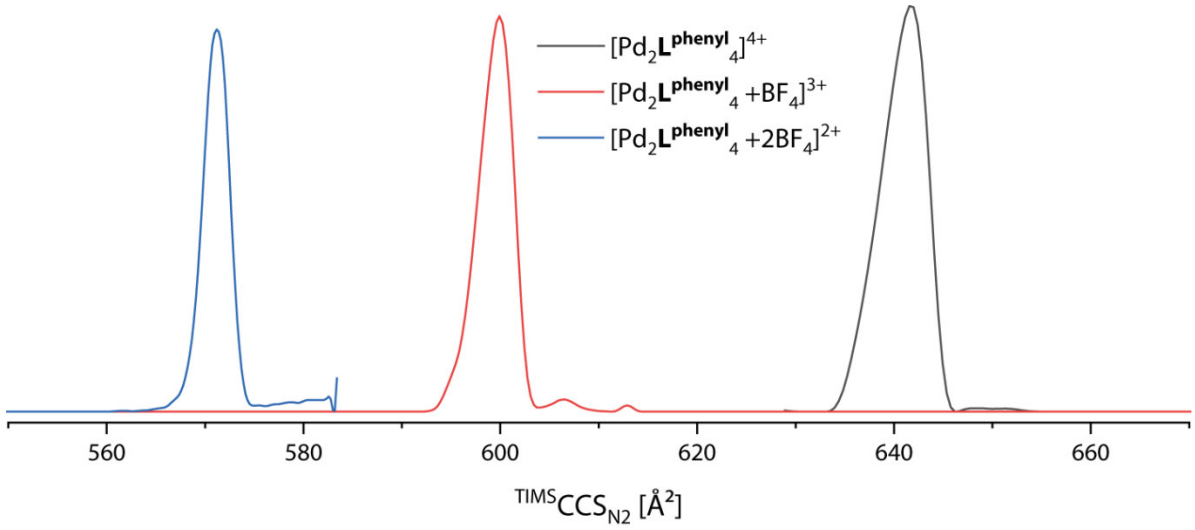

Figure 2.43. Overlaid TIMS mobilograms of $[Pd_2\mathbf{L}^{phenyl}{}_4](BF_4)_4$. Inverse mobilities were normalized and converted into CCS values.

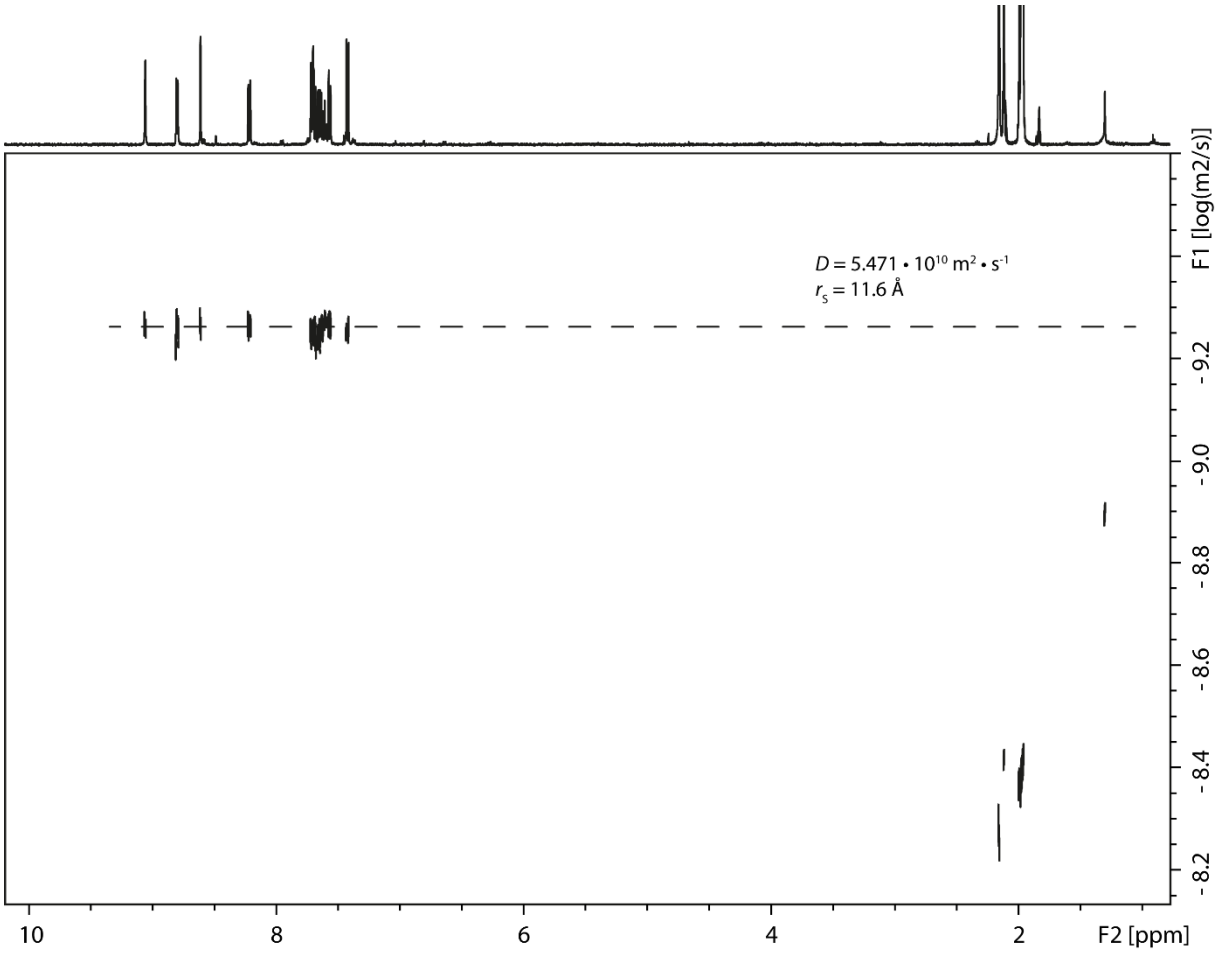

Figure 2.44. ^{1}H DOSY NMR of $Pd_2\mathbf{L}^{phenyl}{}_4$.

2.5.8 Synthesis of $L^{pyrenyl}$

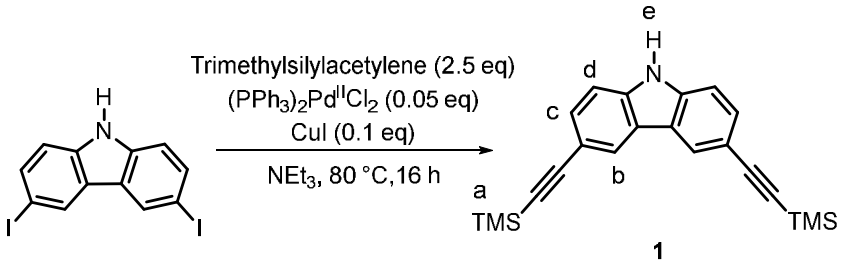

Scheme 2.5. Synthesis of **1**.

3,6-Diiodocarbazole (1.0 eq, 0.48 mmol, 200 mg) was dissolved in 10 mL NEt_3. To that solution trimethylsilylacetylene (2.5 eq, 1.19 mmol, 170 µL) was added. The solution was degassed with three *freeze-pump-thaw*-cycles. After the addition of $(PPh_3)_2Pd(II)Cl_2$ (0.05 eq., 0.024 mmol, 16.7 mg) and CuI (0.1 eq., 0.048 mmol, 9.08 mg) three more *freeze-pump-thaw*-cycles were done. The reaction mixture was then heated and stirred at 80 °C for 16 h. After the reaction the solvent was removed *in vacuo* and the solids were adsorbed on silica. Compound **1** could be obtained after purification with automated flash chromatography (*n*-pentane/EtOAc, 0 % → 25 %) as a white-brown solid (79 %). The product should be stored at –20 °C under an inert atmosphere.

^{1}H NMR (600 MHz, DMSO-d_6) of 1: δ [ppm] = 11.7 (s, 1H, e), 8.36 (s, 2H, b), 7.47 (m, 4H, c, d), 0.25 (s, 18H, a).

^{13}C{^{1}H} NMR (151 MHz, DMSO-d_6) of 1: δ [ppm] = 140.04, 129.64, 124.71, 122.04, 112.65, 111.58, 107.06, 91.62, 0.14.

ESI-MS of 1: measured: 358.1435, calculated for $[C_{22}H_{24}NSi_2]^-$: 358.1453.

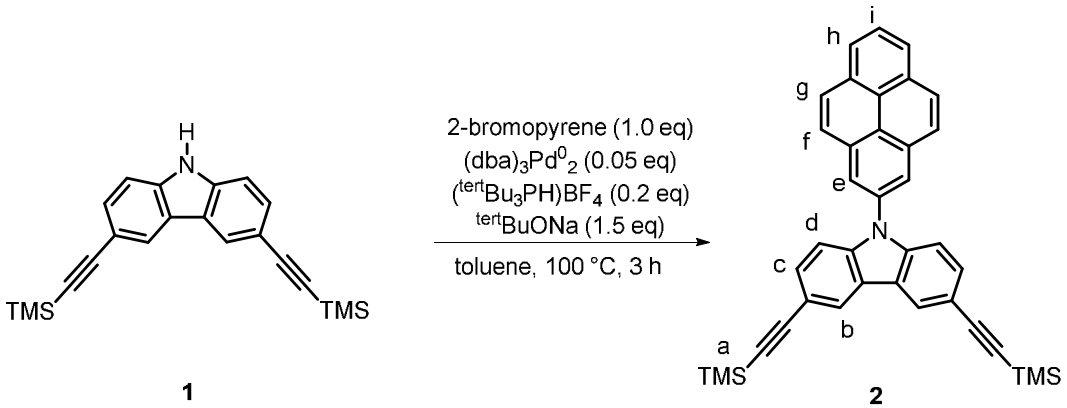

Scheme 2.6. Synthesis of **2**.

2 (1.0 eq, 0.14 mmol, 50 mg), 2-bromopyrene (1.0 eq, 0.14 mmol, 39.1 mg) and ^{tert}BuONa (1.5 eq, 0.21 mmol, 20.0 mg) were dissolved in 3 mL toluene and the solution was degassed with three *freeze-*

pump-thaw-cycles. After the addition of $(dba)_3Pd(0)_2$ (0.05 eq, 7.0 µmol, 8.1 mg) and ($^{tert}Bu_3PH)BF_4$ (0.2 eq, 27.8 µmol, 8.1 mg) three more *freeze-pump-thaw*-cycles were done. The reaction mixture was heated at 100 °C for 3 h. The reaction mixture was allowed to cool down and then the solvent was removed *in vacuo* and the remaining solids were adsorbed on silica. Automated flash chromatography (n-pentane/$CHCl_3$, 0 % → 20 %) yielded compound **2** as a white-yellow solid (39 %).

^{1}H NMR (600 MHz, DMSO-d_6) of 2: δ [ppm] = 8.60 (s, 2H, b), 8.58 (s, 2H, e), 8.42 (d, J = 7.7 Hz, 2H, f), 8.31-8.37 (m, 4H, g, h), 8.18 (t, J = 7.7 Hz, i), 7.56 (d, J = 8.5 Hz, c), 7.48 (d, J = 8.4 Hz, d), 0.28 (s, 18H, a).

^{13}C{^{1}H} NMR (151 MHz, DMSO-d_6) of 2: δ [ppm] = 134.57, 132.85, 131.28, 130.58, 128.95, 127.09, 126.63, 126.04, 124.89, 124.50, 124.14, 123.07, 122.94, 115.25, 110.01, 106.31, 92.66, 55.96, 0.29.

No mass spectrum of compound **2** could be obtained.

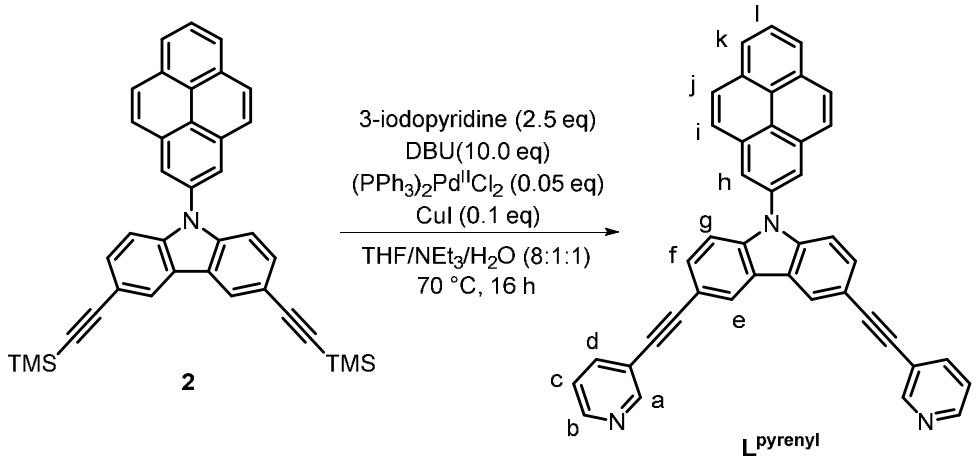

Scheme 2.7. Synthesis of $\mathbf{L^{pyrenyl}}$.

Compound **2** (1.0 eq, 54.8 µmol, 30.7 mg), 3-iodopyridine (2.5 eq, 137 µmol, 28.1 mg) and 1,8-diazabicyclo[5.4.0]-7-undecene (10.0 eq, 548 µmol, 83.4 mg) were dissolved in 2 mL of a mixture of THF, NEt_3 and H_2O (8:1:1) and it was degassed with three *freeze-pump-thaw*-cycles. After the addition of $(PPh_3)_2Pd(II)Cl_2$ (0.05 eq., 2.74 µmol mmol, 1.9 mg) and CuI (0.1 eq., 5.5 µmol, 1.0 mg) three more *freeze-pump-thaw*-cycles were done. The reaction mixture was then heated and stirred at 70 °C for 16 h. After extraction with DCM (three times) most of the solvent was removed and automated flash chromatography (liquid loading, first *n*-pentane/chloroform 0 % → 100 %, then chloroform/methanol 0 % → 10 %) and afterwards washing with CH_3CN yielded $\mathbf{L^{pyrenyl}}$ as a yellow solid (95 %).

^{1}H NMR (DMSO-d_6) of $L^{pyrenyl}$: δ [ppm] = 8.81 (s, 2H, a), 8.73 (s, 2H, e), 8.64 (s, 2H, h), 8.60 (d, *J* = 5.0 Hz, 2H, b), 8.44 (d, *J* = 7.8 Hz, 2H, i), 8.36 (m, 4H, k, j, k), 8.19 (t, J = 7.6 Hz, 1H, l), 8.03 (d, J = 8.0 Hz, 2H, d), 7.73 (d, J = 8.5 Hz, 2H, f), 7.59 (d, J = 8.4 Hz, 2H, g), 7.50 (dd, J_1 = 7.8 Hz, J_2 = 4.8 Hz, 2H, c).

$^{13}C\{^{1}H\}$ NMR (151 MHz, DMSO-d_6) of $L^{pyrenyl}$: δ [ppm] = 151.49, 148.74, 141.25, 138.43, 132.35, 130.67, 130.50, 128.69, 127.18, 126.84, 125.97, 124.81, 123.77, 123.48, 123.19, 122.85, 122.61, 119.90, 113.98, 110.66, 93.54, 85.14.

ESI-MS of $L^{pyrenyl}$: measured: 570.1980, calculated for $[C_{42}H_{23}N_3+H]^+$: 570.1980.

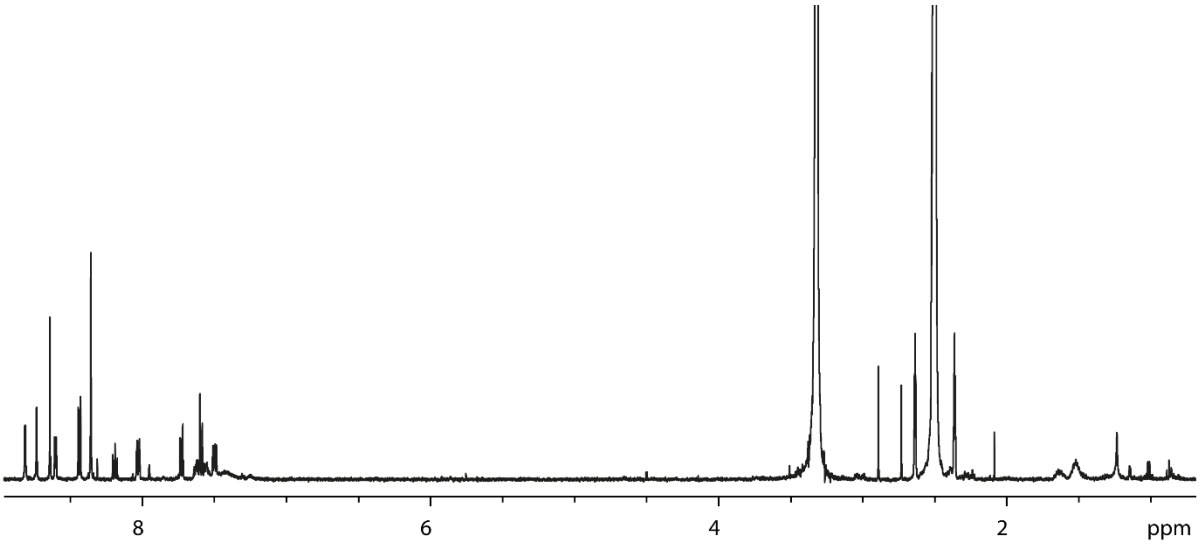

Figure 2.45. ^{1}H NMR (DMSO-d_6) of $\mathbf{L^{pyrenyl}}$.

2.5.9 Formation and characterization of $Pd_2\mathbf{L^{pyrenyl}}_4$

To form $Pd_2\mathbf{L^{pyrenyl}}_4$, the procedure described in 2.5.2 was followed.

^{1}H NMR of $[Pd_2\mathbf{L^{pyrenyl}}_4]^{4+}$: δ [ppm] = 9.06 (s, 8H, a), 8.79 (d, J = 5.5 Hz, 8H, b), 8.70 (s, 8H, e), 8.42 (s, 8H, h), 8.39 (d, J = 7.7 Hz, 8H, i), 8.30 (d, J = 9.0 Hz, 8H, j), 8.22 (m, 16H, d, k), 8.17 (t, J = 7.6 Hz, 4H, l), 7.74 (d, J = 8.7 Hz, 8H, f), 7.64 (dd, J_1 = 7.8 Hz, J_2 = 4.8 Hz, 2H, c), 7.58 (d, J = 8.6 Hz, 8H, g).

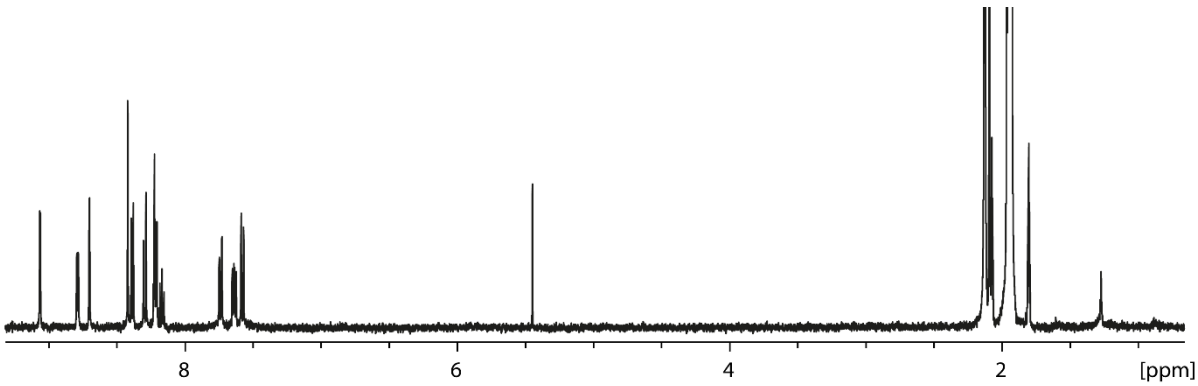

Figure 2.46. ^{1}H NMR of $Pd_2\mathbf{L^{pyrenyl}}_4$.

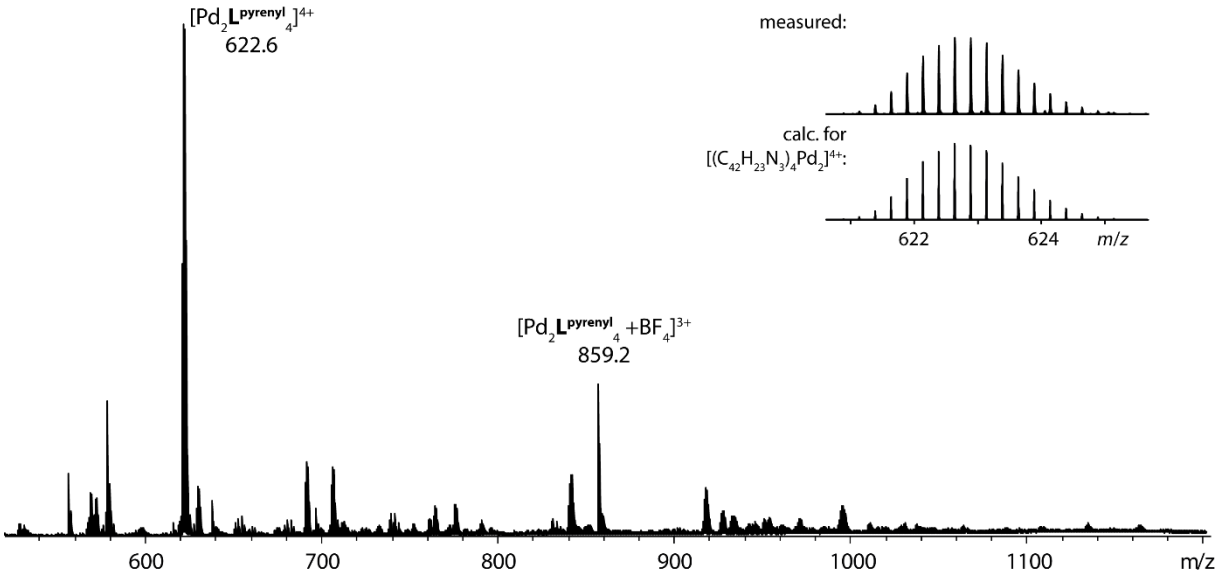

Figure 2.47. ESI MS spectrum of $[Pd_2\mathbf{L}^{pyrenyl}_4](BF_4)_4$.

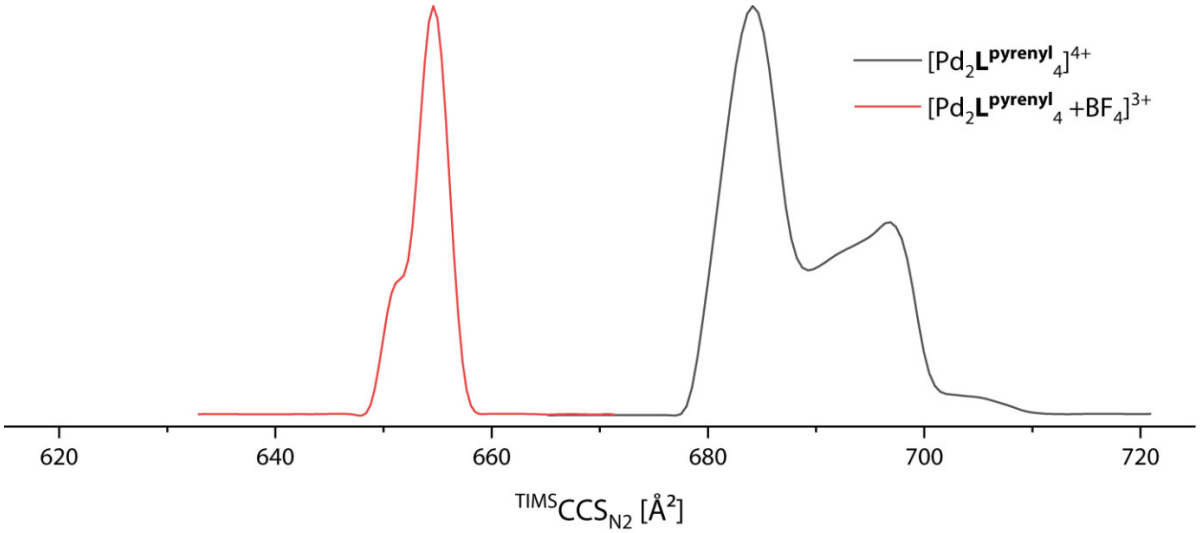

Figure 2.48. Overlaid TIMS mobilograms of $[Pd_2\mathbf{L}^{pyrenyl}_4](BF_4)_4$. Inverse mobilities were normalized and transformed into CCS values.

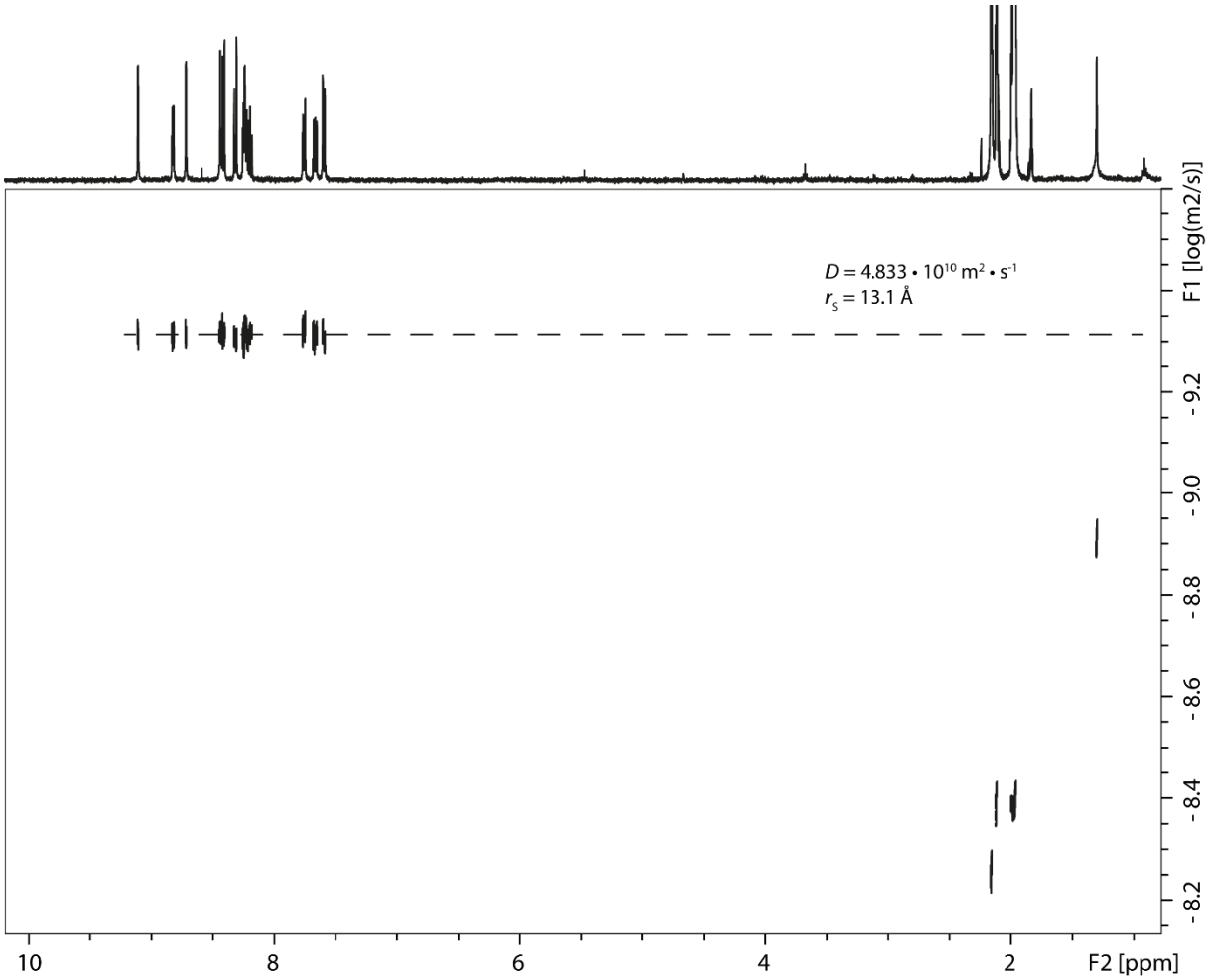

Figure 2.49. ^{1}H DOSY NMR of $Pd_2\mathbf{L}^{\mathbf{pyrenyl}}{}_4$.

2.5.10 Single crystal X-ray diffraction analysis

For the crystallographic analysis of $[Pd_2\mathbf{L}^{\mathbf{pyrenyl}}{}_4](BF_4)_4$ single crystals were grown by slow diffusion of 3 ml diisopropyl ether into 150 µl of a 0.2 mM cage solution in nitromethane over two weeks. The small, thin plate shaped colorless crystals were pipetted from mother liquor onto a glass slide containing NVH oil. To avoid cracking of the crystal, it was quickly mounted onto a 0.06 mm nylon loop and immediately flash cooled in liquid nitrogen. Crystals were stored at cryogenic temperature in dry shippers, in which they were safely transported to macromolecular beamline P11 at Petra III,[85] DESY, Germany. The data was collected at 100(2) K on an Eiger 2X 16M detector using a high precision 1-axis goniostat equipped with a Stäubli sample changing robot. 3600 diffraction images were collected in a 360° ϕ sweep at a chosen wavelength of λ = 0.88561 Å (14KeV) using double crystal monochromator (Si-111 and Si-113 reflections) and a detector distance of 154 mm, 100 % filter transmission, 0.1° step width and 0.2 seconds exposure time per image. Data integration and reduction were undertaken using XDS.[86] The data was cut at 1.0 Å using a mean I/sig(I) > 1 as cutoff criterium.

The structure was solved by direct methods using SHELXT 2018/2[87] and refined by full-matrix least-squares methods against F^2 by SHELXL-2014/7.[88] All non-hydrogen atoms were refined with anisotropic displacement parameters using 22 CPU cores for full-matrix least-squares routines on F2 and ShelXle[89] as a graphical user interface and the DSR program plugin was employed for modeling.[90,91]

Stereochemical restraints for the ligands $\mathbf{L^{pyrenyl}}$ (residue CPP) were generated by the GRADE program using the GRADE Web Server (http://grade.globalphasing.org) and applied in the refinement. A GRADE dictionary for SHELXL contains target values and standard deviations for 1,2-distances (DFIX) and 1,3-distances (DANG), as well as restraints for planar groups (FLAT). All displacements for non-hydrogen atoms were refined anisotropically. The refinement of ADP's for carbon, nitrogen and oxygen atoms was enabled by a combination of similarity restraints (SIMU) and rigid bond restraints (RIGU).14 The contribution of the electron density from disordered counterions and solvent molecules, which could not be modeled with discrete atomic positions were handled using the SQUEEZE[92] routine in PLATON.[93] The solvent mask file (.fab), computed by PLATON, was included in the SHELXL refinement via the ABIN instruction leaving the measured intensities untouched.

The diffractometer was equipped with a low temperature device and used synchrotron. The hydrogen atoms were refined isotropically on calculated positions using a riding model with their U_{iso} values constrained to 1.5 times the U_{eq} of their pivot atoms for terminal sp^3 carbon atoms and 1.2 times for all other carbon atoms. Crystallographic data (including structure factors) for the structures reported in this paper have been deposited with the Cambridge Crystallographic Data Centre. CCDC no. 2253145 contain the supplementary crystallographic data for this paper. Copies of the data can be obtained free of charge from The Cambridge Crystallographic Data Centre via www.ccdc.cam.ac.uk/structures.

Table 2.2. Crystal data and structure refinement for $[Pd_2\mathbf{L}^{pyrenyl}_4](BF_4)_4$.

Compound	$[Pd_2\mathbf{L}^{pyrenyl}_4](BF_4)_4$
CIF ID	cd248d
CCDC number	2253145
Empirical formula	$C_{168}H_{92}B_{3.50}F_{14}N_{12}Pd_2$
Formula weight	2795.17
Temperature [K]	100(2)
Crystal system	monoclinic
Space group (number)	$P2_1/c$ (14)
a [Å]	25.58(3)
b [Å]	37.13(3)
c [Å]	38.88(4)
α [Å]	90
β [Å]	105.151(12)
γ [Å]	90
Volume [Å^3]	35649(58)
Z	8
ρ_{calc} [g/cm^3]	1.042
μ [mm^{-1}]	0.461
F(000)	11356
Crystal size [mm^3]	0.040×0.040×0.005
Crystal color	colorless
Crystal shape	plate
Radiation	synchrotron (λ=0.88561 Å)
2Θ range [°]	1.92 to 43.30 (1.20 Å)
Index ranges	-21 ≤ h ≤ 21 -30 ≤ k ≤ 30 -32 ≤ l ≤ 32
Reflections collected	144173
Independent reflections	21294 R_{int} = 0.0739 R_{sigma} = 0.0412
Completeness to θ = 21.650°	98.6 %
Data / Restraints / Parameters	21294/8052/3592
Goodness-of-fit on F^2	1.678
Final *R* indexes [I≥2σ(I)]	R_1 = 0.1520 wR_2 = 0.4177
Final *R* indexes [all data]	R_1 = 0.1964 wR_2 = 0.4491
Largest peak/hole [eÅ^3]	1.46/-0.68

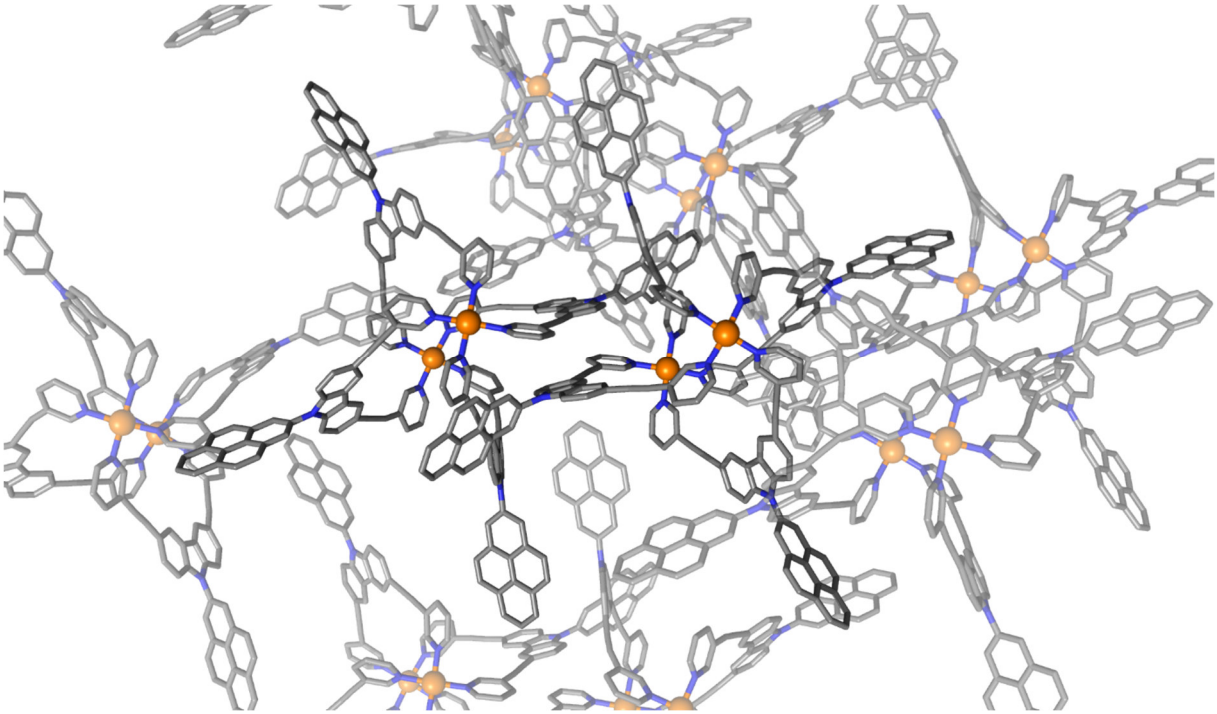

Figure 2.50. Crystal packing of the obtained X-ray structure of $[Pd_2\mathbf{L}^{\mathbf{pyrenyl}}_4](BF_4)_4$. Counter anions, hydrogen atoms and solvent molecules omitted for clarity.

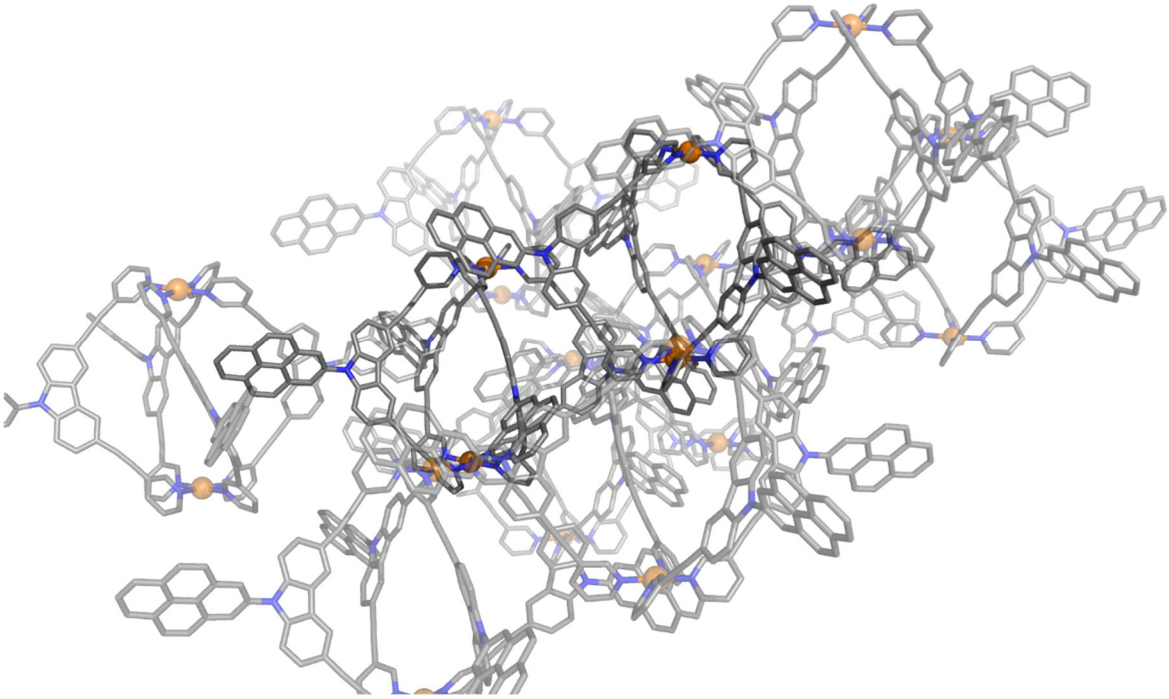

Figure 2.51. Crystal packing of the obtained X-ray structure of $[Pd_2\mathbf{L}^{\mathbf{pyrenyl}}_4](BF_4)_4$. Counter anions, hydrogen atoms and solvent molecules omitted for clarity.

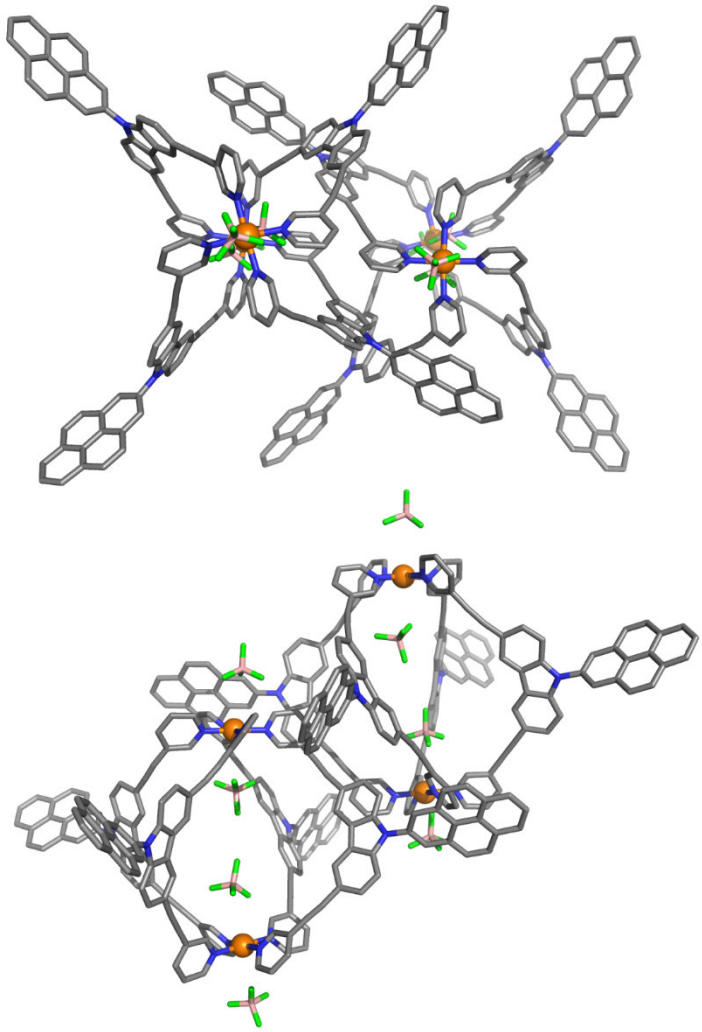

Figure 2.52. Top and side view of asymmetric unit cell of the obtained X-ray structure of $[Pd_2\mathbf{L}^{pyrenyl}_4](BF_4)_4$. Hydrogen atoms and solvent molecules omitted for clarity.

Table 2.3. Crystal data and structure refinement for $[Pd_2\mathbf{L}^{FL}_4](BF_4)_4$.

Empirical formula	$C_{142.50}H_{88}F_{7.50}N_8O_{11.50}Pd_2S_{2.50}$
Formula weight	2531.65
Temperature [K]	100(2)
Crystal system	triclinic
Space group (number)	$P\overline{1}$ (2)
a [Å]	23.488(4)
b [Å]	26.176(5)
c [Å]	28.556(5)
α [Å]	91.789(9)
β [Å]	93.686(14)
γ [Å]	101.499(19)
Volume [Å^3]	17151(5)
Z	4
ρ_{calc} [g/cm^3]	0.980
μ [mm^{-1}]	0.523
F(000)	5162

Crystal size [mm^3]	0.120×0.030×0.010
Crystal colour	colourless
Crystal shape	plate
Radiation	synchrotron (λ=0.88558 Å)
2Θ range [°]	1.78 to 53.14 (0.99 Å)
Index ranges	-23 ≤ h ≤ 23 -25 ≤ k ≤ 26 -28 ≤ l ≤ 28
Reflections collected	103244
Independent reflections	27719 R_{int} = 0.0434 R_{sigma} = 0.0362
Completeness to θ = 26.568°	74.9 %
Data / Restraints / Parameters	27719/6748/3133
Goodness-of-fit on F^2	1.688
Final R indexes [I≥2σ(I)]	R_1 = 0.1251 wR_2 = 0.3917
Final R indexes [all data]	R_1 = 0.1470 wR_2 = 0.4091
Largest peak/hole [eÅ^3]	1.08/-1.16

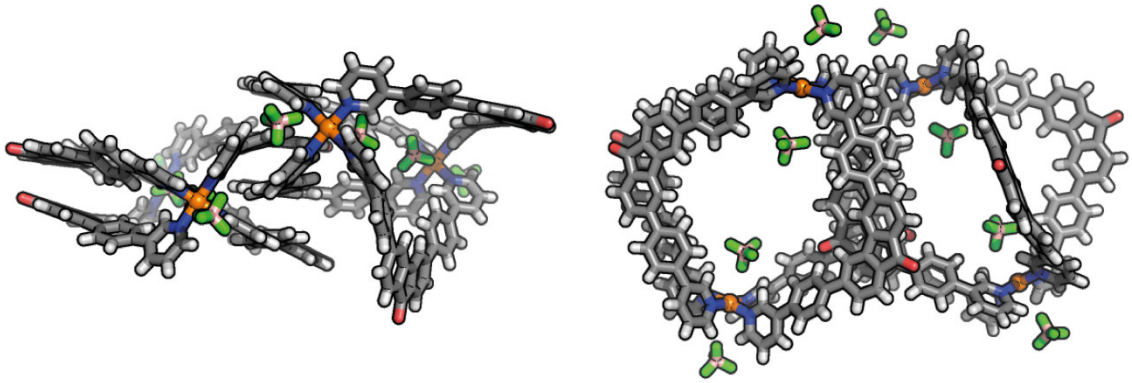

Figure 2.53. Top and side view of asymmetric unit cell of the obtained X-ray structure of $[Pd_2\mathbf{L}^{\mathbf{FL}}_4](BF_4)_4$. Solvent molecules omitted for clarity.

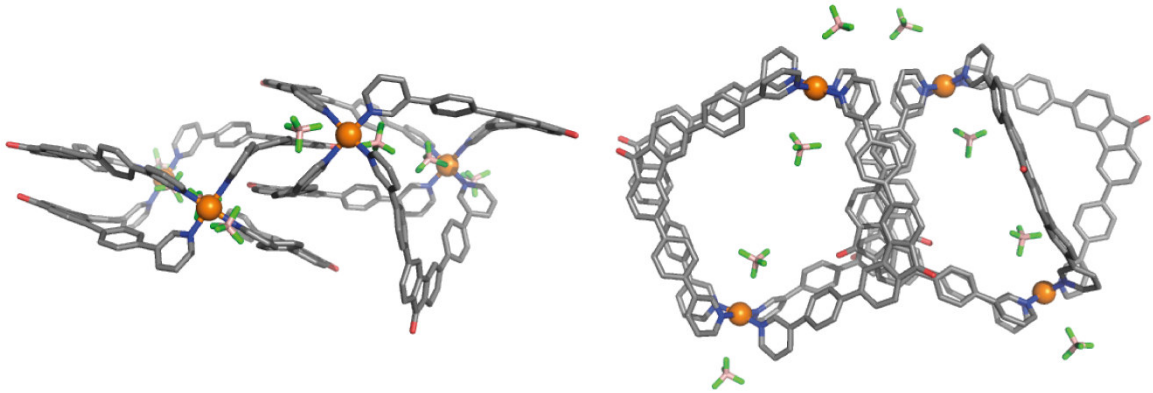

Figure 2.54. Top and side view of asymmetric unit cell of the obtained X-ray structure of $[Pd_2\mathbf{L}^{\mathbf{FL}}{}_4](BF_4)_4$. Hydrogen atoms and solvent molecules omitted for clarity.

2.5.11 Synthesis of $\mathbf{L}^{\mathbf{pyEG4}}$ and characterizations

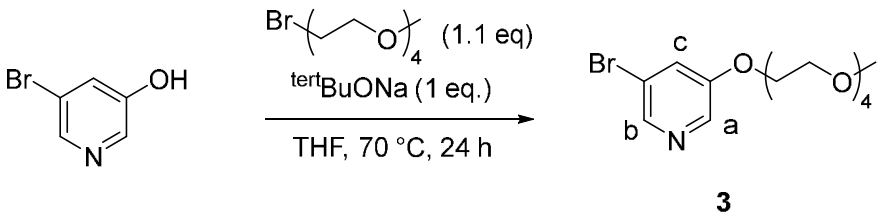

3

Scheme 2.8. Synthesis of **3**.

5-Bromopyridin-3-ol (1 eq., 1 mmol, 174 mg) and ^{tert}BuONa (1 eq., 1 mmol, 96.1 mg) were dissolved in 10 mL THF and stirred at 25 °C for 15 min. Triethylene glycol 2-bromoethyl methyl ether (1.1 eq., 1.1 mmol, 231 µL) was added and the reaction mixture was then stirred at 70 °C for 24 h. Then, the reaction mixture was taken up in ethyl acetate and filtrated over cotton wool. Silica was added and the solvent was removed *in vacuo*. Purification with automated flash chromatography (DCM/MeOH 0 % → 10 %) yielded **3** as yellow oil (94 %).

^{1}H NMR of 3: δ [ppm] = 8.26 (d, J = 1.7 Hz, a), 8.25 (d, J = 2.5 Hz, b), 7.55 (m, c), 3.26 – 4.20 (PEG).

^{13}C{^{1}H} NMR of 3: δ [ppm] = 156.58, 143.56, 137.90, 124.71, 120.97, 72.58, 71.36, 71.18, 71.10, 70.95, 69.97, 69.37. Of 14 expected signals only 12 are found, likely due to signal overlap in the area of 70.9 ppm to 71.2 ppm.

ESI-MS of 3: measured: 364.0755, calculated for $[C_{14}H_{22}BrNO_5+H]^+$: 364. 0754.

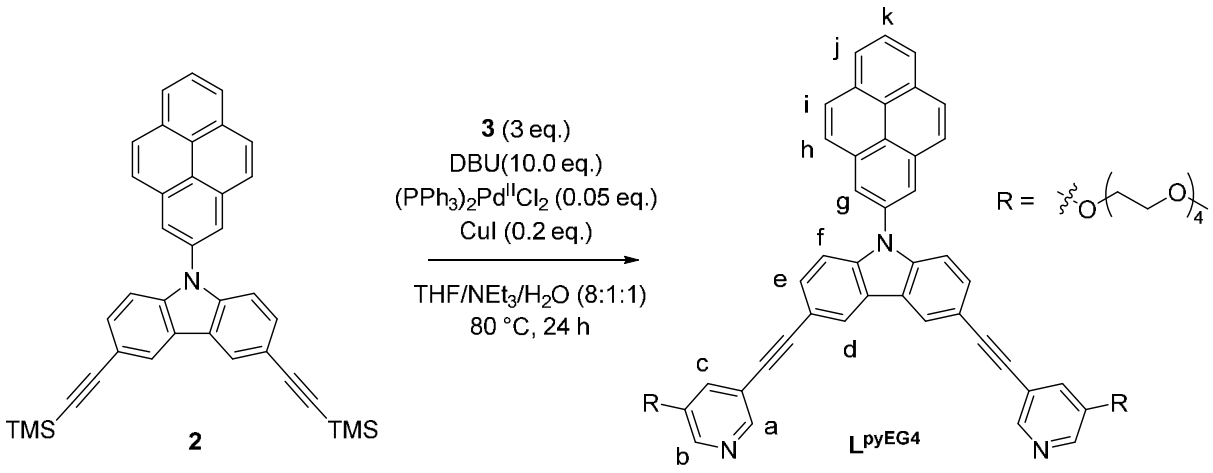

Scheme S1. Synthesis of $\mathbf{L^{pyEG4}}$.

Compound **2** (1 eq., 179 µmol, 100 mg), **3** (3 eq., 536 µmol, 195 mg) and 1,8-diazabicyclo[5.4.0]-7-undecene (10.0 eq., 1.79 mmol, 267 µL) were dissolved in 3 mL of a mixture of THF, NEt_3 and H_2O (8:1:1) and it was degassed with three *freeze-pump-thaw*-cycles. After the addition of $(PPh_3)_2Pd(II)Cl_2$ (0.05 eq., 8.93 µmol, 6.27 mg) and CuI (0.2 eq., 35.7 µmol, 6.8 mg) three more *freeze-pump-thaw*-cycles were done. The reaction mixture was then heated and stirred at 80 °C for 24 h. The reaction mixture was allowed to cool down and was then taken up with acetone and adsorbed on silica. Purification with automated flash chromatography (DCM/MeOH 0 % → 10 %) yielded $\mathbf{L^{pyEG4}}$ as a yellow solid (80 %).

^{1}H NMR (DMSO-d_6) of $\mathbf{L^{pyEG4}}$: δ [ppm] = 8.81 (s, 2H, a), 8.73 (s, 2H, e), 8.64 (s, 2H, h), 8.60 (d, J = 5.0 Hz, 2H, b), 8.44 (d, J = 7.8 Hz, 2H, i), 8.36 (m, 4H, k, j, k), 8.19 (t, J = 7.6 Hz, 1H, l), 8.03 (d, J = 8.0 Hz, 2H, d), 7.73 (d, J = 8.5 Hz, 2H, f), 7.59 (d, J = 8.4 Hz, 2H, g), 7.50 (dd, J_1 = 7.8 Hz, J_2 = 4.8 Hz, 2H, c).

^{13}C{^{1}H} NMR (151 MHz, DMSO-d_6) of $\mathbf{L^{pyEG4}}$: δ [ppm] = 151.49, 148.74, 141.25, 138.43, 132.35, 130.67, 130.50, 128.69, 127.18, 126.84, 125.97, 124.81, 123.77, 123.48, 123.19, 122.85, 122.61, 119.90, 113.98, 110.66, 93.54, 85.14.

ESI-MS of $\mathbf{L^{pyEG4}}$: measured: 570.1980, calculated for $[C_{42}H_{23}N_3+H]^+$: 570.1980.

To form $Pd_2\mathbf{L^{pyEG4}}_4$, the procedure described in 2.5.2 was followed.

^{1}H NMR (600 MHz) of $Pd_2\mathbf{L^{pyEG4}}_4$**:** δ [ppm] = 8.77 (s, 2H, a), 8.63 (s, 2H, d), 8.57 (s, 2H, b), 8.38 (m, 4H, g, h), 8.26 (d, J = 9.2 Hz, 2H, j), 8.17 (m, 3H, I, k), 7.85 (s, 2H, c), 7.71 (d, J = 8.7 Hz, 2H, e), 7.55 (d, J = 8.4 Hz, 2H, f), 4.30 (m, PEG), 3.84 (m, PEG), 3.2 – 3.7 (m, PEG).

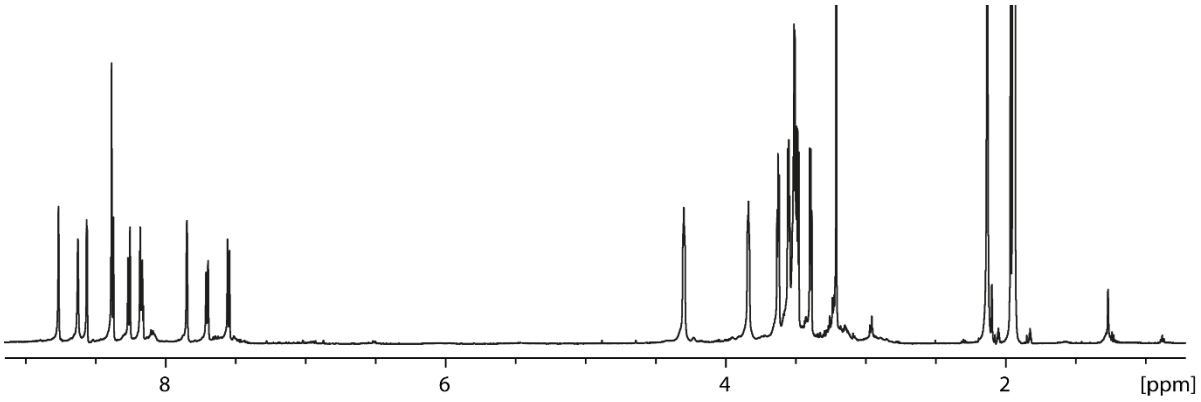

Figure 2.55. ^{1}H NMR of $Pd_2\mathbf{L}^{\mathbf{pyrenyl}}{}_4$.

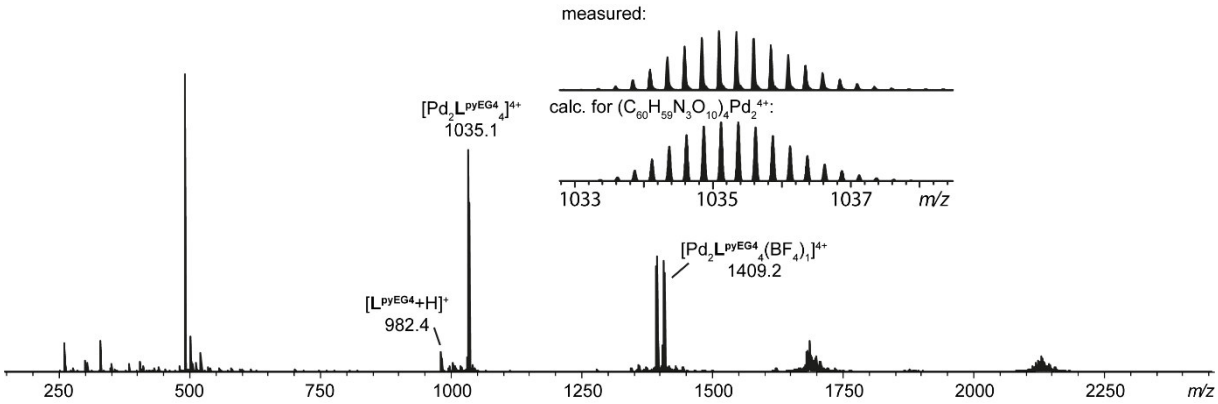

Figure 2.56. ^{1}H NMR of $Pd_2\mathbf{L}^{\mathbf{pyEG4}}{}_4$.

2.5.12 Fluorescence studies on $Pd_2\mathbf{L}^{\mathbf{pyEG4}}{}_4$

Six samples were prepared for each the free $\mathbf{L}^{\mathbf{pyEG4}}$ and for $Pd_2\mathbf{L}^{\mathbf{pyEG4}}{}_4(BF_4)_4$. The solvents were CD_3CN/D_2O mixtures ranging from 0 % to 50 % water content. The ligand concentration was kept constant at 0.28 mM leading to a cage concentration of 0.07 mM. The ^{1}H NMR spectra were measured and are shown in Figure 2.57 and Figure 2.58.

The signals of the free ligand and the once of the cage experience with increasing water content a slight upfield shift, a drop in intensity and broadening, which indicate aggregation caused by hydrophobic effect. To be noted here is that no free ligand is visible at least in the spectra with low water content of the cage, showing that the measured fluorescence likely stems from the cage.

$\mathbf{L}^{\mathbf{pyEG4}}$ is highly fluorescent. The spectrometer sensitivity was put on *medium*. The fluorescence got mostly quenched upon addition of palladium(II), which is why the sample of the cage in pure CD3CN was measured with the sensitivity *high*. With water content the fluorescence became stronger again, likely due to aggregation induced emission, which is why the sensitivity was put to *medium* again.

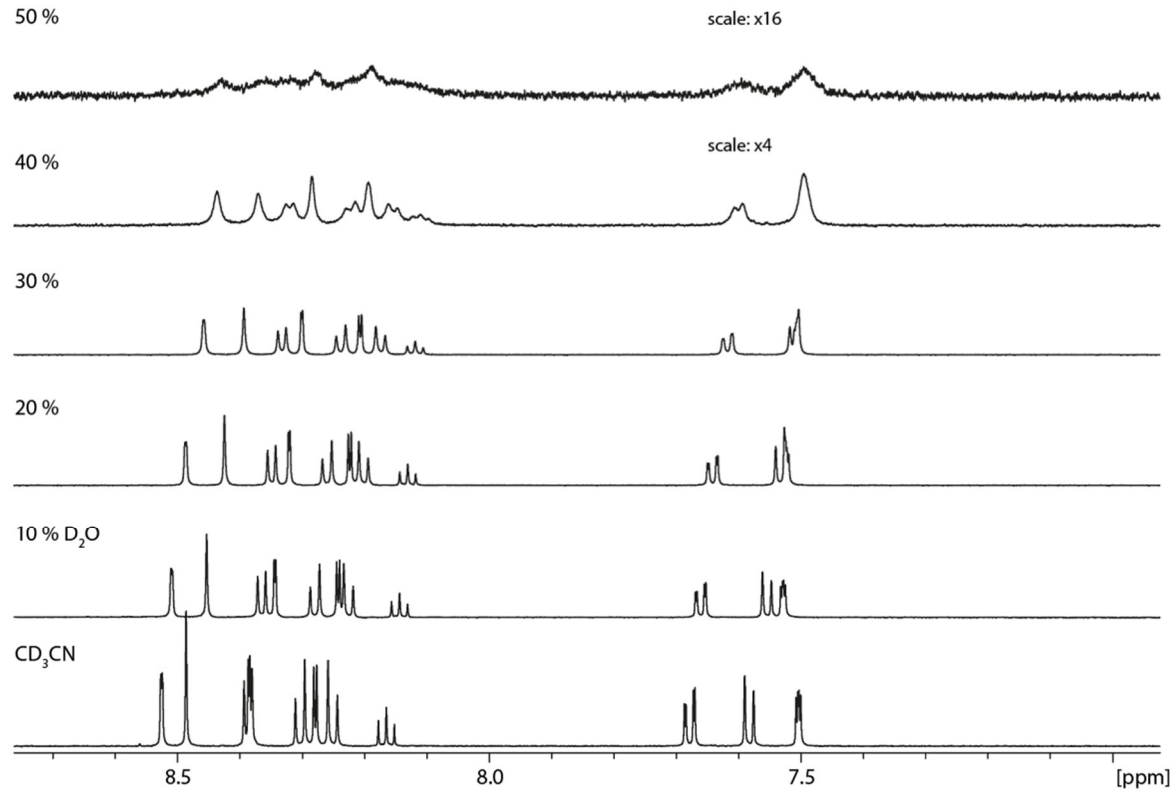

Figure 2.57. ^{1}H NMR spectra of $\mathbf{L^{pyEG4}}$ with varying water content.

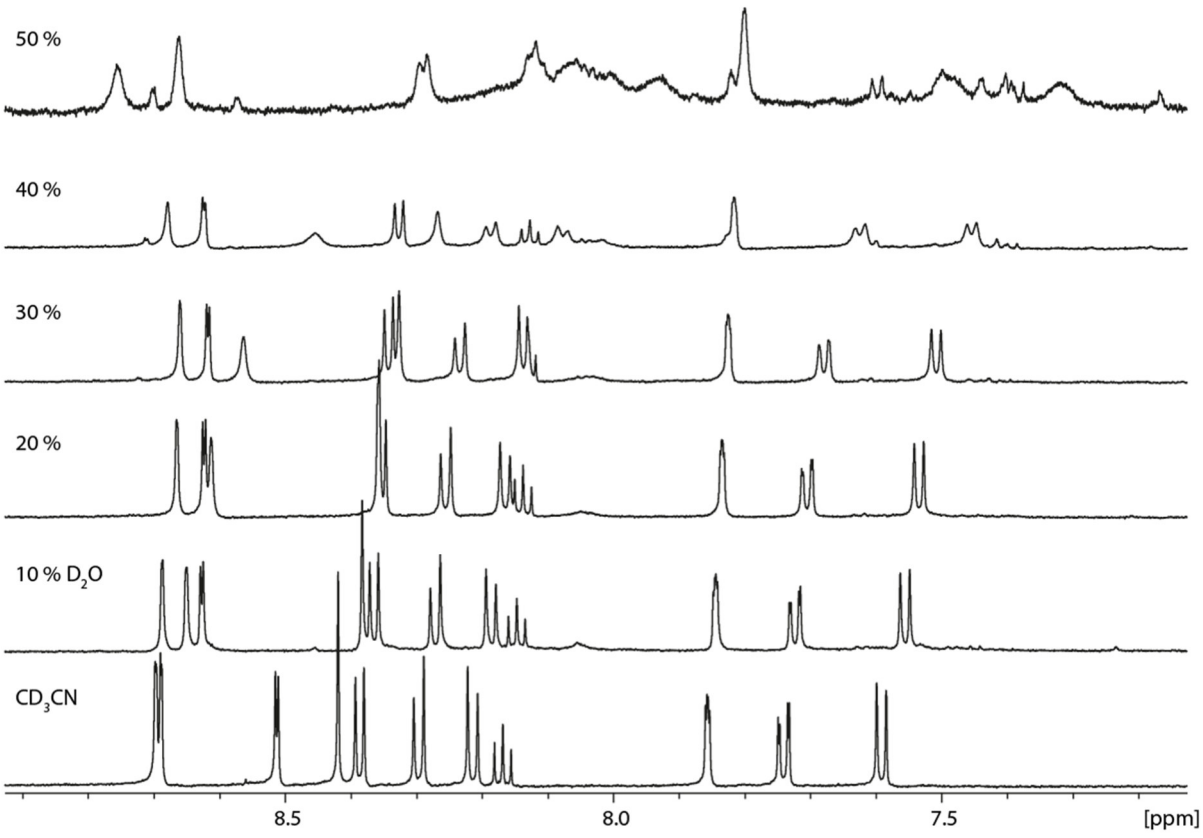

Figure 2.58. Aromatic region of ^{1}H NMR spectra of $Pd_2\mathbf{L^{pyEG4}}_4$ with varying water content.

2.6 Computational details

2.6.1 Molecular Dynamics Simulations with GFN2-xTB

The MD simulations were done with the xtb software, version 6.4.1,[94] using the default GFN2-xTB method.[70] We used the --omd flag, meaning that the run starts with a normal geometry optimization. The temperature was set to 303 K for gas phase MDs. The Pd-N-C_{para} angle was always constrained to 180° using the default force constant because it was observed that this angle is too flexible according to GFN2-xTB, see Section 2.6.12. The simulation time was 1000 ps for all species and for the double cages with octyl, decyl or dodecyl side chains additional 5000 ps were simulated. Other than that, and if not stated otherwise, always default settings were used. To obtain starting structures in which the side chains are already partially backfolded, preliminary MDs for about 500 ps with the same settings were conducted starting from structures with completely stretched out side chains.

2.6.2 Collidoscope, general settings

The theoretical collision cross sections ($^{theo}CCS_{N2}$) were calculated using the Collidoscope software, version 1.4, from Prell et al.[46] The temperature was set to 303 K, however, the exact temperature during the measurement cannot be determined precisely. Ion-quadrupole interactions were kept disabled. The number of energy states was increased from 4 to 16, resulting in about 500,000 trajectories. The CM5 point charges were calculated with GFN1-xTB, using the xtb software, version 6.4.1, from Grimme et al.[95,96] In Section 2.6.6 Mulliken charges were used, alternatively. These were also calculated with GFN1-xTB. As Collidoscope does not have Lennard-Jones parameters for B, F and Pd we used the parameters from C for the B and Pd atoms (both rather buried in the structures of the cages and counter anions) and parameterized F (more exposed) ourselves as described in Section 2.6.5.

2.6.3 HPCCS, general settings

For the calculation of $^{theo}CCS_{N2}$ values with the HPCCS software,[45] version 1.0 was used. The same CM5 point charges used for calculations with Collidoscope were also used here. The content of the config.in file was

```
1    500   20    50    1000  303   2
```

Meaning 500,000 trajectories, 303 K and N_2 as inert gas. For Pd and B the LJ-parameters from C were used. Other than that, default settings were used.

2.6.4 IMoS, general settings

For the calculation of $^{theo}CCS_{N2}$ values with the IMoS software,[32] version 10c ("IMoS110cL64LJ") was used. The same CM5 point charges used for calculations with Collidoscope were also used here. The

Trajectory Method with the normal 12-6-4 potential, 500,000 trajectories, 303 K and N_2 as inert gas was chosen. For Pd and B the LJ-parameters from C were used. Other than that, default settings were used.

2.6.5 Optimization of Fluorine Lennard-Jones parameters for Collidoscope

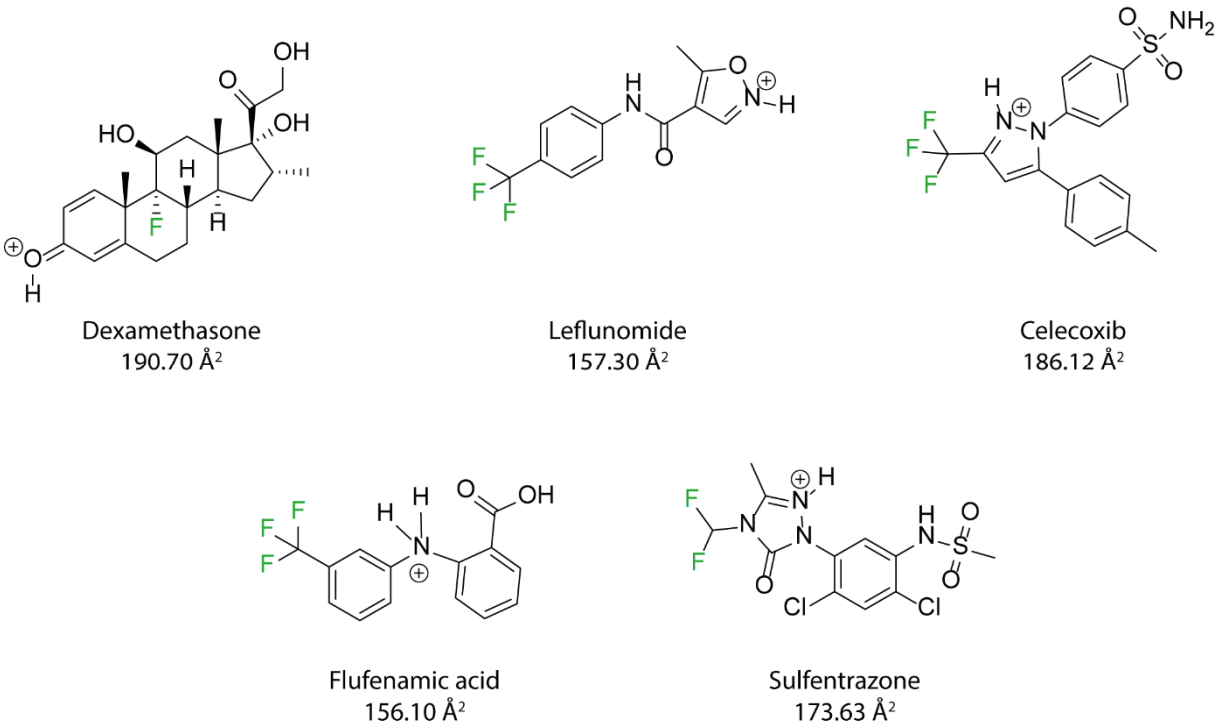

Figure 2.59. Compounds used for the parameterization of fluorine.

Several IMS measurements of drug-sized molecules containing at least one fluorine atom were found in the literature: Dexamethasone,[97] Leflunomide,[98] Flufenamic Acid,[98] Celecoxib,[44] and Sulfentrazone.[44] All species were single protonated and would have been uncharged otherwise. The ions were modeled and optimized with r^{2}SCAN-3c. Following the procedure described by Larriba and coworkers,[82] we varied the parameters ε_F (from 0 J/mol to 1500 J/mol in 50 J/mol steps) and σ_F (from 1 to 4 Å in 0.125 Å steps) and calculated F_{opt} each as defined by Larriba et al.[82] The according 3D plot is shown in Figure ***2.60***. As can be seen a valley of local minima is obtained. We thus chose ε_F = 500 J/mol randomly and minimized σ_F with a 0.01 Å step size, resulting in 2.67 Å.

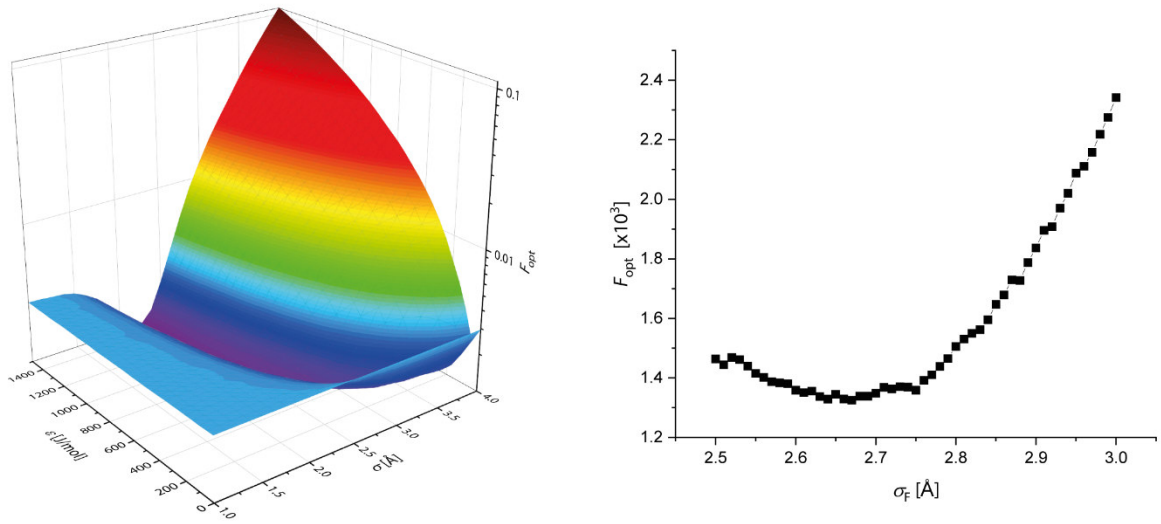

Figure 2.60. Left: Plot of F_{opt} against ε_F and σ_F. Right: Plot of F_{opt} against and σ_F, keeping ε_F constant at 500 J/mol.

We validated the results with the training set and with a test set consisting of $[Pd_2\mathbf{L}^{small}{}_4+BF_4]^{3+}$ and $[Pd_2\mathbf{L}^{small}{}_4+2BF_4]^{2+}$ were $\mathbf{L}^{small}$ is a short bis-monodentate ligand shown in Figure 2.61, as well as the free, single-protonated ligand **o-L^1** and the 4+, 3+ and 2+ species of the resulting Pd_2**o-L^1**$_4$ cage. **o-L^1** is another banana-shaped bis-monodentate ligand with pyridine donor groups and alkyne spacers, that is presented more detailed in Chapter 3.[99] The backbone of **o-L^1** is a dithienyl-hexafluoropentenyl group and we are here only considering the open-ring form. As can be seen in Table 2.4, not only the theoretical CCS values for the training set but also for the test set greatly improved showing that the new parameters are acceptable.

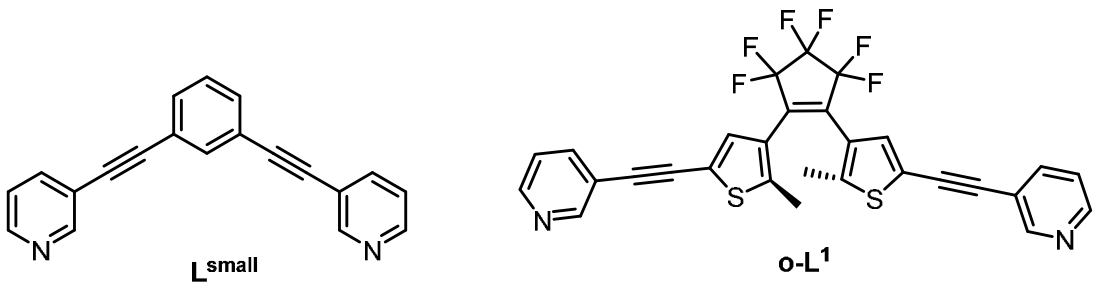

Figure 2.61. Ligands $\mathbf{L}^{small}$ and **o-L^{DTE}** used to form $Pd_2\mathbf{L}_4$ assemblies for verification of new LJ parameters for fluorine.

Table 2.4. Experimental and theoretical CCS values and relative deviations for various species containing fluorine. Values using the LJ parameters for fluorine from oxygen are compared to values with optimized LJ parameters.

Species	$^{TIMS}CCS_{N2}$	$^{theo}CCS_{N2}$($\varepsilon_F=\varepsilon_O$, $\sigma_F=\sigma_O$)		$^{theo}CCS_{N2}$(ε_F=500 kJ/mol, σ_F=2.67 Å)	
	[Å²]	$^{theo}CCS_{N2}$ [Å²]	Δ%	$^{theo}CCS_{N2}$ [Å²]	Δ%
[Celecoxib +H]$^+$	186.12	198.0	+6.4%	185.1	-0.6%
[Dexamethasone +H]$^+$	190.7	188.8	-1.0%	188.4	-1.2%
[Flufenamic acid +H]$^+$	156.1	170.1	+9.0%	158.6	+1.6%
[Leflunomide +H]$^+$	157.3	161.7	+2.8%	151.9	-3.4%
[Sulfentrazone +H]$^+$	173.63	182.4	+5.1%	173.6	+0.0%
[Pd_2**L**$^{small}_4$]$^{4+}$	503 ± 3	498.6	-0.9%	498.6	-0.9%
[Pd_2**L**$^{small}_4$+BF_4]$^{3+}$	452 ± 2	463.0	+2.4%	459.2	+1.6%
[Pd_2**L**$^{small}_4$+2BF_4]$^{2+}$	430 ± 1	456.8	+6.1%	448.8	+4.3%
[**o-L**^{DTE} +H]$^+$	227 ± 2	256.0	+13.0%	241.1	+6.4%
[Pd_2 **o-L**$^{DTE}_4$]$^{4+}$	600 ± 6	638.7	+6.4%	608.0	+1.3%
[Pd_2 **o-L**$^{DTE}_4$+BF_4]$^{3+}$	562 ± 5	610.4	+8.7%	577.8	+2.9%
[Pd_2 **o-L**$^{DTE}_4$+2BF_4]$^{2+}$	531 ± 3	591.6	+11.4%	554.7	+4.5%

To investigate whether the two counter anions are most likely inside or one inside and one outside for the species [Pd_2**L**$^{small}_4$ +2BF_4]$^{2+}$, [Pd_2**L**$^{methyl}_4$ +2BF_4]$^{2+}$ and [Pd_2**o-L**$^{DTE}_4$ +2BF_4]$^{2+}$, single point energy differences between inside-inside and inside-outside bound configurations on ωB97M-V/def2-TZVP level were calculated. Additionally, the Pd-Pd distances from the optimized inside-inside model were measured. Apparently, for the small cage the inside-outside version is favored by 10.9 kJ/mol, simply because the Pd-Pd distance is only 11.6 Å, causing a very small distance between the two BF_4^-. For the methyl carbazole cage, representative for all carbazole mono cages, the inside-outside version is still favored, even though not as much (4.4 kJ/mol difference, Pd-Pd distance: 13.3 Å). For the large open DTE cage, the inside-inside version is clearly favored by 14.3 kJ/mol due to the high Pd-Pd distance of 17.0 Å.

2.6.6 $^{theo}CCS_{N2}$ calculation using different Trajectory Method software

Table 2.5. $^{TIMS}CCS_{N2}$ values of $[Pd_2\mathbf{L}^{methyl}_4]^{4+}$, $[Pd_2\mathbf{L}^{methyl}_4+BF_4]^{3+}$ and $[Pd_2\mathbf{L}^{methyl}_4+2BF_4]^{2+}$ and the according $^{theo}CCS_{N2}$ values using either Collidoscope, Collidoscope with Mulliken instead of CM5 point charges, HPCCS or IMoS and the relative deviations to the $^{TIMS}CCS_{N2}$ values. Unit is Å².

	$^{TIMS}CCS_{N2}$	Collidoscope		HPCCS		IMoS		Collidoscope, Mulliken	
$[Pd_2\mathbf{L}^{methyl}_4]^{4+}$	582 ± 3	596.8	+2.5 %	623.8	+7.2 %	615.8	+5.8 %	600.3	+3.1 %
$[Pd_2\mathbf{L}^{methyl}_4 +BF_4]^{3+}$	542 ± 2	563.8	+4.1 %	592.6	+9.4 %	588.9	+8.7 %	565.9	+4.5 %
$[Pd_2\mathbf{L}^{methyl}_4 +2BF_4]^{2+}$	520 ± 2	554.4	+6.7 %	586.0	+12.8 %	581.6	+11.9 %	555.8	+7.0 %

2.6.7 $^{theo}CCS_{N2}$ calculation of snapshots from the trajectories

To obtain $^{theo}CCS_{N2}$ values averaged over time, snapshots of the trajectory file for every picosecond (actually only every 24/25th of a picosecond, because the time step used was 4 fs) were extracted and used for CCS calculation without further geometry optimization. The plots of the resulting $^{theo}CCS_{N2}$ and relative deviations to $^{TIMS}CCS_{N2}$ over time are shown in Figure 2.62 toFigure ***2.65*** and the averaged values are listed in Table 2.6.

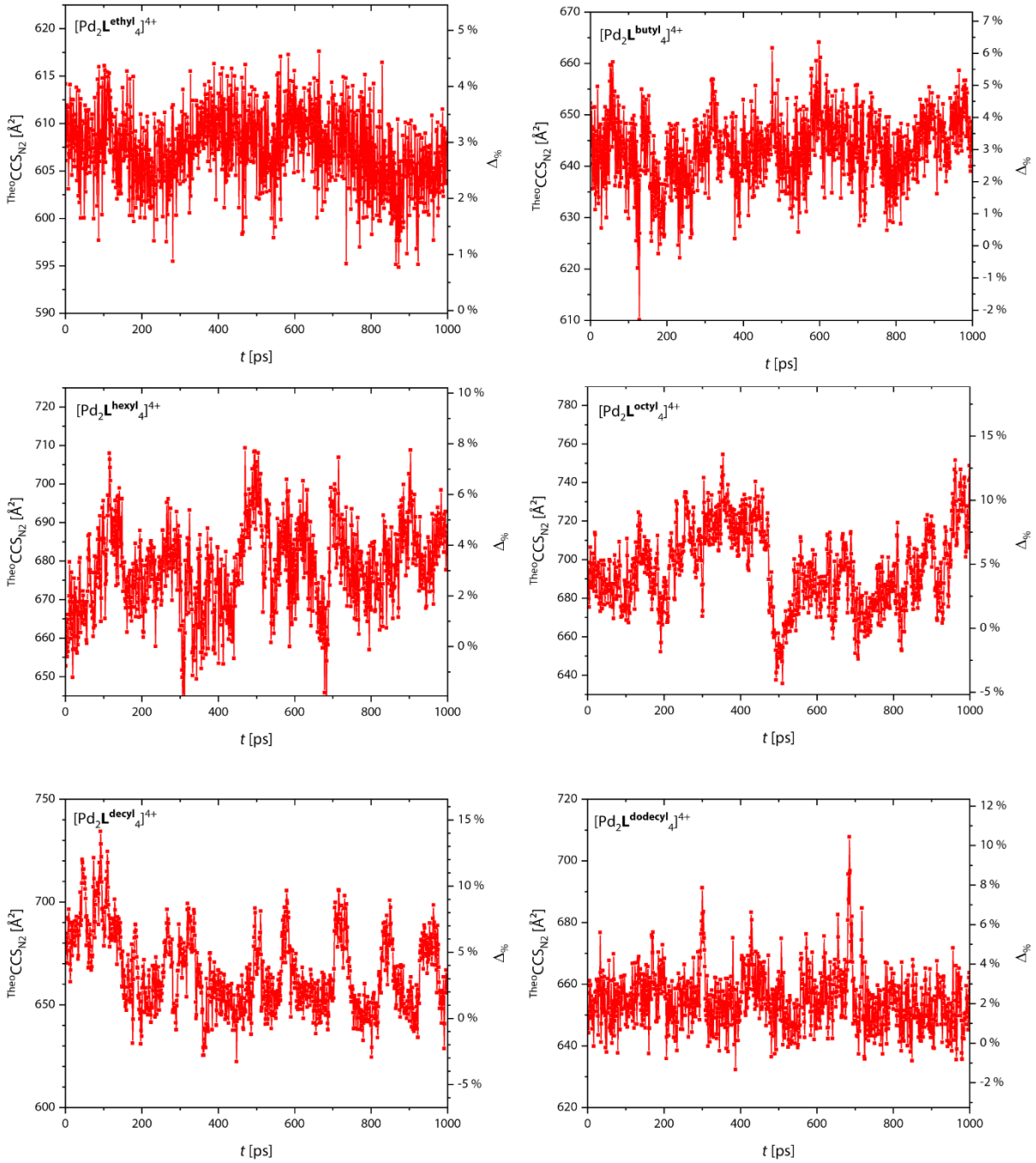

Figure 2.62. $^{theo}CCS_{N2}$ values for $[Pd_2L^R{}_4]^{4+}$ calculated from the snapshots taken every picosecond from the MD simulations plotted against time. Right y-axis shows the relative deviation to the experimental CCS ($^{TIMS}CCS_{N2}$).

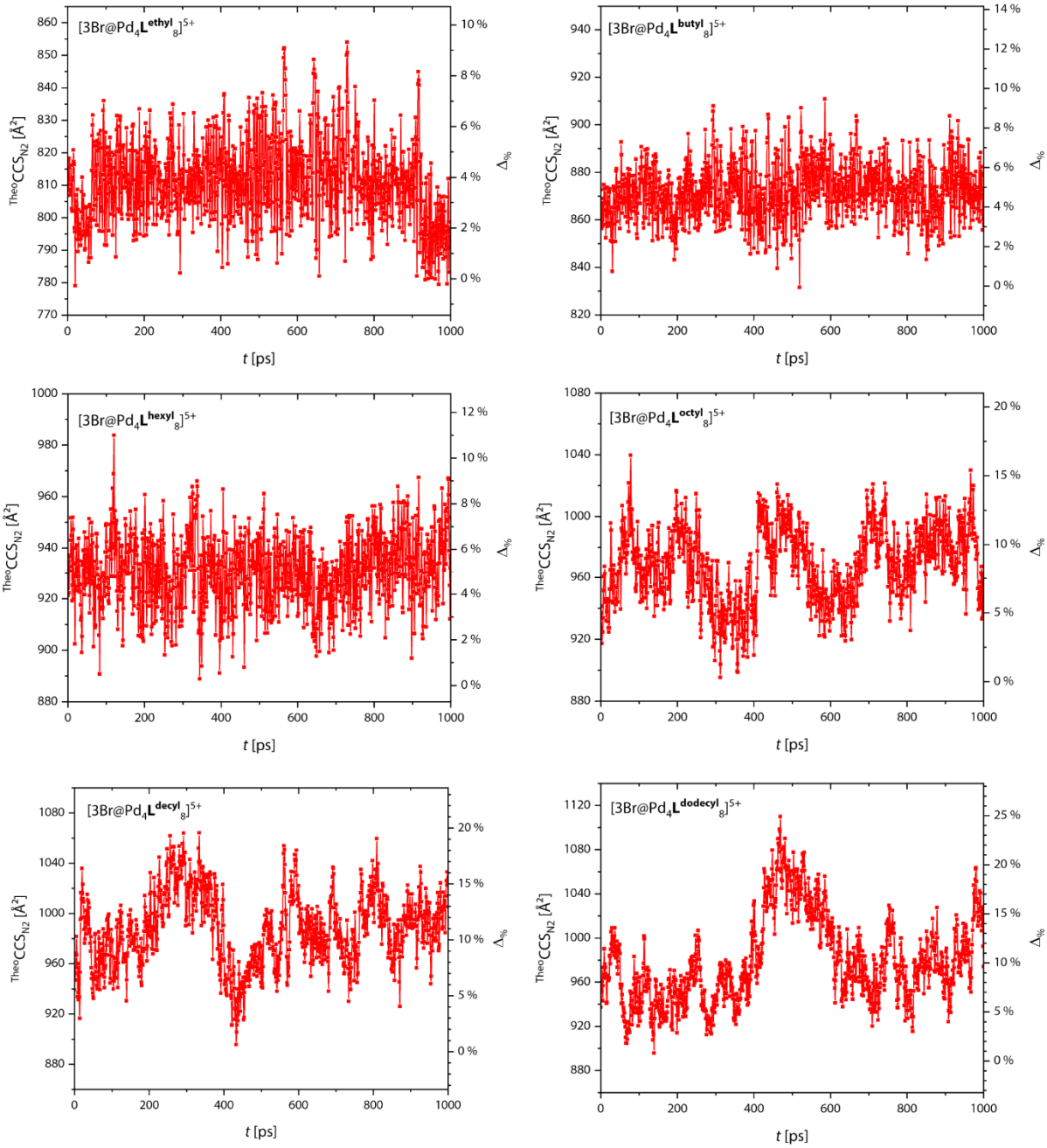

Figure 2.63. $^{theo}CCS_{N2}$ values for $[3Br@Pd_4L^R_8]^{5+}$ calculated from the snapshots taken every picosecond from the MD simulations plotted against time. Right y-axis shows the relative deviation to the experimental CCS ($^{TIMS}CCS_{N2}$).

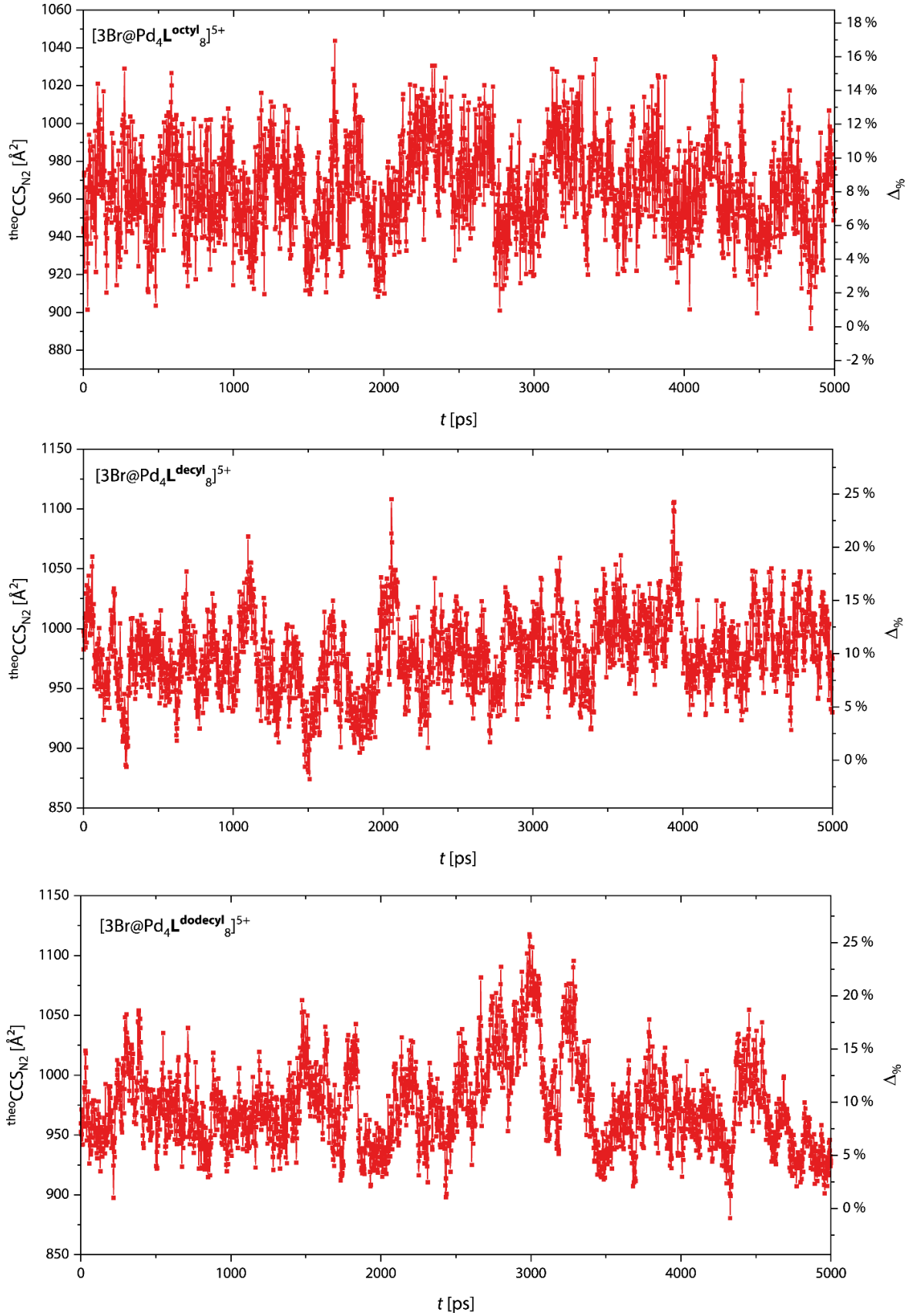

Figure 2.64. $^{theo}CCS_{N2}$ values for $[3Br@Pd_4L^R{}_8]^{5+}$ with R being either octyl, decyl or dodecyl calculated from the snapshots taken every picosecond from the longer MD simulations plotted against time. Right y-axis shows the relative deviation to the experimental CCS ($^{TIMS}CCS_{N2}$).

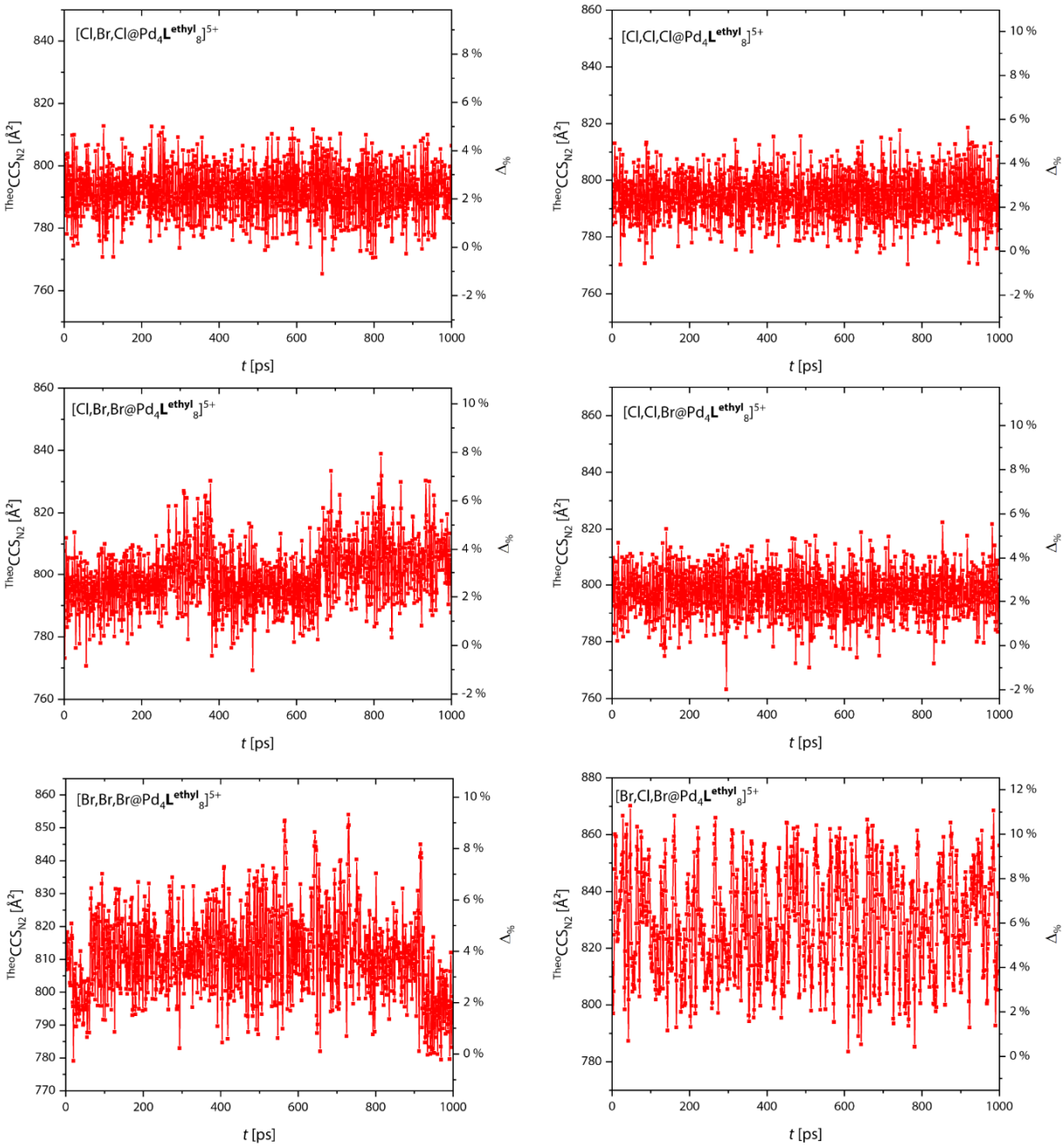

Figure 2.65. $^{theo}CCS_{N2}$ values for $[3X@Pd_4\mathbf{L}^{ethyl}_8]^{5+}$ with X being either Cl or Br and calculated from the snapshots taken every picosecond from the MD simulations plotted against time. Right y-axis shows the relative deviation to the experimental CCS ($^{TIMS}CCS_{N2}$).

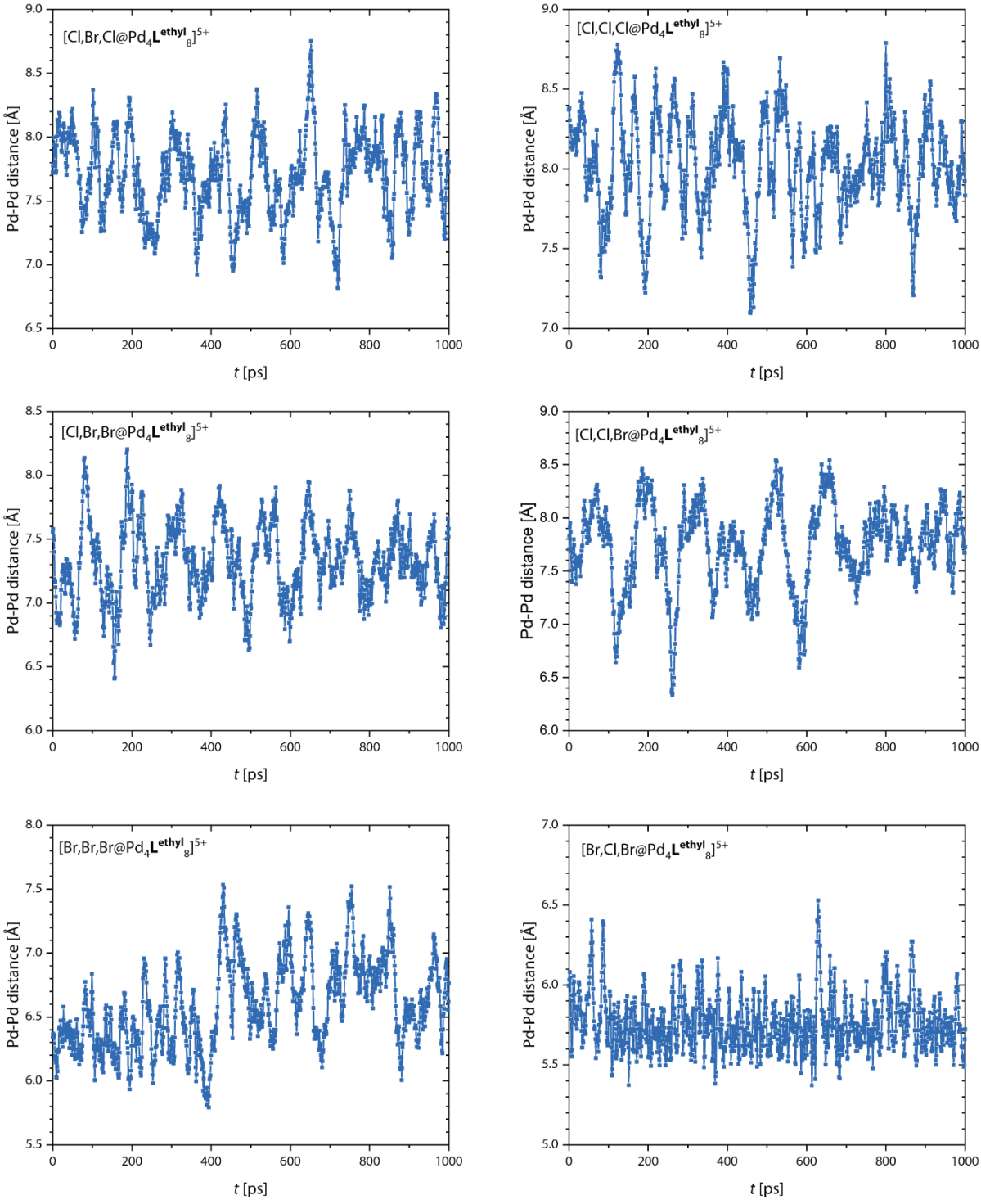

Figure 2.66. Pd-Pd distance of the central cavity in $[3X@Pd_4\mathbf{L}^{ethyl}_8]^{5+}$ with X being either Cl or Br plotted against time.

Table 2.6. Experimental and theoretical CCS_{N2} values for $[Pd_2\mathbf{L}^{\mathbf{R}}{}_4]^{4+}$ and $[3X@Pd_4\mathbf{L}^{\mathbf{R}}{}_8]^{5+}$ with R = ethyl, butyl, hexyl, octyl, decyl, dodecyl and X = Cl, Br. Experimental errors are the HWHM (half width of half maxima) of the measured signals. Theoretical errors are the standard deviations.

System	$^{TIMS}CCS_{N2}$ [Å²]	$^{theo}CCS_{N2}$ [Å²]	$\Delta_{\%}$
$[Pd_2\mathbf{L}^{\mathbf{ethyl}}{}_4]^{4+}$	590 ± 1	607 ± 4	+2.9 %
$[Pd_2\mathbf{L}^{\mathbf{butyl}}{}_4]^{4+}$	625 ± 2	643 ± 7	+3.0 %
$[Pd_2\mathbf{L}^{\mathbf{hexyl}}{}_4]^{4+}$	658 ± 3	678 ± 11	+3.1 %
$[Pd_2\mathbf{L}^{\mathbf{octyl}}{}_4]^{4+}$	664 ± 2	695 ± 21	+4.7 %
$[Pd_2\mathbf{L}^{\mathbf{decyl}}{}_4]^{4+}$	643 ± 3	666 ± 19	+3.5 %
$[Pd_2\mathbf{L}^{\mathbf{dodecyl}}{}_4]^{4+}$	641 ± 2	655 ± 9	+2.2 %
$[3Cl@Pd_4\mathbf{L}^{\mathbf{ethyl}}{}_8]^{5+}$	775 ± 2	794 ± 8	+2.5 %
$[Cl,Br,Cl@Pd_4\mathbf{L}^{\mathbf{ethyl}}{}_8]^{5+}$	774 ± 1	792 ± 8	+2.3 %
$[Cl,Cl,Br@Pd_4\mathbf{L}^{\mathbf{ethyl}}{}_8]^{5+}$	777 ± 2	797 ± 7	+2.4 %
$[Br,Cl,Br@Pd_4\mathbf{L}^{\mathbf{ethyl}}{}_8]^{5+}$	782 ± 3	833 ± 18	+6.6 %
$[Cl,Br,Br@Pd_4\mathbf{L}^{\mathbf{ethyl}}{}_8]^{5+}$	779 ± 1	803 ± 15	+3.3 %
$[3Br@Pd_4\mathbf{L}^{\mathbf{ethyl}}{}_8]^{5+}$	781 ± 1	811 ± 13	+3.8 %
$[3Br@Pd_4\mathbf{L}^{\mathbf{butyl}}{}_8]^{5+}$	832 ± 3	872 ± 12	+4.8 %
$[3Br@Pd_4\mathbf{L}^{\mathbf{hexyl}}{}_8]^{5+}$	886 ± 3	931 ± 14	+5.0 %
$[3Br@Pd_4\mathbf{L}^{\mathbf{octyl}}{}_8]^{5+}$	893 ± 3	968 ± 25	+8.5 %
$[3Br@Pd_4\mathbf{L}^{\mathbf{decyl}}{}_8]^{5+}$	890 ± 3	989 ± 29	+11.1 %
$[3Br@Pd_4\mathbf{L}^{\mathbf{dodecyl}}{}_8]^{5+}$	889 ± 3	982 ± 40	+10.5 %
$[3Br@Pd_4\mathbf{L}^{\mathbf{octyl}}{}_8]^{5+}$ (5 ns)	893 ± 3	965 ± 24	+8.2 %
$[3Br@Pd_4\mathbf{L}^{\mathbf{decyl}}{}_8]^{5+}$ (5 ns)	890 ± 3	978 ± 32	+9.9 %
$[3Br@Pd_4\mathbf{L}^{\mathbf{dodecyl}}{}_8]^{5+}$ (5 ns)	889 ± 3	974 ± 36	+9.6 %
$[3Br@Pd_4\mathbf{L}^{\mathbf{octyl}}{}_8]^{5+}$ (BW)	893 ± 3	970	+8.6 %
$[3Br@Pd_4\mathbf{L}^{\mathbf{decyl}}{}_8]^{5+}$ (BW)	890 ± 3	935	+5.1 %
$[3Br@Pd_4\mathbf{L}^{\mathbf{dodecyl}}{}_8]^{5+}$ (BW)	889 ± 3	954	+7.3 %

2.6.8 $^{theo}CCS_{N2}$ of geometry optimized cage systems and according experimental values

Table 2.7. Experimental and theoretical CCS values as well as relative deviations for the cages that were treated with geometry optimizations.

System	$^{TIMS}CCS_{N2}$ [Å²]	Conformation	$^{theo}CCS_{N2}$ [Å²]	$\Delta_{\%}$
$[Pd_2\mathbf{L}^{\mathbf{methyl}}_4]^{4+}$	582 ± 3	open	596.8	+2.5 %
		single-folded	570.9	-1.9 %
		(double-)folded	532.6	-8.5 %
$[Pd_2\mathbf{L}^{\mathbf{methyl}}_4 + BF_4]^{3+}$	542 ± 2	open	563.8	+4.1 %
		single-folded	539.5	-0.4 %
		(double-)folded	502.3	-7.3 %
$[Pd_2\mathbf{L}^{\mathbf{methyl}}_4 + 2BF_4]^{2+}$	520 ± 2	open	549.4	+5.7 %
		single-folded	527.5	+1.5 %
		(double-)folded	489.3	-5.8 %
$[Pd_2\mathbf{L}^{\mathbf{phenyl}}_4]^{4+}$	642 ± 3	open	667.0	+4.0 %
		single-folded	637.8	-0.6 %
		(double-)folded, D_2	592.7	-7.6 %
		(double-)folded, C_S	592.4	-7.7 %
$[Pd_2\mathbf{L}^{\mathbf{phenyl}}_4 + BF_4]^{3+}$	600 ± 2	Open	638.9	+6.5 %
		single-folded	604.5	+0.8 %
		(double-)folded, D_2	564.2	-5.9 %
		(double-)folded, C_S	565.5	-5.7 %
$[Pd_2\mathbf{L}^{\mathbf{phenyl}}_4 + 2BF_4]^{2+}$	571 ± 1	Open	625.8	+9.6 %
		single-folded	598.5	+4.8 %
		(double-)folded, D_2	550.7	-3.6 %
		(double-)folded, C_S	550.0	-3.7 %
$[Pd_2\mathbf{L}^{\mathbf{pyrenyl}}_4]^{4+}$	691* 691* 684 ± 3 697 ± 3	Open	807.3	+16.9 %
		single-folded	753.9	+9.2 %
		(double-)folded, D_2	679.6	-0.7 %
		(double-)folded, C_S	686.0	-1.6 %
$[Pd_2\mathbf{L}^{\mathbf{pyrenyl}}_4 + BF_4]^{3+}$	653* 653* 651 ± 1 655 ± 2	open	784.7	+20.2 %
		single-folded	735.9	+12.7 %
		(double-)folded, D_2	657.5	+1.0 %
		(double-)folded, C_S	662.7	+1.2 %

*These values are averages of the two overlapping signals, because that would make more sense for open or single-folded.

2.6.9 Headers for ORCA calculations

All geometry optimizations, frequency calculations, single point energy calculations and local energy decomposition calculations were conducted with ORCA 5.0.2.[100] All geometry optimizations in this work were done with the semiempirical method r^{2}SCAN-3c, if not noted otherwise.[71] The chemically relevant settings in the header of the input files are:

```
! r2SCAN-3c Opt
%geom trust -0.1 end
```

The numerical frequency calculations were also done with r^{2}SCAN-3c. No inharmonic frequencies were found. The chemically relevant settings in the header of the input files are:

```
! r2SCAN-3c NumFreq
```

The chemically relevant settings in the header of the input files for energy calculations on ωB97M-D4/def2-TZVP or ωB97M-V/def2-TZVP level are:

```
! wB97M-D4 def2-TZVP TightSCF
```

or respectively

```
! wB97M-V def2-TZVP TightSCF
```

The chemically relevant settings in the header of the input files for calculations with HFLD are:

```
! HFLD cc-pVTZ cc-pVTZ/C RIJCOSX TightPNO VeryTightSCF
```

For the calculation of inter-fragment dispersion only cutouts of the optimized structures containing only one stacked pair of ligands and not palladium was used.

The chemically relevant settings in the header of the input files for calculations with DLPNO-CCSD(T)/TightPNO/def2-TZVP are:

```
! DLPNO-CCSD(T) def2-TZVP def2-TZVP/C RIJCOSX TightPNO VeryTightSCF
```

2.6.10 Optimized models

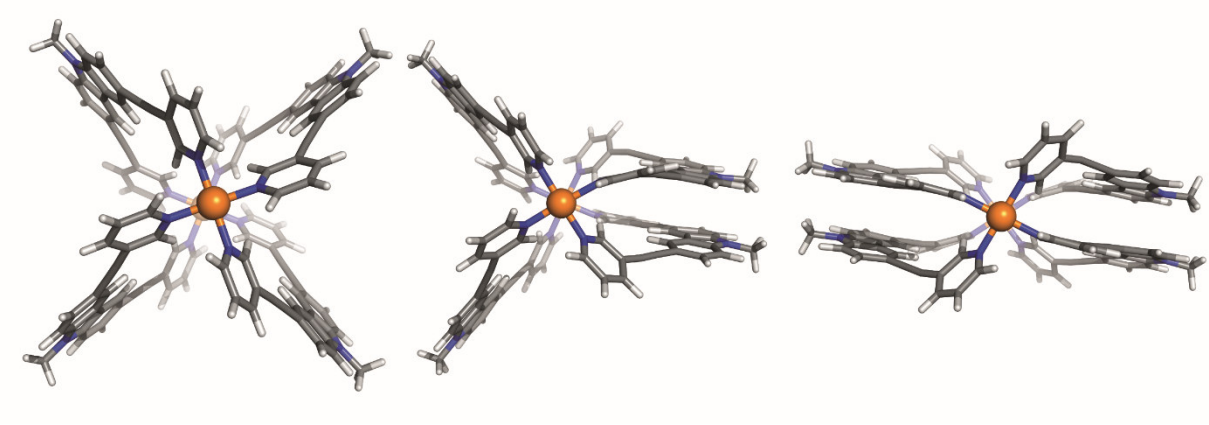

Figure 2.67. Geometry optimized models of $[Pd_2\mathbf{L}^{\mathbf{methyl}}{}_4]^{4+}$ in different conformations. From left to right: open, single-folded, (double-)folded.

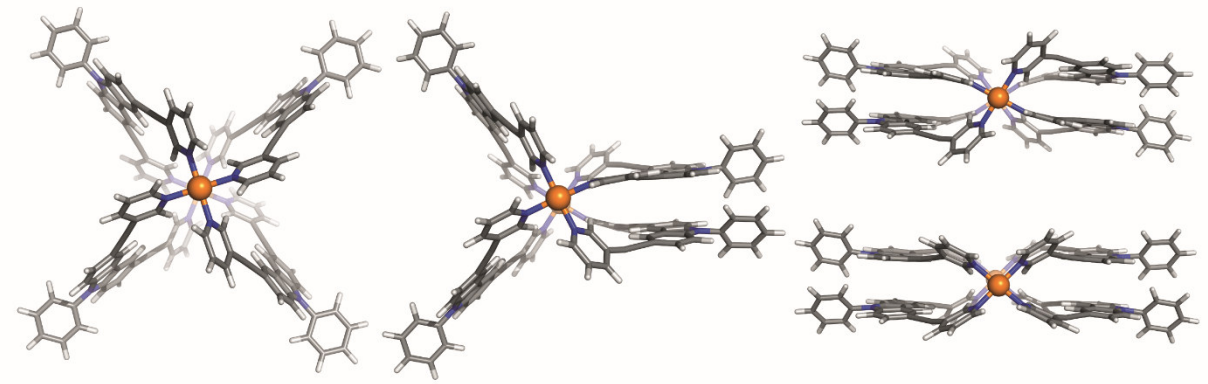

Figure 2.68. Geometry optimized models of $[Pd_2\mathbf{L}^{\mathbf{phenyl}}{}_4]^{4+}$ in different conformations. From left to right: open, single-folded, (double-)folded. Upper left: (double-)folded, C_S-symmetric. Lower left: (double-)folded, D_2-symmetric.

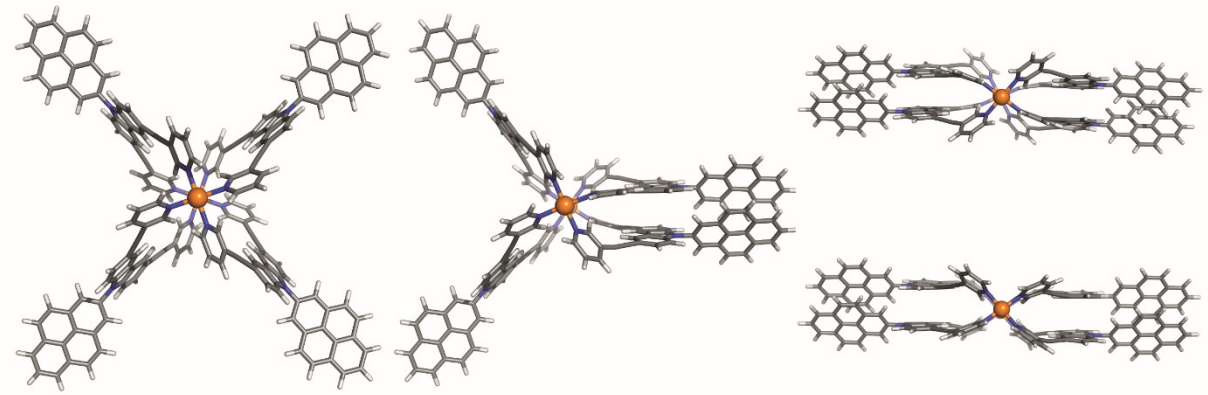

Figure 2.69. Geometry optimized models of $[Pd_2\mathbf{L}^{\mathbf{pyrenyl}}{}_4]^{4+}$ in different conformations. From left to right: open, single-folded, (double-)folded. Upper left: (double-)folded, C_S-symmetric. Lower left: (double-)folded, D_2-symmetric.

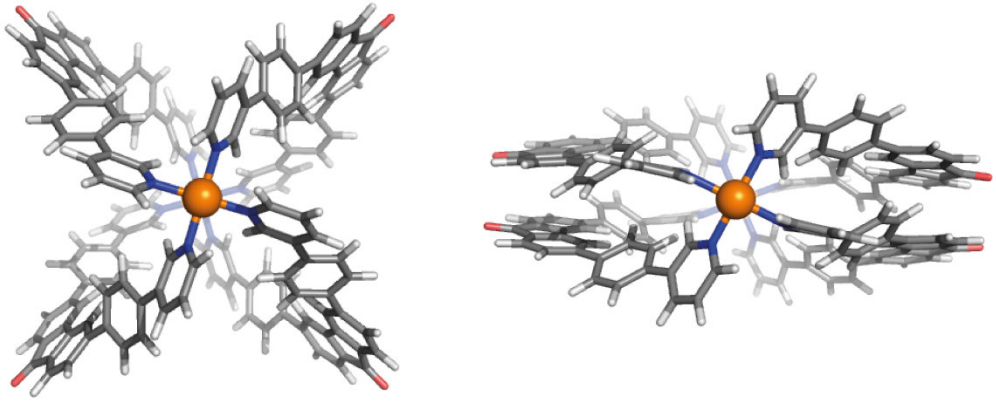

Figure 2.70. Top view of optimized open and folded conformation of $[Pd_2\mathbf{L}^{\mathbf{FL}}{}_4]^{4+}$.

2.6.11 Free energy calculations also considering the single-folded conformer

As the possibility of a single-folded conformer in the gas phase for any of the cages $[Pd_2\mathbf{L}^{\mathbf{methyl}}{}_4]^{4+}$, $[Pd_2\mathbf{L}^{\mathbf{phenyl}}{}_4]^{4+}$ and $[Pd_2\mathbf{L}^{\mathbf{pyrenyl}}{}_4]^{4+}$ cannot be cancelled out by theoretical CCS calculations, further DFT calculations were performed. Just like for the open and double-folded conformers we calculated ΔE_{DFT} and ΔG_{RRHO} for the single-folded conformer. The calculated energy differences to the open conformer are, together with the energy differences between double-folded and open, which were already mentioned in the main text, listed in Table 2.8. As can be seen, the considered energy terms for single-folded are always between those for open and double-folded and the energy increase or decrease from open to single-folded to double-folded is always nearly linear showing no sign of significant positive or negative cooperativity.

Table 2.8. ΔE_{el} and ΔG_{RRHO} values calculated for the open, single-folded and double-folded conformers of $[Pd_2\mathbf{L}^{\mathbf{methyl}}{}_4]^{4+}$, $[Pd_2\mathbf{L}^{\mathbf{phenyl}}{}_4]^{4+}$, $[Pd_2\mathbf{L}^{\mathbf{pyrenyl}}{}_4]^{4+}$ and $[Pd_2\mathbf{L}^{\mathbf{FL}}{}_4]^{4+}$.

System	Energy term	$E^{\text{single-folded}}$-E^{open}	$E^{\text{double-folded},D2}$-$E^{\text{open}}$	$E^{\text{double-folded},CS}$-$E^{\text{open}}$
$[Pd_2\mathbf{L}^{\mathbf{methyl}}{}_4]^{4+}$	ΔE_{DFT}	+66.7	+135.1	-
	ΔE_{D4}	–62.1	–127.0	-
	ΔE_{VV10}	–66.0	–135.8	-
	ΔG_{RRHO}	+6.5	+13.3	-
	ΔG_{D4}	+11.1	+21.4	-
	ΔG_{VV10}	+7.2	+12.6	-
$[Pd_2\mathbf{L}^{\mathbf{phenyl}}{}_4]^{4+}$	ΔE_{DFT}	+71.2	+144.1	+147.9
	ΔE_{D4}	–73.1	–151.3	–151.7
	ΔE_{VV10}	–78.4	–163.8	–163.4
	ΔG_{RRHO}	+6.6	+16.1	+17.5
	ΔG_{D4}	+4.7	+8.9	+13.7
	ΔG_{VV10}	–0.6	–3.5	+2.0
$[Pd_2\mathbf{L}^{\mathbf{pyrenyl}}{}_4]^{4+}$	ΔE_{DFT}	+81.1	+167.1	+172.8
	ΔE_{D4}	–122.8	–255.5	–257.7
	ΔE_{VV10}	–131.9	–276.7	–277.8
	ΔG_{RRHO}	+10.2	+26.7	+28.5
	ΔG_{D4}	–31.5	–61.7	–56.3
	ΔG_{VV10}	–40.6	–82.9	–76.4
$[Pd_2\mathbf{L}^{\mathbf{FL}}{}_4]^{4+}$	ΔE_{DFT}	+47.0	+107.1	-
	ΔE_{D4}	-89.2	-176.2	-
	ΔE_{VV10}	-97.1	-192.5	-
	ΔG_{RRHO}	+8.0	+16.0	-
	ΔG_{D4}	-42.1	-69.4	-
	ΔG_{VV10}	-34.2	-53.1	-

2.6.12 Geometry optimizations using different DFT methods, angle scans and CSD-searches

As mentioned in the main text, MD simulations with GFN2-xTB without constraints led to heavy distortions at the Pd centers. Especially problematic is the angle between the palladium atom, the donating nitrogen atom and the carbon atom in para position to the nitrogen atom (Pd-N-C_{para}). To check whether these distortions and therefore the folding of $[Pd_2\mathbf{L}^{\mathbf{pyrenyl}}_4]^{4+}$ in the gas phase are realistic we performed motif searches for this angle in the Cambridge Structural Database (CSD 5.41) using a single Pd-pyridine group as motif. The results are shown in a form of a histogram in Figure 2.71. As can be seen, angles up to around 157° are rare but realistic. When specifying that "the Pd atom and the N atom must not be part of a circle", to avoid chelate complexes, far less results were found. Here, only examples up to around 168° are found.

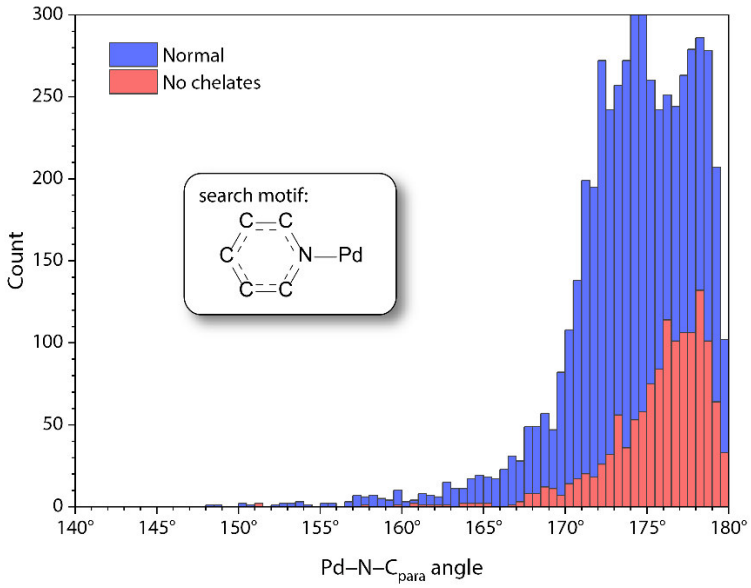

Figure 2.71. Result of a motif search in the CSD 5.41 database with and without specifying that "the Pd atom and the N atom must not be part of a circle".

We optimized the model of $[Pd_2\mathbf{L}^{\mathbf{methyl}}_4]^{4+}$ in (double-)folded conformation with GFN2-xTB, r^{2}SCAN-3c, and ωB97M-V/def2-TZVP. The average and smallest angles from the optimized models are listed in Table 2.9. As can be seen, the situation greatly improves with increasing level of theory with an average angle of 169.3° when optimized with ωB97M-D4/def2-TZVP. The semiempirical method r^{2}SCAN-3c shows acceptable angles as well.

Table 2.9. Average and smallest Pd-N-C_{para} angles of the double-folded model of $[Pd_2\mathbf{L}^{methyl}{}_4]^{4+}$ optimized with different methods.

	GFN2-xTB	r²SCAN-3c	ωB97M-D4/def2-TZVP
Average	157° ± 2°	166° ± 1°	169.3° ± 0.6°
Minimum	154.0°	164.0°	168.5°

Additionally, we performed relaxed angle scans of that angle in a smaller $[Pd(pyridine)_4]^{2+}$ complex using either GFN2-xTB or r²SCAN-3c. For higher level ωB97M-D4/def2-TZVP and DLPNO-CCSD(T)[101]/TightPNO/def2-TZVP energies the geometries from the scan with r²SCAN-3c were taken. The energy increase with increasing distortion of the Pd-N-C_{para} angle is plotted in Figure 2.72. Apparently r²SCAN-3c and ωB97M-V already perform very close to the reference, while GFN2-xTB performs poorly in this regard.

In GFN2-xTB MD simulations with BF_4^- counter anions we noticed that the Pd complexes are even more flexible due to a charge transfer. We repeated the angle scans, this time with a BF_4^- in close proximity to the complex and noticed an increased flexibility even for the higher methods. However, the flexibility rise decreases with increasing level of theory. In addition, we note that here geometry optimized structures are considered while in the experiment the BF_4^- is constantly moving and not perfectly close to the Pd complex, which would further decrease any charge transfer.

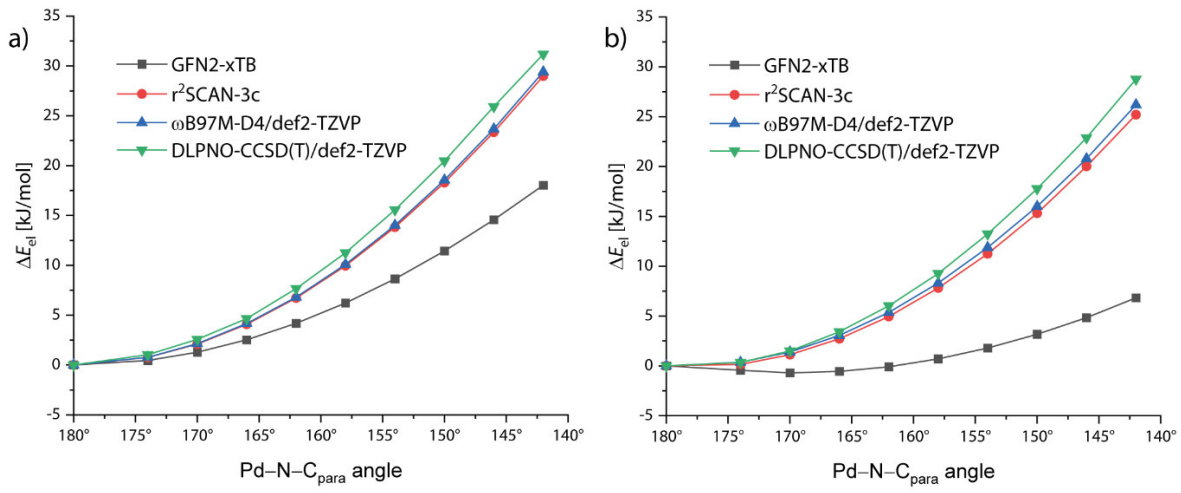

Figure 2.72. Relaxed angle scans for one of the Pd-N-C_{para} angles in a) a $[Pd_2(pyridine)_4]^{2+}$ complex and b) a $[Pd_2(pyridine)_4]^{2+}$ complex with a BF_4^- in proximity. For ωB97M-D4/def2-TZVP and DLPNO-CCSD(T)/TightPNO/def2-TZVP energies the geometries from the relaxed scan with r²SCAN-3c were taken.

2.6.13 Benchmarking of disperion correction methods with coupled cluster

Single point energy calculations of gas phase cage systems with either ωB97M-D4/def2-TZVP or ωB97M-V/def2-TZVP led to in part large energy differences. The VV10 dispersion correction in general leads to stronger dispersive interactions than the D4 correction. Both corrections are widely used and their accuracy has been proven, repeatedly.[102] To get an idea which correction is better suitable for the here investigated systems both methods are compared to DLPNO-CCSD(T)[80]/TightPNO/cc-pVTZ. For this, two different fragments were cut out: Two methyl and alkynyl substituted carbazole backbones from $[Pd_2\mathbf{L}^{\mathbf{methyl}}{}_4]^{4+}$ and two pyrene units from $[Pd_2\mathbf{L}^{\mathbf{pyrenyl}}{}_4]^{4+}$. The compared fragments were taken both from the open and the double-folded conformers to avoid the need for any counterpoise correction.

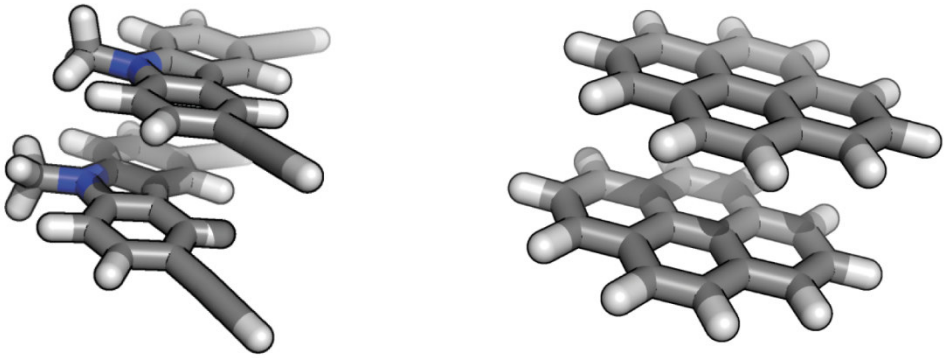

Figure 2.73. Fragments used for comparison of different dispersion corrections with local coupled cluster. The left fragment was taken from the model of $[Pd_2\mathbf{L}^{\mathbf{methyl}}{}_4]^{4+}$ and the right was taken from the model of $[Pd_2\mathbf{L}^{\mathbf{pyrenyl}}{}_4]^{4+}$.

Table 2.10 lists the according energy differences for both fragments. Not only ωB97M-D4 and ωB97M-V were compared with DLPNO-CCSD(T) but also GFN2-xTB, which was used for MD simulations, and r^{2}SCAN-3c, which was used for the geometry optimizations and frequency calculations. Surprisingly, GFN2-xTB performs better than r^{2}SCAN-3c in both cases. D4 is incorporated in both, which leads to the conclusion that the repulsive, electrostatic contributions are overestimated in r^{2}SCAN-3c for these cases. But because the error from the π stacking is still rather low and this method performs well regarding the Pd-pyridine angle, it is still regarded as suitable for the applications it was used for. Regarding the carbazole backbone, both ωB97M-D4 and ωB97M-V perform fine. When VV10 is used, the folding is overestimated by 1.8 kJ/mol, when D4 is used it is underestimated by 1.5 kJ/mol. Regarding the pyrene, ωB97M-D4 matches the reference with only 0.2 kJ/mol, while ωB97M-V deviates with 2.8 kJ/mol, indicating that D4 is slightly more suitable here.

These computed differences appear minor but the here investigated systems are only fragments of larger systems meaning that any small error amplifies when the whole cage is considered. To be noted

also is the fact that the electronic structure may differ significantly in the cage than compared to the fragments which weakens the importance of these results.

Table 2.10. Single point energy differences of fragments from double-folded and open conformations 4of either $[Pd_2\mathbf{L}^{methyl}_4]^{4+}$ (two carbazole backbones) or $[Pd_2\mathbf{L}^{pyrenyl}_4]^{4+}$ (two pyrene units) using different theoretical models. Unit is kJ/mol.

Method	Δ*E* (carbazole)	Δ*E* (pyrene)
GFN2-xTB	–48.9	–54.4
r^2SCAN-3c	–42.9	–48.0
ωB97M/def2-TZVP	+11.0	+8.1
D4	–58.5	–61.5
VV10	–61.8	–64.1
ωB97M-D4/def2-TZVP	–47.5	–53.4
ωB97M-V/def2-TZVP	–50.8	–56.0
DLPNO-CCSD(T)/TightPNO/cc-pVTZ	–49.0	–53.2

2.7 Literature

[1] K. E. Ebbert, L. Schneider, A. Platzek, C. Drechsler, B. Chen, R. Rudolf, G. H. Clever, *Dalton T* **2019**, DOI 10.1039/c9dt01814j.

[2] M. E. Ridgeway, M. Lubeck, J. Jordens, M. Mann, M. A. Park, *Int J Mass Spectrom* **2018**, *425*, 22–35.

[3] F. A. Fernandez-Lima, D. A. Kaplan, M. A. Park, *Rev Sci Instrum* **2011**, *82*, 126106.

[4] F. Fernandez-Lima, D. A. Kaplan, J. Suetering, M. A. Park, *Int J Ion Mobil Spectrom* **2011**, *14*, 93–98.

[5] K. Michelmann, J. A. Silveira, M. E. Ridgeway, M. A. Park, *J Am Soc Mass Spectr* **2015**, *26*, 14–24.

[6] J. A. Silveira, K. Michelmann, M. E. Ridgeway, M. A. Park, *J Am Soc Mass Spectr* **2016**, *27*, 585–595.

[7] D. R. Hernandez, J. D. DeBord, M. E. Ridgeway, D. A. Kaplan, M. A. Park, F. Fernandez-Lima, *Analyst* **2014**, *139*, 1913–1921.

[8] A. A. Shvartsburg, R. D. Smith, *Anal Chem* **2008**, *80*, 9689–9699.

[9] R. Guevremont, *J Chromatogr A* **2004**, *1058*, 3–19.

[10] K. Giles, J. Ujma, J. Wildgoose, S. Pringle, K. Richardson, D. Langridge, M. Green, *Anal Chem* **2019**, *91*, 8564–8573.

[11] E. A. Mason, H. W. Schamp, *Ann Phys-new York* **1958**, *4*, 233–270.

[12] E. A. Mason, E. W. McDaniel, **2019**, DOI 10.1002/3527602852.

[13] V. Gabelica, A. A. Shvartsburg, C. Afonso, P. Barran, J. L. P. Benesch, C. Bleiholder, M. T. Bowers, A. Bilbao, M. F. Bush, J. L. Campbell, I. D. G. Campuzano, T. Causon, B. H. Clowers, C. S. Creaser, E. D. Pauw, J. Far, F. Fernandez-Lima, J. C. Fjeldsted, K. Giles, M. Groessl, C. J. Hogan, S. Hann, H. I. Kim, R. T. Kurulugama, J. C. May, J. A. McLean, K. Pagel, K. Richardson, M. E. Ridgeway, F. Rosu, F. Sobott, K. Thalassinos, S. J. Valentine, T. Wyttenbach, *Mass Spectrom Rev* **2019**, DOI 10.1002/mas.21585.

[14] H. E. Revercomb, E. A. Mason, *Anal Chem* **1975**, *47*, 970–983.

[15] M. N. Young, C. Bleiholder, *J Am Soc Mass Spectr* **2017**, *28*, 619–627.

[16] T. Wyttenbach, G. von Helden, J. J. Batka, D. Carlat, M. T. Bowers, *J Am Soc Mass Spectr* **1997**, *8*, 275–282.

[17] M. F. Mesleh, J. M. Hunter, A. A. Shvartsburg, G. C. Schatz, M. F. Jarrold, *J Phys Chem* **1996**, *100*, DOI 10.1021/jp961623v.

[18] C. Larriba-Andaluz, J. S. Prell, *Int Rev Phys Chem* **2020**, *39*, 569–623.

[19] L. Polewski, A. Springer, K. Pagel, C. A. Schalley, *Accounts Chem Res* **2021**, *54*, 2445–2456.

[20] E. Kalenius, M. Groessl, K. Rissanen, *Nat Rev Chem* **2019**, *3*, 4–14.

[21] O. H. L. Williams, N. J. Rijs, *Front Chem* **2021**, *9*, 682743.

[22] J. Ujma, M. D. Cecco, O. Chepelin, H. Levene, C. Moffat, S. J. Pike, P. J. Lusby, P. E. Barran, *Chem Commun* **2012**, *48*, 4423–4425.

[23] B. Song, Z. Zhang, K. Wang, C. Hsu, O. Bolarinwa, J. Wang, Y. Li, G. Yin, E. Rivera, H. Yang, C. Liu, B. Xu, X. Li, *Angew Chem-ger Edit* **2017**, *129*, 5342–5346.

[24] I. Regeni, B. Chen, M. Frank, A. Baksi, J. J. Holstein, G. H. Clever, *Angewandte Chemie Int Ed* **2020**, *60*, 5673–5678.

[25] A. Platzek, S. Juber, C. Yurtseven, S. Hasegawa, L. Schneider, C. Drechsler, K. E. Ebbert, R. Rudolf, Q. Yan, J. J. Holstein, L. V. Schäfer, G. H. Clever, *Angew. Chem. Int. Ed.* **2022**, *61*, e202209305.

[26] W. M. Bloch, S. Horiuchi, J. J. Holstein, C. Drechsler, A. Wuttke, W. Hiller, R. A. Mata, G. H. Clever, *Chem Sci* **2023**, *14*, 1524–1531.

[27] C. Vicent, V. Martinez-Agramunt, V. Gandhi, C. Larriba-Andaluz, D. G. Gusev, E. Peris, *Angew Chem-ger Edit* **2021**, *133*, 15540–15545.

[28] J. S. Prell, *Compr Anal Chem* **2018**, 1–22.

[29] P. Bonakdarzadeh, F. Topić, E. Kalenius, S. Bhowmik, S. Sato, M. Groessl, R. Knochenmuss, K. Rissanen, *Inorg Chem* **2015**, *54*, 6055–6061.

[30] E. Mack, *J Am Chem Soc* **1925**, *47*, 2468–2482.

[31] G. von Helden, M. Hsu, P. R. Kemper, M. T. Bowers, *J Chem Phys* **1991**, *95*, 3835–3837.

[32] C. Larriba, C. J. Hogan, *J Phys Chem* **2013**, *117*, 3887–3901.

[33] C. Bleiholder, S. Contreras, M. T. Bowers, *Int J Mass Spectrom* **2013**, *354*, 275–280.

[34] C. Bleiholder, T. Wyttenbach, M. T. Bowers, *Int J Mass Spectrom* **2011**, *308*, 1–10.

[35] C. Bleiholder, *Analyst* **2015**, *140*, 6804–6813.

[36] Z. Zhou, X. Xiong, Z.-J. Zhu, *Bioinformatics* **2017**, *33*, 2235–2237.

[37] Z. Zhou, J. Tu, X. Xiong, X. Shen, Z.-J. Zhu, *Anal Chem* **2017**, *89*, 9559–9566.

[38] P.-L. Plante, E. Francovic-Fontaine, J. C. May, J. A. McLean, E. S. Baker, F. Laviolette, M. Marchand, J. Corbeil, *Anal Chem* **2019**, *91*, 5191–5199.

[39] Z. Zhou, M. Luo, X. Chen, Y. Yin, X. Xiong, R. Wang, Z.-J. Zhu, *Nat Commun* **2020**, *11*, 4334.

[40] A. Celma, R. Bade, J. V. Sancho, F. Hernandez, M. Humphries, L. Bijlsma, *J Chem Inf Model* **2022**, *62*, 5425–5434.

[41] C. Ieritano, J. L. Campbell, W. S. Hopkins, *Analyst* **2021**, *146*, 4737–4743.

[42] D. H. Ross, R. P. Seguin, A. M. Krinsky, L. Xu, *J Am Soc Mass Spectr* **2022**, *33*, 1061–1072.

[43] J. O. Hirschfelder, C. F. Curtiss, R. B. Bird, *Phys Today* **1955**, *8*, 17–17.

[44] C. Ieritano, J. Crouse, J. L. Campbell, W. S. Hopkins, *Analyst* **2019**, *144*, 1660–1670.

[45] L. Zanotto, G. Heerdt, P. C. T. Souza, G. Araujo, M. S. Skaf, *J Comput Chem* **2018**, *39*, 1675–1681.

[46] S. A. Ewing, M. T. Donor, J. W. Wilson, J. S. Prell, *J Am Soc Mass Spectr* **2017**, *28*, 587–596.

[47] N. L. Allinger, M. Rahman, J. H. Lii, *J. Am. Chem. Soc.* **1990**, *112*, 8293–8307.

[48] E. V. Peris, C. Vicent, V. Martinez-Agramunt, V. Gandhi, C. Larriba-Andaluz, D. Gusev, *Angewandte Chemie Int Ed* **2021**, DOI 10.1002/anie.202100914.

[49] A. Haack, C. Ieritano, W. S. Hopkins, *Analyst* **2023**, *148*, 3257–3273.

[50] S. Cajahuaringa, L. N. Zanotto, D. L. Z. Caetano, S. Rigo, H. Yviquel, M. S. Skaf, G. Araujo, *2022 Ieee 34th Int Symposium Comput Archit High Perform Comput Sbac-pad* **2022**, *00*, 150–159.

[51] F. F. Nielson, S. M. Colby, D. G. Thomas, R. S. Renslow, T. O. Metz, *Anal Chem* **2021**, *93*, 3830–3838.

[52] D. A. Ivashchenko, N. M. F. S. A. Cerqueira, A. L. Magalhães, *Struct Chem* **2021**, *32*, 1993–2005.

[53] S. M. Colby, D. G. Thomas, J. R. Nuñez, D. J. Baxter, K. R. Glaesemann, J. M. Brown, M. A. Pirrung, N. Govind, J. G. Teeguarden, T. O. Metz, R. S. Renslow, *Anal Chem* **2019**, *91*, 4346–4356.

[54] R. Custelcean, *Chem Soc Rev* **2014**, *43*, 1813–1824.

[55] J. Jiao, Z. Li, Z. Qiao, X. Li, Y. Liu, J. Dong, J. Jiang, Y. Cui, *Nat Commun* **2018**, *9*, 4423.

[56] M. Canton, A. B. Grommet, L. Pesce, J. Gemen, S. Li, Y. Diskin-Posner, A. Credi, G. M. Pavan, J. Andréasson, R. Klajn, *J Am Chem Soc* **2020**, *142*, 14557–14565.

[57] L. Pesce, C. Perego, A. B. Grommet, R. Klajn, G. M. Pavan, *J Am Chem Soc* **2020**, *142*, 9792–9802.

[58] D. Samanta, D. Galaktionova, J. Gemen, L. J. W. Shimon, Y. Diskin-Posner, L. Avram, P. Král, R. Klajn, *Nat Commun* **2018**, *9*, 641.

[59] S. H. Ashworth, *Contemp Phys* **2012**, *53*, 372–373.

[60] F. Jensen, *Introduction to Computational Chemistry*, Wiley, **2017**.

[61] C. J. Cramer, *Essentials of Computational Chemistry: Theories and Models*, Wiley, **2004**.

[62] P. Hohenberg, W. Kohn, *Phys Rev* **1964**, *136*, B864–B871.

[63] W. Kohn, L. J. Sham, *Phys Rev* **1965**, *140*, A1133–A1138.

[64] P. Verma, D. G. Truhlar, *Trends Chem* **2020**, *2*, 302–318.

[65] A. D. Becke, *J Chem Phys* **1993**, *98*, 1372–1377.

[66] S. Grimme, *J Chem Phys* **2006**, *124*, 034108.

[67] W. Thiel, *Wiley Interdiscip Rev Comput Mol Sci* **2014**, *4*, 145–157.

[68] N. D. Yilmazer, M. Korth, *Comput Struct Biotechnology J* **2015**, *13*, 169–175.

[69] A. S. Christensen, T. Kubař, Q. Cui, M. Elstner, *Chem Rev* **2016**, *116*, 5301–5337.

[70] C. Bannwarth, S. Ehlert, S. Grimme, *J Chem Theory Comput* **2019**, *15*, 1652–1671.

[71] S. Grimme, A. Hansen, S. Ehlert, J.-M. Mewes, **n.d.**, DOI 10.26434/chemrxiv.13333520.v2.

[72] R. Zhu, J. Lübben, B. Dittrich, G. H. Clever, *Angewandte Chemie Int Ed* **2015**, *54*, 2796–2800.

[73] N. O. B. Lüttschwager, T. N. Wassermann, R. A. Mata, M. A. Suhm, *Angew. Chem. Int. Ed.* **2013**, *52*, 463–466.

[74] A. Klamt, G. Schüürmann, *J Chem Soc Perkin Transactions 2* **1993**, *0*, 799–805.

[75] P. Pracht, F. Bohle, S. Grimme, *Phys Chem Chem Phys Pccp* **2020**, DOI 10.1039/c9cp06869d.

[76] S. Freye, J. Hey, A. Torras-Galán, D. Stalke, R. Herbst-Irmer, M. John, G. H. Clever, *Angew. Chem. Int. Ed.* **2012**, *51*, 2191–2194.

[77] S. Grimme, *Chem Weinheim Der Bergstrasse Ger* **2012**, *18*, 9955–64.

[78] E. Caldeweyher, S. Ehlert, A. Hansen, H. Neugebauer, S. Spicher, C. Bannwarth, S. Grimme, *J Chem Phys* **2019**, *150*, 154122.

[79] O. A. Vydrov, T. V. Voorhis, *J Chem Phys* **2010**, *133*, 244103.

[80] M. Saitow, U. Becker, C. Riplinger, E. F. Valeev, F. Neese, *J Chem Phys* **2017**, *146*, 164105.

[81] A. Altun, F. Neese, G. Bistoni, *J Chem Theory Comput* **2019**, *15*, 5894–5907.

[82] T. Wu, J. Derrick, M. Nahin, X. Chen, C. Larriba-Andaluz, *J Chem Phys* **2018**, *148*, 074102.

[83] K. Wu, J. Tessarolo, A. Baksi, G. H. Clever, *Angew. Chem. Int. Ed.* **2022**, *61*, e202205725.

[84] Th. Förster, K. Kasper, *Z. für Elektrochem., Berichte Bunsenges. für Phys. Chem.* **2010**, *59*, 976–980.

[85] A. Burkhardt, T. Pakendorf, B. Reime, J. Meyer, P. Fischer, N. Stübe, S. Panneerselvam, O. Lorbeer, K. Stachnik, M. Warmer, P. Rödig, D. Göries, A. Meents, *European Phys J Plus* **2016**, *131*, 56.

[86] W. Kabsch, *Acta Crystallogr. Sect. D: Biol. Crystallogr.* **2010**, *66*, 125–132.

[87] L. Potterton, J. Agirre, C. Ballard, K. Cowtan, E. Dodson, P. R. Evans, H. T. Jenkins, R. Keegan, E. Krissinel, K. Stevenson, A. Lebedev, S. J. McNicholas, R. A. Nicholls, M. Noble, N. S. Pannu, C. Roth, G. Sheldrick, P. Skubak, J. Turkenburg, V. Uski, F. von Delft, D. Waterman, K. Wilson, M. Winn, M. Wojdyr, *Acta Crystallogr. Sect. D: Struct. Biol.* **2018**, *74*, 68–84.

[88] G. M. Sheldrick, *Acta Crystallogr. Sect. C: Struct. Chem.* **2015**, *71*, 3–8.

[89] C. B. Hübschle, G. M. Sheldrick, B. Dittrich, *J. Appl. Crystallogr.* **2011**, *44*, 1281–1284.

[90] D. Kratzert, I. Krossing, *J. Appl. Crystallogr.* **2018**, *51*, 928–934.

[91] D. Kratzert, J. J. Holstein, I. Krossing, *J. Appl. Crystallogr.* **2015**, *48*, 933–938.

[92] A. L. Spek, *Acta Crystallogr. Sect. C: Struct. Chem.* **2015**, *71*, 9–18.

[93] A. L. Spek, *Acta Crystallogr. Sect. D* **2009**, *65*, 148–155.

[94] C. Bannwarth, E. Caldeweyher, S. Ehlert, A. Hansen, P. Pracht, J. Seibert, S. Spicher, S. Grimme, *Wiley Interdiscip. Rev.: Comput. Mol. Sci.* **2021**, *11*, DOI 10.1002/wcms.1493.

[95] A. V. Marenich, S. V. Jerome, C. J. Cramer, D. G. Truhlar, *J Chem Theory Comput* **2012**, *8*, 527–541.

[96] S. Grimme, C. Bannwarth, P. Shushkov, *J Chem Theory Comput* **2017**, *13*, 1989–2009.

[97] I. Campuzano, M. F. Bush, C. V. Robinson, C. Beaumont, K. Richardson, H. Kim, H. I. Kim, *Anal Chem* **2012**, *84*, 1026–1033.

[98] J. W. Lee, H. H. L. Lee, K. L. Davidson, M. F. Bush, H. I. Kim, *Analyst* **2018**, *143*, 1786–1796.

[99] M. Han, R. Michel, B. He, Y. Chen, D. Stalke, M. John, G. H. Clever, *Angew. Chem. Int. Ed.* **2013**, *52*, 1319–1323.

[100] F. Neese, *Wiley Interdiscip. Rev.: Comput. Mol. Sci.* **2022**, *12*, DOI 10.1002/wcms.1606.

[101] Y. Guo, C. Riplinger, U. Becker, D. G. Liakos, Y. Minenkov, L. Cavallo, F. Neese, *J Chem Phys* **2018**, *148*, 011101.

[102] S. Tsuzuki, T. Kaneko, K. Sodeyama, *Chem* **2023**, *8*, DOI 10.1002/slct.202203754.

3 Heteroleptic Coordination Cages Containing Dithienylethene Photoswitches

3.1 Introduction

Light is a waste-free, clean, easily accessible stimulus for chemical systems and is therefore of great interest for creating stimuli responsive systems. By now, many supramolecular systems that change their structure or properties upon light irradiation have been developed.[1] For this, photosensitive building blocks are used that, if they are irradiated and switch (meaning a reversible change in constitution, conformation or configuration), they change their role in the self-assembly which thus leads to changes in the whole supramolecular system. One of the most popular photoswitches in supramolecular chemistry is azobenzene (Figure 3.1).[2]

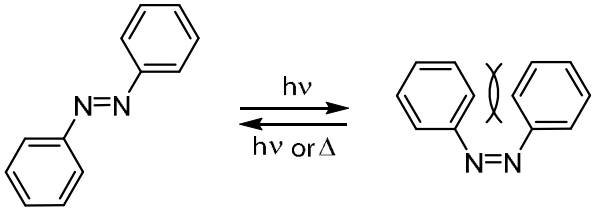

Figure 3.1. *trans*- and *cis*-azobenzene.

The thermodynamically stable *trans* isomer can undergo a change in configuration to the metastable *cis* isomer by irradiation with UV light. *Cis*-azobenzene slowly reacts back to the *trans* isomer upon heating or via irradiation with blue light. One of the reasons why the *cis* isomer is less stable than the *trans* isomer is the steric repulsion of the benzene groups. When azobenzene is used as part of a building block in a supramolecular assembly, its isomerization from *cis* to *trans* usually has a drastic influence on the topology of the whole system as it changes the form of the building block tremendously, as shown by Beves,[3] Nabeshima[4] and Liu[5].

Figure 3.2 gives a brief overview of a recent study by Beves and coworkers.[3] The bis-monodentate ligand has isoquinoline donor groups and an azobenzene backbone. Notably, the azobenzene is modified with electron pulling fluorine groups which alter the photophysical properties and allows nearly quantitative two-way isomerization.[6] When the ligand **L** is in the *trans* form it can self-assemble with Pd^{2+} to a Pd_2*trans*-$\mathbf{L}_4$ cage but irradiation with green light causes isomerization to the *cis* form which prefers a butterfly-like mononuclear Pd*cis*-$\mathbf{L}_2$ topology. Irradiation with purple light or heating reverses the process.

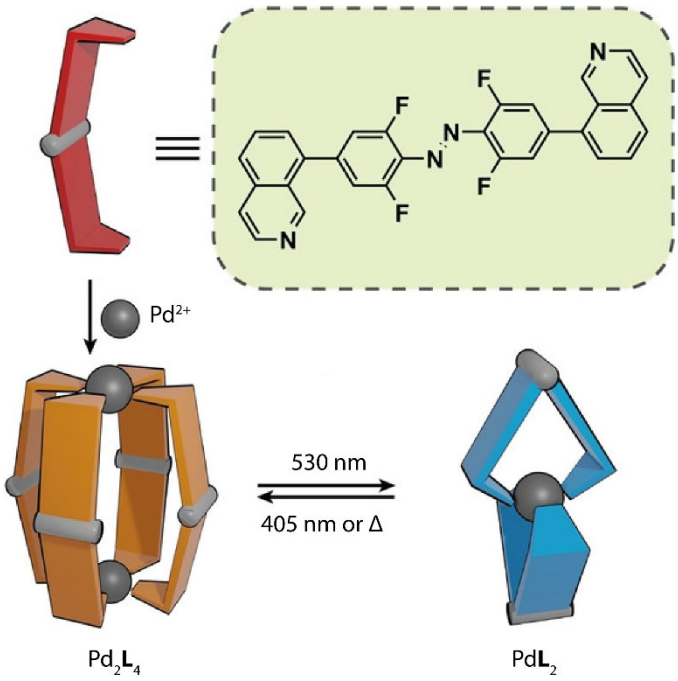

Figure 3.2. Light driven interconversion between a $Pd_2\mathbf{L}_4$ cage and a $Pd\mathbf{L}_2$ butterfly complex where **L** has a modified azobenzene backbone. The graphic was taken from the article and slightly modified. Permission was obtained and is appended in Chapter 5.

Azobenzene can also be incorporated in molecular building blocks in a way that the whole topology of the system is not influenced by the switching event but only certain properties are altered, such as solubility as shown by Fujita[7] and guest binding behavior as shown by Nitschke.[8]

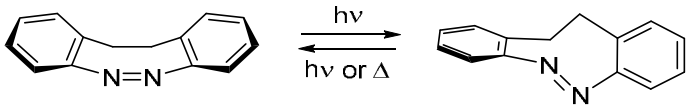

Figure 3.3. *cis*- and *trans*-diazocene.

An alternative is provided by the diazocene class, which shows similarity to azobenzene but here, the *cis* form is the stable isomer and the metastable *trans* form slowly transforms back to the *cis* isomer (Figure 3.3).[9] Just like with *ortho*-fluoroazobenzene the required wavelengths for photoswitching differ from the regular azobenzene. Our group used diazocene as a backbone in a bis-monodentate ligand and showed reversible light-induced switching between a mixture of ring and cage Pd_n*cis*-$\mathbf{L}_{2n}$ ($n \in \{1, 2\}$) and a selectively formed Pd_2*trans*-$\mathbf{L}_4$ cage with different shape which greatly influences the guest binding affinity. This will be discussed in more detail in Chapter 4.[10]

Metastable photoacids are compounds that change their pK_a values upon irradiation, as for example Liao's photoacid.[11] A change in the pH of the solution can greatly influence the coordination bonds and may cause disassembly of any metallosupramolecular construct by protonating the donor functionalities of the ligands as shown by Severin.[12]

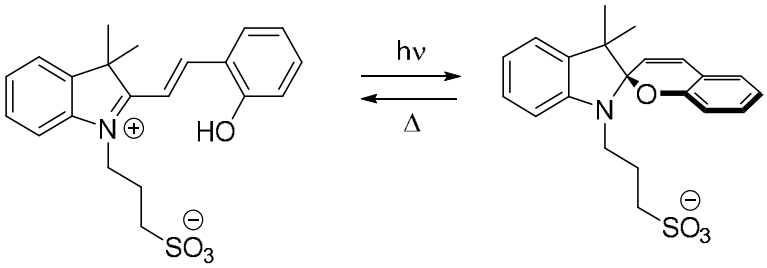

Figure 3.4. Liao's photoacid.

Another popular class of photoswitches are the diarylethenes. Here, excitation with UV light induces a cyclisation reaction including a loss of aromaticity as shown in Figure 3.5. Thienyl groups are often used because the energy penalty for the loss of aromaticity is comparatively low. This makes the photochromic reaction thermally irreversible and fatigue resistant. Using a cyclopentene bridge instead of an ethene bridge also prohibits a competitive *cis* to *trans* isomerization. A hexafluorinated cyclopentene is known to shift the absorption maxima so that the required wavelengths for reaction and back reaction are further apart making it possible to quantitatively populate either one of both states upon irradiation.[13]

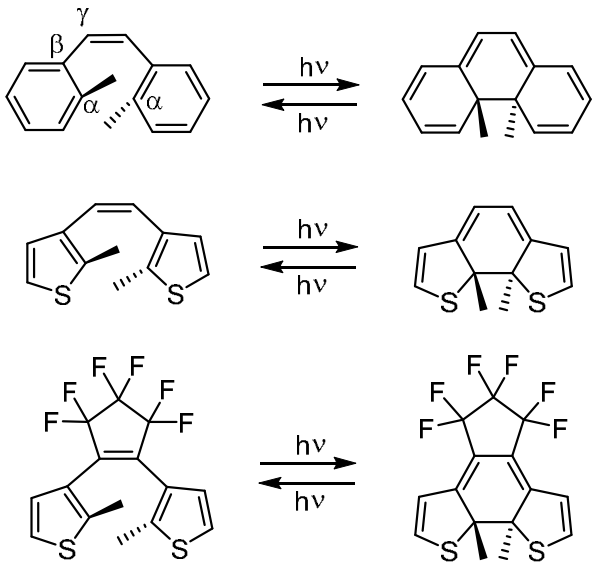

Figure 3.5. Different forms of diarylethene photoswitches. Top: stilbene, middle: dithienylethene, bottom: dithienylperfluorocyclopentene.

As can be seen in Figure 3.6, the orbital flaps at the α carbons, as labeled in Figure 3.5, pointing against each other have the opposite sign for the HOMO but the same sign for the LUMO, which is why bond formation can occur upon photoexcitation. The formed bond closes the six ring which is why this form is called "closed" as opposed to "open". The closed DTE (from now on meaning dithienylperfluorocyclopentene) has several interesting differences to the open DTE. 1) Due to the ring closure, rotation around the bond between the β and the γ carbon is not possible anymore so this

molecule is less flexible. 2) It is chiral with two stereocenters. 3) It is a strong blue chromophore while the open DTE is rather colorless.

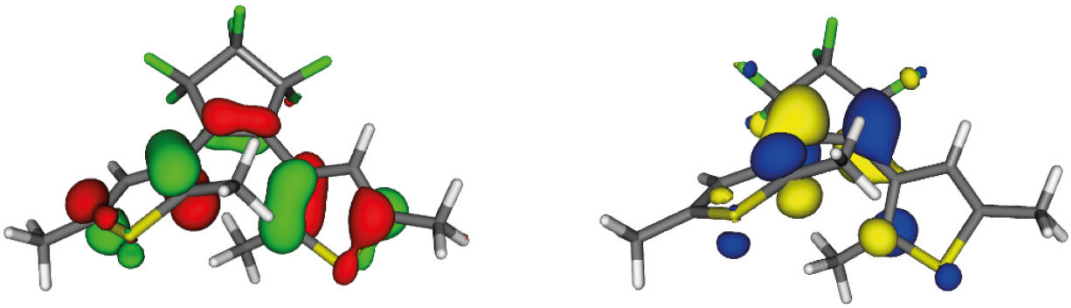

Figure 3.6. HOMO (left) and LUMO (right) of the open DTE photoswitch.

Our group reported the use of DTE as building block in metallosupramolecular chemistry by using it as a backbone for a bent bis-monodentate ligand.[14] The open ligand **o-L^1**, with the DTE in the backbone being in its open form, can switch to the closed isomer **c-L^1** by irradiation with UV light. While the solution of **o-L^1** is colorless, the solution of **c-L^1** is deep blue. The closed ligand can be switched back to the open form by irradiation at 617 nm. After the addition of 0.5 eq. Pd^{2+} to either **o-L^1** or **c-L^1** a Pd_2**L$^1_4$** lantern-shaped cages can be formed. The open and closed cages can also interconvert between each other using the same wavelengths.

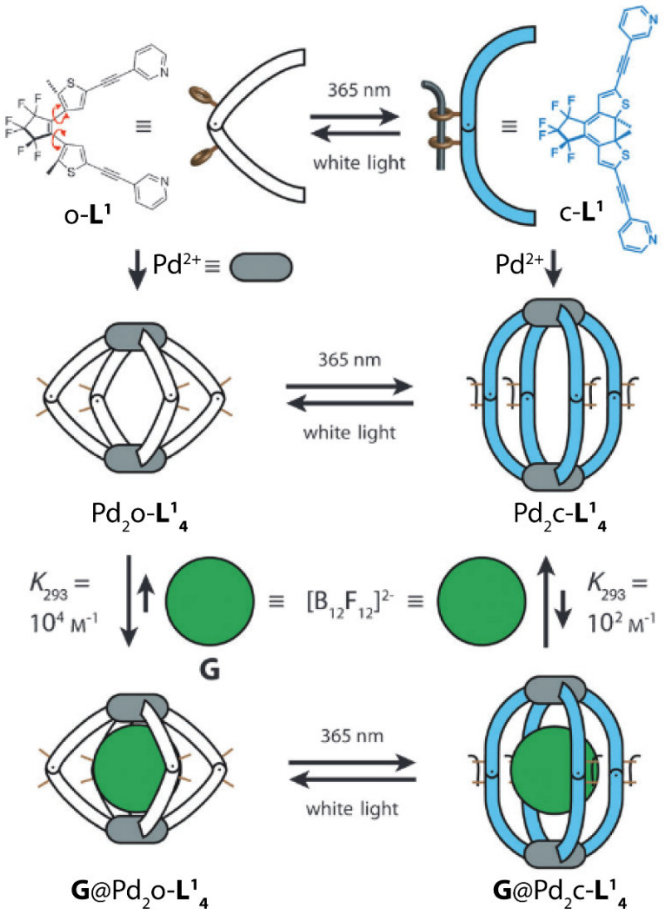

Figure 3.7. First generation DTE ligand **o-L¹** can form a cage which can by irradiation reversibly interconvert to a cage with a less strong binding affinity towards an anionic guest.[14] The graphic was taken from the article and slightly modified. Permission was obtained and is appended in Chapter 5.

The more flexible Pd_2**o-L¹**$_4$ cage has a higher binding affinity towards $B_{12}F_{12}^{2-}$ guest anion than the more rigid Pd_2**c-L¹**$_4$ which is why light can here be used as a clean stimulus for controlled guest release.

The thermodynamics of the guest binding was further investigated by NMR and ITC titrations showing that the guest binding is entropy driven.[15] In the same study a crystal structure of a Pd_2**o-L¹**$_2$**c-L¹**$_2$ could be obtained giving a first idea of an intermediate cage in the switching process. In another follow up study a similar banana shaped DTE ligand and a chiral guest were used to determine the decrease of guest binding affinity by successive ligand switching.[16] It could be shown that already after switching the first of the four ligands from open to close drastically reduces the binding affinity. Schäfer and coworkers investigated the system computationally using MD simulations and could confirm both that the guest encapsulation is entropy driven and that the first switching event has the largest effect on the binding affinity.[17] The group of Nuernberger exploited ultrafast spectroscopy to investigate the influence of different guests and the binding to the Pd on the switching dynamics.[18] Su et al. reported a cage with DTE based ligands where photoswitching can induce aggregation and gelation.[19] In 2021

our group published a complex multi-stimuli-responsive system based on DTE cages and even first reported selectively formed heteroleptic cages with DTE ligands.[20]

Of special interest for this work is the study on a shorter ligand with pyridine donor groups directly at the DTE backbone as shown in Figure 3.8.[21] The closed form, here labeled as **c-L^{DTE}**, has a computed binding angle of 138° and self-assembles with palladium(II) cations to a Pd_{24} **c-L^{DTE}**$_{48}$ rhombicuboctahedral sphere, matching Fujita's observations of the relation between binding angle and Palladium ligand stoichiometry of these giant spheres.[22,23]

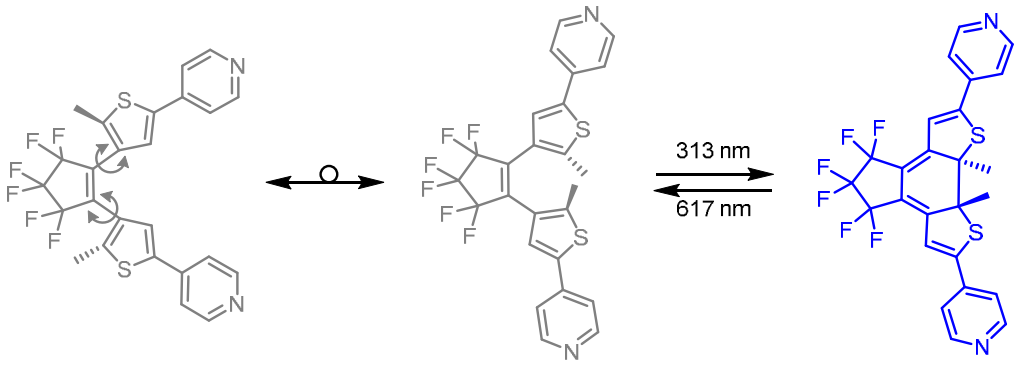

Figure 3.8. Second generation DTE ligand in its open form (left and middle, grey) **o-L^{DTE}** showing its rotational freedom and in its closed form (right, blue) **c-L^{DTE}**.[21]

The open form **o-L^{DTE}**, however, forms upon addition of Pd^{2+} a mixture of a Pd_3**o-L^{DTE}**$_6$ and a Pd_4**o-L^{DTE}**$_8$ ring with the three-ring being the major species. Due to its flexibility, it can vary its binding angle and is therefore able to form smaller assemblies, which are entropically favored. As Figure 3.8 shows, rotation around the σ bonds connecting the perfluorocyclopentene with the thienyl groups also changes the distance between the α carbon atoms that undergo the bond formation upon irradiation. This means that if the ligand is in a conformation as shown on the far left side of the scheme, it is unable to photoswitch to the closed form, simply because the atoms are too far apart and the orbitals cannot overlap. Our group showed that irradiation with light of 313 nm wavelength for several hours is necessary to transform the mixture of Pd_3**o-L^{DTE}**$_6$ and a Pd_4**o-L^{DTE}**$_8$ to the Pd_{24}**o-L^{DTE}**$_{48}$ sphere because in these assemblies the ligand is unable to change its conformation to make photoswitching possible. Only after random breaking of at least one of the dynamic pyridine–palladium bonds the ligand can rotate in a position necessary for bond formation upon irradiation.

3.2 Motivation

Photoswitch moieties make coordination cages structurally responsive to the clean stimulus light, which can influence certain properties like guest binding strength. Of high interest would be the combination of this function with another function like sensing or catalysis within the same cage. If for a catalytic reaction guest binding inside the cage is required, the catalysis could be switched on or off

by irradiation, which could also be a solution for the problem of product inhibition.[24] For applying two or more functions to a coordination cage it is almost necessary that the cage consists of more than one type of ligand, meaning a heteroleptic instead of a homoleptic cage as mentioned in the main introduction.

Shape complementarity is a valuable tool for creating heteroleptic coordination cages selectively.[25] A well working method for creating heteroleptic *cis*-$Pd_2\mathbf{L}^{\mathbf{A}}{}_2\mathbf{L}^{\mathbf{B}}{}_2$ cages is the use of two oversized ligands $\mathbf{L}^{\mathbf{A}}$ with negative binding angles and two undersized ligands $\mathbf{L}^{\mathbf{B}}$ with positive binding angles. $\mathbf{L}^{\mathbf{A}}$ alone tends to form homoleptic $Pd_2\mathbf{L}^{\mathbf{A}}{}_4$ cages that are helically twisted and $\mathbf{L}^{\mathbf{B}}$ tends to form either $Pd_3\mathbf{L}^{\mathbf{B}}{}_6$ or $Pd_4\mathbf{L}^{\mathbf{B}}{}_8$ rings or $Pd_4\mathbf{L}^{\mathbf{B}}{}_8$ tetrahedra.[25] The similarity to **o-L**$^{\mathbf{DTE}}$ is thus given, because **o-L**$^{\mathbf{DTE}}$ forms $Pd_3\mathbf{L}^{\mathbf{B}}{}_6$ and $Pd_4\mathbf{L}^{\mathbf{B}}{}_8$ rings as well. It is therefore interesting to investigate whether **o-L**$^{\mathbf{DTE}}$ and maybe even **c-L**$^{\mathbf{DTE}}$ can form a heteroleptic cage with another shape-complementary ligand and how the switching behavior changes. A possible match for **o-L**$^{\mathbf{DTE}}$ is shown in Figure 3.9 ($\mathbf{L}^{\mathbf{C}}$, labeled $\mathbf{L}^{\mathbf{hex}}$ in Chapter 2). An alternative to Pd_2L_4 cages could be heteroleptic Pd_3L_6 or Pd_4L_8 rings or Pd_4L_8 tetrahedra with other ligands that have small binding angles just as **o-L**$^{\mathbf{DTE}}$. However, here the problem could be the selectivity, as there may be no driving force to form one discrete species with a specific arrangement of the ligands. Figure 3.9 also shows a ligand with a positive binding angle ($\mathbf{L}^{\mathbf{P}}$). $\mathbf{L}^{\mathbf{C}}$ and $\mathbf{L}^{\mathbf{P}}$ combined with Palladium form the cage $Pd_2\mathbf{L}^{\mathbf{P}}{}_2\mathbf{L}^{\mathbf{C}}{}_2$ selectively and they have shown to form heteroleptic cages with other ligands as well.[26]

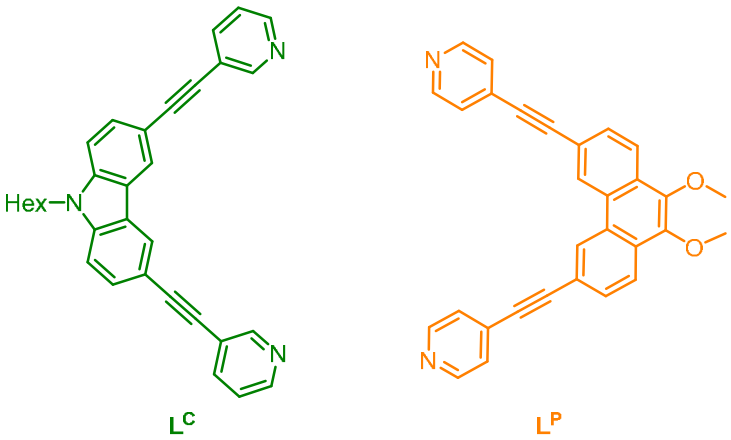

Figure 3.9. A bis-monodentate ligand with a slightly negative binding angle (left, $\mathbf{L}^{\mathbf{C}}$) and a bis-monodentate ligand with a positive binding angle (right, $\mathbf{L}^{\mathbf{P}}$). Together they form the heteroleptic *cis*-$Pd_2\mathbf{L}^{\mathbf{C}}{}_2\mathbf{L}^{\mathbf{P}}{}_2$ selectively.

Of special interest would also be a heteroleptic cage with the closed DTE ligand **c-L**$^{\mathbf{DTE}}$. To our knowledge, a heteroleptic cage from a combination of an oversized ligand with negative binding angle and a ligand with large positive binding angle over 120° has not been reported yet but a combination with $\mathbf{L}^{\mathbf{P}}$ could be possible because the sum of two times the binding angle of **c-L**$^{\mathbf{DTE}}$ (138°) and two times the binding angle of $\mathbf{L}^{\mathbf{P}}$ (60°) is 396°, which close to the sum of angles of a quadrilateral or more specific a rhombus. Mukherjee and coworkers first reported a heteroleptic triangular prism formed by

combination of a bis-monodentate ligand with a small binding angle with a ligand with a large binding angle.[27] Severin and coworkers also reported triangular prism, a rectangular cuboid and a triangular anti-prism.[28,29] Hence, these examples demonstrate that achieving such a geometry with **c-L^{DTE}** may be possible and worth studying.

3.3 Results and Discussion

3.3.1 Combination of o-L^{DTE} with L^{C}

A heteroleptic cage with two times **o-L^{DTE}** and two times **L^{C}** could be formed, although not selectively as both homoleptic species could still be detected. Figure 3.10 shows the ^{1}H NMR spectrum with assignments. Further analyses including 2D NMR spectra, ESI mass and ion mobility spectra are shown in the experimental section. As an explanation for the observed low selectivity could be that the shapes of **o-L^{DTE}** and **L^{C}** are not matching well enough. While **o-L^{DTE}** can vary its binding angle, the variation also changes the distance between the two nitrogen atoms in the pyridine donor groups. A compromise has to be found between the optimal binding angle and the optimal N–N distance. Much more flexibility is given in the homoleptic Pd$_3$**o-L^{DTE}**$_6$, where all ligands can greatly vary their binding angle.

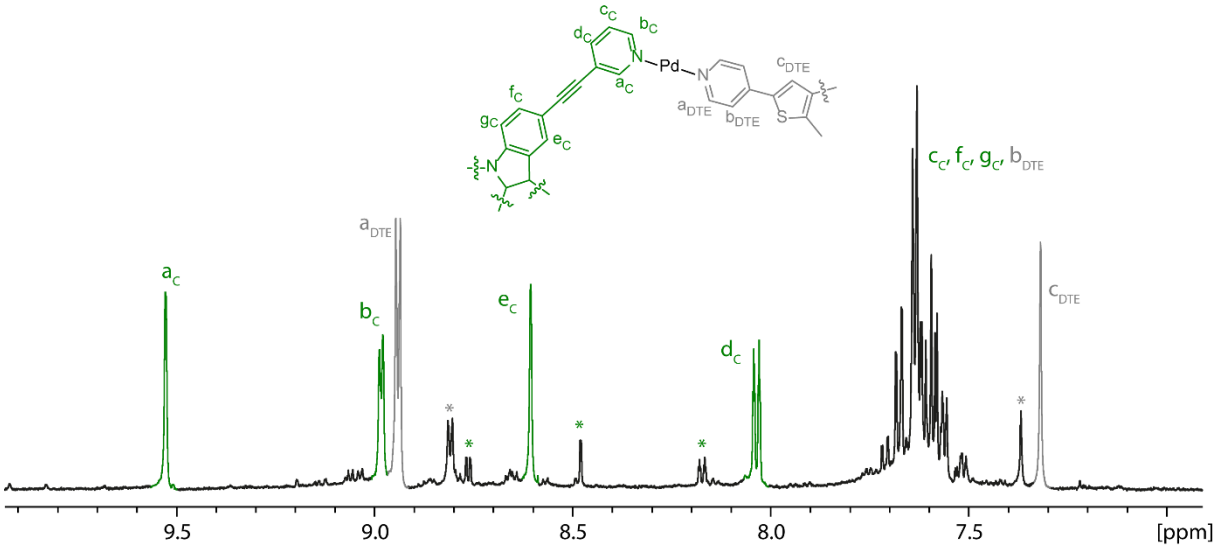

Figure 3.10. Partial ^{1}H NMR spectrum (600 MHz) of Pd$_2$**o-L^{DTE}**$_2$**L^{C}**$_2$. Homoleptic species are marked with asterisks in green for Pd$_2$**L^{C}**$_4$ and grey for Pd$_3$**o-L^{DTE}**$_6$.

Figure 3.11 shows a model of the proposed structure as a crystal structure could not be obtained. In the proposed structure of Pd$_2$**o-L^{DTE}**$_2$**L^{C}**$_2$ the ligands are in *cis* position because of simple geometric considerations, past experiences with these binding angles and because it was not possible to realistically model a tentative *trans*-Pd$_2$**o-L^{DTE}**$_2$**L^{C}**$_2$ isomer. The two different ligands seem to match perfectly; only a slight bend at the alkyne linkers of **L^{C}** is observed. As can be seen in Figure 3.11, the thienyl groups are twisted in a way that the two α-carbon atoms, that could undergo a bond formation

upon irradiation, are far apart, as it was proposed for the Pd_3**o-L**$^{DTE}{}_3$ ring, and thus the behavior upon irradiation is presumed to be the same.

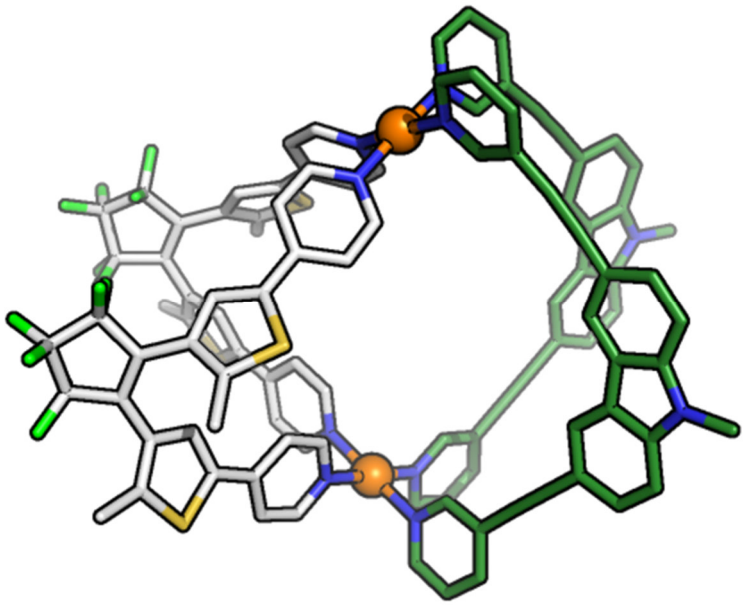

Figure 3.11. Geometry optimized model (r^2SCAN-3c) of cis-Pd_2**o-L**$^{DTE}{}_2$**L**$^{C}{}_2$. Hydrogen atoms omitted and hexyl chains replaced by methyl groups for clarity.

Indeed, upon irradiation with 313 nm under the same conditions (10 min irradiation with Hg lamp, see Chapter 5 for details) that leads to full conversion of only the ligand **o-L**^{DTE} to **c-L**^{DTE}, no change in the ^{1}H NMR spectrum could be observed except for the appearance of very minor signals of **c-L**^{DTE} and a slight change of the solution's color to light blue (Figure 3.29).

3.3.2 Combination of o-L^{DTE} with L^{P}

Combining **o-L**^{DTE} with **L**^{P} and $[Pd(CH_3CN)_4](BF_4)_2$ resulted in a broad ^{1}H NMR spectrum with no identifiable species, as shown in the experimental section (Figure 3.31). Analysis with mass spectrometry reveals that the mixture contains Pd_3 species with all possible ratios of **o-L**^{DTE} and **L**^{P}, ranging from Pd_3**o-L**$^{DTE}{}_6$**L**$^{P}{}_0$ to Pd_3**o-L**$^{DTE}{}_0$**L**$^{P}{}_6$, see Figure 3.12. No Pd_4 species could be detected.

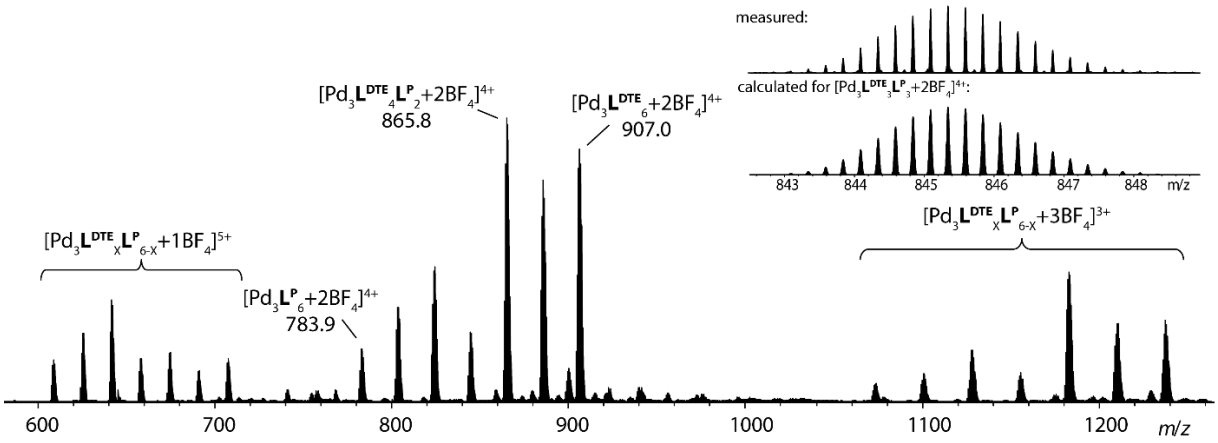

Figure 3.12. ESI mass spectrum of Pd_3**o-L**$^{DTE}_{X}$**L**$^{P}_{X-6}$.

More than seven different Pd_3 species are possible when combining **o-L**^{DTE} and **L**^{P}, because three different stereoisomers of Pd_3**o-L**$^{DTE}_4$**L**$^{P}_2$, Pd_3**o-L**$^{DTE}_3$**L**$^{P}_3$ and Pd_3**o-L**$^{DTE}_2$**L**$^{P}_4$ could exist each. Figure 3.13 shows all 13 possible combinations schematically.

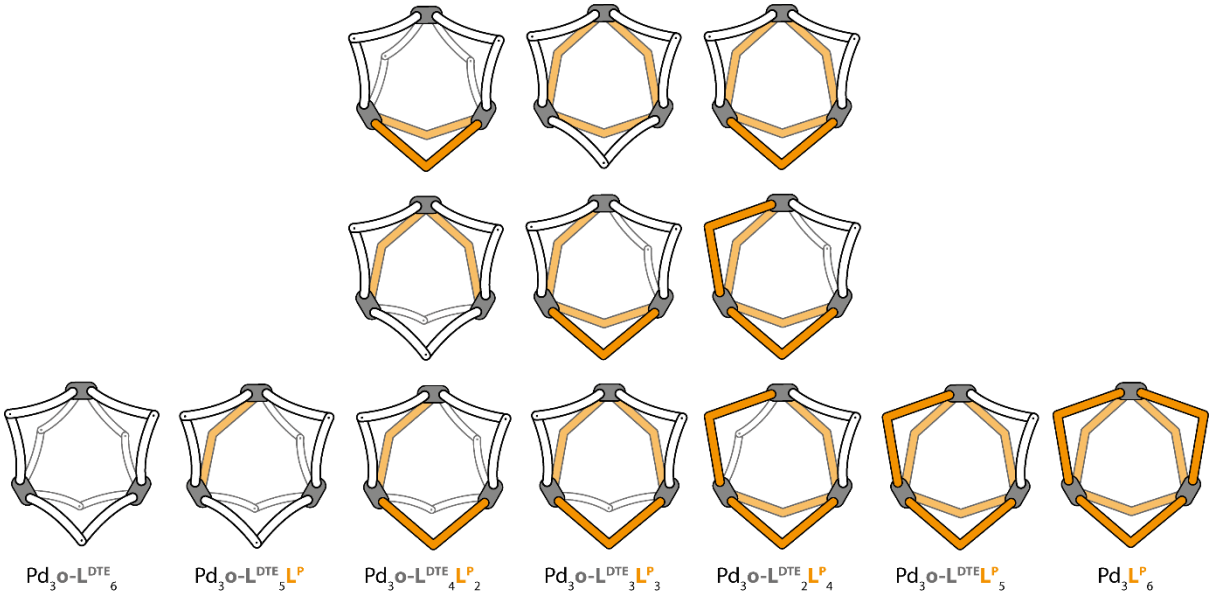

Figure 3.13. Schematical representation of all 13 possible combinations of **L**^{DTE} and **L**^{P} as Pd_3 rings.

The ion mobilities of the mixture were measured via TIMS and converted to $^{TIMS}CCS_{N2}$ which are shown in Figure 3.14. As expected, the CCS increases with increasing amount of the larger **L**^{P} in the ring. For the homoleptic rings and for the rings containing five of the one and only one of the other ligand a clear Gauss-shaped signal is observed, which also matches the expectation that only one isomer of each of these ratios is present. Interestingly, also Pd_3**o-L**$^{DTE}_3$**L**$^{P}_3$ and Pd_3**o-L**$^{DTE}_2$**L**$^{P}_4$ show Gauss-shaped signals without shoulders, even though up to three signals could be expected, see Figure 3.13. But for Pd_3**o-L**$^{DTE}_4$**L**$^{P}_2$ an overlap of two signals is observed indicating that two isomers out of three possible are present.

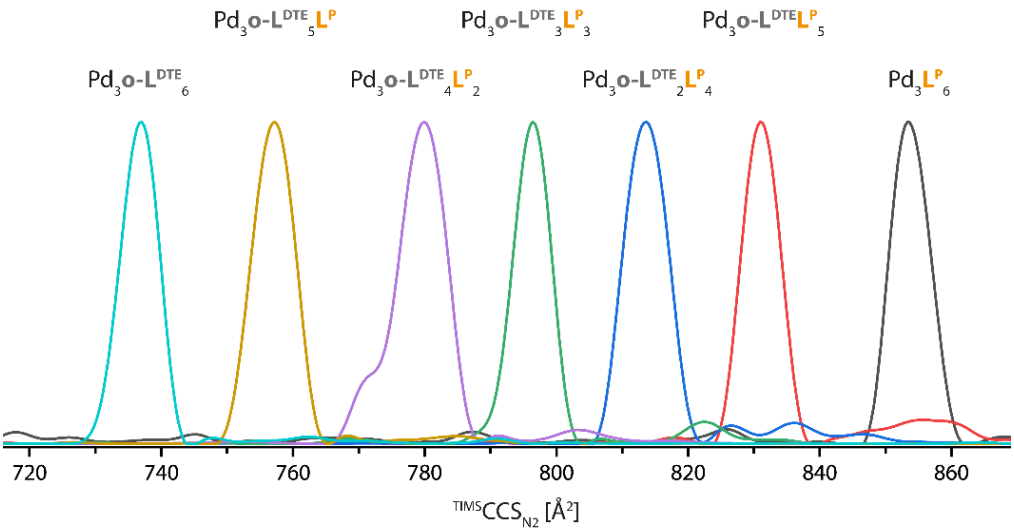

Figure 3.14. Overlaid TIMS mobilograms of Pd_3**o-L**$^{DTE}_X$**L**$^{P}_{X\text{-}6}$ (X ϵ {0,…,6}). Inverse mobilities were normalized and converted into CCS values. All species shown have two BF_4^- counter anions and thus an overall positive charge of 4.

While it remains unclear which of the isomer(s) of the Pd_3**o-L**$^{DTE}_X$**L**$^{P}_{X\text{-}6}$ (*X* ϵ {2,…,4}) are present in the mixture, a possible explanation could be that the species in which two **o-L**^{DTE} bridge the same two Pd^{2+} centers and are thus on the same edge of the three-ring are thermodynamically favored. **o-L**^{DTE} is both shorter and more flexible than **L**^{P}, which should cause a shorter Pd–Pd distance, when these are bridged by two **o-L**^{DTE} ligands. This increases the probability of a BF_4^- being between both Pd^{2+} centers due to electrostatic interactions causing a templation effect. Both, for Pd_3**o-L**$^{DTE}_3$**L**$^{P}_3$ and Pd_3**o-L**$^{DTE}_2$**L**$^{P}_4$, only one isomer with **o-L**^{DTE} on the same edge is possible (see Figure 3.13, second row, fourth and fifth column). For Pd_3**o-L**$^{DTE}_4$**L**$^{P}_2$, all three possible isomers feature edges bridged by two DTE-based ligands, but only two species could be detected by TIMS. Here, one isomer even has two pairs of **o-L**^{DTE} bridging the same two Pd^{2+} centers (first row in Figure 3.13) which may be more likely to be one of the observed isomers. Theoretical CCS calculations ($^{theo}CCS_{N2}$) were conducted to further investigate which species are present in solution and to test the accuracy of the newly developed workflow as described in Chapter 2, however, only suggestions can be made in this case due to still improvable accuracy of the theoretical CCS calculation, see Section 3.5.3.

Just as for Pd_2**o-L**$^{DTE}_2$**L**$^{C}_2$, the photoswitching behavior of Pd_3**o-L**$^{DTE}_X$**L**$^{P}_{X\text{-}6}$ was tested. Irradiation with UV light under the same conditions was conducted also leading to no significant change in the NMR, which again shows the similarity to the homoleptic Pd_3**o-L**$^{DTE}_6$ in terms of abolished photoswitching ability.

3.3.3 Combination of c-L^{DTE} with L^{P}

With the aim to form a heteroleptic Pd_6 or Pd_8 species, **c-L**^{DTE} was combined with **L**^{P} and $[Pd(CH_3CN)_4](BF_4)_2$ in acetonitrile. The resulting ^{1}H NMR spectrum is similar to that of the giant Pd_{24}**c-**

$\mathbf{L^{DTE}}_{48}$ sphere and shows multiple broad signals as well. The broadening is explained by diffusion effects, often leading to NMR signal broadening of such large species, and by the large amount of diastereomers of Pd_{24}**c-L**$^{DTE}_{48}$ due to **c-L**^{DTE} being chiral but racemic.[21] The spectrum from the combination of ligands does, however, slightly differ in regards to shape, size and number of aromatic signals as Figure ***3.15*** shows. Sharp signals matching those of homoleptic $Pd_3\mathbf{L^P}_6$ are observed and also the three broad signals of Pd_{24}**c-L**$^{DTE}_{48}$ seem to appear in this spectrum, although they have slightly different shape. Interestingly, another broad signal around 8.25 ppm is observed and it is overlapping with the signal belonging to proton *e* of $\mathbf{L^P}$. Signals that match proton signals in the homoleptic $Pd_3\mathbf{L^P}_6$ but are broadened indicate that these protons belong to assemblies of which many different diastereomers exist as it would be expected for Pd_6**c-L**$^{DTE}_6\mathbf{L^P}_6$ or Pd_8**c-L**$^{DTE}_8\mathbf{L^P}_8$ (2^6 or 2^8 diastereomers, respectively).

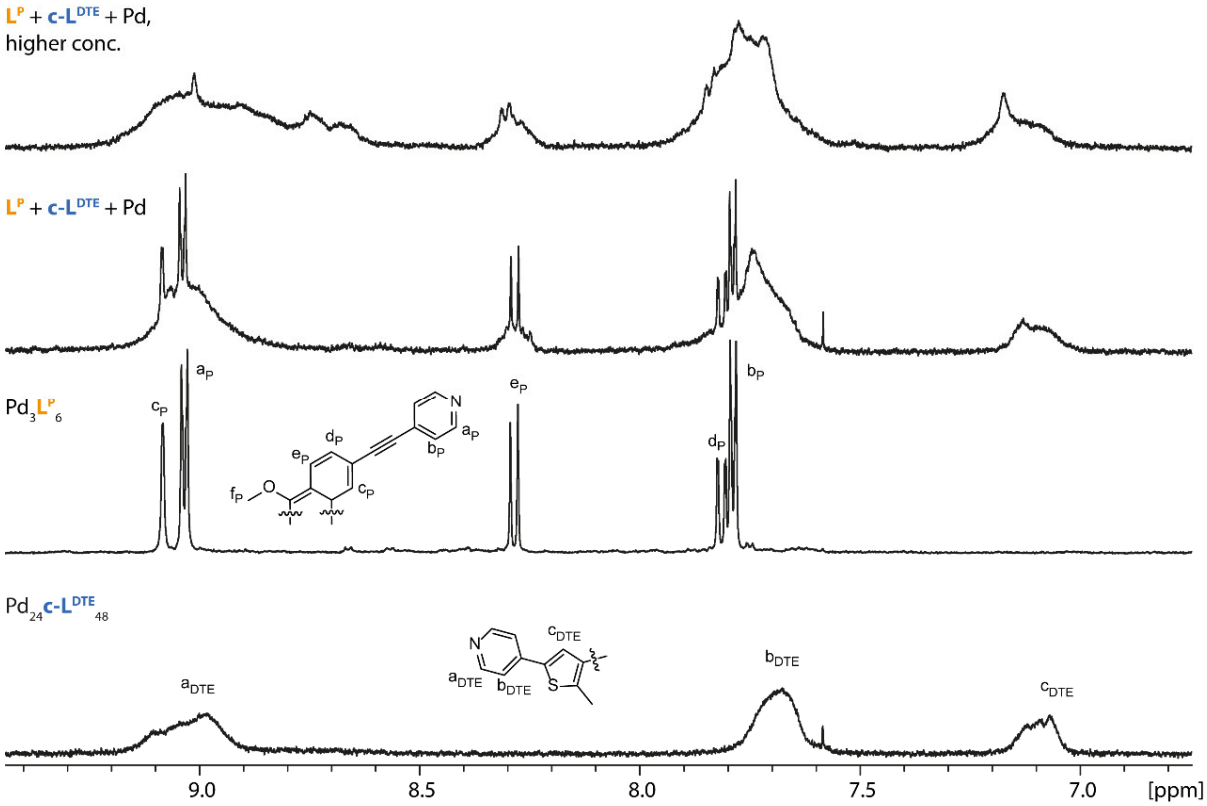

Figure 3.15. Aromatic region of ^{1}H NMR spectra of homoleptic Pd_{24}**c-L**$^{DTE}_{48}$ and $Pd_3\mathbf{L^P}_6$ as well as combination of **c-L**^{DTE}, $\mathbf{L^P}$ and Pd^{2+} with regular (c_{LDTE} = c_{LP} = 0.8 mM) and high (c_{LDTE} = c_{LP} = 1.91 mM) concentration.

With mass spectrometry indeed the existence of a Pd_6**c-L**$^{DTE}_6\mathbf{L^P}_6$ next to a $Pd_3\mathbf{L^P}_6$ species could be proven (Figure **3.35**). Similar to Pd_2**o-L**$^{DTE}_2\mathbf{L^C}_2$ this heteroleptic species seems to be in a thermodynamic equilibrium with the two homoleptic variants:

$$8\ Pd_3\mathbf{L^P}_6 + Pd_{24}\textbf{c-L}^{DTE}_{48} \rightleftharpoons 8\ Pd_6\textbf{c-L}^{DTE}_6\mathbf{L^P}_6 \rightleftharpoons 6\ Pd_8\textbf{c-L}^{DTE}_8\mathbf{L^P}_8$$

As the equation shows, if the heteroleptic Pd_6**c-L**$^{DTE}{}_6$**L**$^{P}{}_6$ species is formed, slightly fewer overall species are present (eight instead of nine equivalents), meaning that the left side is entropically favored in this regard. In the case of a hypothetical Pd_8**c-L**$^{DTE}{}_8$**L**$^{P}{}_8$ only 6 equivalents would be present. The formation of heteroleptic species was tried again but with slightly higher concentrations ($c_{LDTE} = c_{LP} = c_{Pd}$ = 1.91 mM instead of 0.8 mM). This small increase in concentration had a significant influence as now sharp signals of Pd_3**L**$^{P}{}_6$ are not clearly visible in the ^{1}H NMR spectrum anymore (Figure 3.15).

As mentioned before, two topologies with the stoichiometry Pd_6**c-L**$^{DTE}{}_6$**L**$^{P}{}_6$ have been reported before, which are a triangular prism and a triangular anti-prism. Each body has two different edges which leads to four different possible topologies for this heteroleptic assembly. However, due to the ligand's binding angles it was only possible to model one prism and one anti-prism, which are both shown in Figure ***3.16***. For the prism three **c-L**^{DTE} each form the upper and lower triangle and six **L**^{P} are at the sides. For the anti-prism it is vice versa.

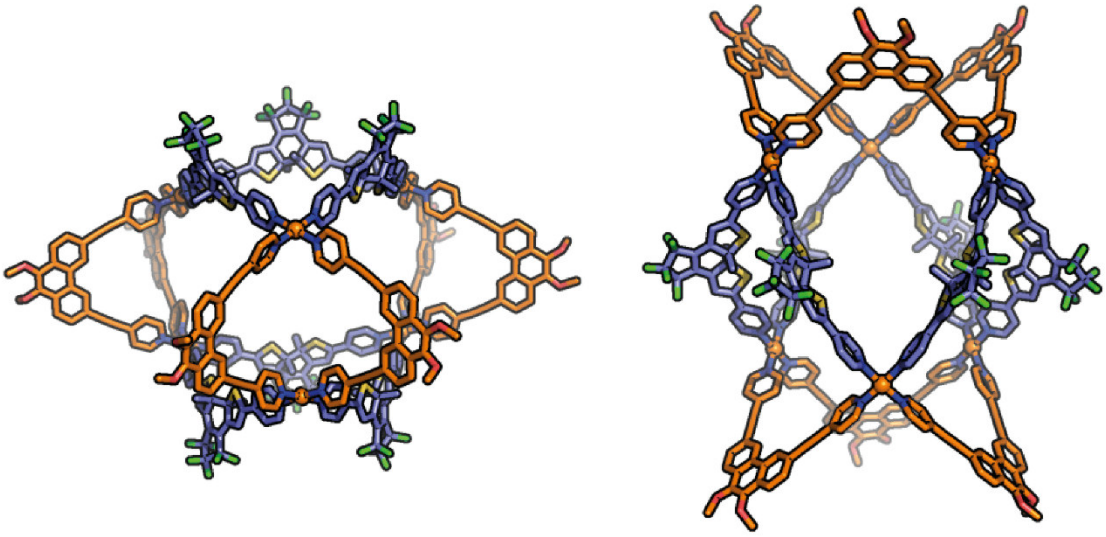

Figure 3.16. Geometry optimized models (r^{2}SCAN-3c) of two possible topologies of Pd_6**c-L**$^{DTE}{}_6$**L**$^{P}{}_6$. Left: prism, right anti-prism. Hydrogen atoms omitted for clarity.

For an indication on the correct topology ion mobility spectra were tried to obtain which was unfortunately unsuccessful, likely due to fragmentation, which is a common problem for large metallosupramolecular complexes.[21] The $^{theo}CCS_{N2}$ of prism and anti-prism of multiple Pd_6**c-L**$^{DTE}{}_6$**L**$^{P}{}_6$ species were calculated anyway and surprisingly the outcome for both topologies are almost identical even though the shape is quite different, see Table 3.4. Simple DFT energy calculations (ωB97M-D4/def2-TZVP) without counter anions and implicit solvent were performed on the optimized models. The energy for the prism is by 136 kJ/mol lower, which can either be contributed to different distances between the twofold positively charged Pd centers or strains of the ligands. In a control experiment in

which only the six Pd(pyridine)$^{2+}$ units are considered the prism is favored by 130 kJ/mol showing that the Coulomb repulsion causes this high energy difference. It remains unclear to what degree this repulsion is dampened by solvent and counter anions, still, these results suggests that the prism forms more likely than the anti-prism.

3.3.4 Switching behavior of complex mixtures containing DTE ligands

A solution to the inability of Pd_3**o-L^{DTE}**$_6$ to photoswitch in comparison to the free ligand **o-L^{DTE}** could be the use of less than 0.5 equivalent of palladium, which leads to a mixture of three-ring (and four-ring) and free ligand. The experiment was conducted using only 0.33 eq $[Pd(CH_3CN)_4](BF_4)_2$ and the ^{1}H NMR spectrum of the expected mixture containing Pd_3**o-L^{DTE}**$_6$ and free **o-L^{DTE}** can be seen in Figure 3.17. Irradiation of the sample with UV light and subsequent heating to reach thermodynamic equilibrium leads to the almost full conversion of free **o-L^{DTE}** to free **c-L^{DTE}**. Pd_3**o-L^{DTE}**$_6$ remains unchanged and interestingly, no indications for the existence of Pd_{24}**c-L^{DTE}**$_{48}$ can be seen in the spectrum. While **c-L^{DTE}** could also bind to the palladium and would therefore be competitive to **o-L^{DTE}**, the smaller assembly Pd_3**o-L^{DTE}**$_6$ is entropically favored over the large sphere. A full switch of all bound or unbound **o-L^{DTE}** to the closed form can therefore not be achieved using only short irradiation times.

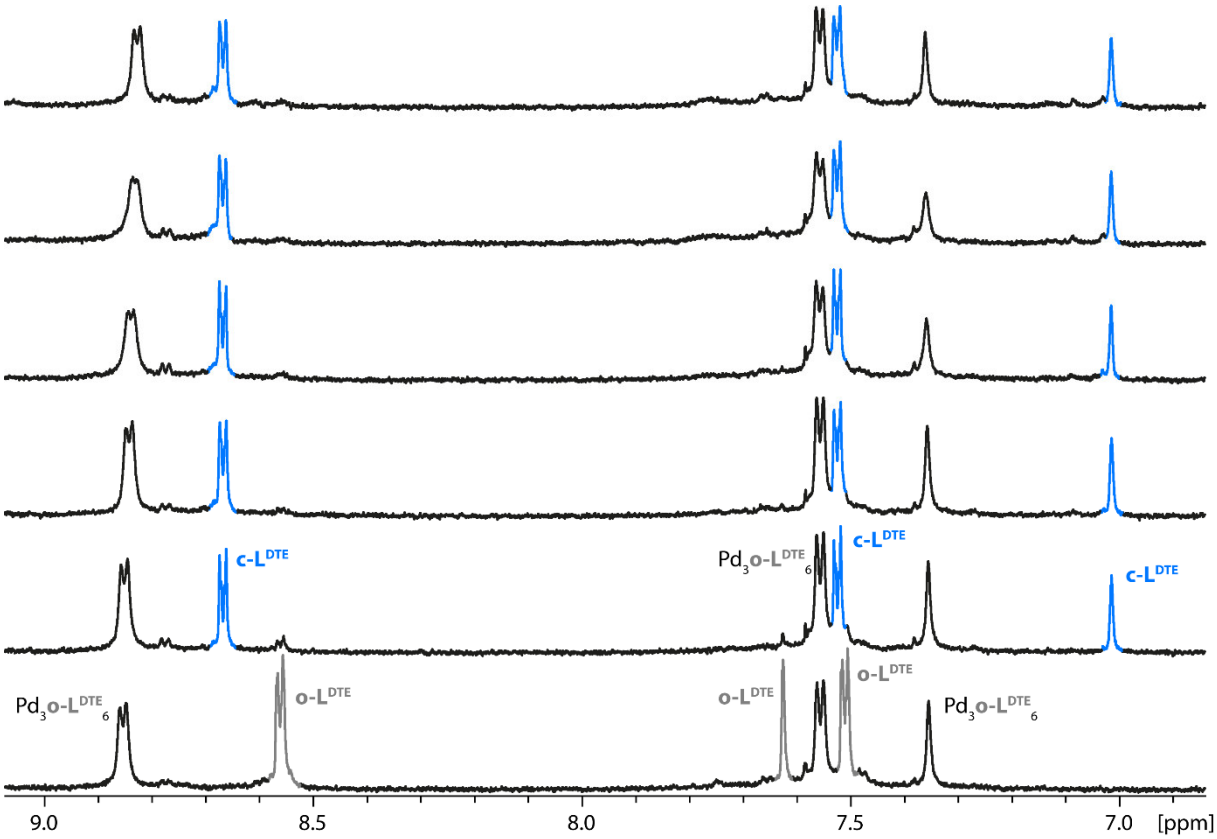

Figure 3.17. Irradiation experiment of mixture of Pd_3**o-L^{DTE}**$_6$ and free ligand **o-L^{DTE}** (using 0.33 eq Pd). Each step: 5 min irradiation at 313 nm, then 70 °C for 1 h.

The experiment was repeated for heteroleptic Pd_2**o-L**$^{DTE}{}_2$**L**$^{C}{}_2$ starting from a mixture of 0.5 eq. **o-L**^{DTE}, 0.5 eq. **L**^{C} and 0.33 eq. $[Pd(CH_3CN)_4](BF_4)_2$. The resulting ^{1}H NMR spectrum (Figure 3.19) shows the signals of Pd_2**o-L**$^{DTE}{}_2$**L**$^{C}{}_2$, free ligands **o-L**^{DTE} and **L**^{C} and minor signals of homoleptic Pd_3**o-L**$^{DTE}{}_6$ and Pd_2**L**$^{C}{}_4$. After irradiation and subsequent heating, the spectrum still shows Pd_2**o-L**$^{DTE}{}_2$**L**$^{C}{}_2$ but with a lower intensity. Also, the signals of free **L**^{C} and **o-L**^{DTE} and homoleptic Pd_3**o-L**$^{DTE}{}_6$ drop in intensity, while the signals for homoleptic Pd_2**L**$^{C}{}_4$ increase and signals belonging to **c-L**^{DTE} appear. The irradiation converts the free **o-L**^{DTE} to **c-L**^{DTE} which changes the overall ratio of **o-L**^{DTE} and **L**^{C} in solution. Subsequent heating (70 °C) leads to re-equilibration of the system including a shift from Pd_2**o-L**$^{DTE}{}_2$**L**$^{C}{}_2$ to Pd_2**L**$^{C}{}_4$, release of free **o-L**^{DTE} and decrease of free **L**^{C}. **c-L**^{DTE} remains non-competitive, just like in the previous experiment. The freed **o-L**^{DTE} can be converted by irradiation again and the heating causes a further release of free **o-L**^{DTE}. After several cycles only homoleptic Pd_2**L**$^{C}{}_4$ and free **c-L**^{DTE} can be detected by ^{1}H NMR, showing that in presence of another, competitive ligand, here **L**^{C}, full conversion can be achieved. Interesting here is also the change in concentrations of Pd_2**L**$^{C}{}_4$ and free **c-L**^{C} upon irradiation even though **L**^{C} is not a photoswitch. This shows the interconnection between the different substrates of this complex system.

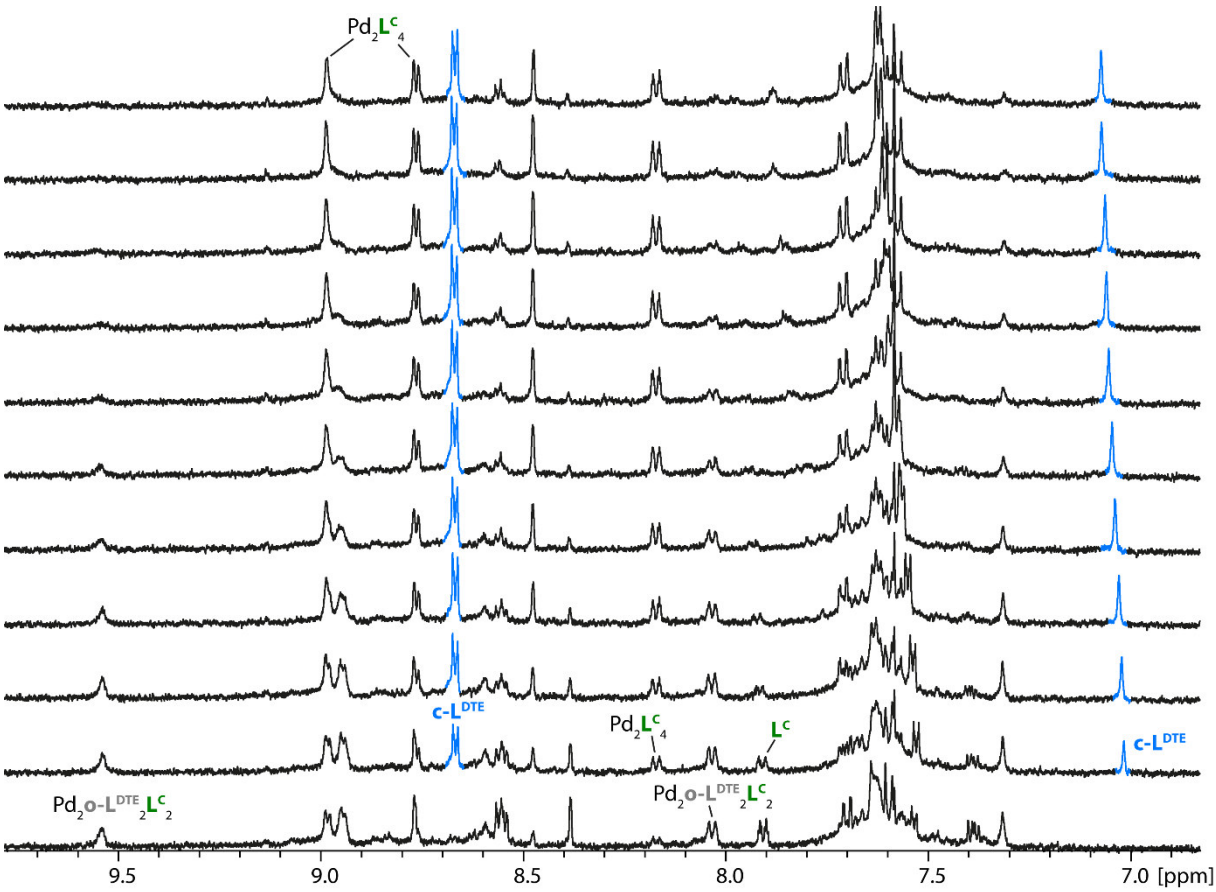

Figure 3.18. Irradiation experiment of mixture of Pd_2**o-L**$^{DTE}{}_2$**L**$^{C}{}_2$ and free ligands **o-L**^{DTE} and **L**^{C}. Each step: 5 min irradiation at 313 nm, then 70 °C for 1 h.

The experiment done with the mixture of heteroleptic Pd_3**o-L**$^{DTE}_{X}$**L**$^{P}_{X-6}$ rings and free ligands **o-L**^{DTE} and **L**^{P} provides similar outcome. Figure 3.19 shows the according ^{1}H spectra. The observation is as expected: Each cycle of irradiation and heating leads to lower concentrations of heteroleptic rings and free **o-L**^{DTE} and **L**^{P} and higher concentrations of homoleptic Pd_3**L**$^{P}_{6}$ and free **c-L**^{DTE}. After several cycles the signal intensity of **o-L**^{DTE} is very low and further irradiation does not lead to further noticeable changes, even though heteroleptic species are still detectable by NMR. In the mass spectrum only Pd_3**L**$^{P}_{6}$, Pd_3**o-L**^{DTE}**L**$^{P}_{6}$ and Pd_3**o-L**$^{DTE}_{2}$**L**$^{P}_{6}$ appear as significant signals, see Figure 3.32. The Pd_6 species could not be detected in the mass spectrum, probably because of the deficiency of palladium in solution only the smaller assemblies are formed.

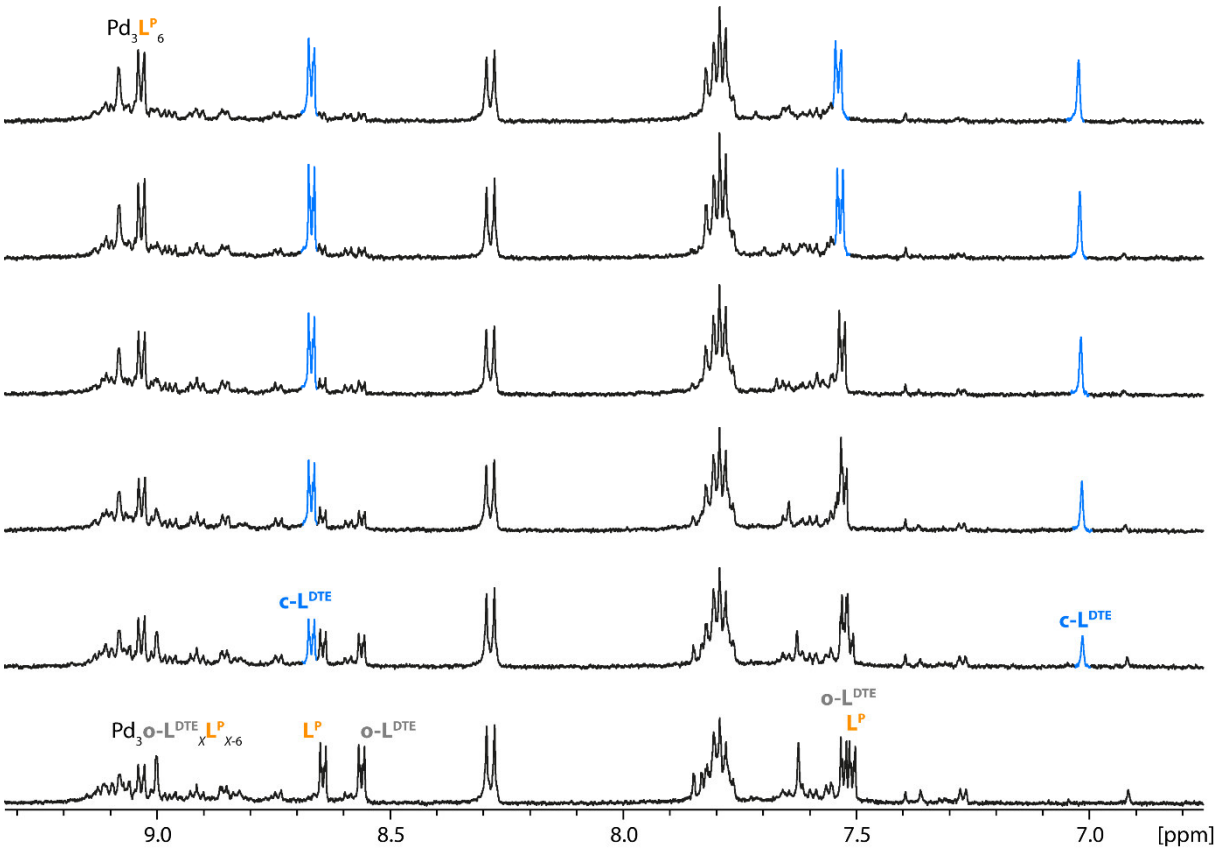

Figure 3.19. Irradiation experiment of mixture of Pd_3**o-L**$^{DTE}_{X}$**L**$^{P}_{X-6}$ (X ϵ {0,…,6}) and free ligands **o-L**^{DTE} and **L**^{P}. Each step: 5 min irradiation at 313 nm, then 70 °C for 1 h.

When combining **o-L**^{DTE}, **L**^{C} and **L**^{P} together with the Pd salt (each 1 eq; the same donor group to Pd ratio as in the previous experiments) the ^{1}H NMR spectrum shows a mixture of heteroleptic Pd_2**o-L**$^{DTE}_{2}$**L**$^{C}_{2}$, Pd_2**L**$^{P}_{2}$**L**$^{C}_{2}$ and free ligands **o-L**^{DTE}, **L**^{C} and **L**^{P}. The comparison with reference spectra is given in Figure 3.36. Further analysis with mass spectrometry shows the existence of Pd_3**o-L**$^{DTE}_{X}$**L**$^{P}_{X-6}$ (X ϵ {0,…,6}) species, additionally, but not the theoretical possible heteroleptic cage Pd_2**L**$^{C}_{2}$**o-L**^{DTE}**L**^{P}. After several cycles of irradiation and heating the mixture only contained Pd_2**L**$^{P}_{2}$**L**$^{C}_{2}$ and free **c-L**^{DTE}, as expected and

shown in Figure 3.20. It is thus possible to switch between a mixture containing at least twelve species to a mixture containing only two species, making the complex system an example of simplexity.

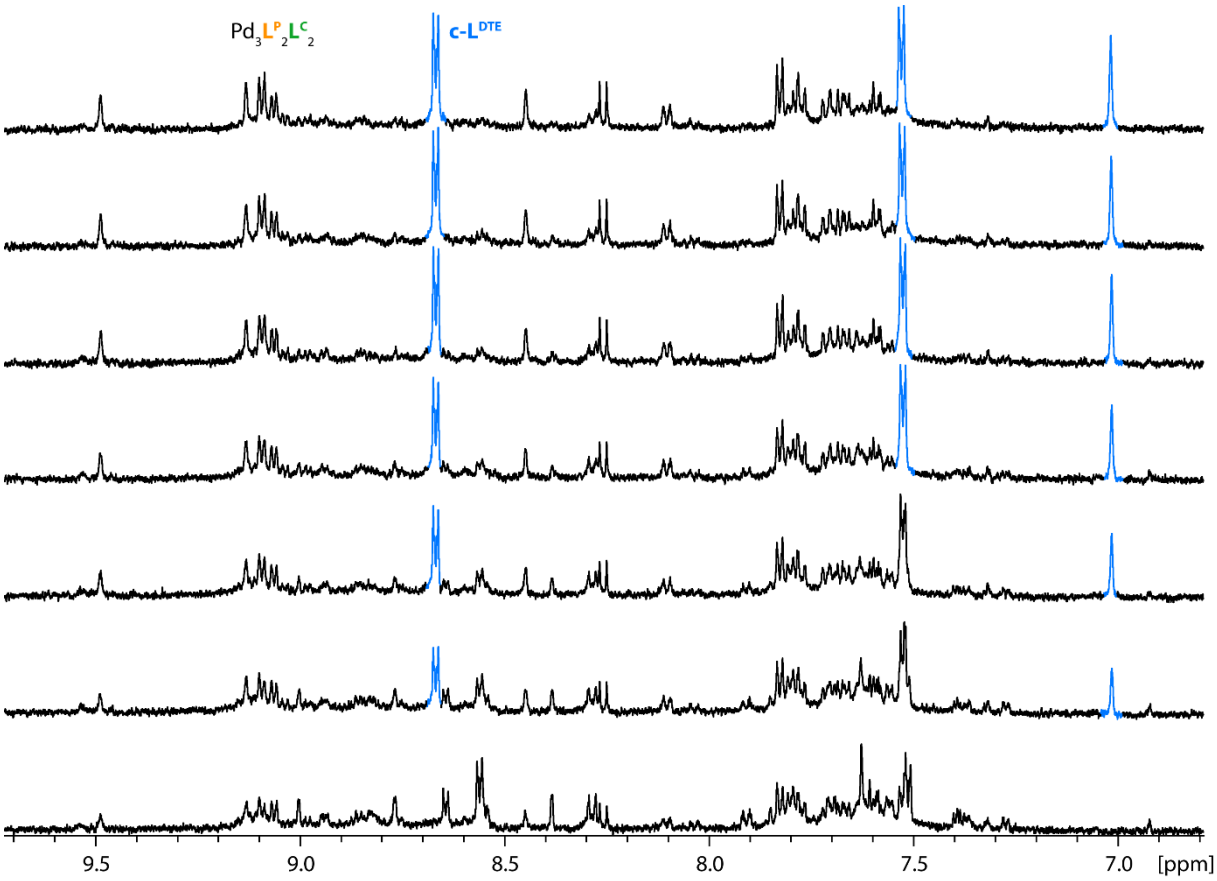

Figure 3.20. Irradiation experiment of mixture of Pd_2**o-L**$^{DTE}{}_2$**L**$^{C}{}_2$, Pd_2**L**$^{P}{}_2$**L**$^{C}{}_2$, Pd_3**o-L**$^{DTE}{}_X$**L**$^{P}{}_{X-6}$ (X ∈ {0,…,6}) and free ligands **o-L**^{DTE}, **L**^{C} and **L**^{P}. Each step: 5 min irradiation at 313 nm, then 70 °C for 1 h.

3.4 Conclusion and Outlook

Several new heteroleptic coordination cages containing the photoswitchable DTE moiety were found and investigated. The Pd_2**o-L**$^{DTE}{}_2$**L**$^{C}{}_2$ cage consists of two of the open DTE ligands **o-L**^{DTE} as undersized ligands with positive binding angle and two times the oversized carbazole ligand **L**^{C} with negative binding angle. In the cage, the ligands are in *cis* position and the DTE backbones of the **o-L**^{DTE} ligands are twisted in a way that the cyclisation reaction cannot occur, even if it is excited by UV light, like it is the case in the homoleptic Pd_3**o-L**$^{DTE}{}_6$. A combination of **o-L**^{DTE} with the phenanthrene ligand **L**^{P}, which also has a positive binding angle, leads to the formation of a complex mixture of Pd_3 rings ranging from homoleptic Pd_3**o-L**$^{DTE}{}_6$**L**$^{P}{}_0$ to homoleptic Pd_3**o-L**$^{DTE}{}_0$**L**$^{P}{}_6$. Even though 13 possible Pd_3 species are theoretically possible, investigation with trapped ion mobility spectrometry (TIMS) shows that only eight species are present in solution. Which of the species form and what the driving force for these are could not be determined but assumptions could be made. This mixture shows the same photoswitching behavior as Pd_3**o-L**$^{DTE}{}_6$ and Pd_2**o-L**$^{DTE}{}_2$**L**$^{C}{}_2$. The closed DTE ligand, **c-L**^{DTE}, forms a

heteroleptic cage with $\mathbf{L^P}$ of the stoichiometry $Pd_6\mathbf{c\text{-}L^{DTE}}_6\mathbf{L^P}_6$, although not selectively. Whether this cage is a prism or an anti-prism could not be determined experimentally but energy calculations on DFT level suggest that the prism is formed due to less strain in the ligands.

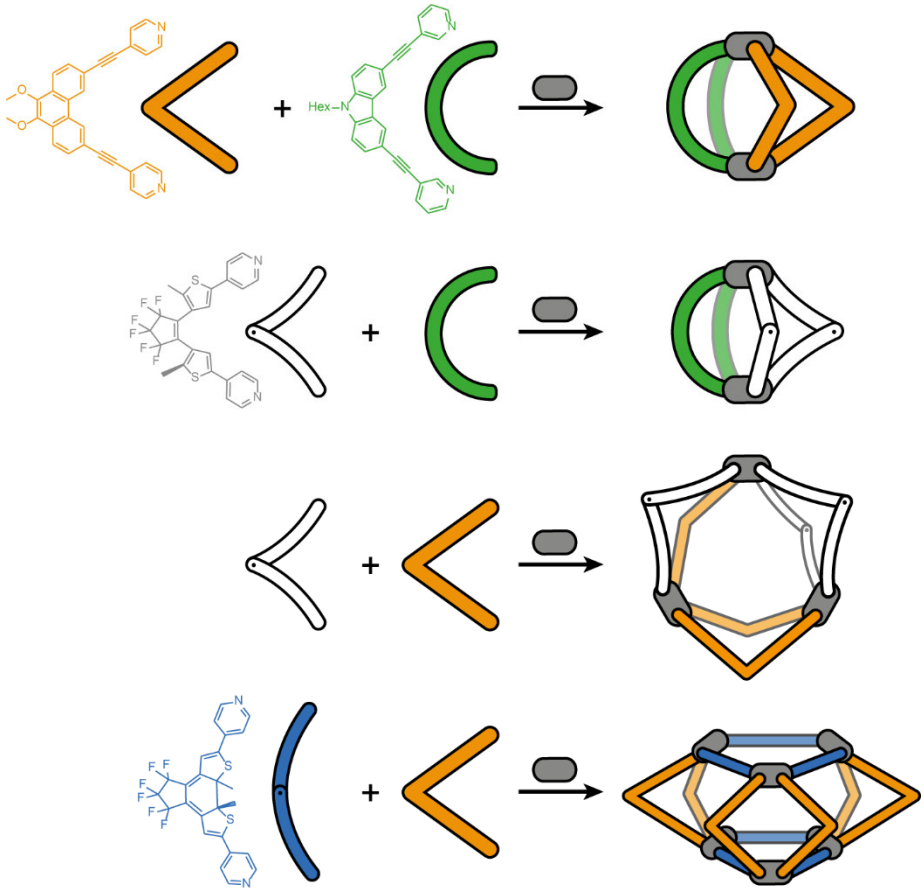

Figure 3.21. Ligands and heteroleptic cages investigated in this study. Orange: $\mathbf{L^P}$, green: $\mathbf{L^C}$, white: $\mathbf{o\text{-}L^{DTE}}$, blue: $\mathbf{c\text{-}L^{DTE}}$, grey: Pd^{2+}. Heteroleptic cages from top to bottom: $Pd_2\mathbf{L^P}_2\mathbf{L^C}_2$, $Pd_2\mathbf{o\text{-}L^{DTE}}_2\mathbf{L^C}_2$, one possible isomer of $Pd_3\mathbf{o\text{-}L^{DTE}}_3\mathbf{L^P}_3$ representatively shown for $Pd_3\mathbf{o\text{-}L^{DTE}}_X\mathbf{L^P}_{X\text{-}6}$ ($X \in \{0,\ldots,6\}$), prism-isomer of $Pd_6\mathbf{c\text{-}L^{DTE}}_6\mathbf{L^P}_6$.

The flexibility given by the DTE backbone opens innumerable structural possibilities for molecular cages and other self-assemblies and only a few of them were investigated in this study. As an outlook, an interesting alternative to $\mathbf{L^C}$ would be a ligand with an even more negative binding angle that would also form a heteroleptic *cis*-$Pd_2\mathbf{L^A}_2\mathbf{L^B}_2$ cage with $\mathbf{o\text{-}L^{DTE}}$ but in a way that the backbone of the latter is twisted so that photoswitching could actually occur. The photoswitching behavior of this heteroleptic cage may then still differ from the free ligand or the lantern shaped $Pd_2\mathbf{L}_4$ cage, with **L** being the first generation DTE ligand of our group, because the DTE unit may not be in a for the bond formation ideal conformation which would slow down to photoswitching.

Because photoswitching of the heteroleptic cages with **o-L^{DTE}** in this study would take an extended amount of irradiation time, the amount of Pd in solution is reduced. This way it is possible to switch between a complex mixture of (multiple) different cages and free ligands to only one type of cage and free closed DTE ligand **c-L^{DTE}**. The full conversion is only possible if a competitive alternative to **o-L^{DTE}** is present, for example another ligand such as **L^{C}** or **L^{P}**. Because **c-L^{DTE}** is non-competitive for entropy reasons, it is possible to switch between mixtures containing several species and mixtures containing only one type of cage and free **c**-L^{DTE}. Figure 3.22 shows the systems that were investigated with irradiation.

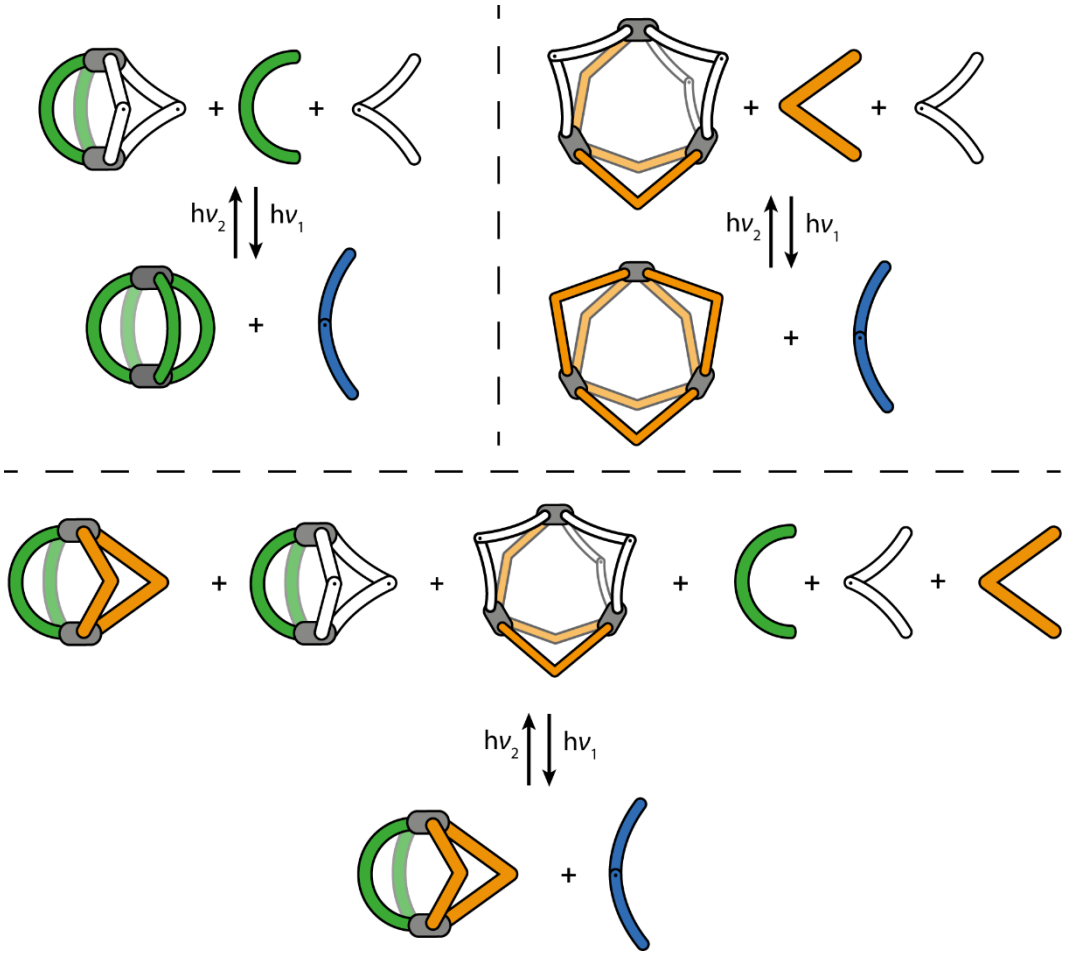

Figure 3.22. Irradiation experiments on complex systems. ν_1 = 313 nm, ν_2 = 617 nm. Upper left: Pd_2**o-L^{DTE}**$_2$**L^{C}**$_2$ and free **L^{C}** and **o-L^{DTE}** convert to Pd_2**L^{C}**$_4$ and **c-L^{DTE}**. Upper right: Pd_3**o-L^{DTE}**$_X$**L^{P}**$_{X-6}$ (X ϵ {0,…,6}) and free **L^{P}** and **o-L^{DTE}** convert to Pd_3**L^{P}**$_6$ and **c-L^{DTE}**. Bottom: Mixture of Pd_2**L^{P}**$_2$**L^{C}**$_2$, Pd_2**o-L^{DTE}**$_2$**L^{C}**$_2$, Pd_3**o-L^{DTE}**$_X$**L^{P}**$_{X-6}$ (X ϵ {0,…,6}) and free **L^{C}**, **L^{P}** and **o-L^{DTE}** convert to Pd_2**L^{P}**$_2$**L^{C}**$_2$ and **c-L^{DTE}**.

The conversion rate of these kind of systems depends on multiple different factors and may be interesting to further investigate. The amount of palladium may have a great influence because a lower amount leads to more free **o-L^{DTE}** in solution, a larger amount would not only slow down the conversion rate but even limit the overall possible conversion. Another influence may be the kinetic stability of

the heteroleptic assemblies. In the conducted experiments the samples were heated to quickly reach the thermodynamic minimum and release **o-L^{DTE}** but the heteroleptic cages may differ in their stability and thus in their rate to adjust to the changed ligand ratios.

Switching with enough palladium and thus without free ligands or other Lewis bases could also be done with these heteroleptic cages, which would, among others, make a conversion from the Pd$_3$**o-L$^{DTE}_X$L$^P_{X-6}$** ($X \in \{0,\ldots,6\}$) mixture to the Pd$_6$**c-L$^{DTE}_6$L$^P_6$** species possible; another form of simplexity. This would be especially interesting because the cavities and thus likely also the guest binding behavior of the two systems differ significantly.

3.5 Experimental Section

3.5.1 Formation and analysis of Pd$_2$L$^P_2$L$^C_2$

Pd$_2$**L$^P_2$L$^C_2$** is characterized in Ref. [26] but the ^{1}H NMR spectrum is only given in DMSO-d6. For completeness Pd$_2$**L$^P_2$L$^C_2$** is also formed in CD_3CN here. 147 µL of each 3 mM ligand stock solution in CD_3CN (1 eq, 0.44 µmol) was combined with 29.3 µL of a 15 mM $[Pd(CH_3CN)_4](BF_4)_2$ stock solution in CD_3CN (1 eq, 0.44 µmol) and 227 µL pure CD_3CN. The sample was then heated at 70 °C for 1 h. Figure 3.23 shows the aromatic region of the ^{1}H NMR spectrum of Pd$_2$**L$^P_2$L$^C_2$** in CD_3CN and the labeling system for the assignment.

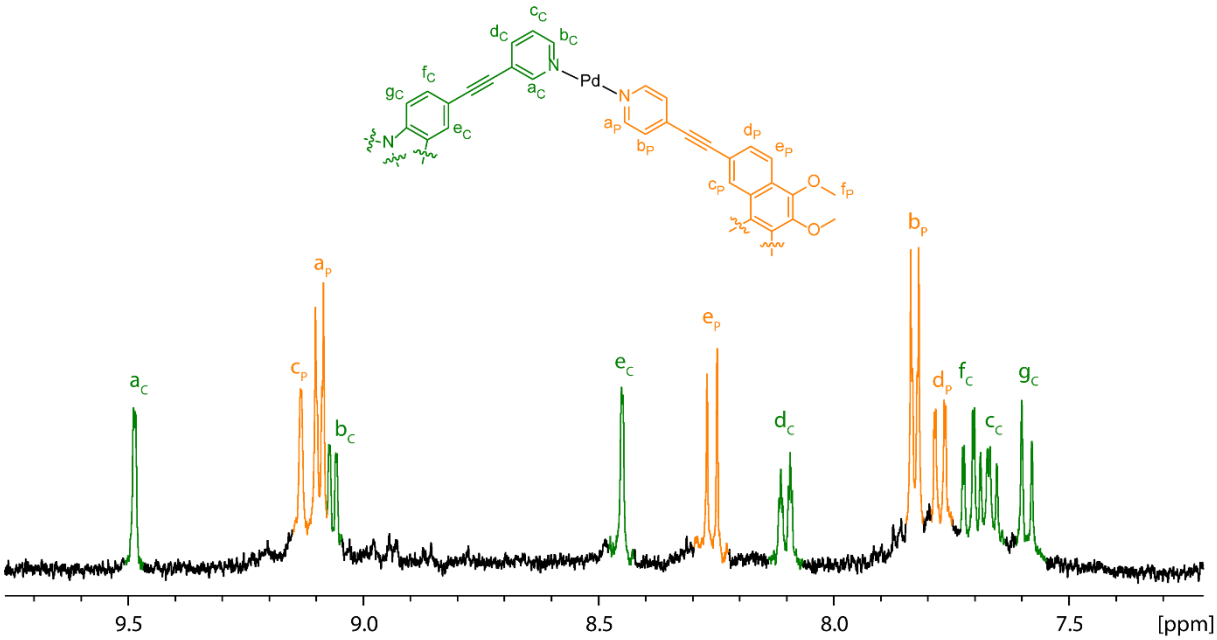

Figure 3.23. Aromatic region of ^{1}H NMR spectrum (400 MHz) of Pd$_2$**L$^P_2$L$^C_2$**.

^{1}H NMR (400 MHz) of Pd$_2$L$^P_2$L$^C_2$: δ [ppm] = 9.49 (s, 4H, a_C), 9.13 (s, 4H, c_P), 9.09 (d, J = 6.5 Hz, 8H, a_P), 9.07 (d, J = 5.9 Hz, 4H, b_C), 8.45 (s, 4H, e_C), 8.26 (d, J = 8.9 Hz, 4H, e_P), 8.10 (d, J = 7.8 Hz, 4H, d_C), 7.83 (d, J = 6.8 Hz, 8H, b_P), 7.77 (d, J = 8.4 Hz, 4H, d_P), 7.71 (d, J = 8.6 Hz, 4H, f_C), 7.67 (dd, J_1 = 8.13 Hz, J_2 = 5.84 Hz, 4H, c_C), 7.59 (d, J = 8.8 Hz, 4H, g_C), 4.05 (s, 12H, f_P).

3.5.2 Formation and analysis of Pd_2**o-L**$^{DTE}_2$**L**$^{C}_2$

147 µL of each 3 mM ligand stock solution in CD_3CN (1 eq, 0.44 µmol) was combined with 29.3 µL of a 15 mM $[Pd(CH_3CN)_4](BF_4)_2$ stock solution in CD_3CN (1 eq, 0.44 µmol) and 227 µL pure CD_3CN. The full ^{1}H NMR spectrum is shown in Figure 3.24; its aromatic region in Figure 3.25 and the corresponding ^{1}H ^{1}H NOESY NMR spectrum in Figure 3.26.

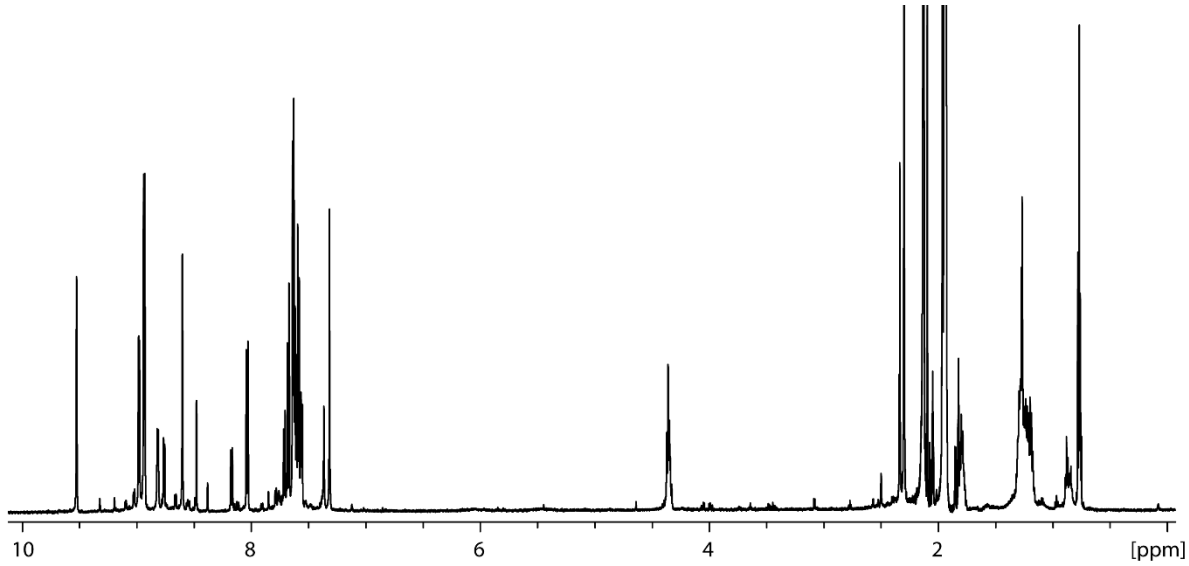

Figure 3.24. Full ^{1}H NMR spectrum (600 MHz) of Pd_2**o-L**$^{DTE}_2$**L**$^{C}_2$.

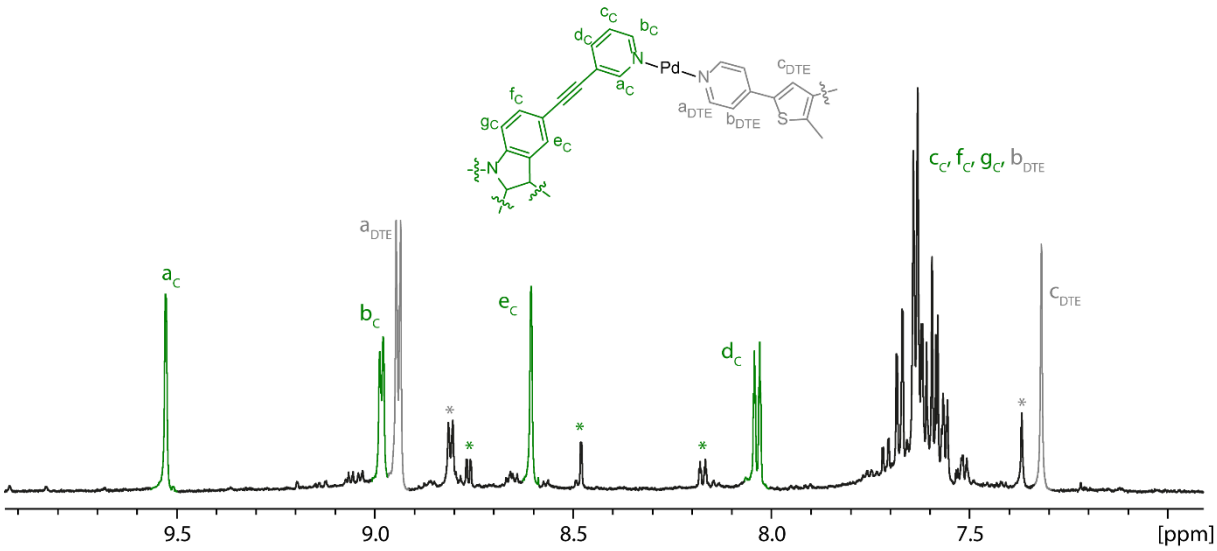

Figure 3.25. Aromatic region of ^{1}H NMR spectrum of Pd_2**o-L**$^{DTE}_2$**L**$^{C}_2$.

^{1}H NMR (600 MHz) of Pd_2o-L$^{DTE}_2$L$^{C}_2$: δ [ppm] = 9.53 (s, 4H, a_C), 8.99 (d, J = 5.2 Hz, 4H, b_C), 8.94 (d, J = 6.7 Hz, 8H, a_{DTE}), 8.61 (s, 4H, e_C), 8.04 (d, J = 8.0 Hz, 4H, d_C), 7.49 – 7.23 (m, c_C, f_C, g_C, b_{DTE}), 7.32 (s, 4H, c_{DTE}), 4.36 (t, J = 7.2 Hz, 4H, N-CH_2-), 2.30 (s, 12H, d_{DTE}), 1.80 (m, 8H, N-CH_2-CH_2-), 1.15-1.33 (m, 24H, -CH_2-), 0.77 (t, J = 7.2 Hz, 12H, -CH_3). Not listed are the signals for homoleptic Pd_2**L**$^{C}_4$ and Pd_3**o-L**$^{DTE}_6$; they are marked with asterisks in the spectrum.

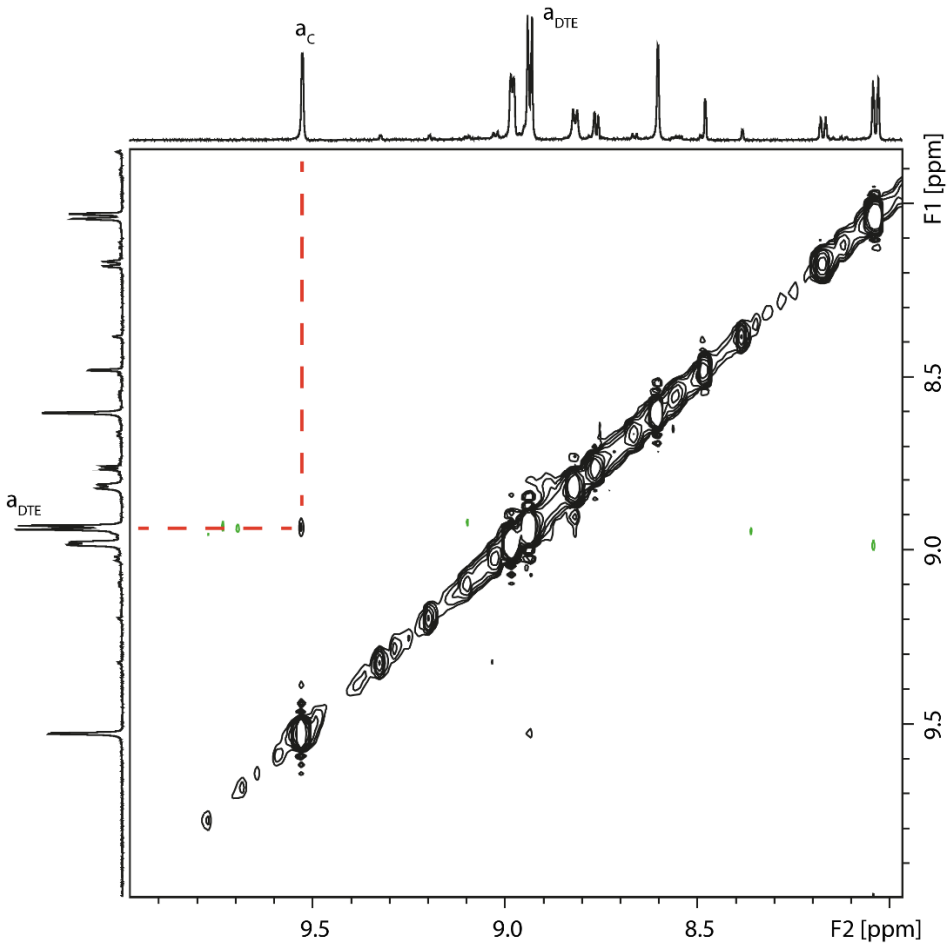

Figure 3.26. Partial ^{1}H ^{1}H NOESY NMR (600 MHz) of Pd_2**o-L**$^{DTE}{}_2$**L**$^{C}{}_2$. Negative cross peaks are colored green.

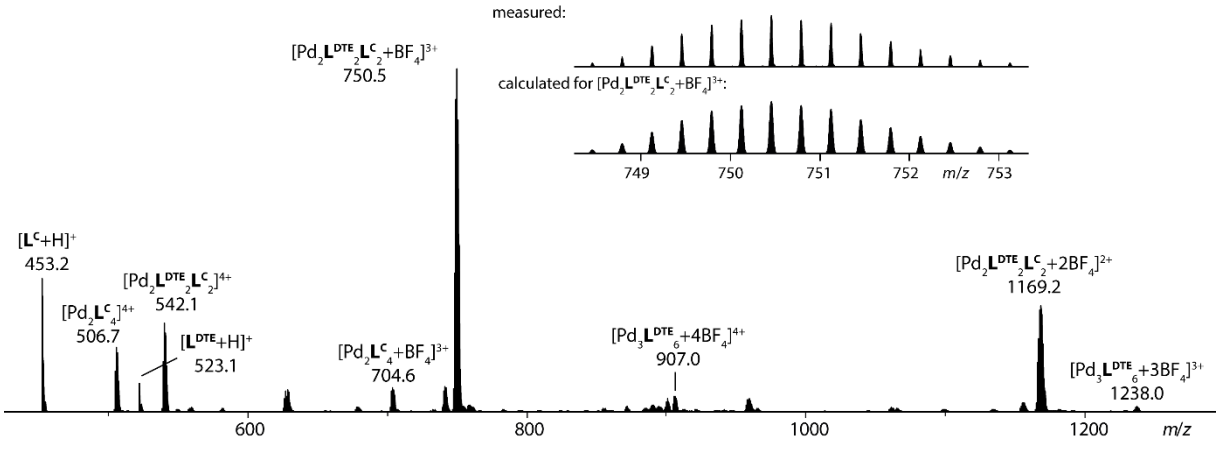

Figure 3.27. Mass spectrum of Pd_2**o-L**$^{DTE}{}_2$**L**$^{C}{}_2$.

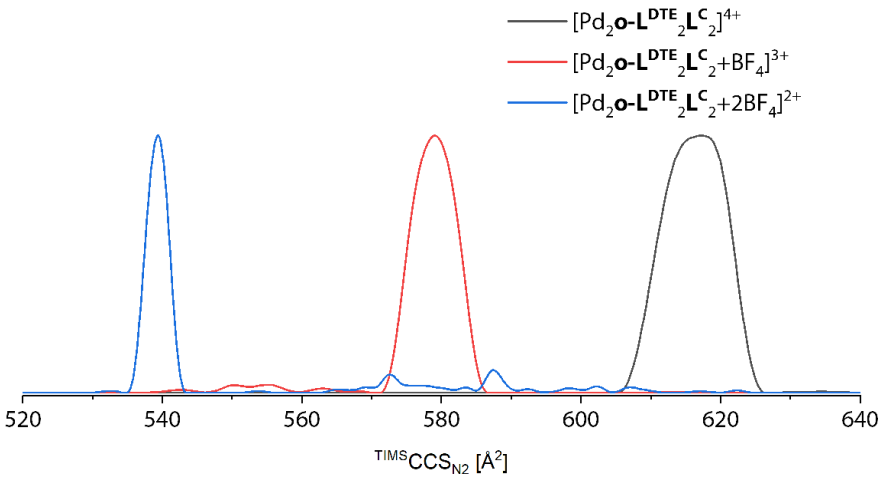

Figure 3.28. Overlaid TIMS mobilograms of Pd_2**o-L**$^{DTE}_2$**L**$^{C}_2$. Inverse mobilities were normalized and converted into CCS values.

Table 3.1. Measured $^{TIMS}CCS_{N2}$ and calculated CCS_{N2}, both from geometry optimized structures (opt) and MD simulations (MD), and relative deviations (Δ%) of Pd_2**o-L**$^{DTE}_2$**L**$^{C}_2$.

Species	$^{TIMS}CCS_{N2}$ [Å^2]	$^{Theo}CCS_{N2}$ [Å^2] (opt)	opt, Δ%	$^{Theo}CCS_{N2}$ [Å^2] (MD)	MD, Δ%
$[Pd_2$**o-L**$^{DTE}_2$**L**$^{C}_2]^{4+}$	617 ± 6	647.414	+4.9%	630 ± 9	+2% ± 1%
$[Pd_2$**o-L**$^{DTE}_2$**L**$^{C}_2$+$BF_4]^{3+}$	579 ± 4	619.554	+7.0%	605 ± 10	+4% ± 2%
$[Pd_2$**o-L**$^{DTE}_2$**L**$^{C}_2$+2$BF_4]^{2+}$	539 ± 2	607.903	+12.7%	588 ± 10	+9% ± 2%

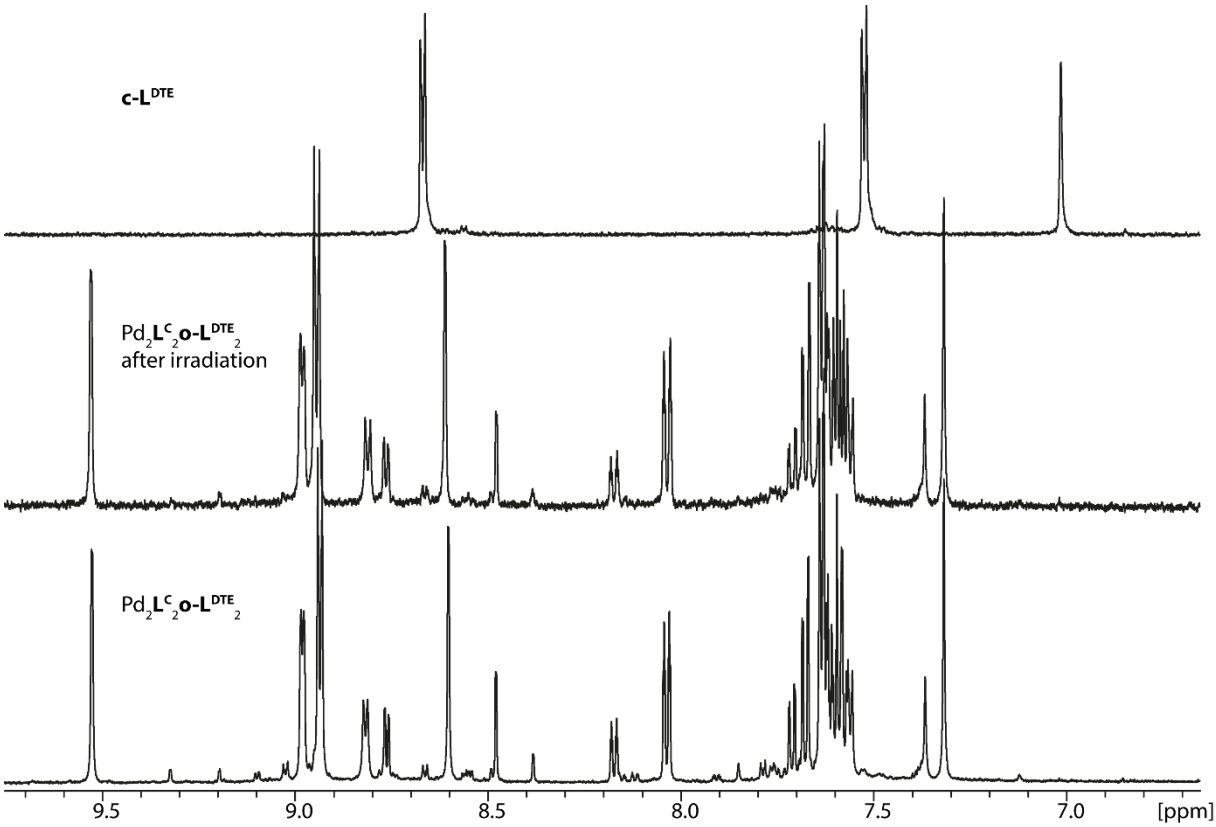

Figure 3.29. ^{1}H NMR spectra (500 MHz top, 600 MHz middle, 500 MHz bottom) of Pd_2**o-L**$^{DTE}{}_2$**L**$^{C}{}_2$ before and after irradiation for 10 min with UV light (313 nm) under the usual conditions and a spectrum of **c-L**^{DTE} for reference.

3.5.3 Formation and analysis of Pd_3**o-L**$^{DTE}{}_X$**L**$^{P}{}_{X\text{-}6}$

147 µL of each 3 mM ligand stock solution in CD_3CN (1 eq, 0.44 µmol) was combined with 29.3 µL of a 15 mM $[Pd(CH_3CN)_4](BF_4)_2$ stock solution in CD_3CN (1 eq, 0.44 µmol) and 227 µL pure CD_3CN.

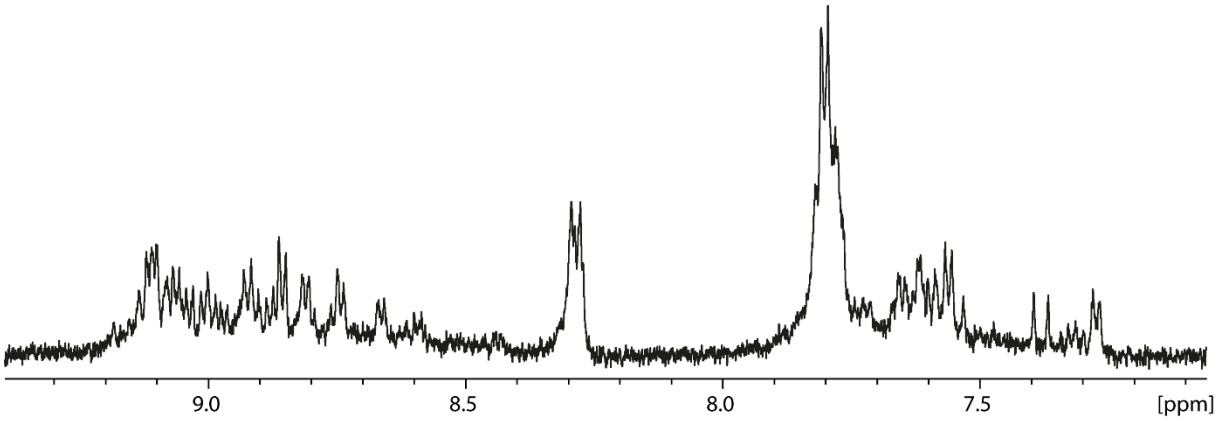

Figure 3.30. Aromatic region of ^{1}H NMR spectrum (600 MHz) of Pd_3**o-L**$^{DTE}{}_X$**L**$^{P}{}_{X\text{-}6}$.

For the $^{Theo}CCS_{N2}$ calculation the 4+ species (containing two BF_4^-) of all possible forms of Pd_3**o-L**$^{DTE}_X$**L**$^{P}_{X\text{-}6}$ (X ϵ {0,…,6}) were modeled and optimized with r^{2}SCAN-3c. It was made sure that the initial conformation of **o-L**^{DTE} was identical in all models. The $^{Theo}CCS_{N2}$ values were calculated following the procedure explained in Chapter 2. The labeling system for the isomers of Pd_3**o-L**$^{DTE}_X$**L**$^{P}_{X\text{-}6}$ (X ϵ {2,…,4}) is given in Figure 3.31. The experimental and theoretical CCS_{N2} values and relative deviations are given in Table 3.2.

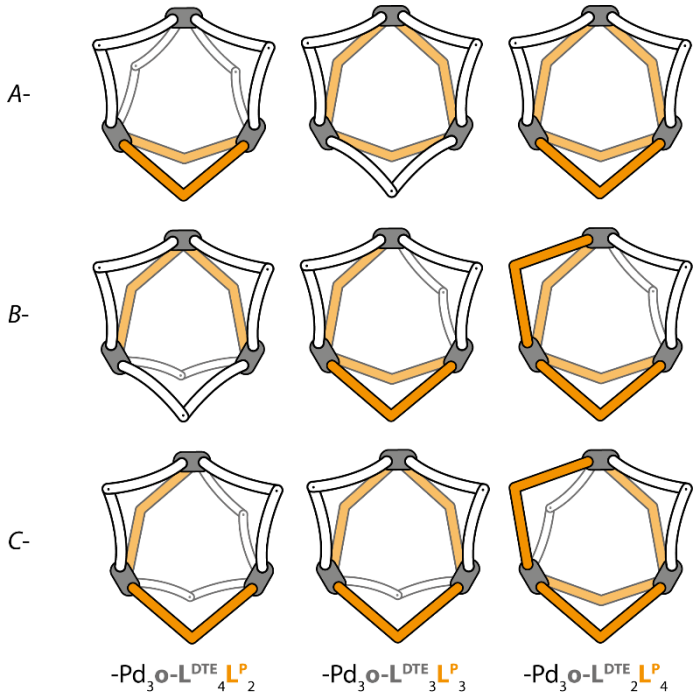

Figure 3.31. Labeling system for the isomers of Pd_3**o-L**$^{DTE}_X$**L**$^{P}_{X\text{-}6}$ (X ϵ {2,…,4}). Example: *B*-Pd_3**o-L**$^{DTE}_3$ **L**^{P} is the ring in the second row and middle column.

Table 3.2. Experimental and theoretical CCS_{N2} values and relative deviations of the Pd_3**o-L**$^{DTE}_X$**L**$^{P}_{X\text{-}6}$ (X ϵ {0,…,6}) species. For Pd_3**o-L**$^{DTE}_4$**L**$^{P}_2$ only the major signal is considered here.

Species	$^{TIMS}CCS_{N2}$ [Å^2]	$^{Theo}CCS_{N2}$ [Å^2]	Δ%
[Pd_3**o-L**$^{DTE}_6$+2BF_4]$^{4+}$	737 ± 7	751.272	1.9%
[Pd_3**o-L**$^{DTE}_5$**L**^{P}+2BF_4]$^{4+}$	757 ± 8	769.829	1.7%
[*A*-Pd_3**o-L**$^{DTE}_4$**L**$^{P}_2$+2BF_4]$^{4+}$	780 ± 8	793.892	1.8%
[*B*-Pd_3**o-L**$^{DTE}_4$**L**$^{P}_2$+2BF_4]$^{4+}$	780 ± 8	802.567	2.9%
[*C*-Pd_3**o-L**$^{DTE}_4$**L**$^{P}_2$+2BF_4]$^{4+}$	780 ± 8	796.291	2.1%
[*A*-Pd_3**o-L**$^{DTE}_3$**L**$^{P}_3$+2BF_4]$^{4+}$	796 ± 7	827.914	4.0%
[*B*-Pd_3**o-L**$^{DTE}_3$**L**$^{P}_3$+2BF_4]$^{4+}$	796 ± 7	817.247	2.6%
[*C*-Pd_3**o-L**$^{DTE}_3$**L**$^{P}_3$+2BF_4]$^{4+}$	796 ± 7	825.755	3.7%
[*A*-Pd_3**o-L**$^{DTE}_2$**L**$^{P}_4$+2BF_4]$^{4+}$	814 ± 8	855.280	5.1%
[*B*-Pd_3**o-L**$^{DTE}_2$**L**$^{P}_4$+2BF_4]$^{4+}$	814 ± 8	861.532	5.9%
[*C*-Pd_3**o-L**$^{DTE}_2$**L**$^{P}_4$+2BF_4]$^{4+}$	814 ± 8	846.177	4.0%
[Pd_3**o-L**^{DTE}**L**$^{P}_5$+2BF_4]$^{4+}$	831 ± 7	887.328	6.8%
[Pd_3**L**$^{P}_6$+2BF_4]$^{4+}$	853 ± 7	917.564	7.5%

As can be seen in Table 3.2, the relative deviation to the experiment (□%) is increasing with increasing amount of $\mathbf{L^P}$ in the system. $\mathbf{L^P}$ is longer and less flexible and makes the shape of the ring further deviate from a perfect sphere causing this systematic error. Because of this, the different isomers of Pd_3**o-**$\mathbf{L^{DTE}}_X\mathbf{L^P}_{X-6}$ ($X \in \{2,\ldots,4\}$) cannot be judged by □% alone but by the coefficient of determination R^2 of the linear fit of □%. Linear fits were thus carried out for all 27 possible combinations of isomers and the resulting R^2 values are listed in Table 3.3. Three different combinations lead to very good fits, with $R^2 \in [0.95;0.96]$, but none of them matches the hypothesis postulated in Section 3.3.2. **o-**$\mathbf{L^{DTE}}$ is very flexible and with increasing amounts of **o-**$\mathbf{L^{DTE}}$ in the system the number of possible conformers increases exponentially. More accurate $^{Theo}CCS_{N2}$ results may be obtained by MD simulations of according length instead of geometry optimizations prior to CCS calculation.

Table 3.3. Coefficient of determination R^2 of the linear fits of □% from Pd_3**o-**$\mathbf{L^{DTE}}_X\mathbf{L^P}_{X-6}$ ($X \in \{0,\ldots,6\}$) using different combinations of isomers of Pd_3**o-**$\mathbf{L^{DTE}}_X\mathbf{L^P}_{X-6}$ ($X \in \{2,\ldots,4\}$).

$\mathbf{L^{DTE}}_4\mathbf{L^P}_2$	$\mathbf{L^{DTE}}_3\mathbf{L^P}_3$	$\mathbf{L^{DTE}}_2\mathbf{L^P}_4$	R^2	$\mathbf{L^{DTE}}_4\mathbf{L^P}_2$	$\mathbf{L^{DTE}}_3\mathbf{L^P}_3$	$\mathbf{L^{DTE}}_2\mathbf{L^P}_4$	R^2
A	*A*	*A*	0.910	*B*	*B*	*C*	0.849
A	*A*	*B*	0.915	*B*	*C*	*A*	0.921
A	*A*	*C*	0.877	*B*	*C*	*B*	0.927
A	*B*	*A*	0.859	*B*	*C*	*C*	0.888
A	*B*	*B*	0.868	*C*	*A*	*A*	0.955
A	*B*	*C*	0.840	*C*	*A*	*B*	0.958
A	*C*	*A*	0.905	*C*	*A*	*C*	0.909
A	*C*	*B*	0.911	*C*	*B*	*A*	0.885
A	*C*	*C*	0.876	*C*	*B*	*B*	0.891
B	*A*	*A*	0.926	*C*	*B*	*C*	0.856
B	*A*	*B*	0.931	*C*	*C*	*A*	0.947
B	*A*	*C*	0.891	*C*	*C*	*B*	0.951
B	*B*	*A*	0.870	*C*	*C*	*C*	0.905
B	*B*	*B*	0.879				

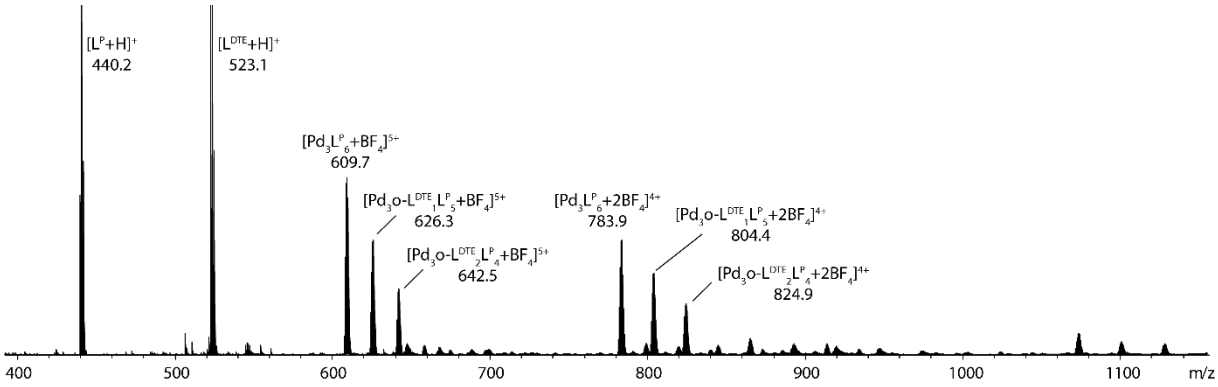

Figure 3.32. Mass spectrum of the last state from the irradiation experiment of the mixture of Pd_3**o-**$\mathbf{L^{DTE}}_X\mathbf{L^P}_{X-6}$ ($X \in \{0,\ldots,6\}$) and free **o-**$\mathbf{L^{DTE}}$ and $\mathbf{L^P}$.

3.5.4 Formation and analysis of Pd_6**c-L**$^{DTE}{}_6$**L**$^{P}{}_6$

350 µL of each a 3 mM stock solution of **o-L**^{DTE} in CD_3CN (1 eq, 1.05 µmol) was transferred to a quartz NMR tube and irradiated using 313 nm for 10 minutes. 350 µL of a 3 mM stock solution of **L**^{P} in CD_3CN (1 eq, 1.05 µmol) and 70 µL of a 15 mM $[Pd(CH_3CN)_4](BF_4)_2$ stock solution in CD_3CN (1 eq, 1.05 µmol) was added.

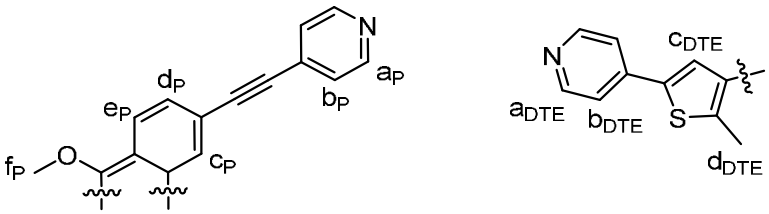

Scheme 3.1. Labeling system for **o-L**^{DTE} and **L**^{P}. An asterisk indicates that the proton belongs to a homoleptic assembly.

^{1}H NMR (500 MHz, 298 K, CD_3CN) of Pd_6o-L$^{DTE}{}_6$L$^{P}{}_6$: δ [ppm] = 8.81-9.18 (br, a_{DTE}, a_{DTE}*, a_P, c_P, a_P*, c_P*), 8.23-8.34 (br, e_P, e_P*), 7.55-7.93 (br, b_{DTE}, b_{DTE}*, b_P, d_P, b_P*, d_P*), 6.99-7.20 (br, c_{DTE}, c_{DTE}*), 4.02-4.14 (f_P, f_P*). Signals d_{DTE} and d_{DTE}* could not be detected as they are broad and overlapping with solvent signals.

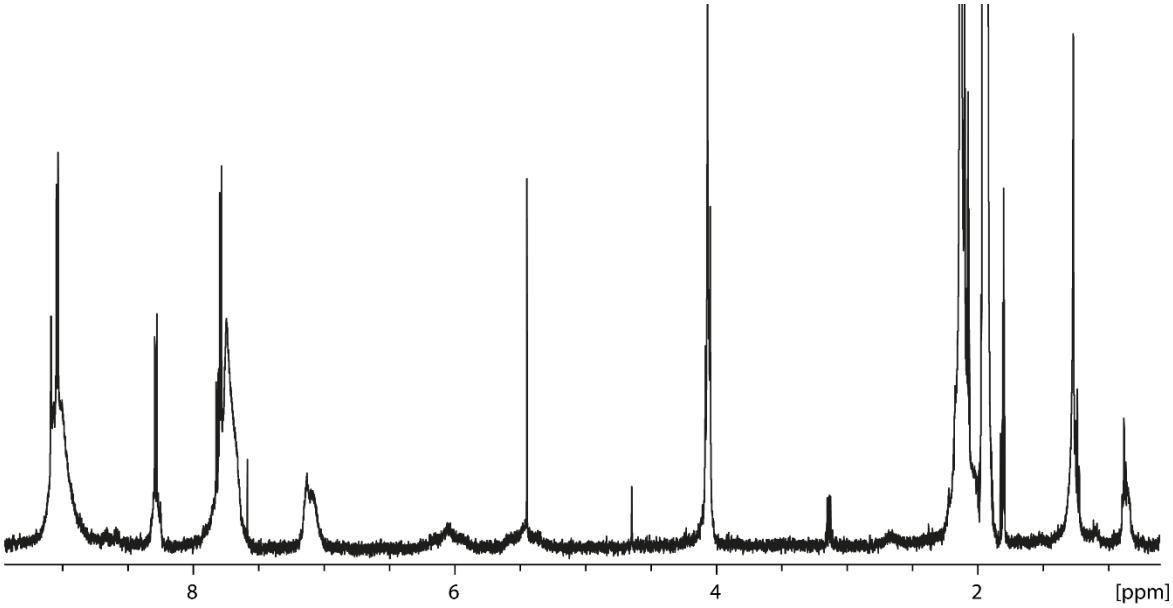

Figure 3.33. ^{1}H NMR spectrum of Pd_6**c-L**$^{DTE}{}_6$**L**$^{P}{}_6$. c_{LDTE} = c_{LP} = 0.8 mM.

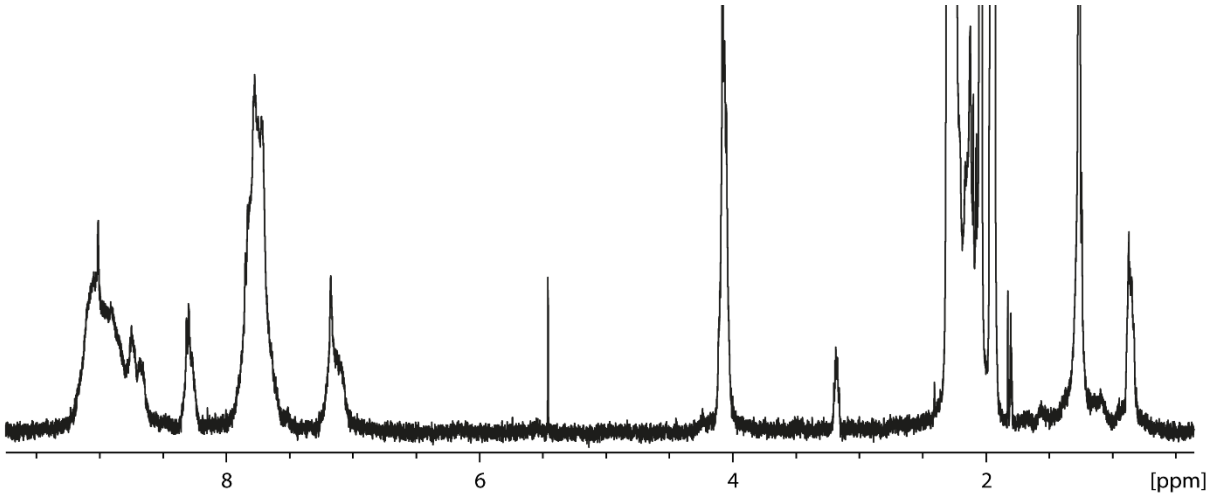

Figure 3.34. ^{1}H NMR spectrum of Pd_6**o-L$^{DTE}_6$L$^{P}_6$**. c_{LDTE} = c_{LP} = 1.91 mM.

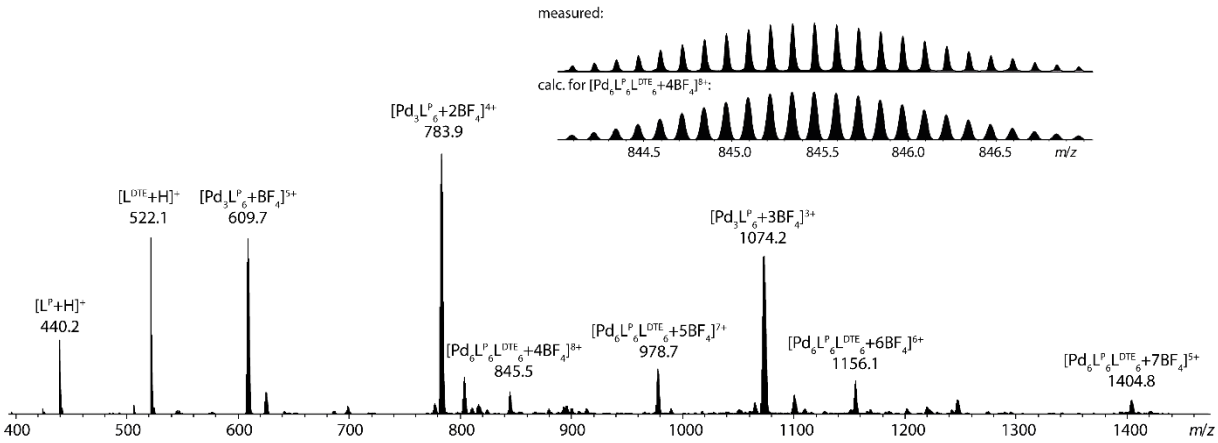

Figure 3.35. ESI mass spectrum of a combination of **c-L^{DTE}**, **L^{P}** and $[Pd(CH_3CN)_4](BF_4)_2$ in acetonitrile c_{LDTE} = c_{LP} = 0.8 mM.

Table 3.4. $^{Theo}CCS_{N2}$ of different Pd_6**L$^{P}_6$c-L$^{DTE}_6$** species.

Species	$^{Theo}CCS_{N2}$ (prism) [Å²]	$^{Theo}CCS_{N2}$ (anti-prism) [Å²]
$[Pd_6$**L$^{P}_6$c-L$^{DTE}_6$**$+4BF_4]^{8+}$	1516.31	1510.16
$[Pd_6$**L$^{P}_6$c-L$^{DTE}_6$**$+5BF_4]^{7+}$	1500.40	1489.96
$[Pd_6$**L$^{P}_6$c-L$^{DTE}_6$**$+6BF_4]^{6+}$	1478.24	1464.55
$[Pd_6$**L$^{P}_6$c-L$^{DTE}_6$**$+7BF_4]^{5+}$	1469.38	1445.62

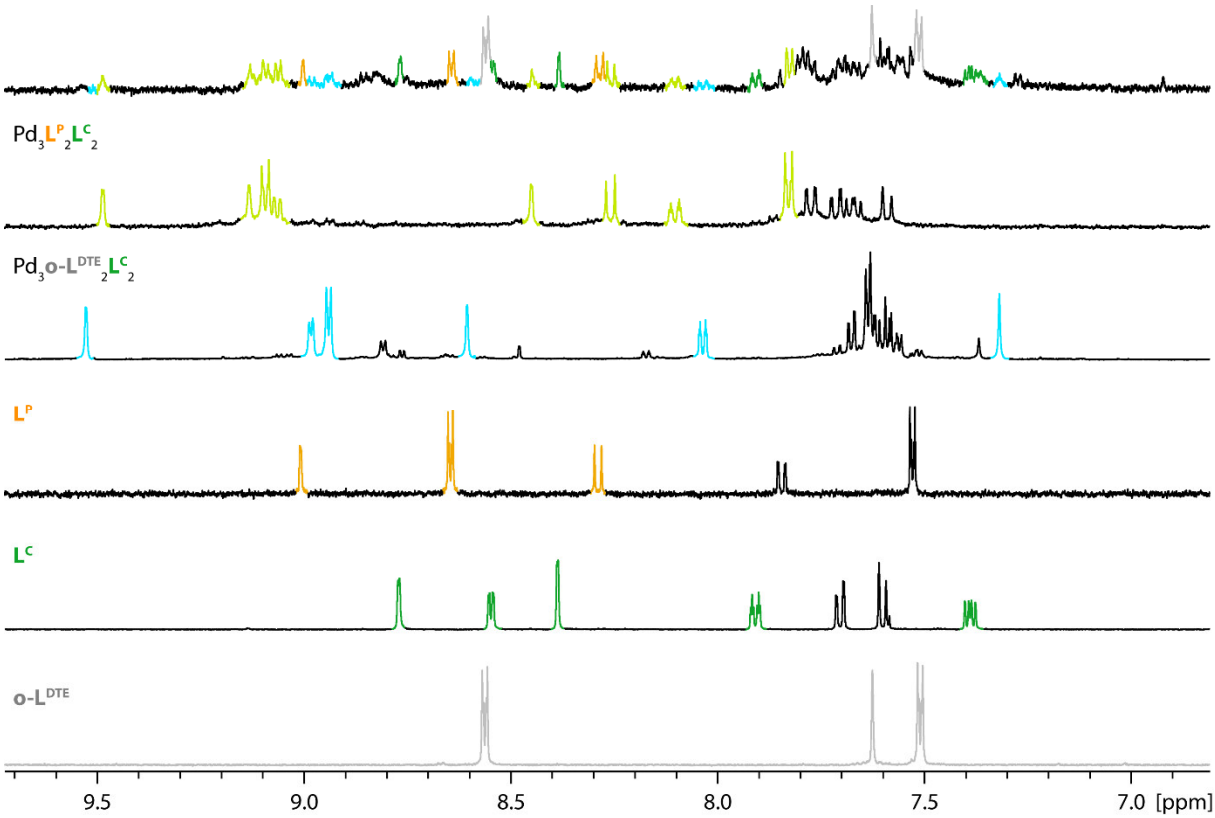

Figure 3.36. ^{1}H NMR spectrum of the combination of **o-L^{DTE}**, **L^{C}**, **L^{P}** and $[Pd(CH_3CN)_4](BF_4)_2$ and according reference spectra.

3.6 Literature

[1] H.-Y. Lin, Y.-T. Wang, X. Shi, H.-B. Yang, L. Xu, *Chem. Soc. Rev.* 2023, *52*, 1129–1154.

[2] F. A. Jerca, V. V. Jerca, R. Hoogenboom, *Nat Rev Chem* 2022, *6*, 51–69.

[3] R. G. DiNardi, A. O. Douglas, R. Tian, J. R. Price, M. Tajik, W. A. Donald, J. E. Beves, *Angew. Chem. Int. Ed.* 2022, *61*, e202205701.

[4] M. Yamamura, Y. Okazaki, T. Nabeshima, *Chem Commun* 2012, *48*, 5724–5726.

[5] S. Fu, Q. Luo, M. Zang, J. Tian, Z. Zhang, M. Zeng, Y. Ji, J. Xu, J. Liu, *Mater Chem Frontiers* 2019, *3*, 1238–1243.

[6] D. Bléger, J. Schwarz, A. M. Brouwer, S. Hecht, *J. Am. Chem. Soc.* 2012, *134*, 20597–20600.

[7] T. Murase, S. Sato, M. Fujita, *Angew. Chem. Int. Ed.* 2007, *46*, 5133–5136.

[8] A. Ghosh, L. Slappendel, B.-N. T. Nguyen, L. K. S. von Krbek, T. K. Ronson, A. M. Castilla, J. R. Nitschke, *J. Am. Chem. Soc.* 2023, *145*, 3828–3832.

[9] R. Siewertsen, H. Neumann, B. Buchheim-Stehn, R. Herges, C. Näther, F. Renth, F. Temps, *J Am Chem Soc* 2009, *131*, 15594–15595.

[10] H. Lee, J. Tessarolo, D. Langbehn, A. Baksi, R. Herges, G. H. Clever, *J Am Chem Soc* 2022, *7*, 3099–3105.

[11] Z. Shi, P. Peng, D. Strohecker, Y. Liao, *J. Am. Chem. Soc.* 2011, *133*, 14699–14703.

[12] R.-J. Li, C. Pezzato, C. Berton, K. Severin, *Chem Sci* 2021, *12*, 4981–4984.

[13] M. Irie, *Chem Rev* 2000, *100*, 1685–1716.

[14] M. Han, R. Michel, B. He, Y. Chen, D. Stalke, M. John, G. H. Clever, *Angew. Chem. Int. Ed.* 2013, *52*, 1319–1323.

[15] R. Li, M. Han, J. Tessarolo, J. J. Holstein, J. Lübben, B. Dittrich, C. Volkmann, M. Finze, C. Jenne, G. H. Clever, *Chemphotochem* 2019, *3*, 378–383.

[16] R.-J. Li, J. J. Holstein, W. G. Hiller, J. Andréasson, G. H. Clever, *J Am Chem Soc* 2019, *141*, 2097–2103.

[17] S. Juber, S. Wingbermühle, P. Nuernberger, G. H. Clever, L. V. Schäfer, *Phys Chem Chem Phys* 2021, DOI 10.1039/d0cp06495e.

[18] K. Artmann, R. Li, S. Juber, E. Benchimol, L. V. Schäfer, G. H. Clever, P. Nuernberger, *Angew. Chem. Int. Ed.* 2022, *61*, e202212112.

[19] S. Wei, M. Pan, Y. Fan, H. Liu, J. Zhang, C. Su, *Chem European J* 2015, *21*, 7418–7427.

[20] R.-J. Li, J. Tessarolo, H. Lee, G. H. Clever, *J Am Chem Soc* 2021, *143*, 3865–3873.

[21] M. Han, Y. Luo, B. Damaschke, L. Gómez, X. Ribas, A. Jose, P. Peretzki, M. Seibt, G. H. Clever, *Angew. Chem. Int. Ed.* 2016, *55*, 445–449.

[22] H. Yokoyama, Y. Ueda, D. Fujita, S. Sato, M. Fujita, *Chem Asian J* 2015, *10*, 2292–2295.

[23] K. Harris, D. Fujita, M. Fujita, *Chem Commun* 2013, *49*, 6703–6712.

[24] R. G. DiNardi, S. Rasheed, S. S. Capomolla, M. H. Chak, I. A. Middleton, L. K. Macreadie, J. P. Violi, W. A. Donald, P. J. Lusby, J. E. Beves, 2024, DOI 10.26434/chemrxiv-2024-vdkfj-v2.

[25] W. M. Bloch, Y. Abe, J. J. Holstein, C. M. Wandtke, B. Dittrich, G. H. Clever, *J Am Chem Soc* 2016, DOI 10.1021/jacs.6b08694.

[26] K. E. Ebbert, L. Schneider, A. Platzek, C. Drechsler, B. Chen, R. Rudolf, G. H. Clever, *Dalton T* 2019, DOI 10.1039/c9dt01814j.

[27] P. Howlader, P. Das, E. Zangrando, P. S. Mukherjee, *J Am Chem Soc* 2016, *138*, 1668–1676.

[28] R. Li, F. Fadaei-Tirani, R. Scopelliti, K. Severin, *Chem European J* 2021, *27*, 9439–9445.

[29] S. Sudan, R.-J. Li, S. M. Jansze, A. Platzek, R. Rudolf, G. H. Clever, F. Fadaei-Tirani, R. Scopelliti, K. Severin, *J Am Chem Soc* 2021, DOI 10.1021/jacs.0c12793.

4 A New Concept for Dissipative Guest Uptake based on Slow Double Cage Formation

4.1 Introduction

Mimicking nature to achieve its efficiency and beauty is one of the main goals of supramolecular chemistry, in particular the subfield of host-guest chemistry, as the idea of creating a cavity for smaller molecules to bind is inspired by enzymes. Most of the many developed cage systems are investigated in the thermodynamic ground state, however, living systems like cells exist outside this equilibrium. The chemical and supramolecular reactions inside cells are highly interconnected, stimuli responsive, and periodic. Keeping this dissipative state alive requires continuous supply of energy, usually chemical energy stored in molecules but also light. If this supply dries up, all reactions will slowly reach the thermodynamic ground state and lose their periodic and directional properties and the cell dies.

Of special interest are complex systems that exist in a dissipative state because of the closeness to natural systems and they are a step towards the even more complex class of oscillating reactions. Many such systems have been developed based on different compound classes, ranging from polymers and materials to drug-sized molecules.[1–4] Also, a few discrete cage systems with dissipative properties have been reported. An often-used approach is the combination of coordination cages or assemblies with either trichloroacetic acid or tribromoacetic acid (TBA). These relatively strong acids have the unique property that the conjugated base slowly disassembles to carbon dioxide and to a trichlorocarbanion or tribromocarbanion, respectively. These carbanions are strong Brønsted bases and are quickly protonated to chloroform or tribromomethane, hence reversing the initial action of the acid.

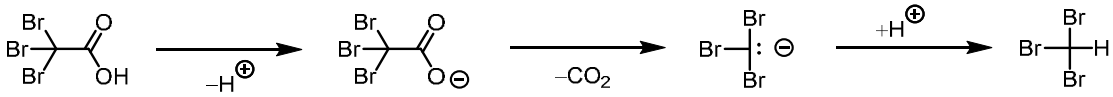

Figure 4.1. Deprotonation of TBA and subsequent decarboxylation and protonation to tribromomethane.

The group of Badjić used TBA to influence a system of three supramolecular building blocks **A**, **B** and **C** that can form different organic cages when combined with each other.[5] **A** is functionalized with aldehyde groups, **B** with aliphatic amines and **C** with aromatic amines. Because **B** is the stronger base than **C**, it is more likely to undergo dynamic imine bond formation with **A** to the cage **AB** but is also easier protonated when TBA is added. This leads to the temporary formation of cage $\mathbf{A_4C_4}$, which is reversed by slow decarboxylation of tribromoacetate. Following the common nomenclature in systems chemistry, cage **AB** plus free building block **C** (**AB** + **C**) is the *ground state*, TBA is the *fuel*, $\mathbf{A_4C_4}$ + **B** is the *transient state* and tribromomethane is the *waste*. The transient state can be kept if a constant supply of fuel is provided.

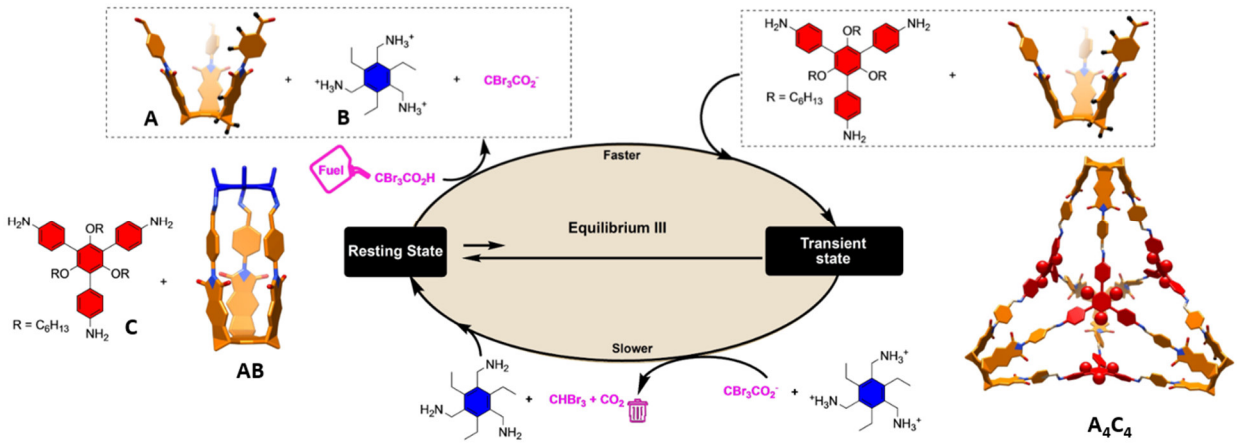

Figure 4.2. Dissipative supramolecular fuel waste cycle of Badjić and coworkers.[5] The graphic was taken from the article, which is open access, and slightly modified.

Many more applications of these kind of acids to create dissipative systems have been reported.[6] Hartley et al. uses a ring closing reaction to temporarily transform tetraethylene and pentaethylene glycol diacetic acids to hydrolytically unstable anhydrides. The so formed crown ethers as transient species can encapsulate alkali ions, which are then released again by the slow back reaction of the anhydrides with water.[7,8]

Nitschke et al. uses PPh_3 as strong binding ligand to temporarily disassemble a Cu(I) templated pseudorotaxane. Slow oxidation of PPh_3 by a catalyst and a pyridine-*N*-oxide as terminal oxidant leads to the reformation of the pseudorotaxane. While PPh_3 serves as fuel that keeps the transient state, which is the absence of the pseudorotaxane, alive, pyridine-*N*-oxide could be labeled as *negative fuel* that slowly breaks down the transient state.

Our group recently reported a waste free light fueled system in which the cage in the transient state can encapsulate a guest but the mixture of ring and cage in the ground state is not. The underlying ligand has a photoswitch (diazocine)[9] as backbone which significantly alters the shape of the ligand upon photoswitching. In the ground state the ligand ***cis*-L** self-assembles with Pd^{2+} to a mixture of Pd_2***cis*-L**$_4$, Pd_3***cis*-L**$_6$ and larger oligomers. Irradiation with UV light switches the ligand to the *trans* form, which then forms the Pd_2***trans*-L**$_4$ selectively. Irradiation with green light or simply letting the system stand at room temperature slowly reverses the process meaning that continuous irradiation with UV light is required to keep the transient state up. Interesting here is that the transient cage can bind a guest anion (2,6-naphthalene bissulfonate) meaning that the system can "do" something and is active in the dissipative state, which is not the case in the ground state.

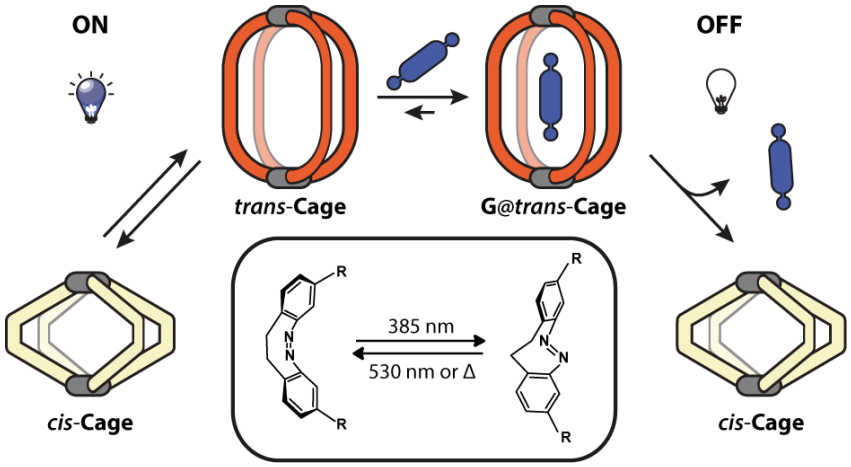

Figure 4.3. Schematic example of light fueled waste free dissipative guest binding.[10] The graphic was taken from the article, which is open access, and slightly modified.

4.2 Motivation

Transient species are found in almost every field of chemistry but of special interest are those, which 1) are detectable and exist in a humanly tangible timespan of seconds to days 2) differ from the ground state not only structurally or electronically but also in their interaction with other compounds **X**. This interaction should be orthogonal to the formation and decay of the transient species **T** as shown in Figure 4.4 and thus not be influenced by either the fuel or waste but only by the presence of **T**. This interaction or reaction with **X** must be reversible, otherwise it prevents the decay of **T**. Here, **A** can be the ground state that is transformed to **T** by a fuel, which is not shown here. **T** then slowly converts to **B**, which would then together with what the fuel converted to be the waste. Alternatively, **B** could be equal to **A**; in this case the transient state slowly returns to the ground state and the waste only consists of reacted fuel. **A** could also react to **T** without any additional fuel, in which case **A** may even be considered as fuel itself.

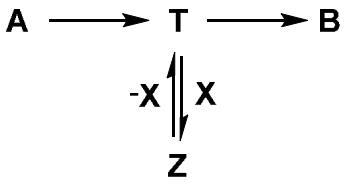

Figure 4.4. General scheme for a dissipative system with an active transient species **T**.

When trying to develop such a complex system with coordination cages an obvious function of **T** would be the ability to bind a guest as it is the case in the recently reported work of our group.[10] In this case, **X** would be the free guest, **Z** the host-guest complex and **T** the empty host.

Interpenetrated double cages as a subfield of supramolecular coordination cages may be a suitable platform as explained in the following. As mentioned in the main introduction of this work, double cages consist of two catenated lantern shaped, monomeric $Pd_2\mathbf{L}_4$ cages (with **L** being a banana shaped

bis-monodentate ligand with for example pyridine donor groups) resulting in one large structure with three small cavities. This formation is often templated by small anions like halogens,[11] nitrates[12] or tetrafluoroborates.[13] Therefore, even though the $Pd_4\mathbf{L}_8$ double cage is larger than its subcomponent $Pd_2\mathbf{L}_4$, it has smaller cavities and thus may not be able to bind large guests that would fit into the monomeric cage. This phenomenon has been thoroughly investigated by the group of Kuroda et al., who showed not only the size limit for the anionic guest in their double cage but also that the equilibrium between monomeric and double cage can be shifted to the former by adding a large excess of guest that fits the monomeric cage but is too large for the cavities in the double cage.[14]

Kuroda also first showed that while the double cage, without the larger guest, is thermodynamically favored, the monomeric cage forms faster.[12] The $Pd_2\mathbf{L}_4$ assembly only consists of six building blocks and the double cage being a $3X@Pd_4\mathbf{L}_8$ assembly consists of 15 building blocks. Thus, the supramolecular self-assembly to the monomeric cage happens faster. It is furthermore obvious that it is an intermediate step in the self-assembly of the double cage. Transformation from monomeric to double cage is initiated by random encapsulation of a free banana-shaped ligand **L** by the monomeric cage as our own, still unpublished data suggests (ion mobility MS based study of former postdoc Dr. Ananya Baksi). The binding affinity of the uncharged **L** to the monomeric cage is likely rather low, which, in addition to the low concentration of free **L**, causes this slow double cage formation process. The group of Hiraoka investigated the kinetic mechanism of the formation of the double cage reported by Kuroda.[15]

It should therefore be possible to temporarily encapsulate a large guest inside a quickly forming monomeric $Pd_2\mathbf{L}_4$ cage which slowly self-assembles to an interpenetrated double cage with is unable to bind the guest in its small cavities. Using the nomenclature defined in Figure 4.4, the ground state **A** would then be the free guest. The fuels added are the ligand **L** and the Pd^{2+} cations, which form a monomeric cage as transient species **T**, which can dynamically form a host-guest complex **Z** with the guest **X**. The slowly formed double cage is the waste and constitutes together with the now not anymore encapsulated guest state **B**.

Even though Kuroda at al. already conducted in-depth research in this area,[14] testing this established hypothesis will be of great value for the field of systems chemistry as it provides a new, and still rare way of dissipative guest binding.

4.3 Results and Discussion

4.3.1 Double cage formation and characterization

The already in Chapter 2 and 3 investigated bis-monodentate ligand $\mathbf{L}^{hex}$ (or $\mathbf{L}^{C}$) with a carbazole backbone, hexyl chain, pyridinyl donor groups and alkynyl spacers forms with $[Pd(CH_3CN)_4](BF_4)_2$ a monomeric cage $Pd_2\mathbf{L}^{hex}_4$. When either chloride or bromide, for example as TBA salt, is added, a mixture of monomeric and $3X@Pd_4\mathbf{L}^{hex}_8$ (X being either Cl^- or Br^-) double cage is formed. The more halide is added, the more the equilibrium shifts towards double cage, however, at some point rings and catenanes $\{trans\text{-}[(PdX_2)_2\mathbf{L}^{hex}_2]\}_n$ ($n \in \{1,\ldots,3\}$), which precipitate leaving free ligand in solution, form because the halides compete with the pyridinyl groups for the palladium.[11]

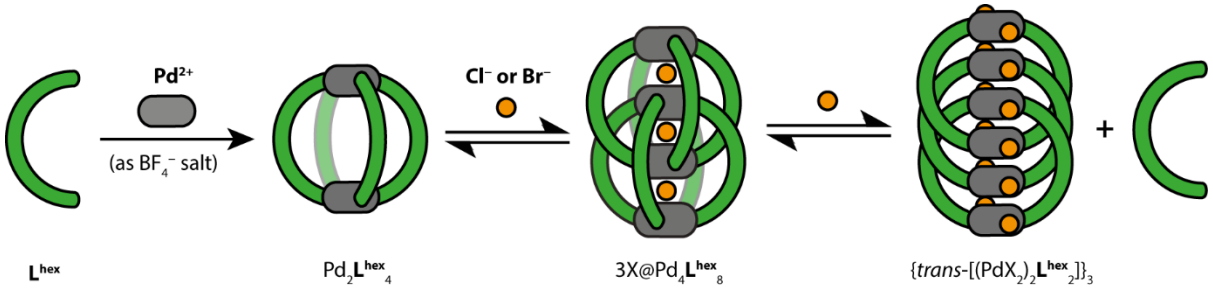

Figure 4.5. Schematic overview of monomeric cage formation and subsequent halide triggered formation of higher aggregates.

We found that nitrate behaves similar to the halides. When 0.5 eq. $Pd(NO_3)_2$ is added to a solution of $\mathbf{L}^{hex}$ in CD_3CN, the directly measured ^1H NMR mainly shows a set of signals very similar to that of $Pd_2\mathbf{L}^{hex}_4$ with BF_4^- counter anions, indicating that the monomeric cage is formed. But also detectable are minor signals matching free $\mathbf{L}^{hex}$ and also strongly upfield and downfield shifted signals similar to the halide templated double cages. Additionally, precipitate was noticed, indicating that rings and maybe catenanes with nitrate binding to Pd form. The sample was briefly heated resulting in an intensity increase of signals assigned to double cage and free ligands and decrease of signals assigned to monomeric cage. The amount of precipitate also increased. These observations suggest that first the monomeric cage $Pd_2\mathbf{L}^{hex}_4$ with nitrate counter anions forms which then slowly transforms to the double cage $3(NO_3)@Pd_4\mathbf{L}^{hex}_8$ and the insoluble rings and catenanes as indicated by the precipitate and the ^1H signals of the free ligand. To check whether the NO_3^- molecules fit inside the rather small cavities of this double cage, a model was drawn and optimized using r^{2}SCAN-3c, see Figure 4.44. Compared to the model from Ref. 11 the symmetry is broken in a way that the $Pd(pyridine)_4$ units are shifted so that the four palladium atoms are not on the same axis and the NO_3^- anions are tilted so that the free electron pairs of the oxygen atoms point towards the palladium centers. The model suggests that a $3(NO_3)@Pd_4\mathbf{L}^{hex}_8$ could indeed exist, although the same double cage but with either chloride or bromide in the pockets would likely be thermodynamically more favorable. An according ESI mass

spectrum proving the existence of the double cage with only nitrate anions was obtained, see Figure **4.19**.

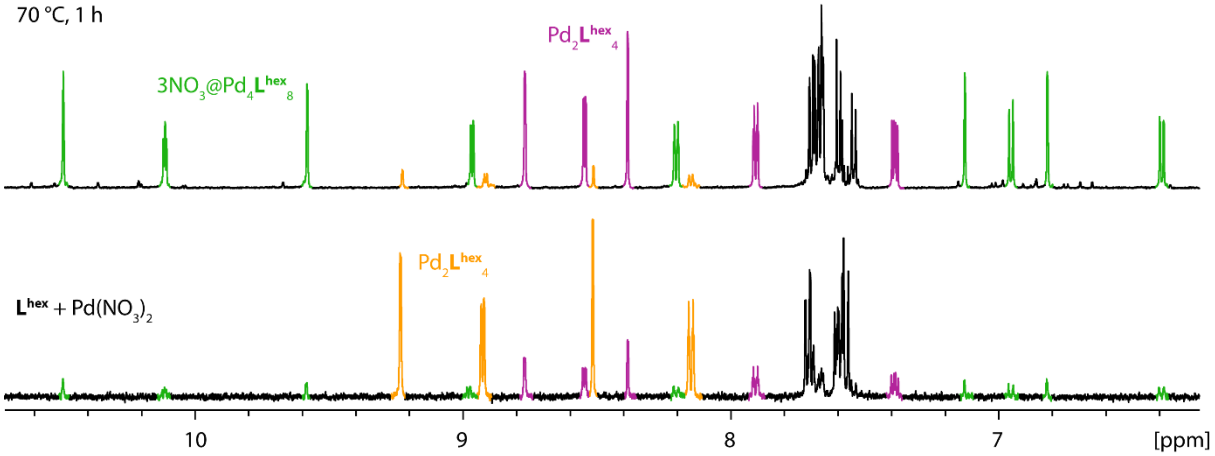

Figure 4.6. Excerpt of ^{1}H NMR (500 MHz bottom, 600 MHz top) of bottom: quickly formed $Pd_2\mathbf{L}^{hex}_4$ (orange) from combination of $\mathbf{L}^{hex}$ and 0.5 eq. $Pd(NO_3)_2$ and minor signals assigned to $3(NO_3)@Pd_4\mathbf{L}^{hex}_8$ (green) and free $\mathbf{L}^{hex}$ (purple); top: same solution after heating for 1 h at 70 °C now showing mainly double cage and free ligand.

$\mathbf{L}^{hex}$ and its metallosupramolecular assemblies show limited solubility in acetonitrile making studies with varying concentrations and host guest experiments difficult. Therefore, $\mathbf{L}^{EG4}$ with a tetraethylene glycolyl chain instead of a hexyl chain was synthesized, see Figure 4.7. $\mathbf{L}^{EG4}$ is well soluble in almost any solvent and allows working at high concentrations. Concentration dependency is a highly relevant factor for both kinetics and thermodynamics of self-assembly, especially for larger systems like $3(NO_3)@Pd_4\mathbf{L}^{EG4}_8$, which consists of 15 reversibly bound building blocks. Therefore, the fast monomeric cage and the subsequent slow double cage formation was monitored with ^{1}H NMR spectroscopy at room temperature for 24 h for different overall $\mathbf{L}^{EG4}$ concentrations, c_L, namely 0.8, 1.6, 3.2 and 6.4 mM. To reach the thermodynamic minimum, the samples were heated at 70 °C for 24 h afterwards. The time dependent ^{1}H NMR spectra and the final spectrum showing the equilibrated state for each ligand concentration are shown in Figure 4.24 to Figure 4.27.

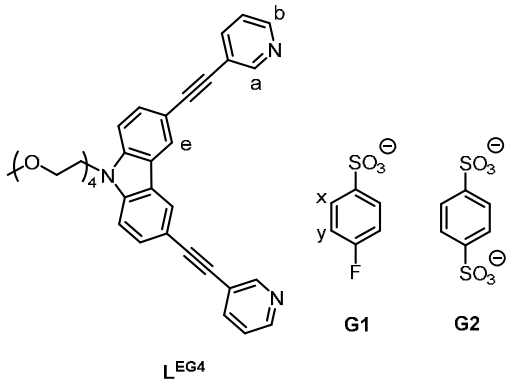

Figure 4.7. Organic bis-monodentate ligand $\mathbf{L}^{\mathbf{EG4}}$ and mono- or disulfonated guests **G1** and **G2**.

In general, it was observed that the $Pd_2\mathbf{L}^{\mathbf{EG4}}{}_4$ signals first increase, then decrease. The signals belonging to $3(NO_3)@Pd_4\mathbf{L}^{\mathbf{EG4}}{}_8$ increase delayed as expected, but then either plateau, only slowly increase further or even decrease. Interestingly, in the spectrum of each sample after heating all monomeric and double cage signals disappeared and a new set of signals is observed. The new signals are partially broad, overlapping and of varying intensity but very similar for all concentrations. Of the sample with c_L = 3.2 mM a ^{1}H DOSY NMR spectrum and a mass spectrum was measured, which are shown in Figure ***4.22*** and Figure 4.23. The ^{1}H DOSY NMR spectrum is rather inconclusive due to overlapping of signals of different species. The solution likely contains a mixture of $Pd_x\mathbf{L}^{\mathbf{EG4}}{}_y(NO_3)_z$ oligomers with different size. In the mass spectrum no monomeric or double cage could be detected; instead, the spectrum shows species with about 5000 to 6500 u. For comparison for the double cage species $[3(NO_3)@Pd_4\mathbf{L}^{\mathbf{EG4}}{}_8]^{5+}$ a mass of around 5089 u was measured, see Figure 4.19. As NO_3^- can also bind to Pd, it is assumed that these higher aggregates are either catenanes similar to those reported in Ref. 11 or polymers in which $\mathbf{L}^{\mathbf{EG4}}$ ligands are connected via $Pd(NO_3)_2$ complexes. Both would cause a release of free $\mathbf{L}^{\mathbf{EG4}}$, for which the ^{1}H NMR signal at 7.2 ppm could be an indication. Apparently both the monomeric and the double cage are only kinetic products and the actual thermodynamic products are the not further investigated higher aggregates.

The concentrations of monomeric and double cage were obtained by comparing the integrals of ^{1}H NMR signals of the according species with an internal standard and are shown in Figure 4.8. In general, it was observed for all samples that the measured concentrations of $Pd_2\mathbf{L}^{\mathbf{EG4}}{}_4$ and $3(NO_3)@Pd_4\mathbf{L}^{\mathbf{EG4}}{}_8$ are much lower than theoretically possible. For example, with c_L = 3.2 mM the theoretically possible $Pd_2\mathbf{L}^{\mathbf{EG4}}{}_4$ concentration is 800 µM and the one for $3(NO_3)@Pd_4\mathbf{L}^{\mathbf{EG4}}{}_8$ is 400 µM, but the observed concentrations are much lower, see Figure 4.8. This is because the systems are monitored while being out of chemical equilibrium and many different subspecies are present simultaneously, but in too low concentrations or as oligomeric mixtures, and thus not detectable by NMR.

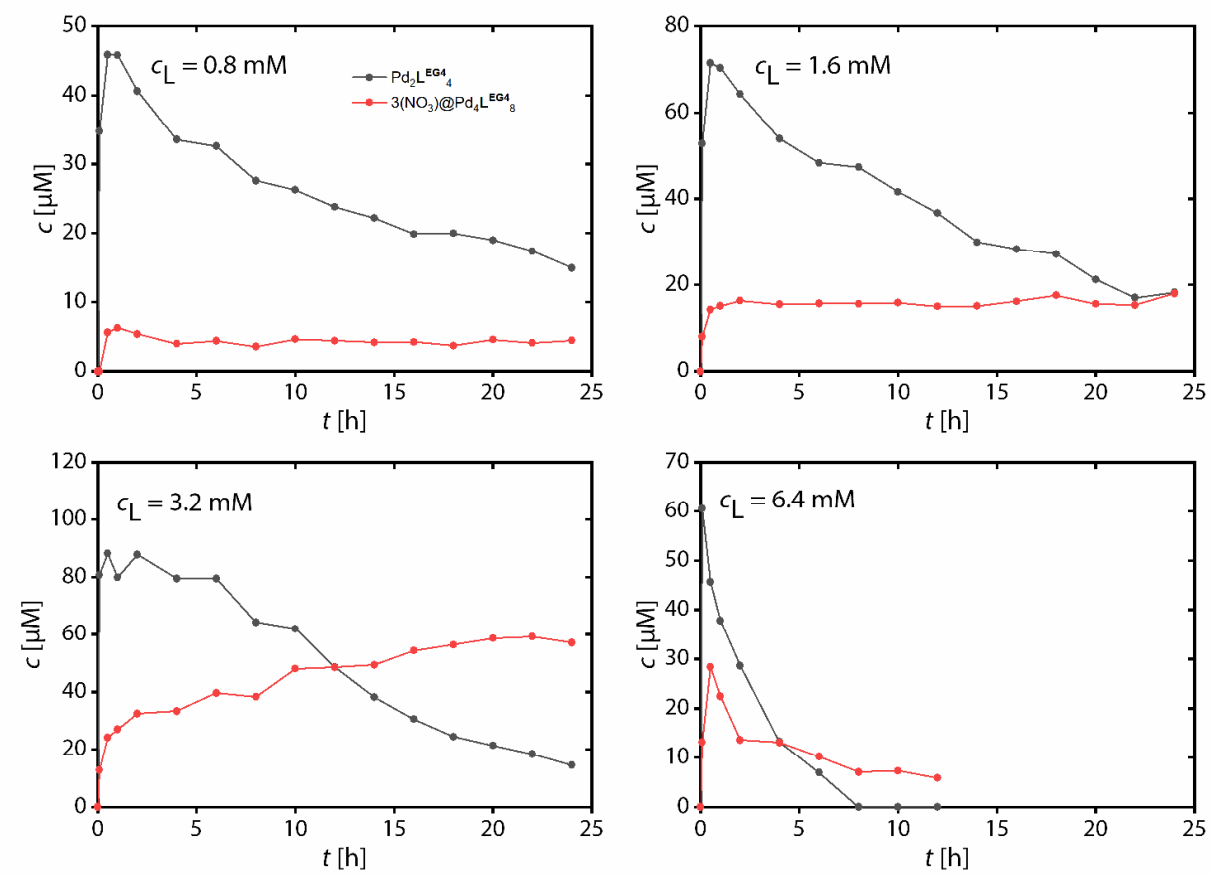

Figure 4.8. Monomeric and double cage concentration over time after the addition of the according amount of $Pd(NO_3)_2$ to $\mathbf{L^{EG4}}$ solutions with varying concentrations.

It was observed for all samples that the signals belonging to the monomeric cage first quickly increase and then slowly decrease. The maximum of c_M (monomeric cage $Pd_2\mathbf{L^{EG4}}_4$ concentration) is reached within the first hour for all concentrations but faster for the higher concentrations. The maximal c_M concentration $c_{M,max}$ is only slightly dependent on the overall $\mathbf{L^{EG4}}$ concentration c_L: c_L = 0.8 mM ⇒ $c_{M,max}$ = 46 µM; c_L = 1.6 mM ⇒ $c_{M,max}$ = 71 µM; c_L = 3.2 mM ⇒ $c_{M,max}$ = 88 µM; c_L = 6.4 mM ⇒ $c_{M,max}$ = 60 µM. Lower c_L obviously leads to lower c_M, however, very high c_L lead to a faster formation of higher aggregates like the double cage and therefore also causes lower c_M. Of these four investigated concentrations c_L = 3.2 mM leads to the highest $c_{M,max}$. The depletion of monomeric cage is different for each c_L. While the half-life time (the time at which $c_M = c_{M,max}/2$ is reached) is reached after 13 h for the lower three concentrations and only with c_L = 6.4 mM it is reached after about 1.5 h. The remaining c_M relative to $c_{M,max}$ after 24 h differs for all concentrations: c_L = 0.8 mM ⇒ 33 %; c_L = 1.6 mM ⇒ 25 %; c_L = 3.2 mM ⇒ 16 %; c_L = 6.4 mM ⇒ 0 %. At higher concentrations the probability to form assemblies with more building blocks is increased. The double cage signals also raise fast at first but then either reach a plateau for c_L = 0.8 mM and c_L = 1.6 mM or increase slowly for the next 23 h and then reach a plateau for c_L = 3.2 mM or in the case of c_L = 6.4 mM even quickly decrease. For c_L = 6.4 mM signal

integration after 12 h was not possible because here already higher aggregates start to form at room temperature. Using low ligand concentration leads to a prolongation of the transient state, and a high concentration leads to a shorting of the same, which may both be unwanted.

Using the ligand concentration of 3.2 mM the experiment was also conducted at a higher temperature of 55 °C. Concentrations are plotted in Figure 4.9 and ^{1}H NMR spectra are shown in Figure 4.28. The initial $Pd_2\mathbf{L}^{\mathbf{EG4}}{}_4$ concentration is much higher as compared to at room temperature reaching 222 µM. This is because the self-assembly is accelerated by the higher temperature. However, the monomeric cage concentration drops quickly again and reaches 25 µM after one hour, which is only 11.2 % of the highest measured concentration. The $3(NO_3)@Pd_4\mathbf{L}^{\mathbf{EG4}}{}_8$ concentration increases fast at first at first, then slower but still faster and reaches higher concentrations than at room temperature. This shows that the higher the temperature the shorter the lifetime of the transient state.

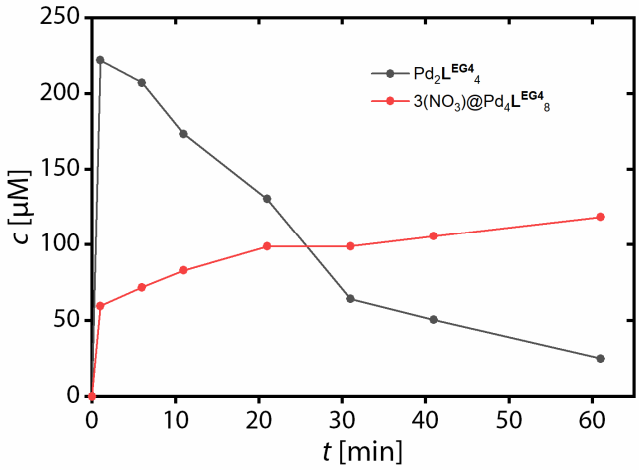

Figure 4.9. Monomeric and double cage concentration over time after the addition of the according amount of $Pd(NO_3)_2$ to a 3.2 mM $\mathbf{L}^{\mathbf{EG4}}$ solution at 55 °C.

4.3.2 Guest binding studies

For the aim of achieving dissipative guest binding, a guest molecule that binds inside $Pd_2\mathbf{L}^{\mathbf{EG4}}{}_4$ but not the according double cage and does not interact with the higher aggregates is required. Aliphatic and aromatic sulfonate anions have proven to be suitable guests for these kind of coordination cages as they are negatively charged and non-coordinative and thus do not compete with the pyridine donor groups. This study focusses on 4-fluorobenzenesulfonate, here labeled as **G1**, which is only monosulfonated and contains a fluorine atom, which allows tracking via ^{19}F NMR spectroscopy. Benzene-1,4-disulfonate (**G2**), which is twofold negatively charged and should therefore bind stronger to the cage, was also investigated for comparison. Skeletal formulae of both guests are shown in Figure ***4.7***.

^{1}H NMR titration experiments were conducted to determine the binding affinities of each guest to the $Pd_2\mathbf{L}^{\mathbf{EG4}}{}_4$ monomeric cage with BF_4^- counter anions. The titration experiment regarding **G1** is shown in Figure 4.29. The ^{1}H NMR signal of proton *a* experiences a downfield shift upon guest addition. Likely the sulfonate group of **G1** is close to the Pd complex inducing a slight decrease in electron density in that area. The downfield shifting of the signal assigned to proton *b* could either also be explained by this or could indicate outside binding, alternatively. The signal of proton *e* shifts upfield, indicating a close contact with **G1** as well. he ^{1}H NMR signals of **G1** at lower equivalents are broadened and strongly downfield shifted as compared to the ones of free **G1** indicating that a high percentage of **G1** in solution is bound to the cage. Upon further addition of **G1** the signals become sharper and are more upfield, getting closer to their initial positions. With higher amount of guest more and more guest is not bound to the cage. No precipitation during the titration was observed owing to the good solubility of $\mathbf{L}^{\mathbf{EG4}}$. To find out whether **G1** can also bind outside the cage the interaction of **G1** with the double cage $3(NO_3)@Pd_4\mathbf{L}^{\mathbf{EG4}}{}_8$ was investigated, see Figure 4.32. Here, the addition of **G1** only caused a shift of the signal of outside pointing proton *b*, indicating that **G1** can also bind outside. As **G1** binds in fast exchange to $Pd_2\mathbf{L}^{\mathbf{EG4}}{}_4$ and 1:2 guest binding can be considered, Bindfit was used to determine the binding constants of $K_{\mathbf{G1}}{}^{\mathbf{11}}$ = 9594 L · mol^{-1} (4.1 % error) and $K_{\mathbf{G1}}{}^{\mathbf{12}}$ = 889 L · mol^{-1} (1.3 % error).[16]

The mass spectrum measured from the sample after addition of six eq. **G1** shows signals of both $[Pd_2\mathbf{L}^{\mathbf{EG4}}{}_4+\mathbf{G1}]^{3+}$ and $[Pd_2\mathbf{L}^{\mathbf{EG4}}{}_4+2\mathbf{G1}]^{2+}$, see Figure 4.31. The results of an NMR based job plot experiment, see Figure 4.36, indicate a 1:1 binding, but, if the second guest binds rather weakly, as the NMR titration suggests, the effect of it may not influence the job plot. From theoretical investigations it can be assumed that if a second guest binds the monomeric cage, it will likely bind outside, see Section 4.6 for further discussion.

G2 binds $Pd_2\mathbf{L}^{\mathbf{EG4}}{}_4$ in slow exchange as expected.[17] The high binding constant is explained by **G2** being twofold negatively charged and the sulfonate groups are in para position to each other and thus close to the Pd^{2+} centers. After a few steps of titrating **G2** to $Pd_2\mathbf{L}^{\mathbf{EG4}}{}_4$ precipitation is observed. The stacked ^{1}H NMR spectra are shown in Figure 4.33.

4.3.3 Dissipative Guest Binding

To test whether dissipative guest binding is possible in the temporarily formed monomeric cage $Pd_2\mathbf{L}^{\mathbf{EG4}}{}_4$ **G1** was chosen because it is fluorinated which makes it possible to trace the experiment by ^{19}F NMR spectroscopy. Both $\mathbf{L}^{\mathbf{EG4}}$ and Pd^{2+} are considered as fuel in system, however, for practical reasons $\mathbf{L}^{\mathbf{EG4}}$ was provided in excess. ^{1}H and ^{19}F NMR spectra of a CD_3CN solution (0.55 mL) containing **G1** (1 eq., 0.8 mM), excess $\mathbf{L}^{\mathbf{EG4}}$ (12 eq., 9.6 mM) and 1,3,5-trimethoxybenzene (2 eq., 1.6 mM) as reference standard were measured. The ^{1}H NMR spectrum shows sharp signals of **G1**, as expected. The ^{19}F NMR

spectrum shows one sharp signal at –115.5 ppm. 58.7 µL of a 15 mM $Pd(NO_3)_2$ stock solution in CD_3CN (2 eq.) was added and the ^1H and ^{19}F NMR spectra were directly recorded. The system was monitored by measuring further ^1H and ^{19}F NMR spectra after 1, 3, 7 and 24 hours. The addition of $Pd(NO_3)_2$ and subsequent monitoring was repeated two times. The chemical shift of the ^{19}F NMR signal of **G1** is plotted against time in Figure 4.10. The concentrations of $\mathbf{L}^{\mathbf{EG4}}$, $Pd_2\mathbf{L}^{\mathbf{EG4}}{}_4$ and $3NO_3@Pd_4\mathbf{L}^{\mathbf{EG4}}{}_8$ over time are shown in Figure 4.11. The according NMR spectra are shown in Figure 4.37 and Figure 4.38.

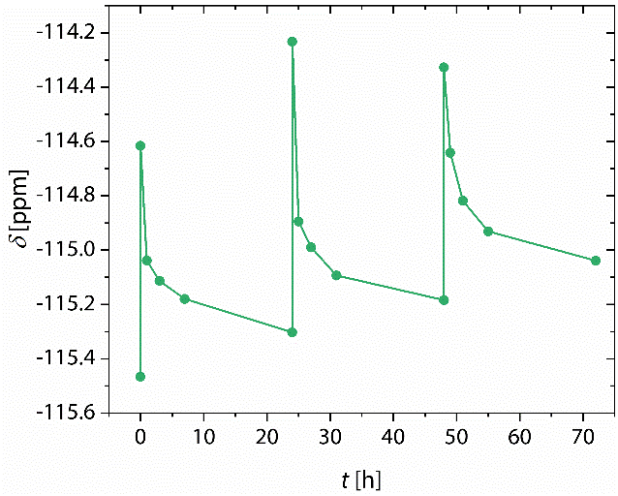

Figure 4.10. Chemical shift of the ^{19}F NMR signal of **G1** over time.

After the initial addition, the ^{19}F NMR spectrum exhibits broadening and a downfield shift to approximately –114.6 ppm, suggesting a significant proportion of **G1** is bound in HG complexes. It is important to note that immediately following the addition of $Pd(NO_3)_2$, numerous intermediate subspecies like $Pd_2\mathbf{L}^{\mathbf{EG4}}{}_2$ that could potentially bind **G1** exist, albeit undetectable by NMR spectroscopy. However, an hour later, a sharper signal at –115.0 ppm, which is a bit more upfield shifted (but still significantly different than the signal of the free guest), is observed, indicating consolidation of the host-guest species with $Pd_2\mathbf{L}^{\mathbf{EG4}}{}_4$. The from the ^1H spectrum obtained concentration of $Pd_2\mathbf{L}^{\mathbf{EG4}}{}_4$ is 43 µM, which is much lower and decreases faster than observed in the experiment without **G1** and without excess of $\mathbf{L}^{\mathbf{EG4}}$, see Figure 4.8. The according concentration of $3NO_3@Pd_4\mathbf{L}^{\mathbf{EG4}}{}_8$ is right after $Pd(NO_3)_2$ addition at 42 µM and reaches its preliminary maximum of 85 µM after three hours, which is significantly higher than observed in the previous experiment. Another difference is that here the concentration decreases quickly again. In this experiment the excess of $\mathbf{L}^{\mathbf{EG4}}$ accelerates the formation of higher aggregates, which explains the aforementioned observations.

The ^{19}F NMR signal was measured at –115.3 ppm after 24 h, which is close to its initial position of –115.5 ppm showing that most **G1** molecules are unbound again. In the ^1H NMR spectrum after 24 h almost no signs of $Pd_2\mathbf{L}^{\mathbf{EG4}}{}_4$ and $3NO_3@Pd_4\mathbf{L}^{\mathbf{EG4}}{}_8$ are detectable; the spectrum only shows the signals belonging to free $\mathbf{L}^{\mathbf{EG4}}$ and **G1** and the signals of the latter are close to their initial positions but still

broadened. It is assumed that higher oligomers form but remain colloidal. As can be seen in Figure ***4.10***, after the addition of $Pd(NO_3)_2$ the concentration of free $\mathbf{L^{EG4}}$ immediately drops but then slightly increases again over the next 24 h, which supports this hypothesis.

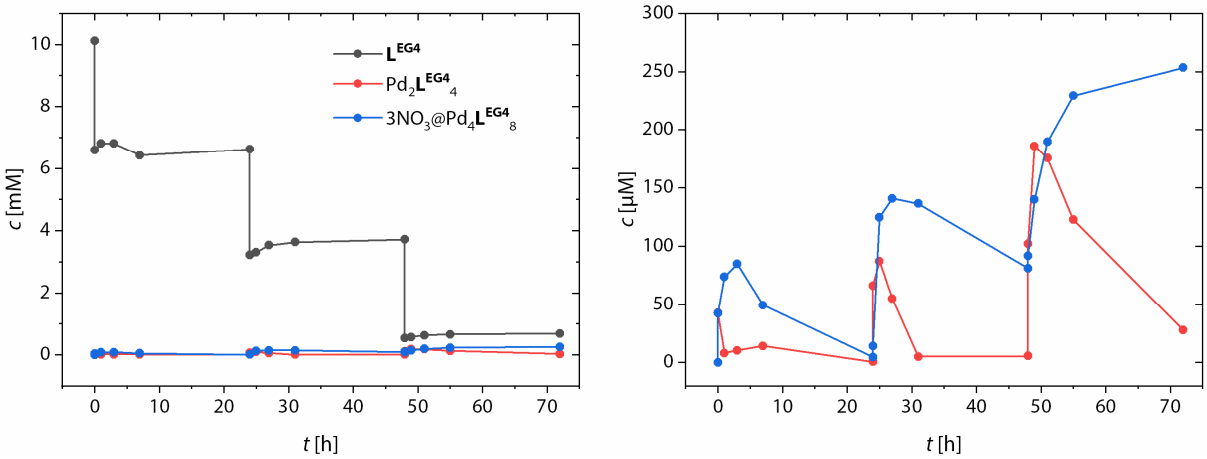

Figure 4.11. Concentration of free ligand $\mathbf{L^{EG4}}$, monomeric cage $Pd_2\mathbf{L^{EG4}}_4$ and double cage $3NO_3@Pd_4\mathbf{L^{EG4}}_8$ over time. $\mathbf{L^{EG4}}$ was provided in excess and 2 guest eq. $Pd(NO_3)_2$ was added every 24 h.

To test whether the transient state could be renewed by further providing fuel to the system the same amount of $Pd(NO_3)_2$ (2 eq.) was added two more times and after each time the system was monitored for 24 h. Each time the system was fueled the ^{19}F signal of the guest broadened and shifted downfield and then slowly sharpened and shifted back upfield again. The most downfield shifted ^{19}F signal was observed in the second cycle right after $Pd(NO_3)_2$ addition, which could be caused by measurement inaccuracies as the system changes quickly within the first seconds. In general, the ^{19}F signal is with each cycle more downfield shifted as more free $\mathbf{L^{EG4}}$ is consumed and the solution is diluted and therefore the formation of higher aggregates is slowed down and more monomeric cage remains longer in solution. This can also be seen in Figure 4.11, which shows that both the $Pd_2\mathbf{L^{EG4}}_4$ and $3NO_3@Pd_4\mathbf{L^{EG4}}_8$ concentration is higher and decreases slower in each cycle.

For comparison the same experiment was repeated with the stronger binding **G2**. The according ^1H NMR spectra are shown in Figure 4.39. Interestingly, after the first addition of $Pd(NO_3)_2$ a large amount of precipitate, which is likely $\mathbf{G2}@Pd_2\mathbf{L^{EG4}}_4$ was noticed. The ^1H NMR spectrum shows only minor signs of the presence of $\mathbf{G2}@Pd_2\mathbf{L^{EG4}}_4$ and $3NO_3@Pd_4\mathbf{L^{EG4}}_8$ in solution and no signals belonging to empty $Pd_2\mathbf{L^{EG4}}_4$. After 24 h no free **G2** could be detected. Further cycles of adding $Pd(NO_3)_2$ led to the observation of $3NO_3@Pd_4\mathbf{L^{EG4}}_8$ in a similar amount as compared to the previous experiment with **G1**, see Figure 4.12, and even empty $Pd_2\mathbf{L^{EG4}}_4$ could be detected in the second and third cycle. The free binding enthalpy together with the lattice energy of $[\mathbf{G2}@Pd_2\mathbf{L^{EG4}}_4](NO_3)_2$ must be so high that it is thermodynamically favored over the double cage and over the $Pd_n\mathbf{L^{EG4}}_n(NO_3)_{2n}$ species. This shows

another boundary of this method for dissipative guest binding: If the guest binds too strongly, aggregation to larger, interlocked assemblies is inhibited.

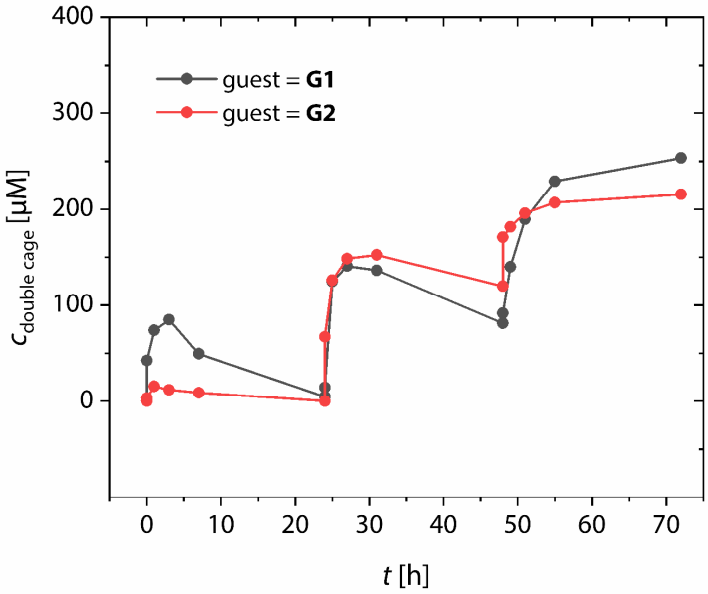

Figure 4.12. $3(NO_3)@Pd_4\mathbf{L}^{EG4}{}_8$ concentration in the dissipative system using either **G1** or **G2**.

Next, it was tested whether the transient state could be held up by constant supply of fuel. For this $\mathbf{L}^{EG4}$ was again provided in excess but this time after the first addition of 2 eq. $Pd(NO_3)_2$ every 15 minutes 0.24 eq. of it was further added. An NMR spectrum was recorded directly after addition and after seven minutes. The experiment was conducted twice to record both the ^1H and the ^{19}F NMR spectrum. The according NMR spectra are shown in Figure 4.40 and Figure 4.41, the concentrations of free $\mathbf{L}^{EG4}$, $Pd_2\mathbf{L}^{EG4}{}_4$ and $3NO_3@Pd_4\mathbf{L}^{EG4}{}_8$ are plotted over time in Figure 4.13 and Figure 4.14 shows the chemical shift of the ^{19}F NMR signal of **G1**. After the first addition of the fuel $Pd_2\mathbf{L}^{EG4}{}_4$ increases to 100 µM and would then slowly decrease again over time but the regular addition of $Pd(NO_3)_2$ leads to new monomeric cage formation and it was possible to keep the $Pd_2\mathbf{L}^{EG4}{}_4$ concentration nearly constant for two hours.

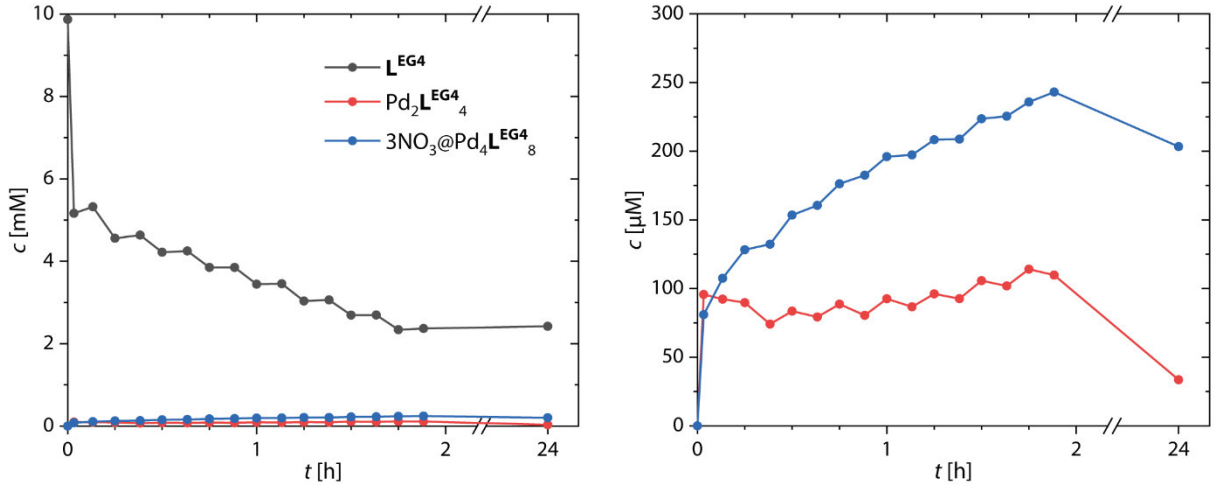

Figure 4.13. Upholding of the transient state by frequent addition of small amounts of $Pd(NO_3)_2$. Shown are the concentrations of free ligand $\mathbf{L}^{EG4}$, monomeric cage $Pd_2\mathbf{L}^{EG4}{}_4$ and dimeric cage $3NO_3@Pd_4\mathbf{L}^{EG4}{}_8$ over time.

The amount of $3NO_3@Pd_4\mathbf{L}^{EG4}{}_8$ increases quickly at first, similar to $Pd_2\mathbf{L}^{EG4}{}_4$, and then slowly further accumulates and reaches about 250 µM after 2 h. The ^{19}F NMR signal of **G1** behaves as expected. After addition of the first 2 eq. $Pd(NO_3)_2$ a downfield shift to –114.45 ppm and signal broadening is observed. The signal shifts back to about –114.81 ppm within the first 30 min and could be held constant from there on showing that the transient state can be kept up by constant fuel supply. The system was left at room temperature for 22 h causing the $Pd_2\mathbf{L}^{EG4}{}_4$ concentration to drop to 33 µM and that of $3NO_3@Pd_4\mathbf{L}^{EG4}{}_8$ to 203 µM. The ^{19}F NMR signal shifted back to –115.03 ppm. Subsequently, the sample was heated at 70 °C for another 24 h to reach thermal equilibrium. Afterwards, only traces of the monomeric and double cage were detectable and the ^{19}F NMR signal was detected at –115.24 ppm showing nearly complete relaxation to the ground state of the system. Interestingly, no signs of the oligomers are observed which may be due to the still large excess of free $\mathbf{L}^{EG4}$.

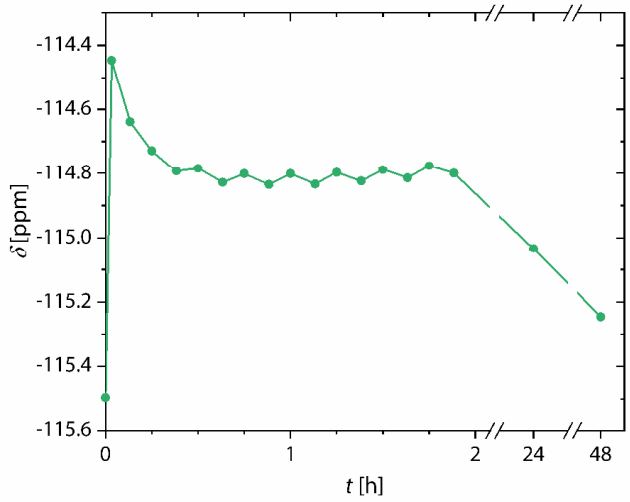

Figure 4.14. Upholding of the transient state by frequent addition of small amounts of $Pd(NO_3)_2$. Shown is the chemical shift of the ^{19}F NMR signal of **G1**.

Whether the system can fully relax back to its ground state meaning that the guest does not interact with any other species as it is the case before the addition of fuel, the experiment was repeated with a stochiometric amount of $\mathbf{L^{EG4}}$. Now the observed initial $Pd_2\mathbf{L^{EG4}}_4$ concentration is much higher, up to 275 µM, than compared to the experiments where $\mathbf{L^{EG4}}$ is used in excess, because here less donor groups compete for the Pd^{2+}. After 24 h the monomeric cage concentration has decreased to approximately 14 % of the highest measured concentration but still at 38 µM. At first the ^{19}F NMR signal jumped from its initial position at –115.50 ppm to –113.97 ppm and then slowly shifted upfield again. After 24 h it is found at –114.85 ppm and the signal got sharper again, see Figure 4.43. With the aim to fully relax the system so that the guest shows no more interaction with any other species the sample was heated for 24 h at 70 °C. However, while no more monomeric or double cage was observed and the familiar pattern of ^1H NMR signals assigned to the oligomers appeared the ^{19}F NMR signal of **G1** was at –115.05 ppm, still 0.45 ppm away from the initial position. This shows that the guest weakly interacts with the waste, which are the oligomers.

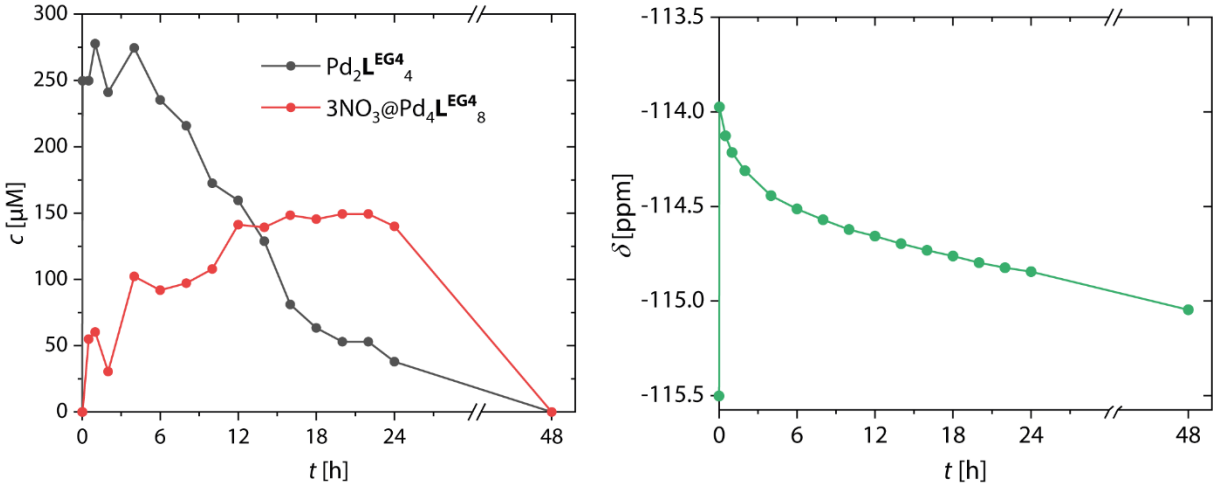

Figure 4.15. Concentration of $Pd_2\mathbf{L}^{\mathbf{EG4}}{}_4$ and $3NO_3@Pd_4\mathbf{L}^{\mathbf{EG4}}{}_8$ (left) and chemical shift of the ^{19}F NMR signal of **G1** when only 4 eq. $\mathbf{L}^{\mathbf{EG4}}$ and 2 eq. $Pd(NO_3)_2$ is added to 1 eq. **G1** ($c_{\mathbf{G1}}$ = 0.8 mM). For the last 24 h the sample was heated at 70 °C.

4.4 Conclusion and Outlook

The arc shaped bis-monodentate ligand $\mathbf{L}^{\mathbf{EG4}}$ self-assembles upon addition of $Pd(NO_3)_2$ quickly to a $Pd_2\mathbf{L}^{\mathbf{EG4}}{}_4$ monomeric cage with a large cavity. This cage can take up a suitable guest, such as a sulfonated aromatic anion. But the monomeric cage slowly dimerizes to a quadruply catenated double cage with three smaller pockets, in which the guest cannot bind. The double cage even further converts to a so far unknown assembly, likely colloidal oligomers. The system can therefore be labeled as dissipative with the host guest complex **G1**@$Pd_2\mathbf{L}^{\mathbf{EG4}}{}_4$ being the transient species and $\mathbf{L}^{\mathbf{EG4}}$ and Pd^{2+} being the positive fuel meaning that they keep up the transient state. NO_3^- can be labeled as negative fuel as it templates the double cage formation or probably partially binds the palladium covalently in the unknown assembly and therefore contributes to the diminishing of the transient state. The double cage and the unknown assembly are the waste that slowly accumulate in the system. Figure 4.16 shows this new concept schematically.

It was shown that the fuel could either be provided in large batches, so that each batch of fuel causes first a high amount of guest to be bound and then a slow release of the guest over time or fuel could be added constantly to keep the amount of bound guest constant.

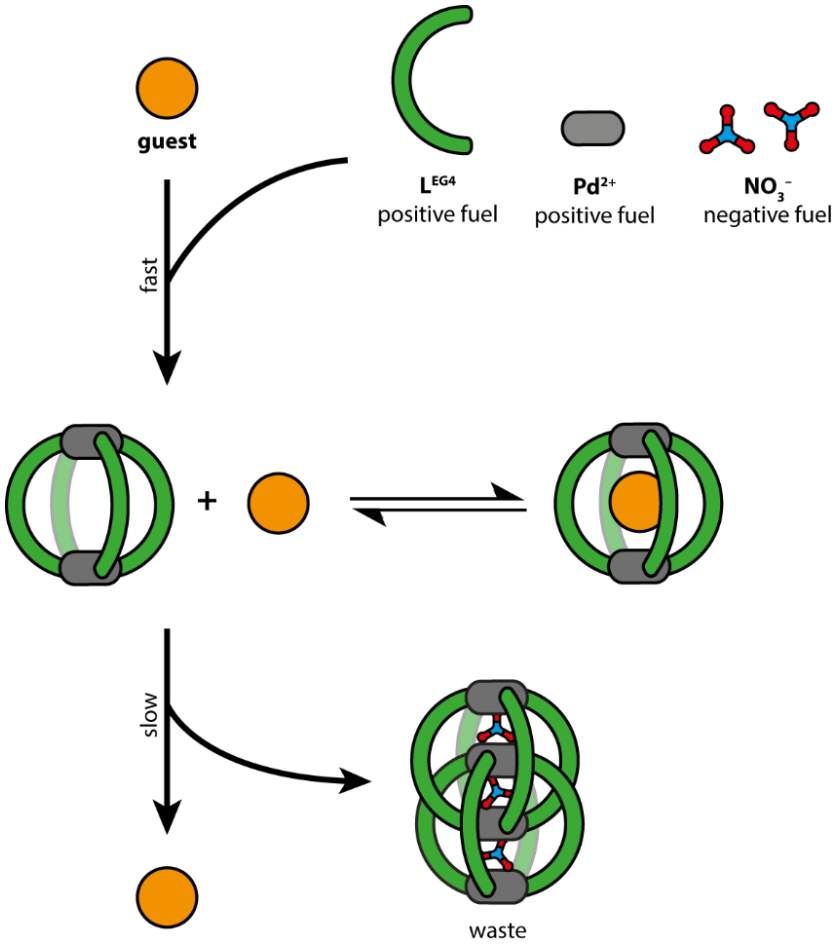

Figure 4.16. Concluding simplified scheme of the here investigated dissipative host-guest binding system.

The parameters and boundaries of the system's functioning were tested. The lower the overall concentration the longer the transient state could be kept up, yet even at a ligand concentration of 0.8 mM the unknown assembly is still the thermodynamic product. At higher concentrations the transient state is rather short-lived. A similar behavior is observed at a higher temperature: At 55 °C the lifetime of the transient state is not only drastically reduced but also the measured concentration of discrete species is higher because the self-assembly processes are accelerated. If the chosen guest binds the monomeric cage too strongly, dimerization is inhibited, as was shown with **G2**.

To conclude, a new method for dissipative guest binding based on known metallosupramolecular concepts was found and investigated. It greatly supplements the small but rapidly growing pool of dissipative systems, which could be the basis for even more complex systems, slowly approximating the complexity of nature.

Further things to try would be the use of a less soluble ligand than $\mathbf{L^{EG4}}$, perhaps even the traditional $\mathbf{L^{hex}}$ with hexyl side chains. Here the thermodynamic product is rather insoluble in acetonitrile and therefore it can precipitate so that the system's waste can be removed physically. Here it could be the

problem that the guest may precipitate together with the waste, which is problematic as it would not allow the reactivation of the transient state when new fuel is applied.

The here conducted experiments are rather proofs of concept and show the very basic properties and variables of this system. For an in-depth understanding further kinetic studies to determine rate constants could be tried, although the system is already highly complicated and the self-assemblies to the different species are multi-step processes. Variation of ligand and guest may lead to a cleaner outcome, for instance the avoidance of oligomer formation.

4.5 Experimental Details

4.5.1 Syntheses and characterizations

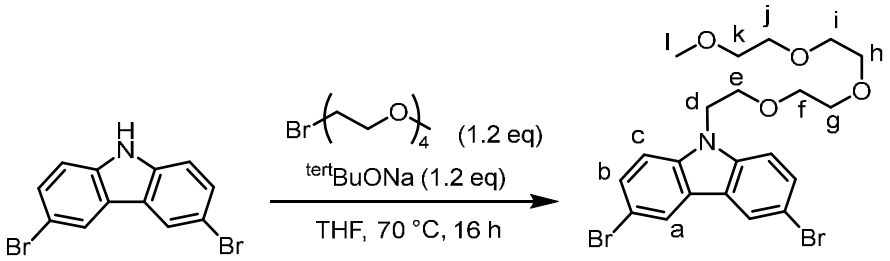

Scheme 4.1. Synthesis of 3,6-dibromo-9-EG4-carbazole.

3,6-Dibromocarbazole (1 eq, 6 mmol, 1950 mg) and ^{tert}BuONa (1.2 eq, 7.2 mmol, 808 mg) were dissolved in 30 mL THF. While the solution was stirring at 70 °C, triethylene glycol 2-bromoethyl methyl ether (1.2 eq, 7.2 mmol, 1.51 mL) was slowly added. After 16 h the reaction mixture was cooled down to room temperature. The solvent was removed in vacuo and the product was purified with automated flash chromatography (DCM/MeOH, 0 % to 5 %). The product is a yellow oil (4.5 mmol, 2301 mg, 74 %).

^{1}H NMR (600 MHz, 298 K, CD_3CN) of 3,6-dibromo-9-EG4-carbazole: δ [ppm] = 8.25, (s, 2H, a), 7.58 (d, *J* = 8. 7 Hz, 2H, b), 7.50 (d, *J* = 9.0 Hz, 2H, c), 4.48 (t, *J* = 5.3 Hz, 2H, d), 3.82 (t, J = 5.2 Hz, 2H, e), 3.23 – 3.62 (m, f-l).

^{13}C{^{1}H} NMR (126 MHz, 298 K, DMSO-d_6) of 3,6-dibromo-9-EG4-carbazole: δ [ppm] = 140.86, 129.86, 124.36, 124.10, 112.83, 112.51, 72.561, 71.569, 71.14, 71.04, 70.91, 70.09, 58.87, 44.52, 32.34.

APCI-MS of 3,6-dibromo-9-EG4-carbazole: measured: 538.00, calculated for $[C_{21}H_{25}Br_2NO_4+Na]^+$: 538.0016.

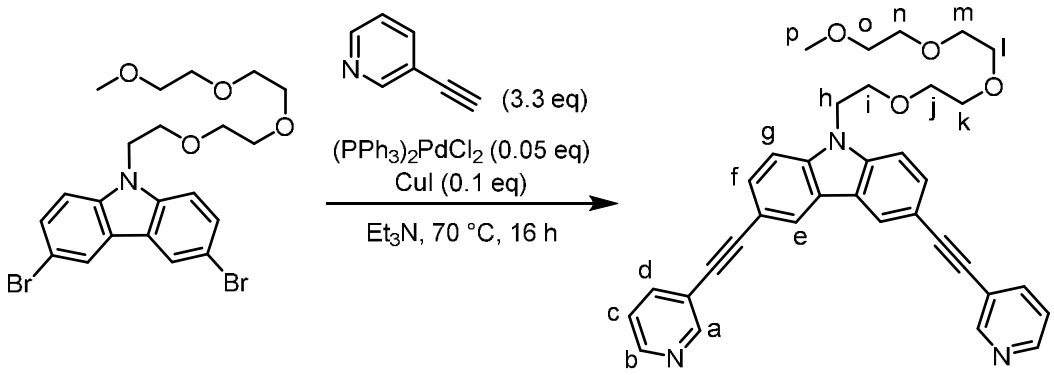

Scheme 4.2. Synthesis of **L^{EG4}**.

3,6-dibromo-9-EG4-carbazole (1 eq, 4.5 mmol, 2301 mg) and 3-ethynylpyridine (3.3 eq, 14.7 mmol, 1520 mg) were dissolved in 20 mL Et_3N and degassed with three *freeze-pump-thaw*-cycles. Then, $(PPh_3)_2PdCl_2$ (0.05 eq, 223 µmol, 157 mg) and CuI (0.1 eq, 447 µmol, 85.1 mg) were added and three more *freeze-pump-thaw*-cycles were performed. The reaction mixture was then stirred at 70 °C for 16 h. The reaction mixture was taken up with EtOAc and filtrated over celite. The solvent was removed *in vacuo* and solids were purified with automated flash chromatography (EtOAc/MeOH, 0% to 10%). The product was finally purified via gel permeation chromatography and was obtained as yellow oil (3.85 mmol, 2156 mg, 85 %).

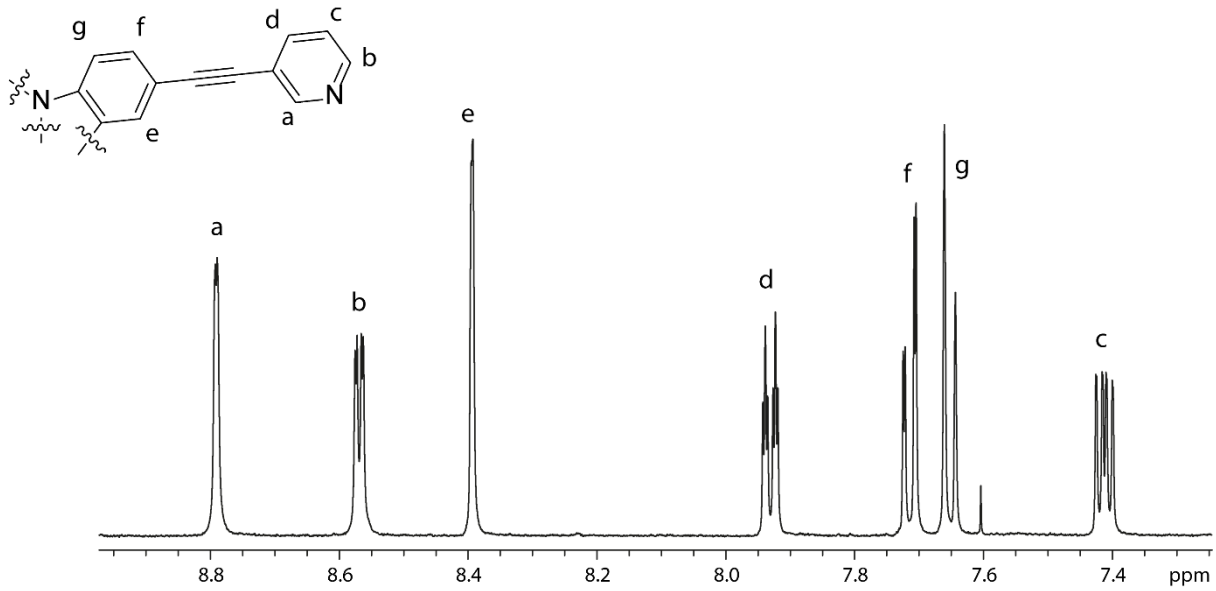

Figure 4.17. Aromatic region of ^{1}H NMR spectrum of **L^{EG4}** and proton labeling.

^{1}H NMR (500 MHz, 298 K, CD_3CN) of L^{EG4}: δ [ppm] = 8.79 (s, 2H, a), 8.57 (d, J = 4.9 Hz, 2H, b), 8.40 (s, 2H, e), 7.93 (d, J = 8.1 Hz, 2H, d), 7.716 (d, J = 8.4 Hz, 2H, f), 7.65 (d, J = 8.5 Hz, 2H, g), 7.41 (dd, J_1 = 8.1 Hz, J_2 = 4.8 Hz, 2H, c), 4.56 (t, J = 5.2 Hz, 2H, h), 3.88 (t, J = 5.3 Hz, 2H, i), 3.23 – 3.48 (m, j-p).

^{13}C{^{1}H} NMR (126 MHz, 298 K, CD_3CN) of L^{EG4}: δ [ppm] = 152.87, 149.50, 142.28, 139.08, 130.71, 125.13, 124.39, 123.25, 121.52, 113.97, 111.51, 94.45, 85.43, 72.52, 71.56, 71.11, 71.02, 70.98, 70.86,

70.06, 58.81, 44.45, 29.68. Of 22 expected signals 23 were counted, which could be explained by an impurity.

ESI-MS of L^{EG4}: measured: 560.2526, calculated for $[C_{35}H_{33}N_3O_4+H]^+$: 560.2544.

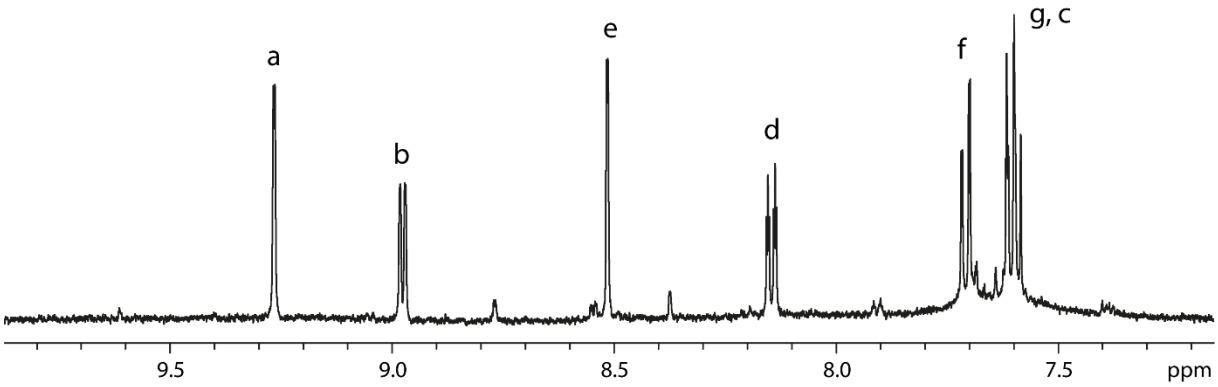

Figure 4.18. Aromatic region of ^{1}H NMR spectrum of $[Pd_2\mathbf{L}^{EG4}_4]^{4+}$ with nitrate counter anions.

^{1}H NMR (500 MHz, 298 K, CD_3CN) of $Pd_2\mathbf{L}^{EG4}_4$**:** *δ* [ppm] = 9.27 (s, 2H, a), 8.98 (d, *J* = 4.9 Hz, 2H, b), 8.51 (s, 2H, e), 8.15 (d, *J* = 8.1 Hz, 2H, d), 7.71 (d, *J* = 8.4 Hz, 2H, f), 7.60 (m, 4H, g,c), 4.51 (t, *J* = 5.2 Hz, 2H, h), 3.88 (t, *J* = 5.3 Hz, 2H, i), 3.23 – 3.48 (m, j-p).

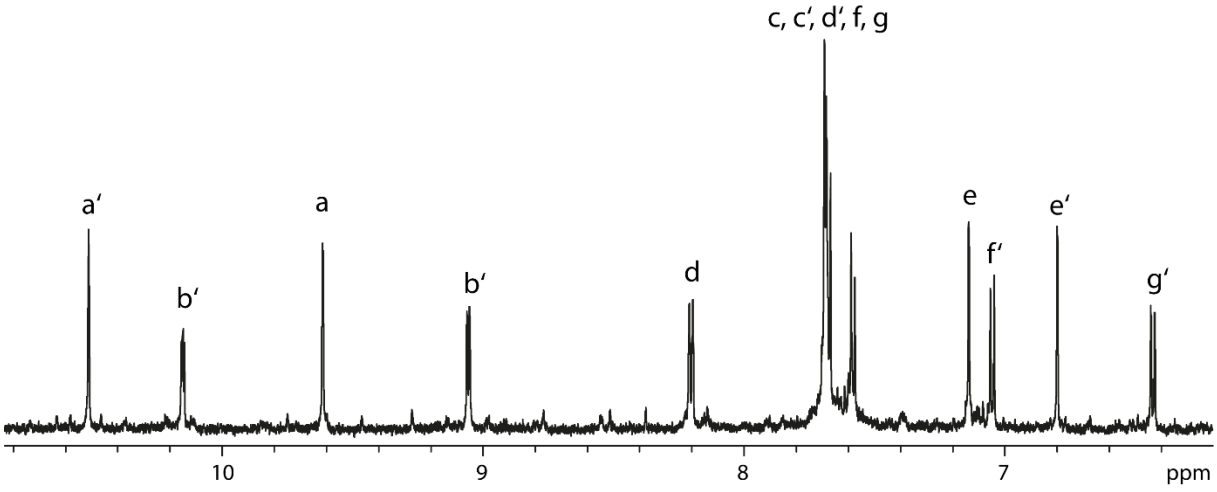

^{1}H NMR (500 MHz, 298 K, CD_3CN) of $[3NO_3@Pd_2\mathbf{L}^{EG4}_4]$**:** *δ* [ppm] = 10.51 (s, 2H, a'), 10.15 (d, *J* = 4.6 Hz, 2H, b'), 9,61 (s, 2H, a), 9.06 (d, *J* = 6.0 Hz, 2H, b), 8.20 (d, *J* = 8.2 Hz, 2H, d or d') 7.54-7.78 (m, b,b'), 7.14 (s, 2H, e or e'), 7.05 (d, *J* = 8.6 Hz, 2H, f' or f), 6.80 (s, 2H, e' or e), 6.43 (d, *J* = 8.5 Hz, 2H, g' or g), 4.52 (t, *J* = 5.2 Hz, 2H, h), 3.88 (t, *J* = 5.3 Hz, 2H, i), 3.23 – 3.48 (m, j-p).

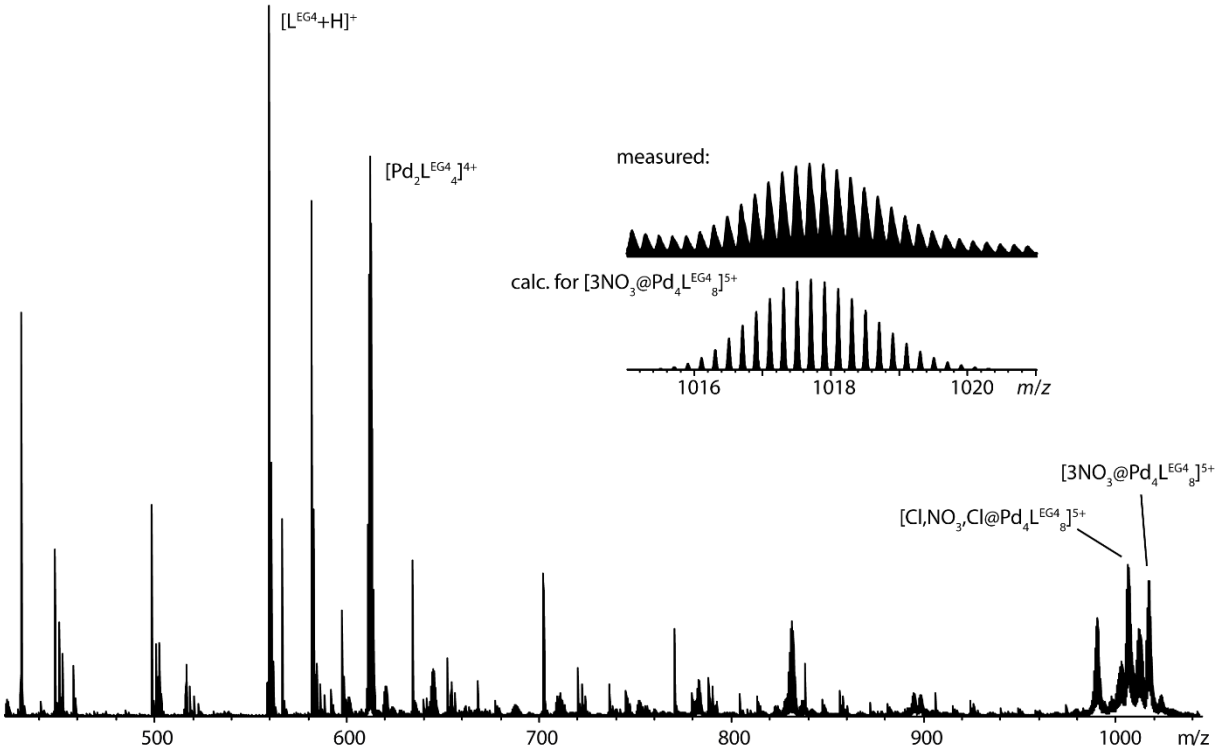

Figure 4.19. ESI mass spectrum of $3NO_3@Pd_4\mathbf{L}^{\mathbf{EG4}}{}_8$.

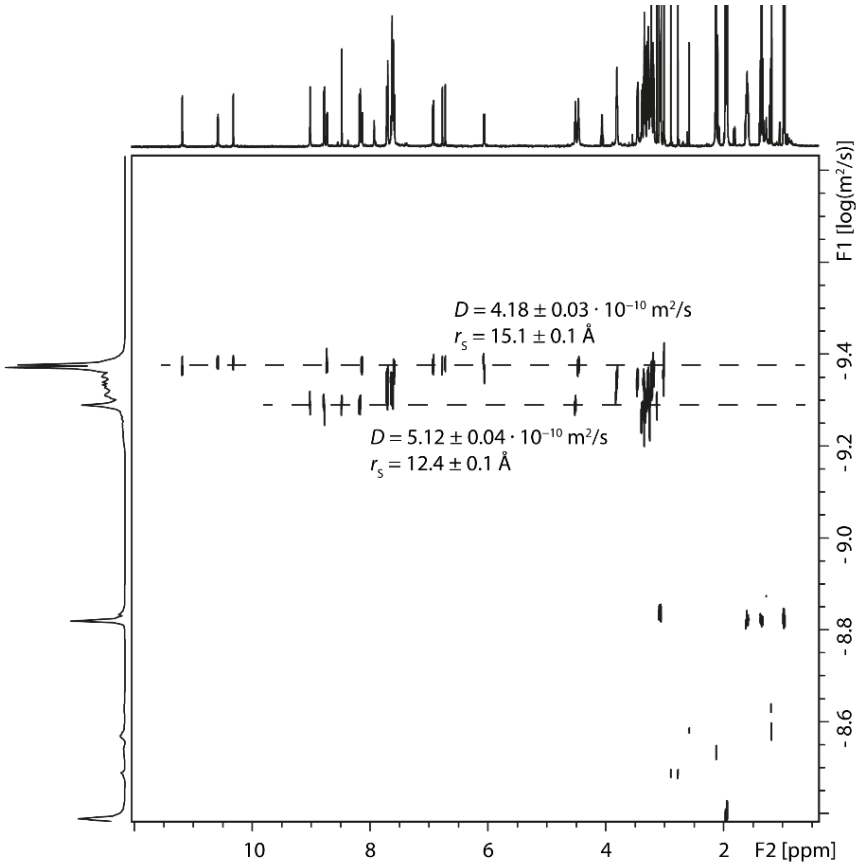

Figure 4.20. ^{1}H DOSY NMR of a mixture of $Pd_2\mathbf{L}^{\mathbf{EG4}}{}_4$ and $3Br@Pd_4\mathbf{L}^{\mathbf{EG4}}{}_8$.

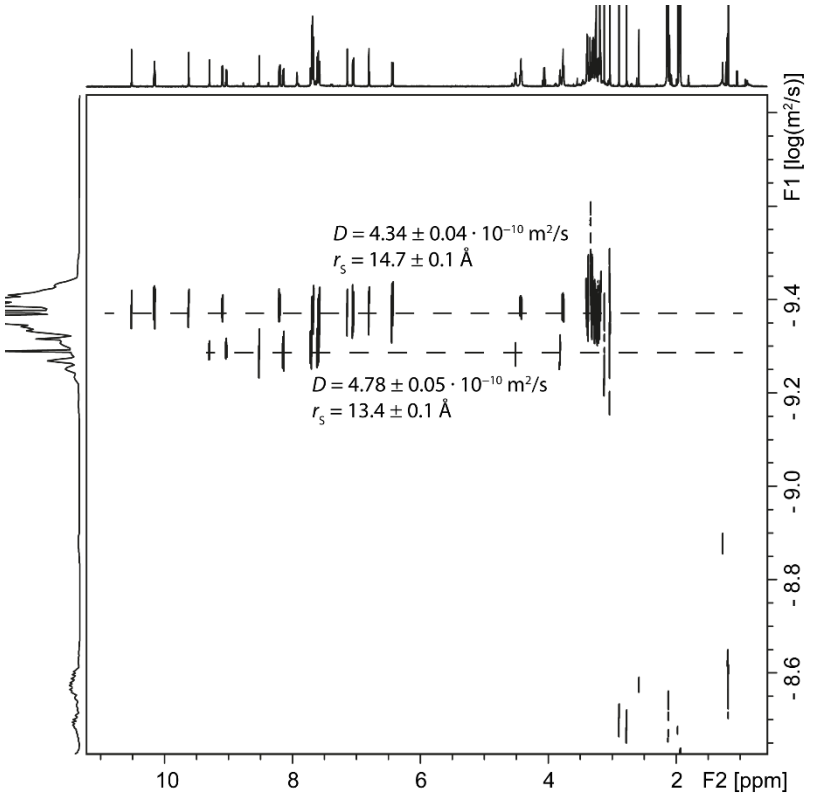

Figure 4.21. ^{1}H DOSY NMR of a mixture of $Pd_2\mathbf{L}^{\mathbf{EG4}}{}_4$ and $3NO_3@Pd_4\mathbf{L}^{\mathbf{EG4}}{}_8$.

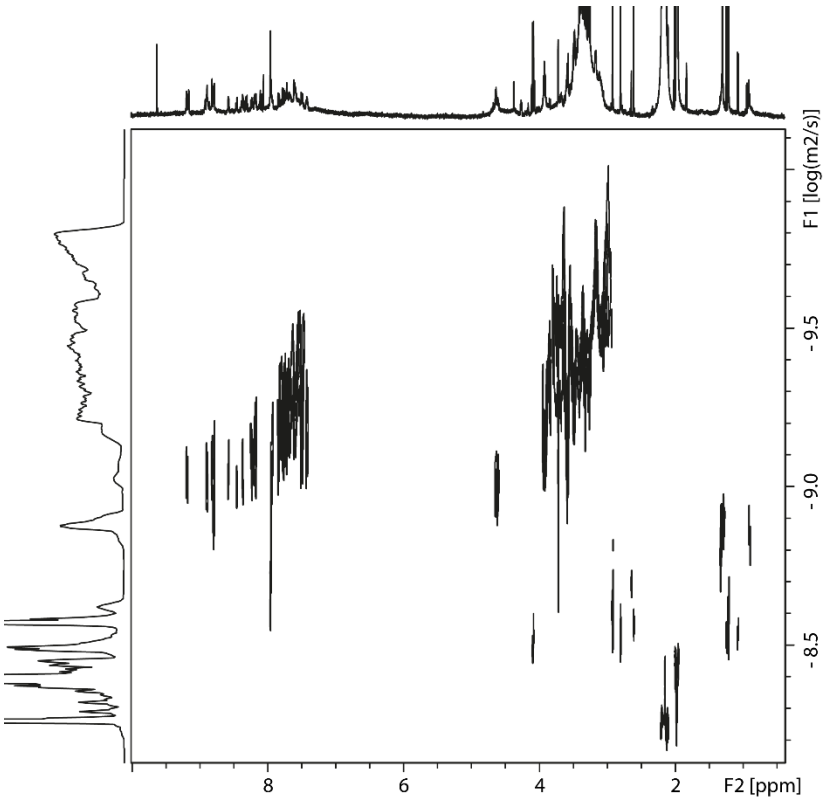

Figure 4.22. ^{1}H DOSY NMR of the product of $\mathbf{L}^{\mathbf{EG4}}$ and $Pd(NO_3)_2$ after heating at 70 °C over night.

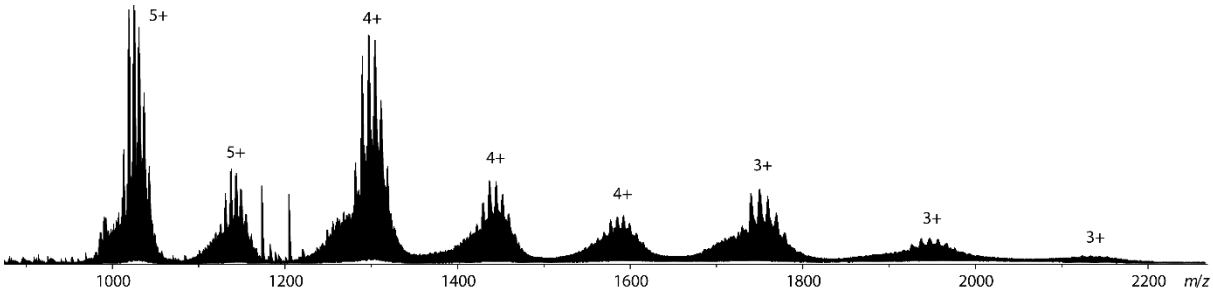

Figure 4.23. Excerpt of the ESI mass spectrum of a mixture of a sample containing $\mathbf{L^{EG4}}$ and $Pd(NO_3)_2$ after heating at 70 °C over night. The species' charges are given for each cluster of signals.

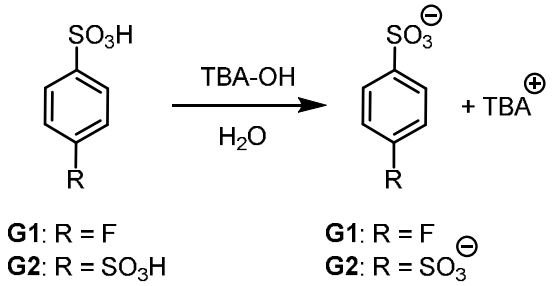

Scheme 4.3. Preparation of **G1** and **G2**.

G1 and **G2** were bought as sulfonic acids and were neutralized with tetrabutylammonium hydroxide (TBA-OH) in water. Removal of the solvent yielded the tetrabutylammonium sulfonate salts as white solids.

4.5.2 Formation of $3NO_3@Pd_4\mathbf{L^{hex}}_8$

To a solution of $\mathbf{L^{hex}}$ in CD_3CN (0.88 µmol, 521 µL, 1.69 mM) a solution of $Pd(NO_3)_2$ in CD_3CN was added. (0.44 µmol, 29.3 µL, 15 mM) immediately yielding a monomeric $Pd_2\mathbf{L^{hex}}_4$ cage solution (0.22 µmol, 550 µL, 0.4 mM). ^{1}H NMR spectrum was directly recorded. The sample was heated at 70 °C for 1 h and measured again. Spectra are shown in Figure 4.6.

4.5.3 Formation of $3NO_3@Pd_4\mathbf{L^{EG4}}_8$ at different concentrations

Four CD_3CN solutions with the volumes 535, 521, 491 and 433 µL containing 0.44, 0.88, 1.76 and 3.62 µmol $\mathbf{L^{EG4}}$ were prepared. Each sample also contained 0.44 µmol 1,3,5-trimethylbenzene as standard. To these samples 14.7, 29.3, 58.7 and 117 µL of a 15 mM $Pd(NO_3)_2$ stock solution was added and the ^{1}H NMR spectra were directly recorded. After that, the samples were measured again every 30 min for the following 24 h. The temperature during the experiment was 25 °C constantly. Finally, the samples were heated over night at 70 °C. The according spectra are shown in Figure 4.24 toFigure ***4.27***.

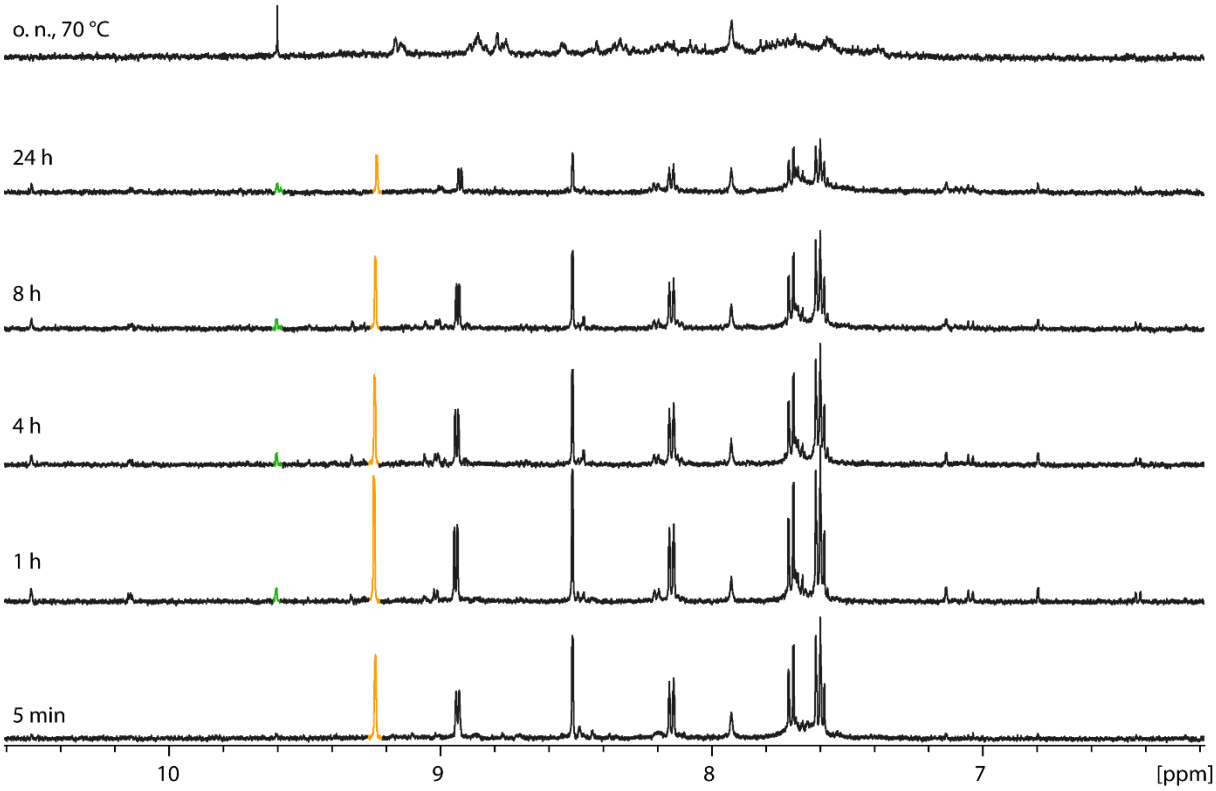

Figure 4.24. ^{1}H NMR spectra showing the transformation of $Pd_2\mathbf{L}^{\mathbf{EG4}}{}_4$ to $3NO_3@Pd_4\mathbf{L}^{\mathbf{EG4}}{}_8$ and higher aggregates. Overall ligand concentration: 0.8 mM.

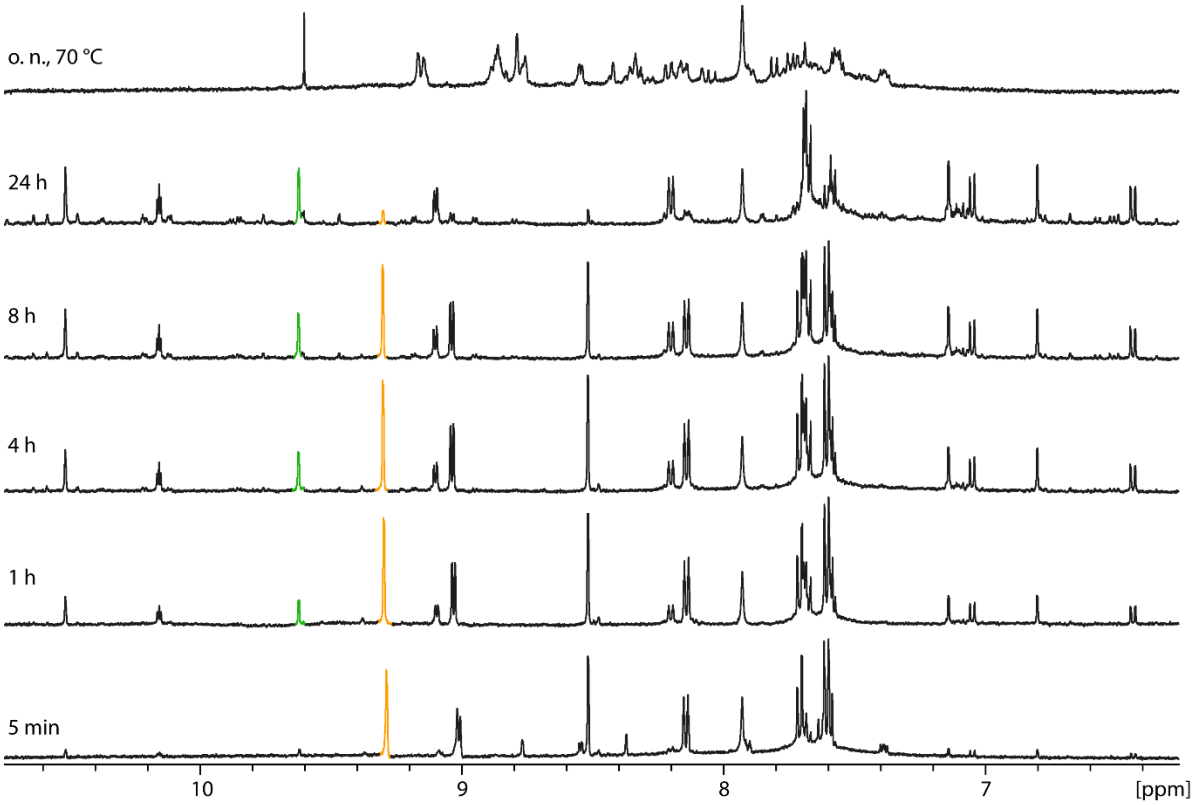

Figure 4.25. ^{1}H NMR spectra showing the transformation of $Pd_2\mathbf{L}^{\mathbf{EG4}}{}_4$ to $3NO_3@Pd_4\mathbf{L}^{\mathbf{EG4}}{}_8$ and higher aggregates. Overall ligand concentration: 1.6 mM.

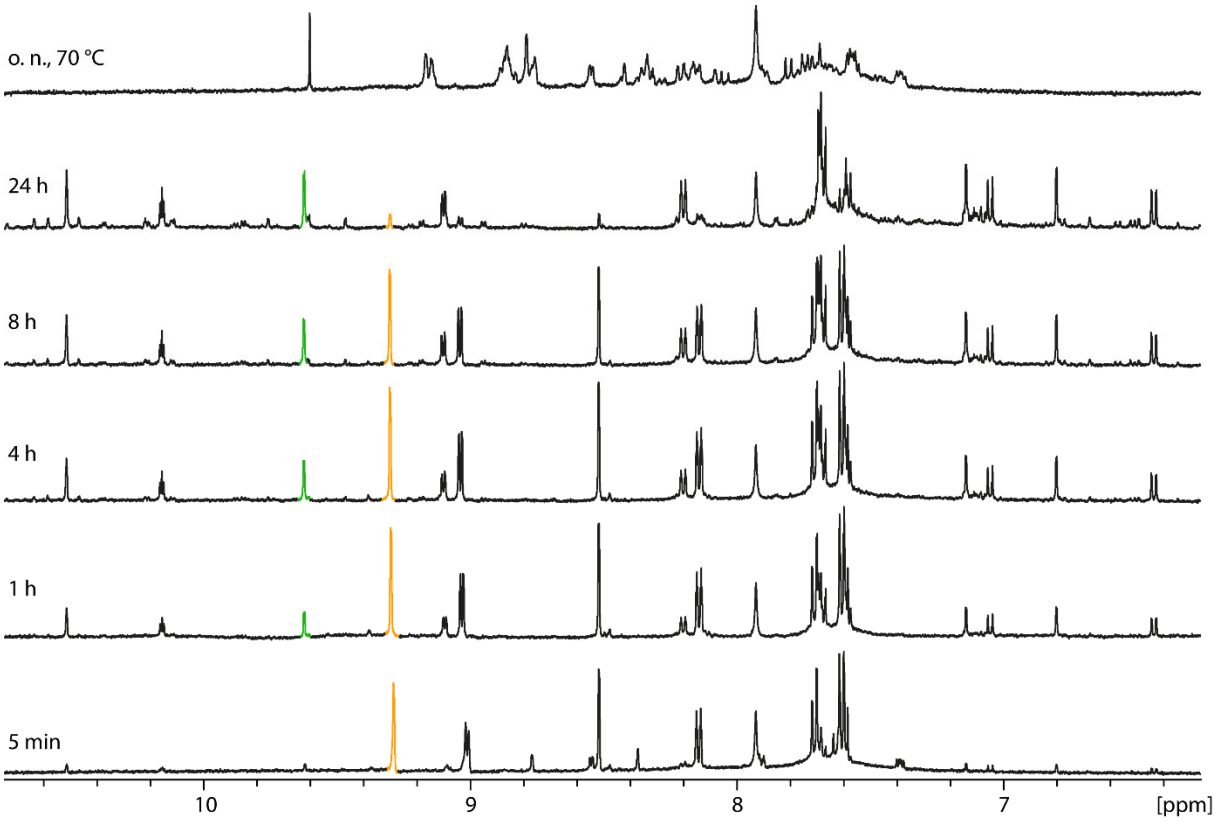

Figure 4.26. ^{1}H NMR spectra showing the transformation of $Pd_2\mathbf{L}^{\mathbf{EG4}}{}_4$ to $3NO_3@Pd_4\mathbf{L}^{\mathbf{EG4}}{}_8$ and higher aggregates. Overall ligand concentration: 3.2 mM.

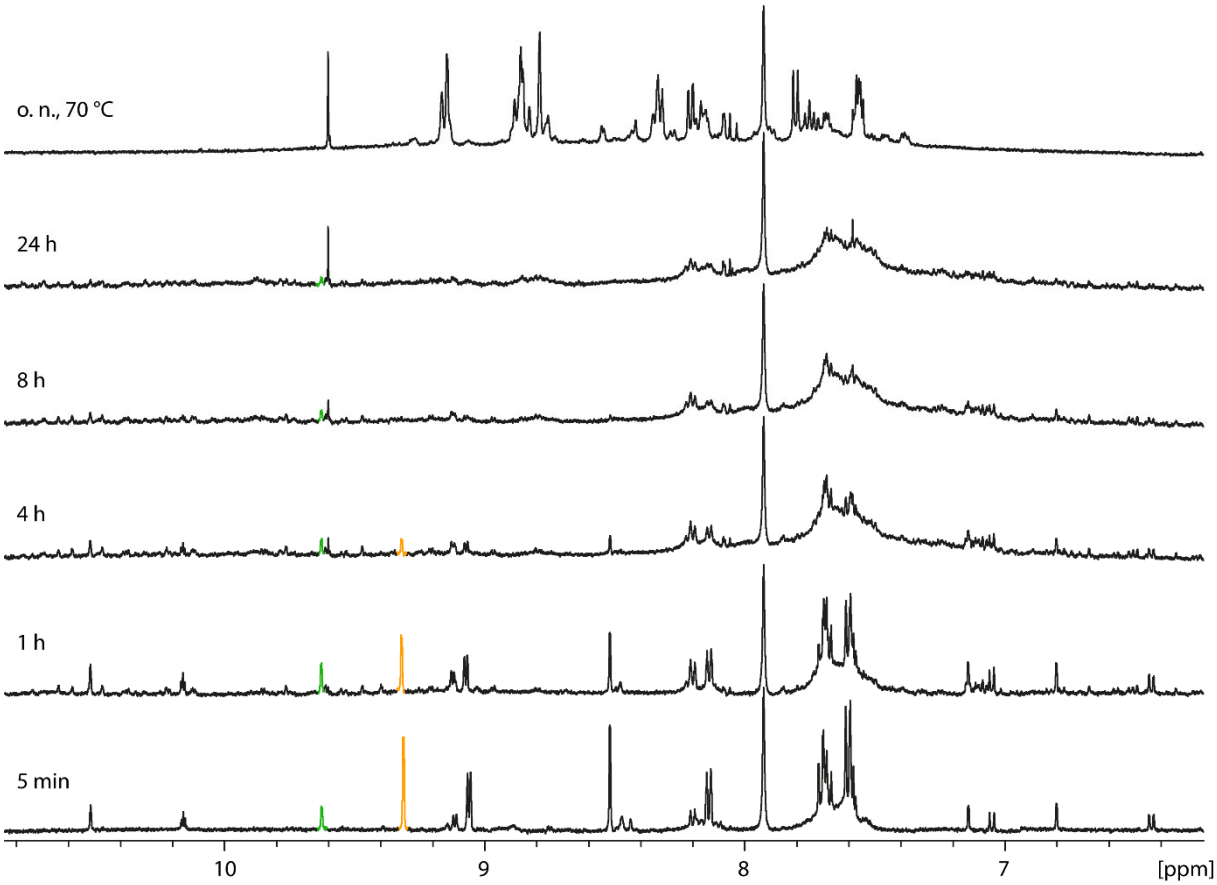

Figure 4.27. ^{1}H NMR spectra showing the transformation of $Pd_2\mathbf{L}^{\mathbf{EG4}}{}_4$ to $3NO_3@Pd_4\mathbf{L}^{\mathbf{EG4}}{}_8$ and higher aggregates. Overall ligand concentration: 6.4 mM.

4.5.4 Formation of $3NO_3@Pd_4\mathbf{L}^{\mathbf{EG4}}{}_8$ at 55 °C

A sample with the volume 491 µL containing 1.76 µmol $\mathbf{L}^{\mathbf{EG4}}$ and 0.44 µmol 1,3,5-trimethylbenzene was prepared and heated to 55 °C. To this sample 58.7 µL of a 15 mM $Pd(NO_3)_2$ stock solution was added and the ^{1}H NMR spectrum was directly recorded. After that, the sample was measured again every 30 min for the following 24 h. The temperature during the experiment was 55 °C constantly. The according spectra are shown in Figure 4.28.

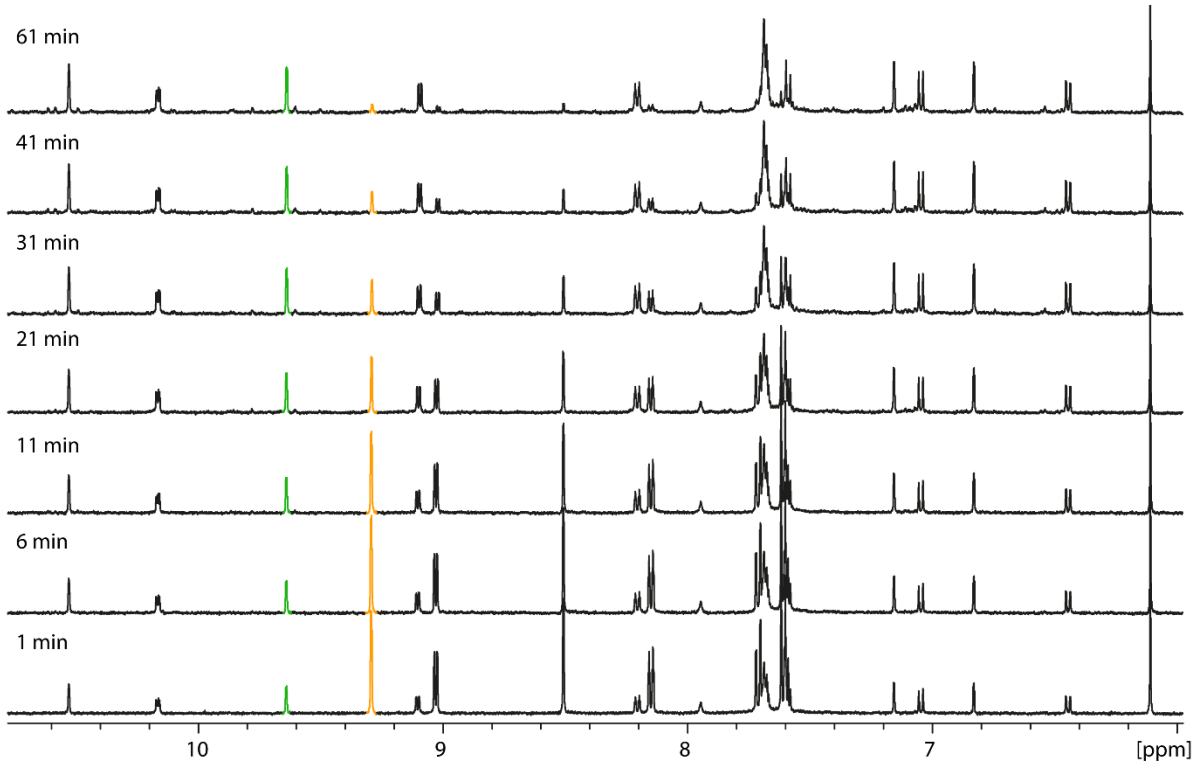

Figure 4.28. ^{1}H NMR spectra showing the transformation of $Pd_2\mathbf{L}^{\mathbf{EG4}}{}_4$ to $3NO_3@Pd_4\mathbf{L}^{\mathbf{EG4}}{}_8$ and higher aggregates at 55 °C (328 K). Overall ligand concentration: 3.2 mM.

4.5.5 Host guest binding studies

In order to determine the binding affinity of **G1** to $Pd_2\mathbf{L}^{\mathbf{EG4}}{}_4$ a host guest titration was conducted. 0.55 mL of a CD_3CN solution containing $\mathbf{L}^{\mathbf{EG4}}$ (0.88 µmol, 1.6 mM) and $Pd(BF_4)_2$ (0.44 µmol, 0.8 mM) and thus 0.4 mM $Pd_2\mathbf{L}^{\mathbf{EG4}}{}_4$ cage with BF_4^- counter anions was prepared. To that sample G1 was titrated in steps of 0.2 eq until 2.0 eq was reached; then in steps of 0.5 eq until 6.0 eq (15 mM G1 stock solution, 0.2 eq: 2.93 µL, 0.5 eq: 7.33 µL). ^{1}H and ^{19}F NMR spectra were measured after each titration step, see Figure 4.29 and Figure ***4.30***. ^{1}H NMR shifts of protons *a*, *b* and *e* were considered for the analysis with Bindfit. After the titration an ESI mass spectrum of the sample was recorded, see Figure 4.31.

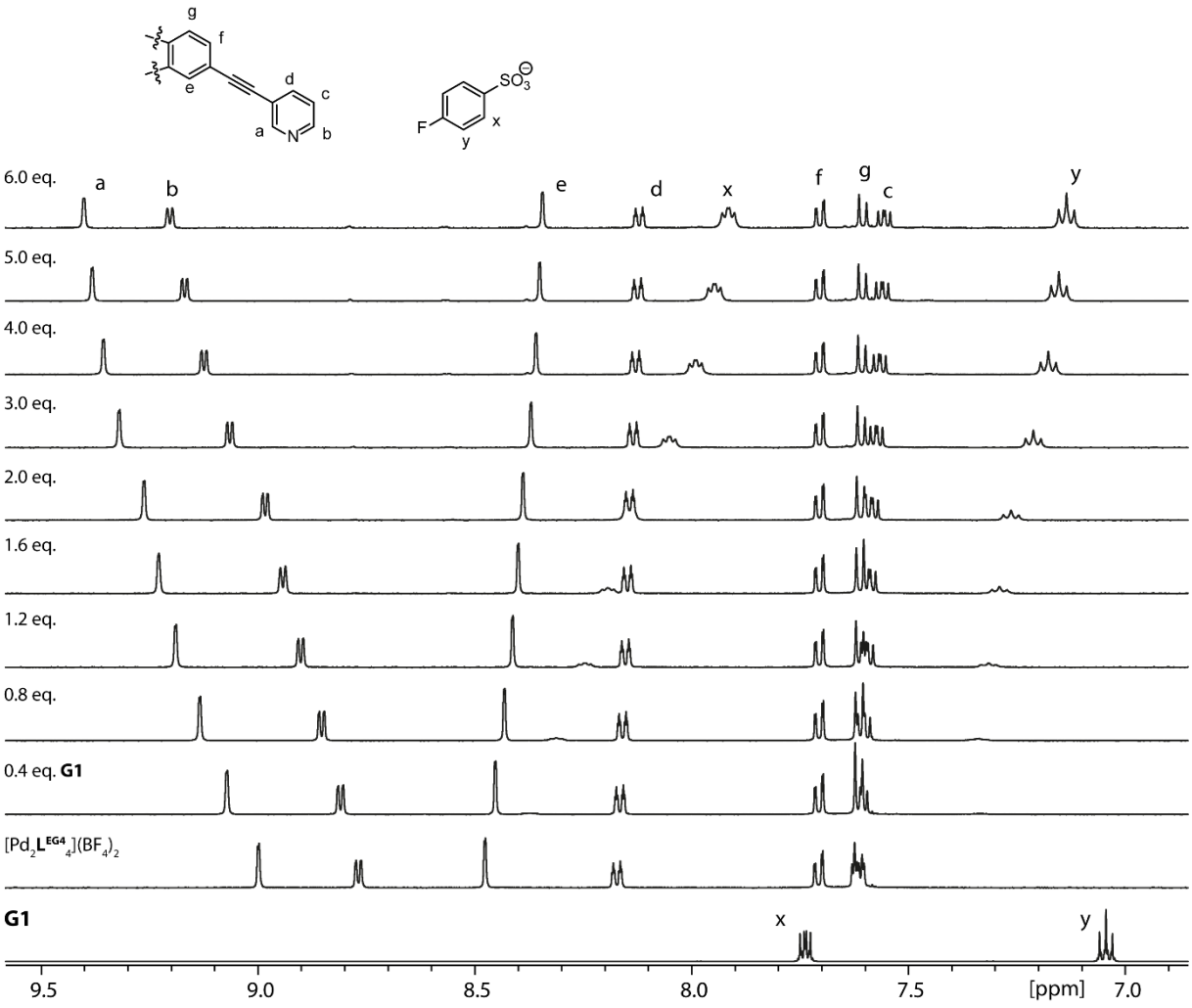

Figure 4.29. ^{1}H NMR spectra of host-guest titration of **G1** to $Pd_2\mathbf{L}^{\mathbf{EG4}}{}_4$ with BF_4^- counter anions.

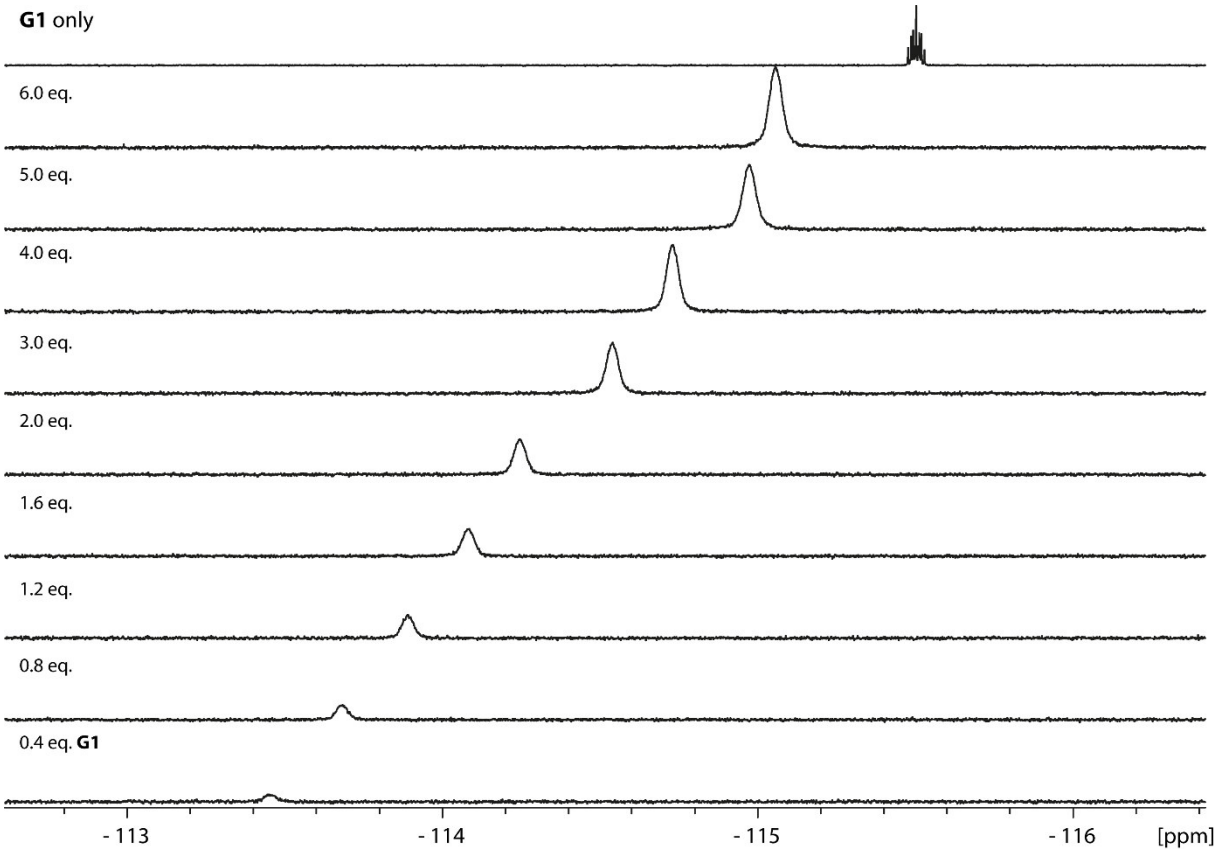

Figure 4.30. ^{19}F NMR spectra of host-guest titration of **G1** to $Pd_2\mathbf{L}^{\mathbf{EG4}}{}_4$ with BF_4^- counter anions.

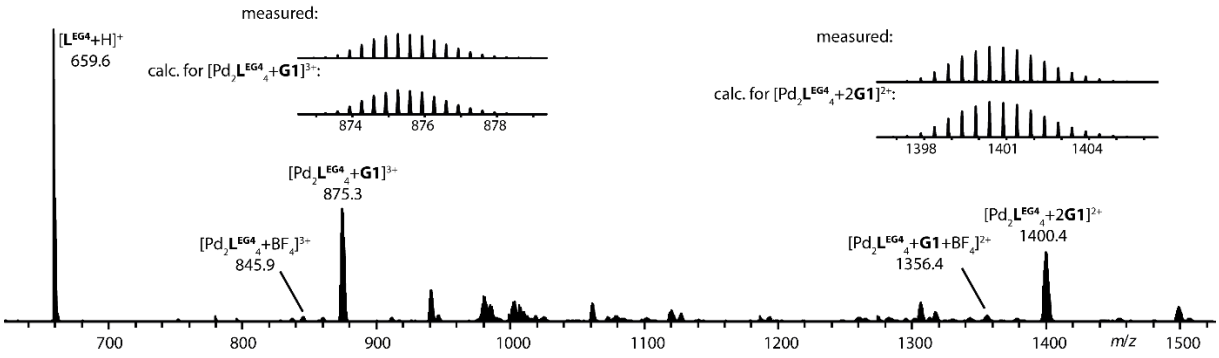

Figure 4.31. ESI mass spectrum (pos. mode) of a mixture containing $[Pd_2\mathbf{L}^{\mathbf{EG4}}{}_4](BF_4)_4$ (0.4 mM) and 6 equivalents **G1**.

To investigate the interaction of **G1** with $3NO_3@Pd_4\mathbf{L}^{\mathbf{EG4}}{}_8$ a sample of the latter was prepared following the procedure described in Section 4.5.3 with overall $\mathbf{L}^{\mathbf{EG4}}$ concentration of 3.2 mM. To that sample one double cage equivalent of **G1** was added (14.7 µL of 15 mM **G1** stock solution) and the sample was directly measured again. The ^1H NMR spectra with and without **G1** are shown in Figure 4.32.

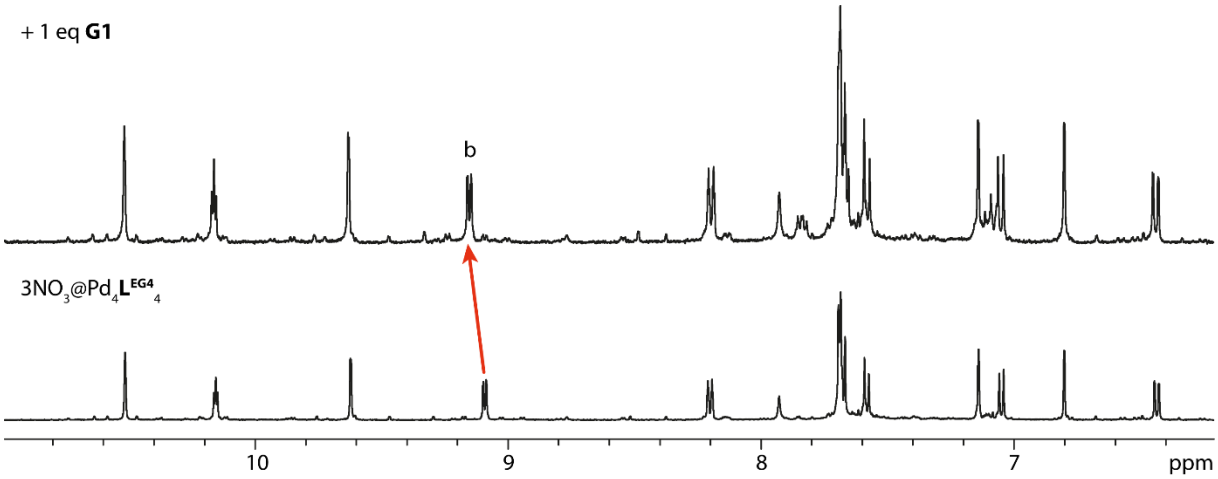

Figure 4.32. ^{1}H NMR spectra (bottom: 500 MHz, top: 400 MHz) of $3NO_3@Pd_4\mathbf{L}^{EG4}{}_8$ in CD_3CN (bottom) and the addition of 1 eq **G1** (top). The shifting of the NMR signal of outside pointing proton *b* upon guest addition is marked with a red arrow.

For the host guest titration experiment with **G2** the same procedure as with **G1** was used except for different guest equivalents for each titration steps. The according 1H NMR spectra and the titration steps are given in Figure 4.33.

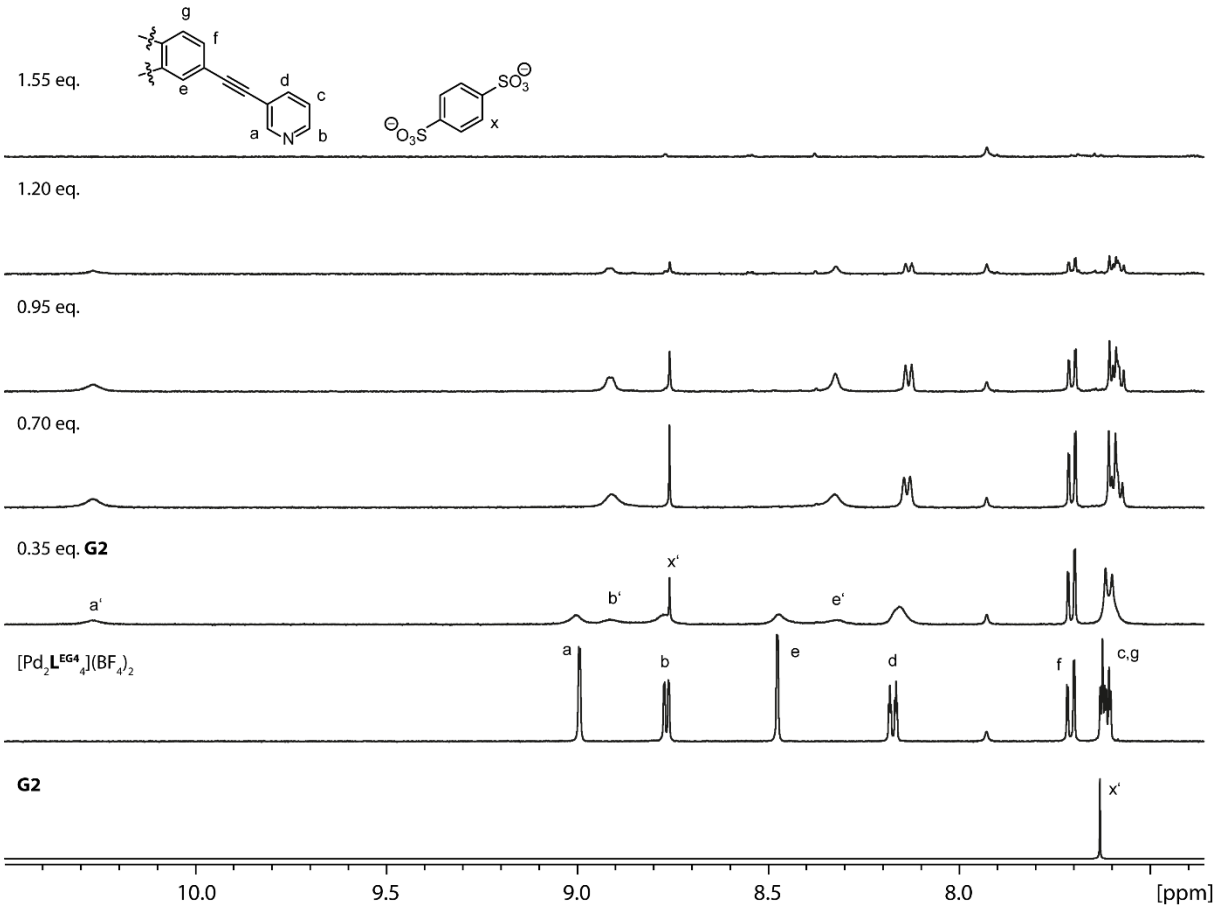

Figure 4.33. ^{1}H NMR spectra of host guest titration of **G2** to $Pd_2\mathbf{L}^{EG4}{}_4$ with BF_4^- counter anions.

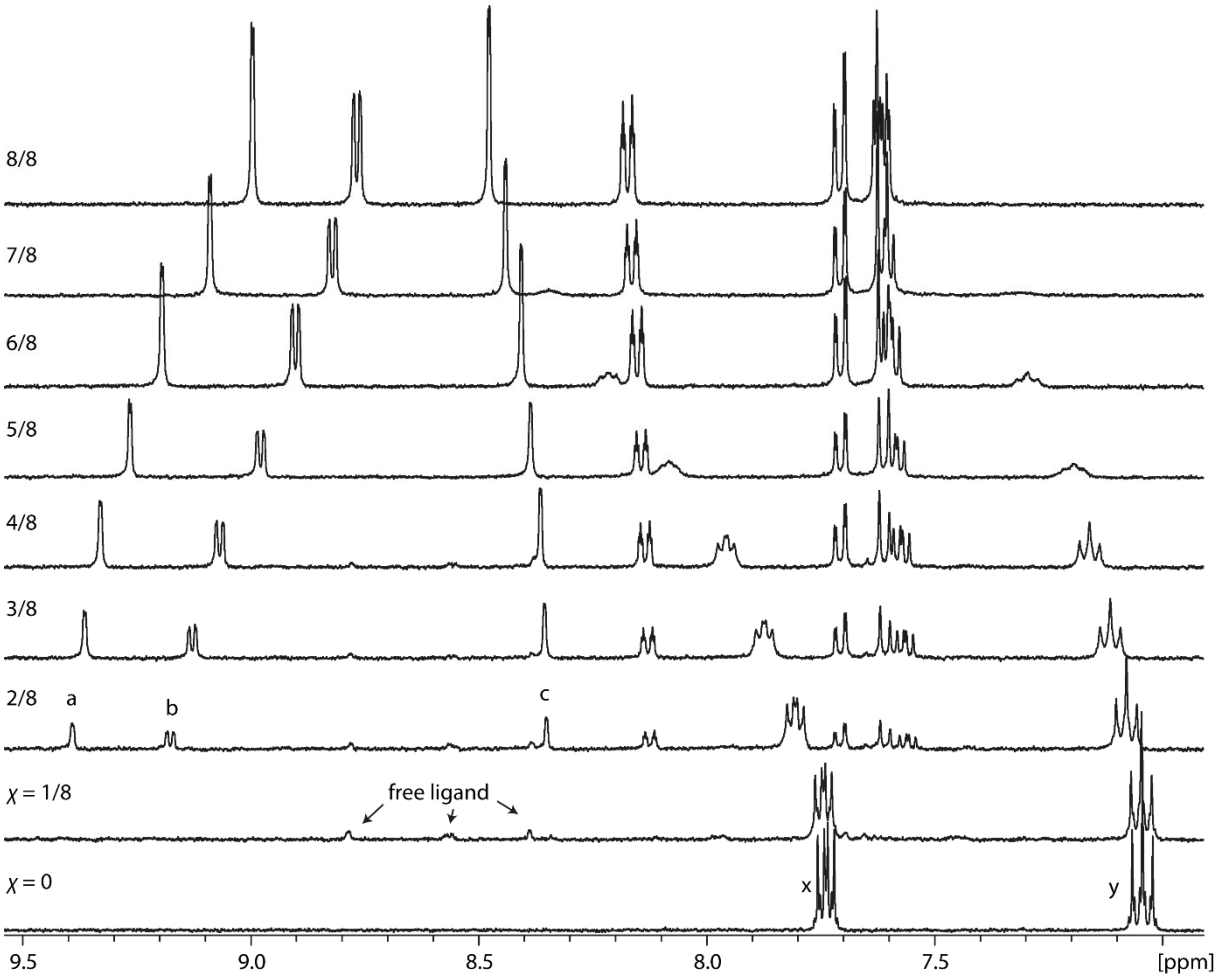

Figure 4.34. ^{1}H NMR spectra (400 MHz) of a solution of $[Pd_2\mathbf{L}^{\mathbf{EG4}}{}_4](BF_4)_4$ and **G1** in CD_3CN with varying ratios. Mole fraction $\chi = c_{cage}/(c_{cage}+c_{\mathbf{G1}})$.

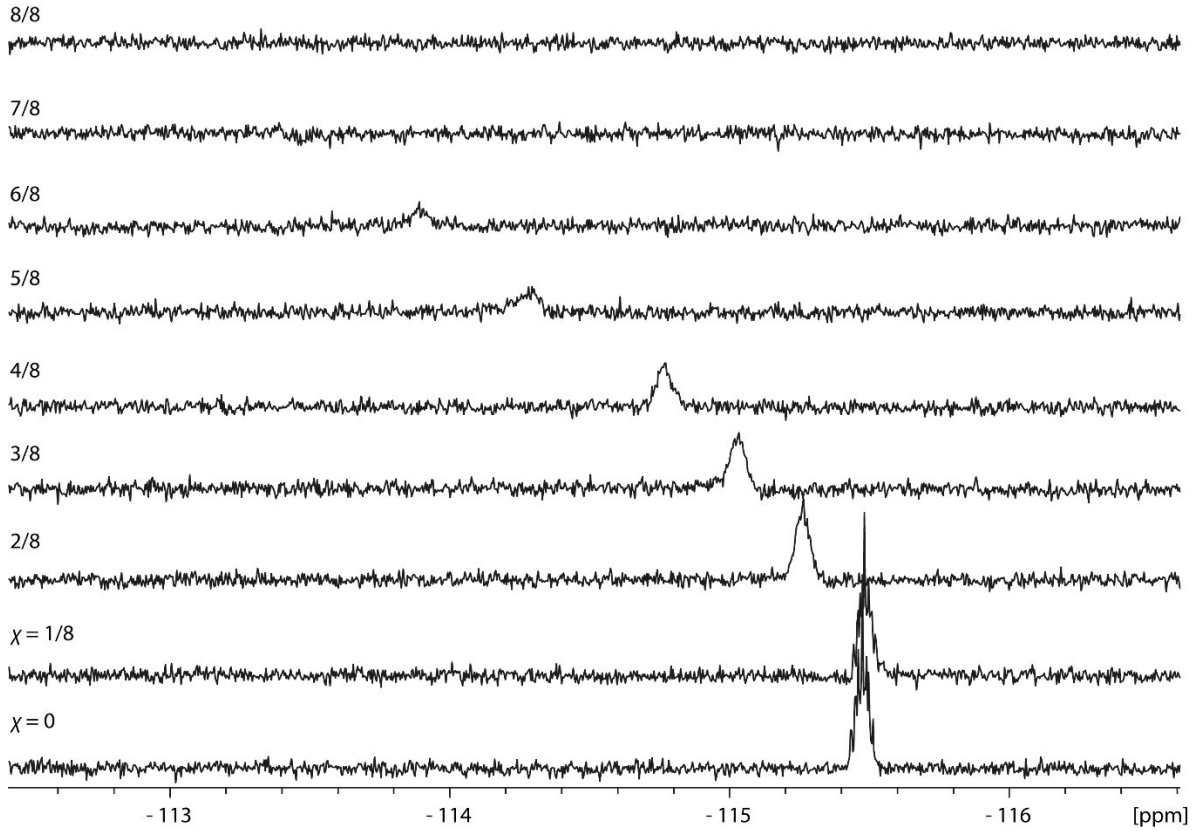

Figure 4.35. ^{19}F NMR spectra (377 MHz) of a solution of $[Pd_2\mathbf{L}^{\mathbf{EG4}}{}_4](BF_4)_4$ and **G1** in CD_3CN with varying ratios. Mole fraction $\chi = c_{cage}/(c_{cage}+c_{\mathbf{G1}})$.

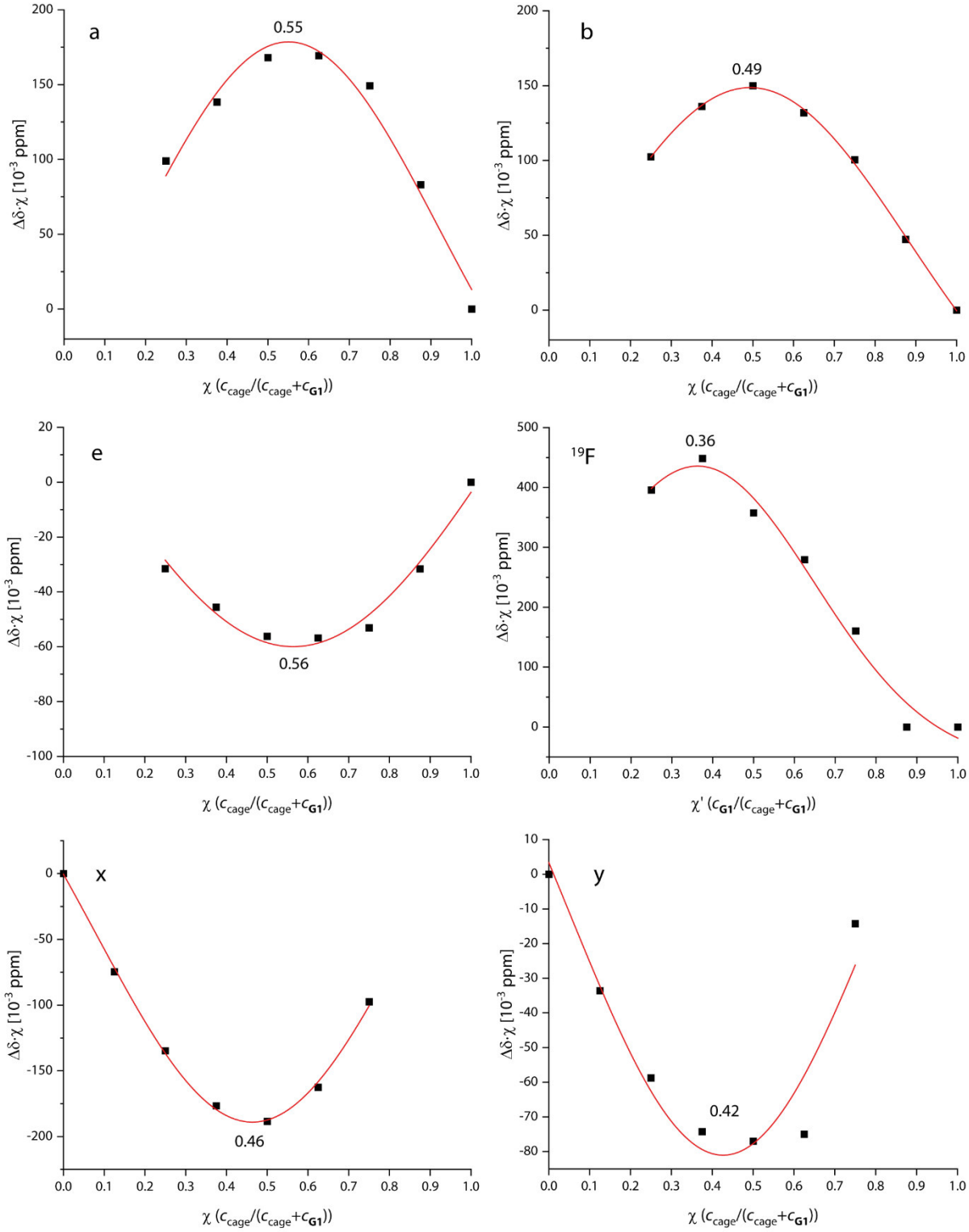

Figure 4.36. Job plots of the $[Pd_2\mathbf{L}^{\mathbf{EG4}}{}_4](BF_4)_4$-**G1**-host-guest-system considering ^{1}H NMR shifts of signals of either proton *a*, *b*, *e*, *x* or *y* or the ^{19}F NMR shift of **G1**. Red curves are Gauss fits and inserted numbers are maxima of the curves.

4.5.6 Dissipative guest binding studies

For the first experiment regarding dissipative guest binding as laid out in Section 4.3.3 and Figure 4.10 and Figure ***4.11*** first 491.3 µL of a CD_3CN solution containing $\mathbf{L}^{\mathbf{EG4}}$ (12 eq, 5.28 µmol), **G1** (1 eq, 0.44

µmol) and 1,3,5-trimethoxybenzene (1 eq, 0.44 µmol) was prepared. To that solution a $Pd(NO_3)_2$ solution (2 eq, 0.88 µmol, 15 mM, 58.7 µL) was added and the ^{1}H and ^{19}F NMR spectra were directly recorded. It was then measured again every few hours over the next 24 h. Then the same amount of $Pd(NO_3)_2$ solution was added again two more times and each time the sample was again observed by NMR for 24 h. The according NMR spectra are shown in Figure 4.37 andFigure ***4.38***.

The same experiment was repeated with **G2** using the exact same conditions. Figure 4.39 shows the ^{1}H NMR spectra.

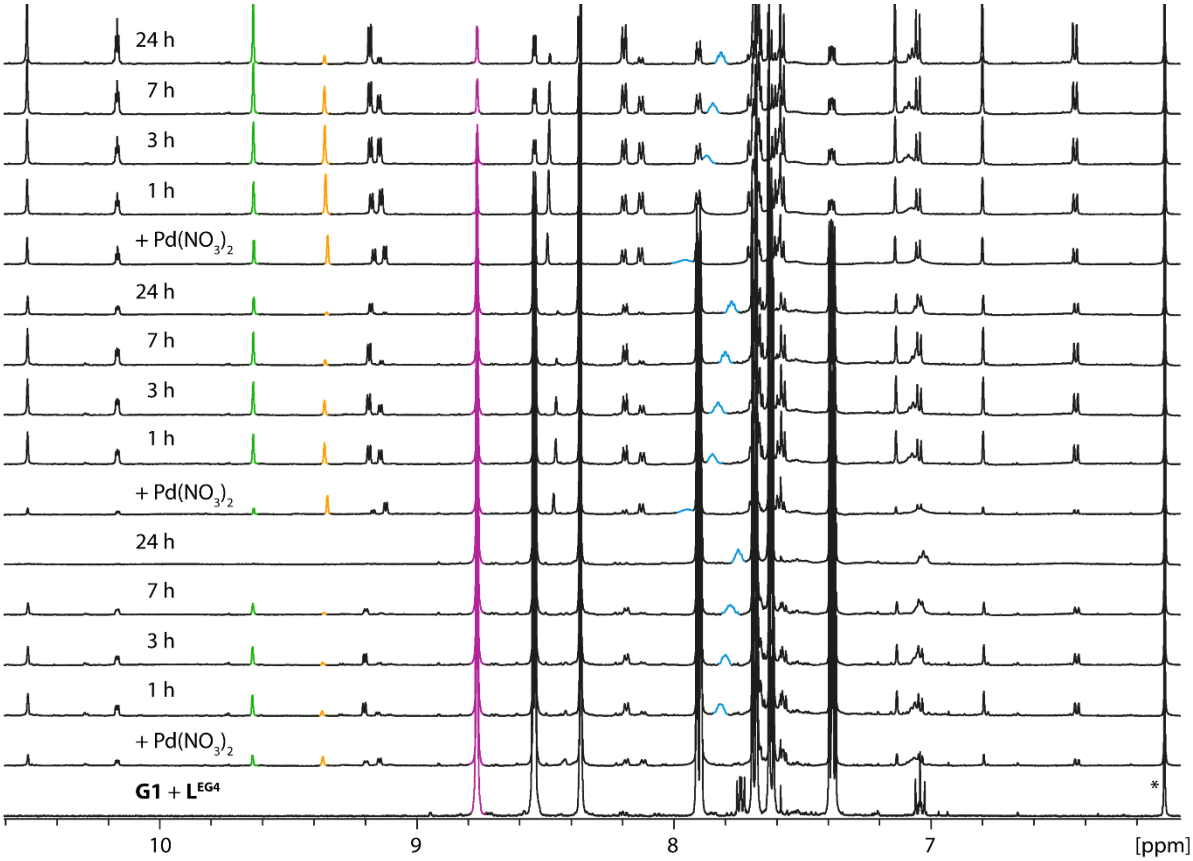

Figure 4.37. ^{1}H NMR spectra of **G1** (0.8 mM) and $\mathbf{L^{EG4}}$ (12 eq., 9.6 mM). Three times addition of $Pd(NO_3)_2$ (2 eq., 1.6 mM) and measurement over time.

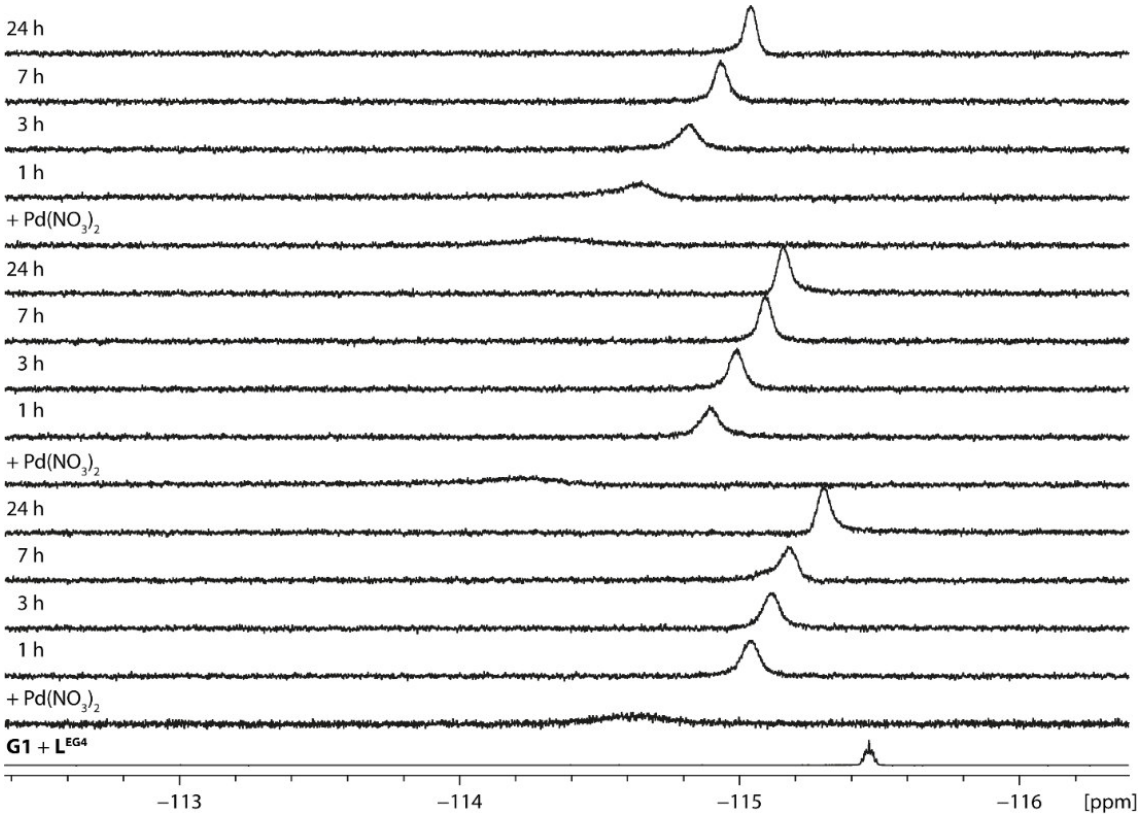

Figure 4.38. ^{19}F NMR spectra of **G1** (0.8 mM) and $\mathbf{L^{EG4}}$ (12 eq., 9.6 mM). Three times addition of $Pd(NO_3)_2$ (2 eq., 1.6 mM) and measurement over time.

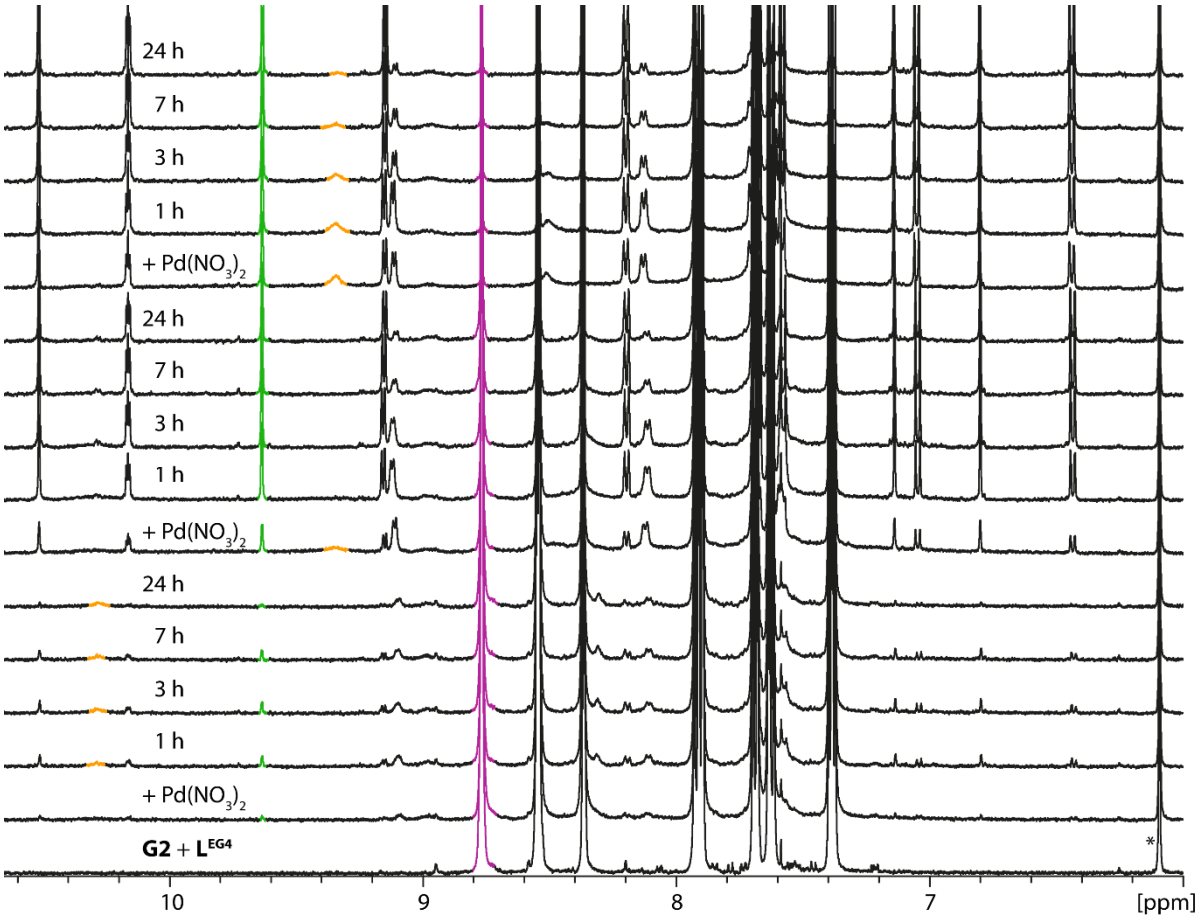

Figure 4.39. ^{1}H NMR spectra of **G2** (0.8 mM) and **L^{EG4}** (12 eq., 9.6 mM). Three times addition of $Pd(NO_3)_2$ (2 eq., 1.6 mM) and measurement over time.

For trying to keep the dissipative state up by constant addition of fuel (Figure 4.13 and Figure 4.14) first the same sample as described before was prepared. As before, 2 eq. of $Pd(NO_3)_2$ (0.88 µmol, 15 mM, 58.7 µL) was added and ^{1}H and ^{19}F was directly measured. 10 min after the first addition of $Pd(NO_3)_2$ the sample was measured again. 15 min after the first addition of $Pd(NO_3)_2$ another 0.24 eq. of $Pd(NO_3)_2$ (0.1056 µmol, 15 mM, 7.05 µL) was added and the sample was measured directly and after 10 min again. This was repeated for every 15 min for eight rounds (approximately 2 h). Afterwards, the sample was left stand for 24 h and room temperature and measured again. The spectra are shown in Figure ***4.40*** and Figure ***4.41***.

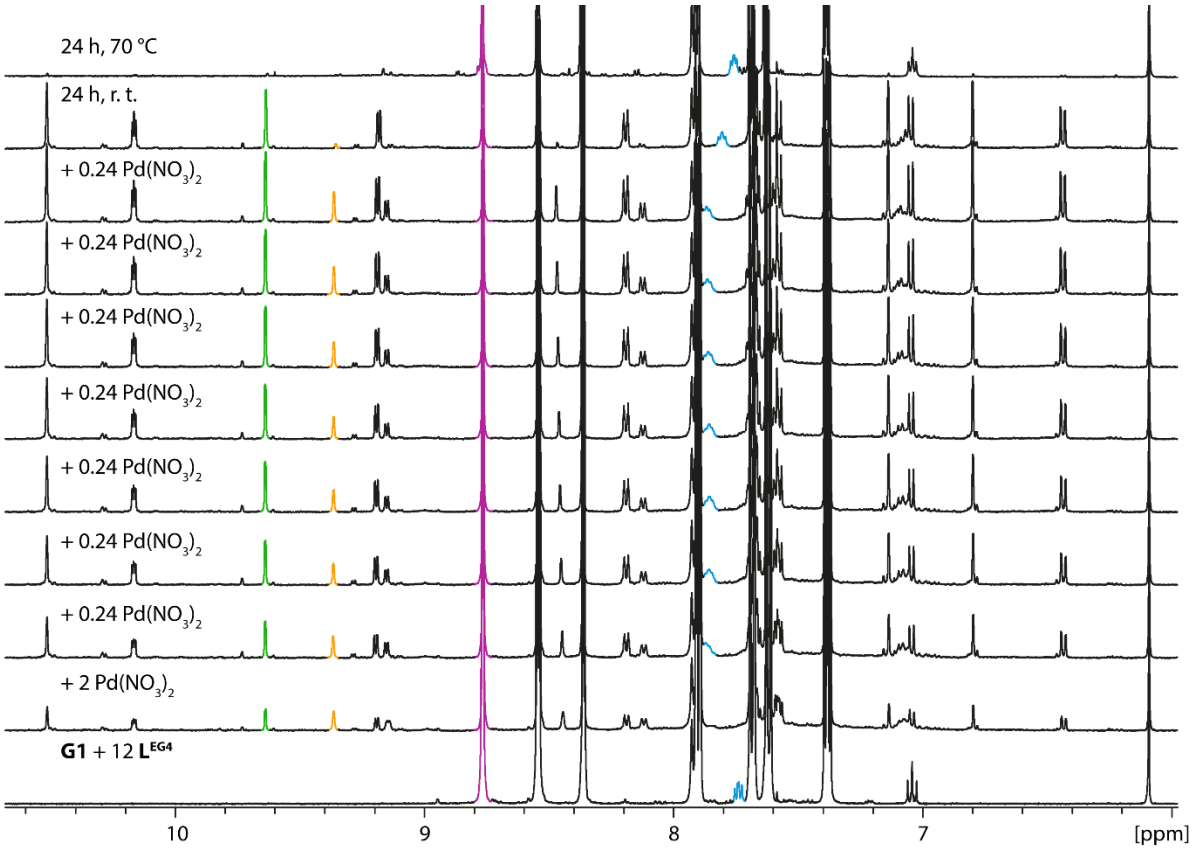

Figure 4.40. ^{1}H NMR spectra of **G1** (1 eq., 0.8 mM) and $\mathbf{L}^{EG4}$ (12 eq.). A single addition of $Pd(NO_3)_2$ (2 eq.), then addition of small amounts of $Pd(NO_3)_2$ every 15 min for 2h.

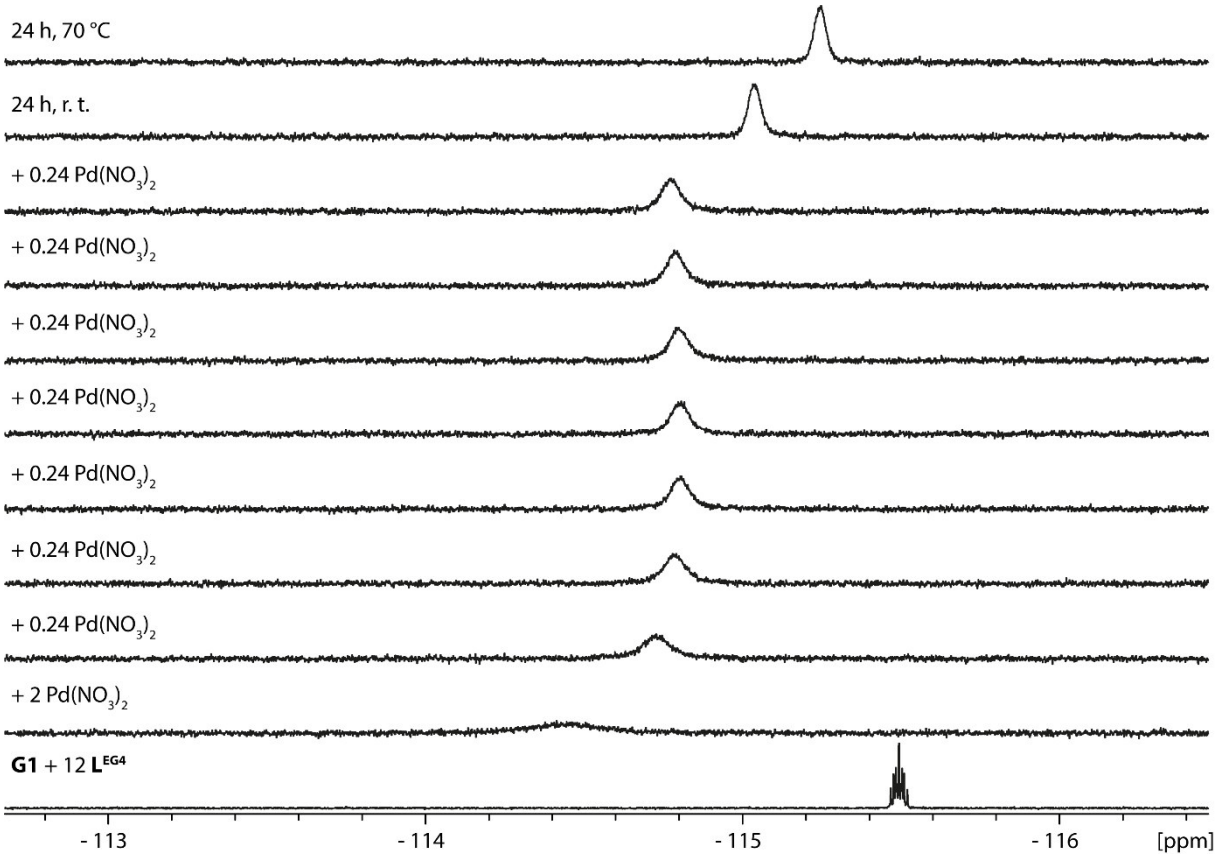

Figure 4.41. ^{19}F NMR spectra of **G1** (1 eq., 0.8 mM) and **L^{EG4}** (12 eq.). A single addition of $Pd(NO_3)_2$ (2 eq.), then addition of small amounts of $Pd(NO_3)_2$ every 15 min for 2h.

For determining whether the system can fully relax back to the thermodynamic ground state, meaning that **G1** is completely unbound again,

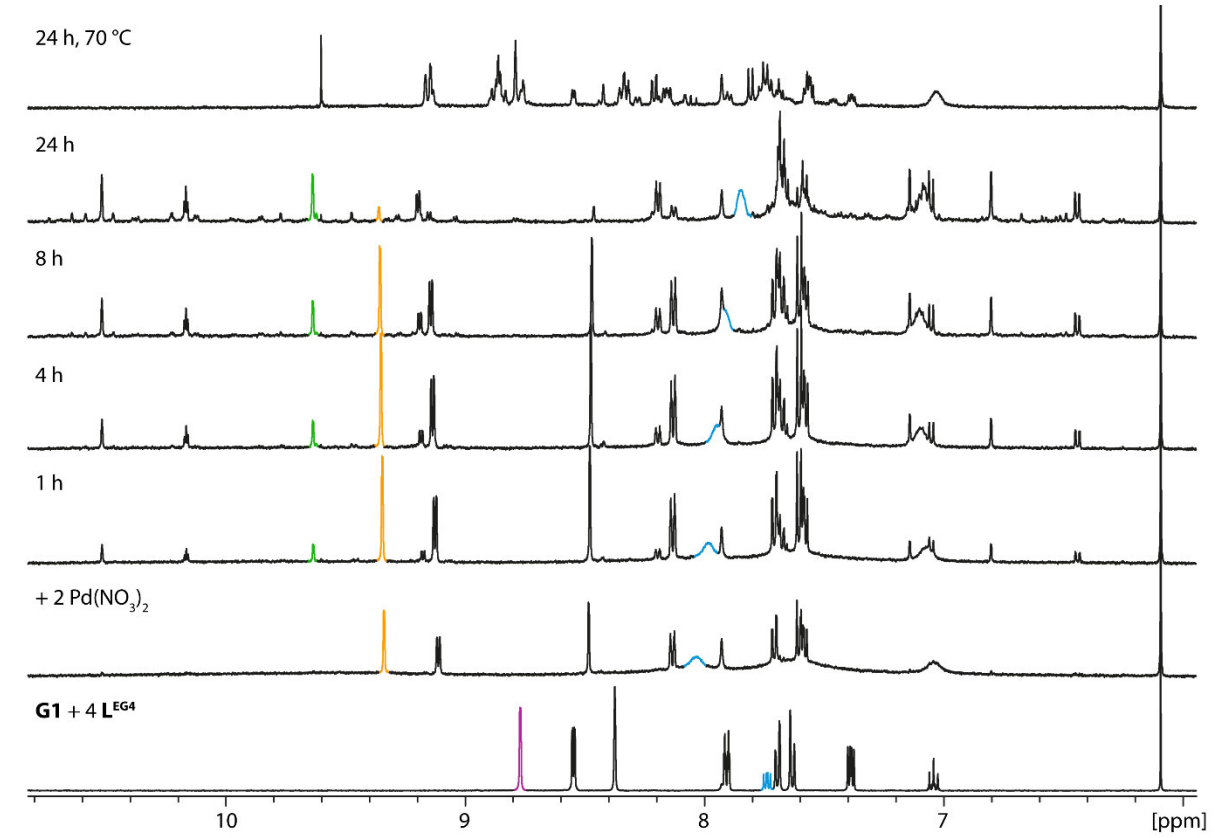

Figure 4.42. ^{1}H NMR spectra of dissipative guest binding study. c_{G1} = 0.8 mM; stochiometric amount of **L^{EG4}** was used.

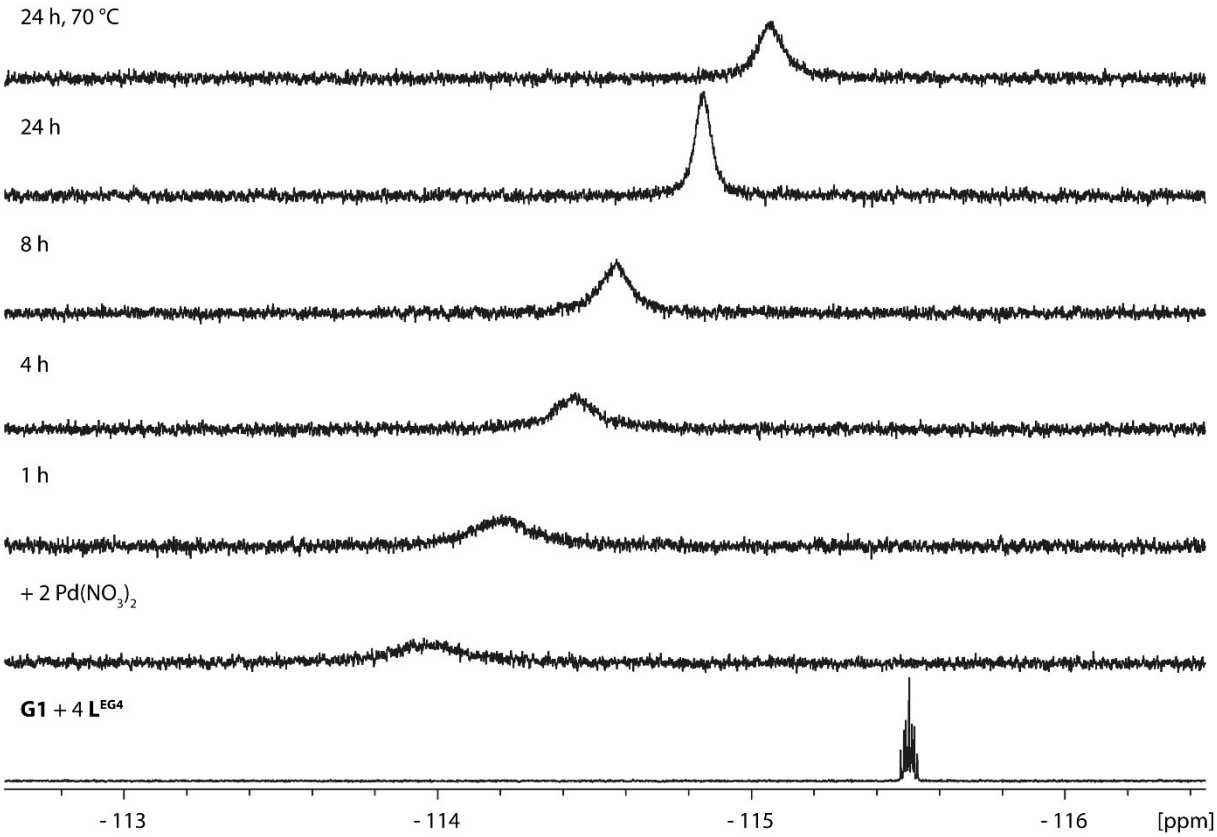

Figure 4.43. ^{19}F NMR spectra of dissipative guest binding study. c_{G1} = 0.8 mM; stochiometric amount of **L^{EG4}** was used.

4.6 Computational Studies

The general calculation procedures and methods listed Section 2.6.9 in were used here as well. The EG4 chains were omitted for the DFT calculations for computational speed up. No implicit solvent was used for the optimizations and frequency calculations but for the single point energies on ωB97M-D4/def2-TZVP level (CPCM(acetonitrile)).

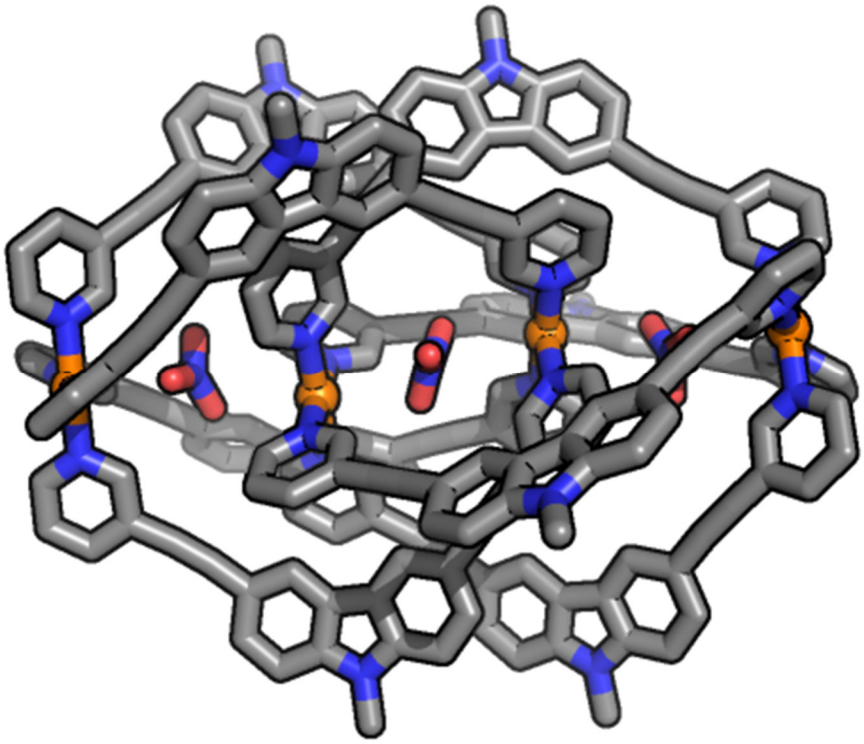

Figure 4.44. Geometry optimized model of $3(NO_3)@Pd_4\mathbf{L}^{EG4}{}_8$. Hydrogen atoms omitted for clarity. Chains omitted for clarity and computational speed up.

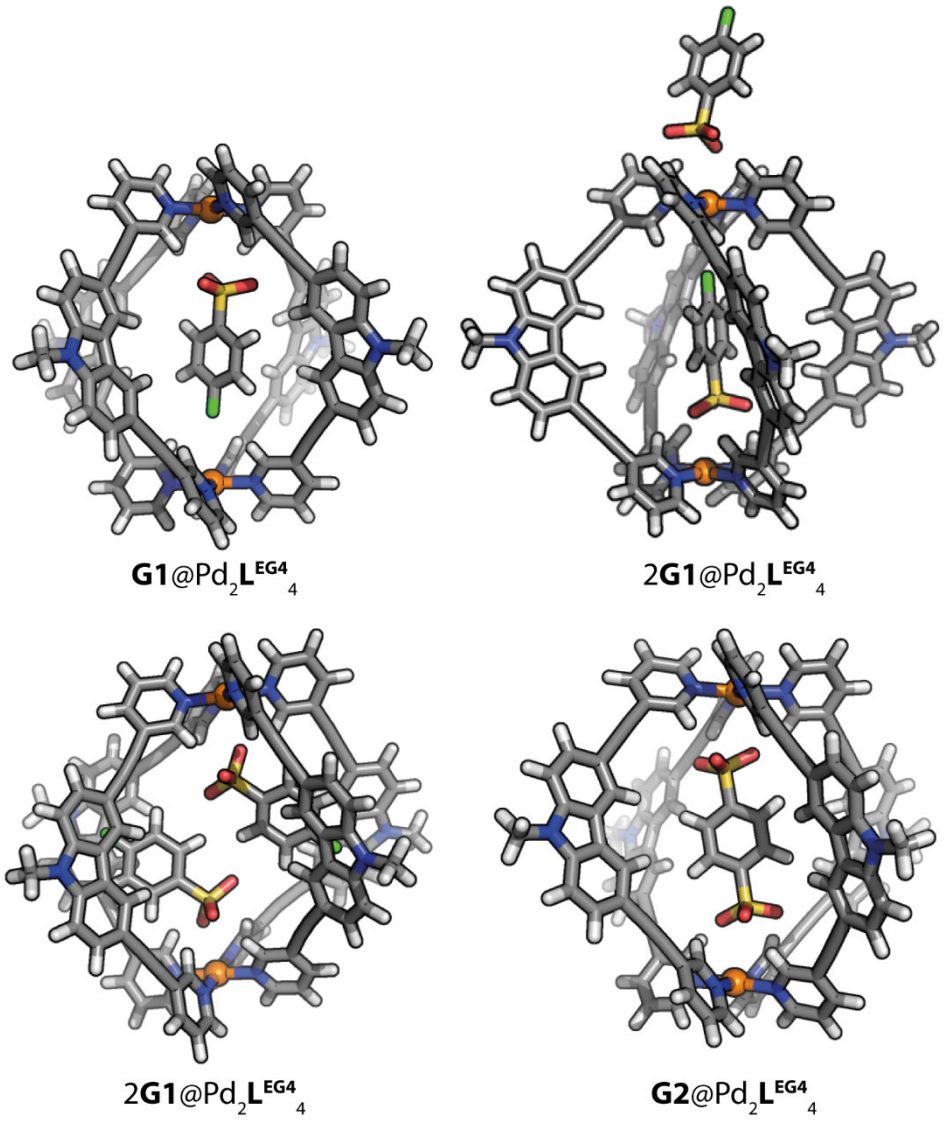

Figure 4.45. Geometry optimized models of HG complexes in this study. The upper right model shows 2**G1**@$Pd_2\mathbf{L}^{\mathbf{EG4}}{}_4$ with one guest binding inside and the other binding outside. The lower left model shows the same complex but with both guests binding inside.

From the optimized models (Figure 4.45) it can be seen that a single **G1** molecule fits perfectly inside $Pd_2\mathbf{L}^{\mathbf{EG4}}{}_4$ and also **G2** seems to fit. The Pd–Pd distance of **G1**@$Pd_2\mathbf{L}^{\mathbf{EG4}}{}_4$ is 13.4 Å and that of **G2**@$Pd_2\mathbf{L}^{\mathbf{EG4}}{}_4$ is with 13.2 Å a bit shorter, which is likely caused by the twofold negative charge of **G2** contracting the cage. Of the models of 2**G1**@$Pd_2\mathbf{L}^{\mathbf{EG4}}{}_4$ with either inside-inside or inside-outside binding, as shown in Figure 4.45, the inside-outside variant appears much more realistic as in the other model the cage is quite distorted and the two anions are very close to each other. DFT energies (ωB97M-D4/def2-TZVP , implicit solvation: CPCM, acetonitrile) actually suggest the inside-inside variant by 30 kJ/mol. However, it is believed that this result is biased as this is driven solely by the dispersion correction ($E_{D4}{}^{ii} - E_{D4}{}^{io}$ = -63 kJ/mol) but the dispersive interaction with the solvent is neglected with this solvent model (inside-outside variant has a higher solvent accessible surface).

4.7 Literature

[1] S. De, R. Klajn, *Adv. Mater.* 2018, *30*, 1706750.

[2] G. Ragazzon, L. J. Prins, *Nat Nanotechnol* 2018, *13*, 882–889.

[3] J. L. -Y. Chen, S. Maiti, I. Fortunati, C. Ferrante, L. J. Prins, *Chem European J* 2017, *23*, 11549–11559.

[4] F. della Sala, S. Neri, S. Maiti, J. L.-Y. Chen, L. J. Prins, *Curr Opin Biotech* 2017, *46*, 27–33.

[5] V. W. L. Gunawardana, T. J. Finnegan, C. E. Ward, C. E. Moore, J. D. Badjić, *Angew. Chem. Int. Ed.* 2022, *61*, e202207418.

[6] E. Olivieri, A. Quintard, *Acs Org Inorg Au* 2023, *3*, 4–12.

[7] M. M. Hossain, I. M. Jayalath, R. Baral, C. S. Hartley, *Chemsystemschem* 2022, *4*, DOI 10.1002/syst.202200016.

[8] L. S. Kariyawasam, C. S. Hartley, *J Am Chem Soc* 2017, *139*, 11949–11955.

[9] R. Siewertsen, H. Neumann, B. Buchheim-Stehn, R. Herges, C. Näther, F. Renth, F. Temps, *J Am Chem Soc* 2009, *131*, 15594–15595.

[10] H. Lee, J. Tessarolo, D. Langbehn, A. Baksi, R. Herges, G. H. Clever, *J Am Chem Soc* 2022, *7*, 3099–3105.

[11] R. Zhu, J. Lübben, B. Dittrich, G. H. Clever, *Angewandte Chemie Int Ed* 2015, *54*, 2796–2800.

[12] M. Fukuda, R. Sekiya, R. Kuroda, *Angew. Chem. Int. Ed.* 2008, *47*, 706–710.

[13] S. Löffler, J. Lübben, L. Krause, D. Stalke, B. Dittrich, G. H. Clever, *J Am Chem Soc* 2015, *137*, 1060–1063.

[14] R. Sekiya, M. Fukuda, R. Kuroda, *J Am Chem Soc* 2012, *134*, 10987–10997.

[15] T. Tateishi, Y. Yasutake, T. Kojima, S. Takahashi, S. Hiraoka, *Commun Chem* 2019, *2*, 25.

[16] P. Thordarson, *Chem Soc Rev* 2010, *40*, 1305–1323.

[17] G. H. Clever, S. Tashiro, M. Shionoya, *Angewandte Chemie Int Ed* 2009, *48*, 7010–7012.

5 Methods and Materials

5.1 Chemicals

Chemicals and standard solvents were purchased from Sigma Aldrich, Acros Organics, Carl Roth, TCI Europe, VWR, abcr or other suppliers and used as received, if not mentioned otherwise. Deuterated solvents were purchased from Eurisotop. For synthesis, HPLC grade solvents and for purification technical solvents were used if not mentioned otherwise.

5.2 Devices

Automated flash chromatography was conducted using a Biotage® Isolera One™ and Biotage® Sfär Silica D Duo 60 µm cartridges.

Recycling gel permeation chromatography was performed on Japan Analytical Industry NEXT and LaboACE instruments using JAIGEL 1-HH and 2-HH columns, 20 mm x 600 mm, with HPLC grade chloroform and an average flowrate of 7 mL/min.

NMR spectroscopic data was measured, if not denoted otherwise, at 298 K with CD_3CN as solvent and following frequencies: 500 MHz for ^{1}H, 565 MHz for ^{19}F and 126 MHz for ^{13}C. Spectrometers used in this study are Bruker AV 400 Avance III HD NanoBay (400 MHz), Bruker AV 500 Avance NEO (500 MHz), Agilent Technologies DD2 (500 MHz), Bruker AV 500 Avance III HD (500 MHz), AV 500 Avance III HD (500 MHz), Bruker AV 600 Avance III HD (600 MHz), Bruker Avance NEO 600 (600 MHz) and Bruker AV 700 Avance III HD (700 MHz). For ^{1}H NMR and ^{13}C NMR spectra signals were referenced to the residual solvent peak (^{1}H: acetonitrile: 1.94 ppm, DMSO: 2.54 ppm, chloroform: 7.26 ppm; ^{13}C: acetonitrile: 118.26 ppm DMSO: 39.52 ppm, chloroform: 77.16 ppm). ^{1}H DOSY NMR spectra were recorded with a *dstebpgp3s* pulse sequence with diffusion delays D20 of 0.08 s and gradient powers P30 of 2500 to 3000 µs.[1,2] T1 analyses of the corresponding signals in the 1D spectra were performed to obtain the diffusion coefficients *D* using the Stejskal-Tanner-Equation.[3,4] Hydrodynamic radii r_H were calculated using the Stokes-Einstein-Equation.[5] The ^{1}H DOSY NMR spectra were recorded and processed by coworkers André Platzek, Elie Benchimol and Laura Neukirch.

UV-vis spectra were recorded on a DAD HP-8453 UV-Vis spectrometer. Fluorescence measurements were performed on a JASCO FP-8300 with a 150 W Xe lamp as light source.

Irradiations at 313 nm were performed by placing a quartz NMR tube in a distance of 5 cm in front of a 300 W Hg arc lamp from LOT-Oriel equipped with a dichroic mirror and 313 nm bandpass filter. Irradiations at 617 nm were performed by placing a quartz NMR tube 2.5 cm in front of a LED irradiation apparatus (3x 1.4 W 617 nm Power LED, 25 nm FWHM) from Sahlmann Photonics, Kiel.

Mass spectra were recorded using either a Bruker compact spectrometer or a Bruker timsTOF spectrometer. As ionization method electrospray ionization (ESI) was used if not denoted otherwise. For the calibration the Agilent ESI-Low Concentration Tuning Mix was used.

Trapped ion mobility spectra were measured with the Bruker timsTOF spectrometer. About 25 µL of each sample in CD_3CN was diluted 1:10 with CH_3CN and electrosprayed at 3 µL/min flow rate. Minimum electrical potentials were optimized for each sample to avoid fragmentation. Typically, the following instrumental parameters were used: Capillary voltage: 2500 V, End plate offset: 200 V, Dry temperature: 75 °C, Funnel 1 RF: 200V, Funnel 2 RF: 200 V, Multiple RF: 200 V, Deflection delta: 60 V, Quadrupole ion energy: 3 V, Collision energy: 3 V, Transfer time: 70 µs, Prepulse storage: 15 µs. Calibration was achieved using the Agilent tuning mix with $^{DT}CCS_{N2}$-values published by Stow *et. al.*[6] Each sample was measured in low (survey) and high (custom) resolution mode. A pressure difference of 1.7 mbar between the entrance and the exit of the TIMS tunnel was used. For high resolution measurements a 0.06 Vs/cm^2 difference and 450 ms ramp time was used and the achieved resolution was >200. All ion mobility measurements in this work were carried out by Dr. Ananya Baksi.

5.3 Computational studies

For all computational studies the high-performance cluster of TU Dortmund University called LiDO3 was used. For geometry optimizations, single point energy calculations, frequency calculations and local energy decomposition calculations ORCA 5.0.2[7] was used if not denoted otherwise. For MD simulations xtb 6.4.1 was used.[8] For further details regarding computational calculations see Section 2.6.9.

5.4 Figure licenses

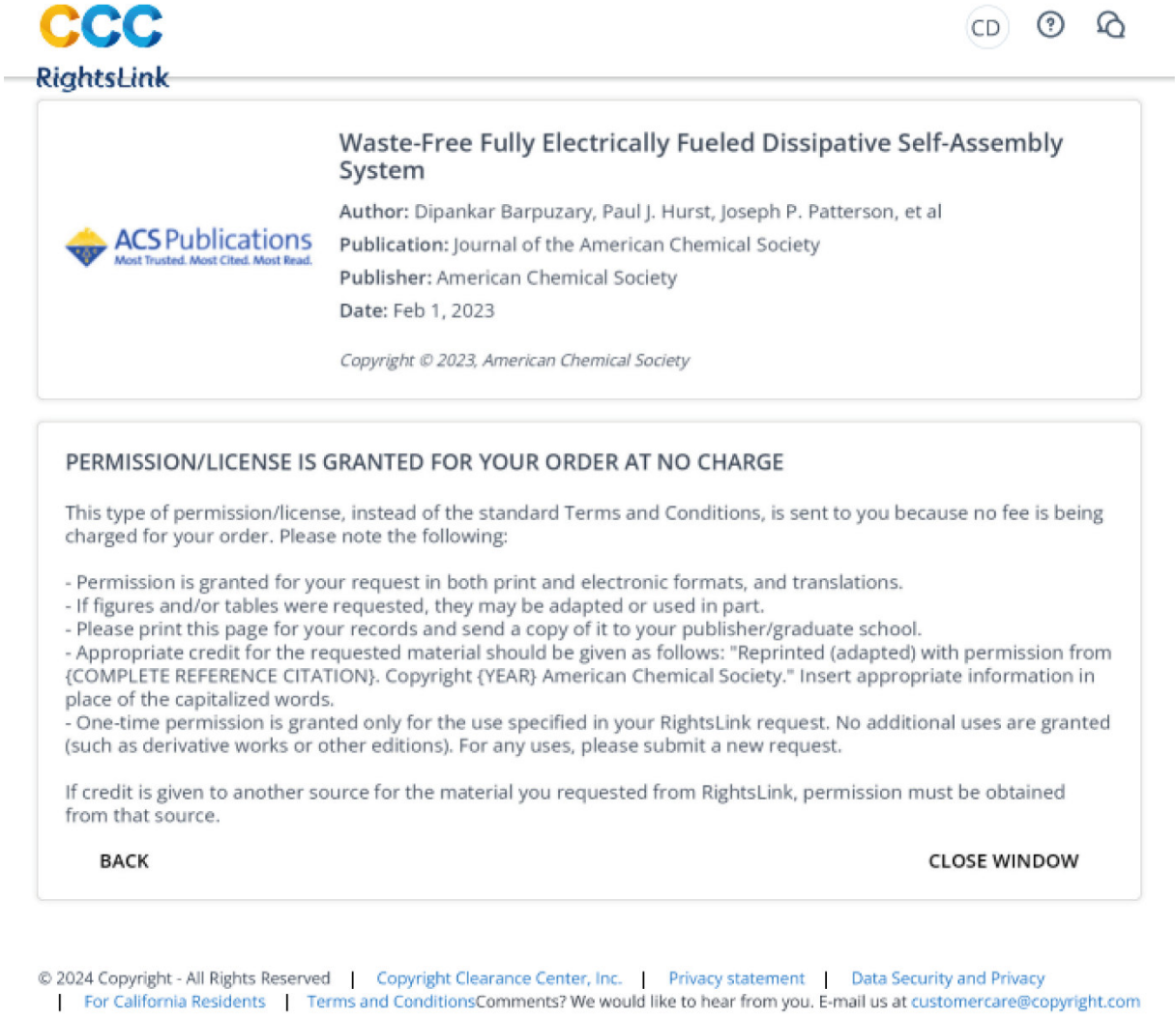

Figure 5.1. License for Figure 1.5.

JOHN WILEY AND SONS LICENSE
TERMS AND CONDITIONS

Jul 06, 2024

This Agreement between Christoph Drechsler / TU Dortmund ("You") and John Wiley and Sons ("John Wiley and Sons") consists of your license details and the terms and conditions provided by John Wiley and Sons and Copyright Clearance Center.

License Number	5822940924206
License date	Jul 06, 2024
Licensed Content Publisher	John Wiley and Sons
Licensed Content Publication	Angewandte Chemie International Edition
Licensed Content Title	Visible-Light-Responsive Self-Assembled Complexes: Improved Photoswitching Properties by Metal Ion Coordination**
Licensed Content Author	Ray G. DiNardi, Anna O. Douglas, Ruoming Tian, et al
Licensed Content Date	Aug 16, 2022
Licensed Content Volume	61
Licensed Content Issue	38
Licensed Content Pages	7
Type of use	Dissertation/Thesis
Requestor type	University/Academic
Format	Electronic
Portion	Abstract
Will you be translating?	No
Title of new work	Complex Systems based on Coordination Cages
Institution name	TU Dortmund
Expected presentation date	Sep 2024
The Requesting Person / Organization to Appear on the License	Christoph Drechsler / TU Dortmund
Requestor Location	TU Dortmund Otto-Hahn-Str. 6 Dortmund, 44227 Germany Attn: TU Dortmund
Publisher Tax ID	EU826007151
Total	0.00 EUR
Terms and Conditions	

Figure 5.2. License for Figure 3.2.

JOHN WILEY AND SONS LICENSE
TERMS AND CONDITIONS

Jul 06, 2024

This Agreement between Christoph Drechsler / TU Dortmund ("You") and John Wiley and Sons ("John Wiley and Sons") consists of your license details and the terms and conditions provided by John Wiley and Sons and Copyright Clearance Center.

License Number	5822941285963
License date	Jul 06, 2024
Licensed Content Publisher	John Wiley and Sons
Licensed Content Publication	Angewandte Chemie International Edition
Licensed Content Title	Light-Triggered Guest Uptake and Release by a Photochromic Coordination Cage
Licensed Content Author	Muxin Han, Reent Michel, Bice He, et al
Licensed Content Date	Dec 3, 2012
Licensed Content Volume	52
Licensed Content Issue	4
Licensed Content Pages	5
Type of use	Dissertation/Thesis
Requestor type	University/Academic
Format	Electronic
Portion	Figure/table
Number of figures/tables	1
Will you be translating?	No
Title of new work	Complex Systems based on Coordination Cages
Institution name	TU Dortmund
Expected presentation date	Sep 2024
Portions	Figure 1
The Requesting Person / Organization to Appear on the License	Christoph Drechsler / TU Dortmund
Requestor Location	TU Dortmund Otto-Hahn-Str. 6 Dortmund, 44227 Germany Attn: TU Dortmund
Publisher Tax ID	EU826007151
Total	0.00 EUR

Figure 5.3. License for Figure 3.7.

5.5 Literature

[1] A. Jerschow, N. Müller, *J Magn Reson* **1997**, *125*, 372–375.

[2] A. Jerschow, N. Müller, *J Magnetic Reson Ser* **1996**, *123*, 222–225.

[3] E. O. Stejskal, J. E. Tanner, *J Chem Phys* **1965**, *42*, 288–292.

[4] J. E. Tanner, E. O. Stejskal, *J Chem Phys* **1968**, *49*, 1768–1777.

[5] A. Einstein, *Ann. Phys.* **1905**, *322*, 549–560.

[6] S. M. Stow, T. J. Causon, X. Zheng, R. T. Kurulugama, T. Mairinger, J. C. May, E. E. Rennie, E. S. Baker, R. D. Smith, J. A. McLean, S. Hann, J. C. Fjeldsted, *Anal. Chem.* **2017**, *89*, 9048–9055.

[7] F. Neese, *Wiley Interdiscip. Rev.: Comput. Mol. Sci.* **2022**, *12*, DOI 10.1002/wcms.1606.

[8] C. Bannwarth, E. Caldeweyher, S. Ehlert, A. Hansen, P. Pracht, J. Seibert, S. Spicher, S. Grimme, *Wiley Interdiscip. Rev.: Comput. Mol. Sci.* **2021**, *11*, DOI 10.1002/wcms.1493.

6 List of Publications

6.1 Published

1. K. E. Ebbert, L. Schneider, A. Platzek, C. Drechsler, B. Chen, R. Rudolf, G. H. Clever, *Dalton Trans.* **2019**, *48*, 11070-11075. Title: “Resolution of minor size differences in a family of heteroleptic coordination cages by trapped ion mobility ESI-MS”
2. K. Wu, B. Zhang, C. Drechsler, J. J. Holstein, G. H. Clever, *Angew. Chem. Int. Ed.* **2020**, *60*, 6403-6407. Title: “Backbone-Bridging Promotes Diversity in Heteroleptic Cages”
3. Platzek, S. Juber, C. Yurtseven, S. Hasegawa, L. Schneider, C. Drechsler, K. E. Ebbert, R. Rudolf, Q.-Q. Yan, J. J. Holstein, L. V. Schäfer, G. H. Clever, *Angew. Chem. Int. Ed.* **2022**, *61,* e202209305. Title: “Endohedrally Functionalized Heteroleptic Coordination Cages for Phosphate Ester Binding”
4. S. Ganta, C. Drechsler, Y.-T. Chen, G. H. Clever, *Chem. Eur. J.* **2022**, *28*, e202104228. Title: “Nonaqueous Emulsion Polycondensation Enabled by a Self-Assembled Cage-like Surfactant”
5. S. Ganta, J.-H. Borter, C. Drechsler, J. J. Holstein, D. Schwarzer, G. H. Clever, *Org. Chem. Front.* **2022**, *9*, 5485-5493. Title: “Photoinduced host-to-guest electron transfer in a self-assembled coordination cage”
6. W. M. Bloch, S. Horiuchi, J. J. Holstein, C. Drechsler, A. Wuttke, W. Hiller, R. A. Mata, G. H. Clever, *Chem. Sci.* **2023**, *14*, 1524-1531. Title: “Maximized axial helicity in a Pd2L4 cage: inverse guest size-dependent compression and mesocate isomerism”
7. M. G. Kalarikkal, C. Drechsler, G. Tusha, L. V. Schäfer, D. Van Craen, *Chem. Eur. J.* **2023**, 29, e202301613. Title: “Chiroptical Recognition of Carboxylates with Charge-Neutral Double-Stranded Zinc(II) Helicates”
8. K. Ebbert, E. Benchimol, C. Drechsler, J. J. Holstein, G. H. Clever. Title: “Ring-Size Control and Guest-Induced Circularly Polarized Luminescence in Heteroleptic $Pd_3A_3B_3$ and $Pd_4A_4B_4$ Assemblies “

6.2 Unpublished

1. C. Drechsler, A. Baksi, A. Platzek, M. Acar, J. J. Holstein, G. H. Clever. Title: “London Dispersion driven Compaction of Coordination Cages in the Gas Phase – A combined Ion Mobility and Theoretical Study”
2. A. Baksi, C. Drechsler, S. Ganta, G. H. Clever. Title: “Mechanistic pathway of Pd4L8 Interlocked Cage Formation”
3. P. Montes-Tolentino, C. Drechsler, J. J. Holstein, G. H. Clever. Title: “Quadruply and Triply Interlocked Isomers based on Pd4L8 Double Cages”
4. C.-S. Kwan, C. Drechsler, G. H. Clever. Title: “Dual Guest Binding in Crown Ether-based Coordination Cages”
5. Q.-Q. Yan, J. Tessarolo, S. Hasegawa, Z.-Y. Han, E. Benchimol, C. Drechsler, J. J. Holstein, Y.-T. Chen, G. H. Clever. Title: “AIE-active metallacycles with adjustable circularly polarized luminescence”
6. S. Ganta, C. Drechsler, A. Baksi, J. J. Holstein, G. H. Clever. Title: “Interlocked Heterobimetallic Cages“
7. C. Drechsler, E. Benchimol, G. H. Clever. Title: “A New Concept for Dissipative Guest Uptake based on Slow Double Cage Formation”

6.3 Conference contributions

1. Koordinationschemie-Treffen 2020, Freiburg, 03.03.2020. Poster title: “Investigation and Simulation of Supramolecular Coordination Cages via Ion Mobility Spectrometry”
2. 5th Summer School SPP1807 “Online” 2021, 04.-05.03.2021. Presentation title: “Investigation and Simulation of Supramolecular Coordination Cages via Ion Mobility Spectrometry”

7 Acknowledgements

Thank you, Prof. Dr. Guido H. Clever, for making this all possible, for letting me contribute to your awesome research, for letting me do my calculations and for being patient with me, for your support, your wisdom and numerous ingenious ideas and for your friendship.

Thank you, Prof. Dr. Stefan M. Kast, for being my second supervisor and thanks to you and your group for igniting my interest in Theoretical Chemistry. It is super important because it often gives the answer to the *why* in Supramolecular Chemistry.

I want to thank Dr. Ananya Baksi for the countless mass and high resolution ion mobility measurements which took many hours of time. Half of the CCS project has been done by her.

I want to thank my students Sümeyra Gürbüz, Pascal Hübner and Mert Acar for their contributions to this work and for the fun time in the lab.

I want to thank Birgit Thormann, Dr. Gabriele Trötscher-Kaus, Maike Wolters, Franziska Klutzny and Laura Schneider for all the great help throughout the years.

I want to thank Dr. David Van Craen for his expertise, his help and the many inspiring discussions.

I want to thank Dr. Julian J. Holstein for his help with the Linux world and with the crystal structures.

I want to thank all group members and collaboration partners whom I had or still have projects with. Thank you for letting me contribute to them.

I want to thank Prof. Dr. Christopher J. Stein, Prof. Dr. Ricardo Mata, Prof. Dr. James Prell, Prof. Dr. Carlos Larriba-Andaluz, Prof. Dr. Stefan Grimme and Prof. Dr. Frank Neese for providing your software free of charge and for your help with the calculations.

I gratefully acknowledge the computing time provided on the Linux HPC cluster at TU Dortmund (LiDO3), partially funded in the course of the Large-Scale Equipment Initiative by the German Research Foundation (DFG) as project 271512359.

Last but not least, thank you to the whole Clever Lab for your collegiality, great support, crucial help, inspiring discussions, fun conversations, joyful lunch breaks and unforgettable parties. You will always be a part of my heart.